Biological and abiotic dissolution of natural, cut and synthetic pyrite surfaces

Dissertation
zur Erlangung des Doktorgrades
der Mathematisch-Naturwissenschaftlichen Fakultät
der Christian-Albrechts-Universität
zu Kiel

vorgelegt von

Dipl.-Min. Katja Etzel

Kiel, im März
2008

Referent:	Prof. Dr. Wulf Depmeier
Korreferent:	Prof. Dr. Astrid Holzheid
Tag der mündlichen Prüfung:	24.04.2008
Zum Druck genehmigt:	Kiel, den 24.04.2008

gez.
Prof. Dr. Jürgen Grotemeyer
(Dekan)

Für meine Familie
und
in memoriam Daniel,
dem es nicht vergönnt war
seine Doktorarbeit zu beenden.

Hiermit erkläre ich an Eides statt, dass die vorliegende Abhandlung, abgesehen der Beratung durch meine akademischen Lehrer, nach Inhalt und Form meine eigene Arbeit darstellt. Ferner habe ich weder diese noch eine ähnliche Arbeit an einer anderen Abteilung oder Hochschule im Rahmen eines Prüfungsverfahrens vorgelegt.

Kiel, den 24.04.2008

gez.

Katja Etzel

Danksagung

Es gibt viele Personen, denen ich zu Dank verpflichtet bin, ohne die es niemals möglich gewesen wäre diese Arbeit zu vollenden. In erster Linie möcht ich meinem Doktorvater Prof. Dr. Wulf Depmeier dafür danken, dass er es mir ermöglicht hat diese Arbeit durchzuführen. Des Weiteren möchte ich der gesamten Gruppe aus Regensburg für die konstruktive Zusammenarbeit und die Durchführung der biologischen Experimente danken, stellvertretend seien hier Prof. Dr. Michael Thomm, Dr. Harald Huber und PD Dr. Reinhard Rachel genannt.

Insbesondere möchte ich mich bei PD Dr. Charles Geiger, PD Dr. Karsten Knorr und Dr. Jan Toporski dafür bedanken, dass sie mich dabei unterstützt haben die Arbeit sprachlich und sachlich korrekt zu verfassen. Frau Brigitte Bey, Frau Marlies Schwitzke, Frau Barbara Mader, Prof. Dr. Michael Czank und Herrn Kay Rath danke ich dafür, dass sie es mir ermöglicht haben 'ihre' Instrumente zu verwenden und mir stets mit Rat und Tat zu Seite gestanden haben. Natürlich möchte ich auch allen denen danken, die ich bis jetzt noch nicht namentlich genannt habe, mich aber in den letzten drei Jahren bei meiner Arbeit und 'allem drum herum' unterstützt haben.

Einen besonderen Dank möchte ich allerdings meiner Familie aussprechen, da es mir ohne deren mentale und finanzielle Unterstützung nicht möglich gewesen wäre diese 'entbehrungsreichen' Zeiten durchzustehen.

Danke!

Contents

List of Figures

List of Tables

Zusammenfassung

Für verschiedene technische Anwendungen ist das kontrollierte Ätzen von Mineraloberflächen von Bedeutung. Da es sich bei Pyrit um einen potentiellen, ungiftigen Kandidaten für photoelektrochemische und photovoltaische Anwendungen handelt, ist es wichtig zu wissen, wie die Oberflächen des Metalsulfids kontrolliert verändert werden können. Die Oxidation von Pyrit kann abiotisch ablaufen aber auch durch Mikroben induziert bzw. beschleunigt werden. Daher beschäftigt sich die vorliegende Arbeit mit der abiotischen und biologischen Oxidation von Pyritoberflächen. Weil natürliche Kristalle oft einen hohen Grad an Verunreinigungen aufweisen, ist ein weiterer Aspekt dieser Arbeit die Synthese von reinen, vielflächigen Pyriteinkristallen. Unter Verwendung des chemischen Gastransports ist es gelungen, Einkristalle in hoher Qualität mit einer Kantenlänge von bis zu 8.5 mm und der Ausbildung von bis zu fünf Formen ({100}, {111}, {210}, {211}, {221}) zu züchten.

In einer Serie systematischer Experimente wurden Ätzmuster als Funktion von Oberflächentyp (natürlich, geschnitten, synthetisch), Oberflächenorientierung, Oxidant (abiotisch, biologisch), Einwirkzeit (ein Tag bis sechs Wochen) und Temperatur (30-85°C) untersucht. Als biologische Oxidanten dienten vier bakterielle sowie vier archaische Stämme. Abiotische Oxidanten waren verschiedene Konzentrationen von Schwefelsäure (0.1, 1, 10 N) und eine gesättigte Lösung von Eisen(III)sulfat.

Zeitaufgelöste Studien zeigten, dass die produzierten Strukturen auf den Oberflächen in Größe und Anzahl mit Verlängerung der Inkubationszeiten zunahmen. Weiter wurde festgestellt, dass mit Erhöhung der Temperatur die Ätzstrukturen ausgeprägter waren. Es wurden signifikante Unterschiede in den Ätzmustern der verschiedenen Oxidanten beobachtet. Archaea und Eisen(III)sulfat produzierten euhedrale Strukturen, deren Formen abhängig von der Symmetrie der jeweiligen Oberfläche sind. Bakterielle Ätzung hingegen produzierte Strukturen, die unabhängig von der Oberflächensymmetrie verlaufen und die duch Schwelfesäure induzierten Strukturen sind sehr schwach ausgeprägt. Im Vergleich der Ätzmuster konnte festgestellt werden, dass die durch Archaea erzeugten am stärksten ausgeprägt waren, gefolgt von denen produziert durch Eisen(III)sulfat. Die kleinsten Strukturen wurden bei bakteriellem Ätzen gefunden. Mit Hilfe des Epifluoreszenz-Mikroskops konnten die Verhältnisse von planktonisch zu sessilen Zellen ermittelt werden. Aus den Verhältnissen konnte geschlossen werden, dass Archaea die Pyritoberflächen sowohl mit dem *Kontakt-* als auch dem *Nicht-Kontakt-*Mechanismus angreifen. Die Analyse der natürlichen und geschnittenen Oberflächen nach den Oxidationsexperimenten zeigte, dass die verwendeten natürlichen Kristalle eine hohe Anzahl an Defekten sowie Unreinheiten aufweisen. Diese Defekte fungieren als bevorzugte Bereiche der Zellanhaftung und als Bereiche beginnender Auflösung. Dies führt dazu, dass auf natürlichen und geschnittenen Oberflächen viele ineinander verwachsene Strukturen sowie Schwammmuster entstanden. Dahingegen ist die Anzahl von Strukturfehlern synthetischer Kristalle geringer, was zu vereinzelten Ätzstrukturen führte. Die Ätzstrukturen auf den synthetischen Oberflächen konnten gut vermessen werde, wodurch es möglich war, die während der Ätzung entstandenen Flächen zu indizieren.

Auch wenn es mit dieser Arbeit gelungen ist, Unterschiede im Ätzverhalten unterschiedlicher Oxidanten auf unterschiedlichen Flächentypen und unterschiedlich orientierten Flächen zu ermitteln, so ist es doch von Nöten, weitere Experimente durchzuführen, um eine Einschätzung abzugeben, ob es bevorzugte Flächen in Bezug auf Zellanheftung bzw. Pyritauflösung gibt.

Abstract

Controlled etching of surfaces is of great interest for several technical applications. Because pyrite is a potential, nontoxic candidate for photoelectrochemical and photovoltaic applications, it is important to know how the surfaces of pyrite can be controllably altered. Pyrite oxidation is a process that can be abiotic and induced through the deployment of microbes. Thus, for better knowledge of abiotic and biological oxidation of pyrite surfaces systematic experiments were performed. And because natural crystals are often impure, the synthesis of high quality pyrite single crystals with diverse forms was studied. High quality crystals with edge lengths of up to 8.5 mm and habits of up to five forms ({100}, {111}, {210}, {211}, {221}) were synthesized with the use of the chemical vapor transport technique.

Etch patterns were studied in a series of experiments as a function of oxidant (biological or abiotic), face-symmetry, surface type (natural, cut, synthetic), duration of exposure (one day to six weeks) and temperature (30 - 85 °C). As biological oxidants, four bacterial and four archaeal strains were used. Abiotic oxidation was performed using different concentrations of sulfuric acid (0.1, 1, 10 N) and saturated solutions of iron(III)sulfate.

Time resolved studies confirm that the degree of surface dissolution increases with incubation time and experiments addressing the effect of temperature showed more pronounced etching effects at higher temperatures. Significant differences in etch patterns were observed after oxidation with the various oxidants. After archaeal and iron(III)sulfate etching euhedral etch pits, showing symmetries of the etched surfaces, were observed. After bacterial oxidation, etch pits having, in some cases, forms that can not be correlated with face-symmetries, were found. Sulfuric acid etching showed very small etch pits. After analyzing all etch patterns, it appears that archaeal etching was more pronounced than etching of all other oxidants, while bacterial etching was least. Epifluorenscence microscopy analysis showed ratios of attached versus planktonic cell, indicating that Archaea used both, *contact* and *non-contact* biooxidation mechanisms to alter surfaces. Dissolution experiments using natural and cut pyrite surfaces showed high numbers of impurities and defects in natural crystals. They served as preferred cell attachment and points where etching commences. The high number of surface defects resulted in superimposed etch pits and 'sponge-like' etch patterns. In contrast, synthetic surfaces showed less defects and etch pits were more stand-alone. These etch pits were measurable, wherefrom it was possible to index faces that occur during etching.

With this study, the effects of various parameters during abiotic and biological dissolution were investigated. However, for a better understanding more study is needed.

Chapter 1

Introduction

Minerals and microorganisms are known and studied for a long time. Often they are connected with each other, for example microorganisms cause mineral precipitation and minerals can, in same cases, be used as an energy source for metabolism of microorganisms. Microorganisms can also influence the distribution of elements in diverse environments at and below the surface of the Earth. Conversely, mineralogical and geochemical factors exert influences on microbial evolution and the microbial communities.

For a long time there was little understanding of the interaction between minerals and microbes. The earliest recorded mining activity that can be attributed to microbes involved the recovery of copper from mine waters at Rio Tinto, Spain in 1670 (Taylor & Whelan, 1943). However the presence of microbes in the leaching fluids was not determined until 1962 (Razzell & Trussell, 1963). The first isolated microbe that was noted for its ability to oxidize sulfur was the bacterial genus *Acidithiobacillus* (formerly known as *Thiobacillus*) by Nathanson (1902). In 1919 Powell & Parr and later Carpenter & Herndon (1933) suggested that sulfide oxidation and acid-mine drainage from coal deposits may be catalyzed by microbes. In 1921 / 22 the acidophilic bacterium, *Acidithiobacillus thiooxidans*, was isolated and identified in soils containing free sulfur and phosphate by Waksman & Jåffe. Rudolfs et al. (1922) reported the microbiological etching of metal-sulfides by an unidentified autotrophic microbe and, thus, the economic importance of the extraction of metals from low-grade sulfide-bearing ores was discovered. The acidophilic autotroph *Acidithiobacillus ferrooxidans* was first isolated by Colmer & Hinkle in 1947. This organism lives in acid-mine drainage ponds, and oxidizes both iron and sulfur (Colmer et al., 1950; Temple & Colmer, 1951; Temple & Delchamps, 1953; Leathen et al., 1953a). By the 1960s, the role of microbes for the oxidation of sulfide had been well established (Bryner et al., 1954, 1957; Lyalikova, 1960; Malouf & Prater, 1961; Silverman et al., 1961). The first scanning microscope

observations of metal-sulfide oxidizing bacteria, *Acidithiobacillus ferrooxidans*, growing on metal-sulfide crystals, were published by Tributsch in 1976. Presently, several metal-sulfide oxidizing organisms are known. They are members of the mesophilic bacteria, such as e.g. *Acidithiobacillus ferrooxidans*, as well as of the thermophilic archaea, e.g. *Sulfolobus metallicus*.

The biological oxidation of sulfides is an important field of research. Biogeochemical dissolution of sulfide minerals is used for the recovery of metals, and can be a source of environmental pollution. Around the world dumps containing sulfides and microbes are present and interactions between both produces acid-mine drainage fields, containing sulfuric acid and hazardous, metal-rich liquids (e.g. Rawlings, 2002). Thus, many investigations addressing interactions between microbes and sulfides were made (e.g. Edwards et al., 1999; Rawlings, 2002; Rohwerder et al., 2003).

The most common metal-sulfide on earth is pyrite (FeS_2). It forms in reducing environments, such as marine sediments, crater lakes, aquifers, water-logged soils, and in exhalative marine hydrothermal systems (Rickard & Luther, 1995). Hence, pyrite can occur in many geologic environments as well as in mine dumps where microbes are present (Trudinger, 1972). Several sulfide oxidizing Bacteria are known and one of the best analyzed pyrite oxidizing organism is *Acidithiobacillus ferrooxidans* (e.g. Edwards et al., 1999; Sand et al., 2006). On the other hand, several sulfide oxidizing Archaea are known, but only a few investigations focusing on archaeal pyrite oxidation exist (e.g. Mikkelsen et al., 2007). Therefore, this work deals with mineral - microbe interactions of bacterial and archaeal strains.

For several technical applications controlled etching of surfaces is of great interest. Thus, a vision of this investigation is to control etching of pyrite surfaces by microbes. Therefore, the effect of biological oxidation of different oxidants on different pyrite surfaces is analyzed. Most known investigations focus on microbiological aspects and only a few investigations address the influence of face-symmetry on biological pyrite oxidation (Keller & Murr, 1982; Ndlovu & Monhemius 2005). However, it is known from abiotic experiments that different faces oxidize in different rates. For example, Guevremont et al. (1998b) demonstrated that oxidation rate for a (111) surface of pyrite is more rapid than for a (100) surface. However, data of biological oxidation rates and etch features as a function of face-symmetry are still missing. Thus, the present study addresses these aspects. It also compares biological with abiotic oxidation.

In most recent investigations, natural sulfides were used for experiments, but they often contain a high concentration of crystal defects and impurities. Thus, for better defined conditions of pyrite oxidation, synthetic crystals could be used and the preparation of synthetic, pure single crystals of pyrite is of great interest. Although large

pyrite crystals are common throughout the world, the growth of synthetic pyrite single crystals generally produced relatively small crystals of a few millimeter size, but of an excellent quality (Fiechter et al., 1986). Thus, another aspect of this work is to synthesize large well-defined single crystals of pyrite with diverse faces for the use in dissolution experiments.

In the literature there are two investigations on biological oxidation of synthetic pyrite. Rodríguez-Leiva & Tributsch (1988) used pyrite single crystals and Sanhueza et al. (1999) pyrite films. Both cultivated *Thiobacillus ferrooxidans* on synthetic pyrite as the only energy source and the main topic of their work was the nature of cell attachment at surfaces, but not as a function of face-symmetry. To fill this gap, the present work addresses the biological oxidation of synthetic pyrite as a function of microbial strain and face-symmetry. So far as the author knows, this work is the first investigation addressing archaeal pyrite oxidation of synthetic pyrite crystals.

In a series of experiments different faces of natural, cut and synthetic pyrite surfaces were etched. For comparison, abiotic oxidation experiments were performed using sulfuric acid and iron(III)sulfate. The biological oxidation experiments were performed using four strains of Bacteria and four strains of Archaea. The oxidation experiments are organized in two sections. The first deals with abiotic and biological oxidation effects on natural and cut {100}, {111} and {210} surfaces. The biological experiments are performed using eight different microbial strains (four mesophilic Bacteria and four thermophilic Archaea) over time intervals from one day up to six weeks. Abiotic experiments are performed with sulfuric acid with different concentrations and iron(III)sulfate solution at different temperatures. The surfaces were characterized before and after exposure to the oxidizing conditions. Experiments were performed to address the characterization of etch patterns as a function of oxidant, surface type, surface symmetry, duration of exposure and temperature. The second section deals with abiotic and biological etching experiments of synthetic pyrite crystals. Here, {100}, {111}, {210}, {211} and {221} faces are involved. The biological oxidation experiments of synthetic pyrite were performed using two archaeal strains. In abiotic experiments iron(III)sulfate at two temperatures was used as oxidant. Again, the surfaces were characterized before and after exposure to the oxidizing conditions. Experiments were performed in time intervals of one, two and four weeks, addressing the characterization of etch patterns as a function of oxidant, face-symmetry, duration of exposure and temperature.

During the experiments, archaeal strains showed more pronounced surface effects than bacterial strains. And abiotic etching with iron(III)sulfate at higher temperatures was more effective than at lower temperatures, while etching effects of sulfuric acid were

negligible. Distinct differences of etching effects were found as a function of surface treatment. On cut surfaces the largest etch effects were observed and the shape of etching features after archaeal etching were strongly dependent of face-symmetry.

Concerning the partitioning of this study, the work is organized as follows: First pyrite, with its physical and chemical properties, will be discussed (Chapter 2). An overview of the microbiology is given, with a description of the microorganisms in Chapter 3. An introduction into the theory of abiotic and biological catalyzed pyrite oxidation is given in Chapter 4. The focus of Chapter 5 is the description of the experimental setup and sample handling. In Chapter 6 the results of the various experiments are given. The results of the dissolution of natural and cut pyrite surfaces are presented in Chapter 6.1. The experimental results of pyrite growth are given in Chapter 6.2 and the results of the dissolution of synthetic pyrites are summarized in Chapter 6.3. Discussion of the experiments is found in Chapter 7 and finally in Chapter 8 a summary with an outlook is presented.

Chapter 2

Metal-sulfide - pyrite

The purpose of this chapter is to review the physical and chemical properties of the metal-sulfide pyrite, FeS_2. In the first section, the Fe-S system is introduced, while in the second section the crystal structure of pyrite and properties of the different surfaces ({100}, {111}, {210}, {211} and {221}) will be given. The third section describes the formation of pyrite single crystals.

2.1 The Fe-S system

Sulfides are an important mineral group that includes many ore minerals. The chemistry of sulfides is of importance from an environmental perspective because metal-sulfides constitute a major component of waste material from mining processes and are accessory minerals in coal. Most sulfide minerals are opaque with distinctive colors and characteristic colored streaks. The general formula for sulfides is X_mS_n, where X represents a metal. Many sulfides show ionic or covalent bonding, whereas others show metallic bonding characteristics. In general, metal-sulfur bonds are weaker than metal-oxygen bonds because the sulfide ion is considerably larger than the oxide ion. This feature makes sulfides soft compared to rock-forming oxides and silicates, thus, sulfides show much lower melting temperatures (Burt et al., 2006).

The Fe-S system has been studied in detail by a number of investigators (e.g. Kullerud, 1967; Ehlers, 1972). Within the Fe-S system several minerals are known, having different composition and structures. The phase diagram above 400°C is shown in Fig. 2.1. The composition of the minerals in the Fe-S system are between FeS and FeS_2, starting with troilite, FeS, mackinawite, FeS_{1-x}, several compositions of $Fe_{1-x}S$, known as pyrrhotite, gamma iron sulfide, Fe_2S_3, symthite, Fe_9S_{11}, greigite, Fe_3S_4, and finally the two polymorphs marcasite and pyrite FeS_2.

Troilite, stoichiometric FeS, is stable below 140°C and crystallizes in the hexago-

nal system, with $a = 5.965\,\text{Å}$ and $c = 11.750\,\text{Å}$ (Gronvold & Haraldsen, 1952; Yund & Hall, 1968). Above 140°C, FeS has the structure of high-temperature hexagonal pyrrhotite whose composition range extends over a considerable distance across the system. Although a common constituent of meteorites, troilite is found only occasionally in terrestrial environments, usually with low-temperature hexagonal pyrrhotite (Craig & Scott, 1974).

Mackinawite, FeS_{1-x}, is a relatively rare tetragonal mineral of near FeS composition and was first described by Evans et al. (1964). It crystallizes in space group $P\,4/nmm$, with $a = 3.675\,\text{Å}$ and $c = 5.030\,\text{Å}$ (Evans et al., 1964). It is found either with troilite

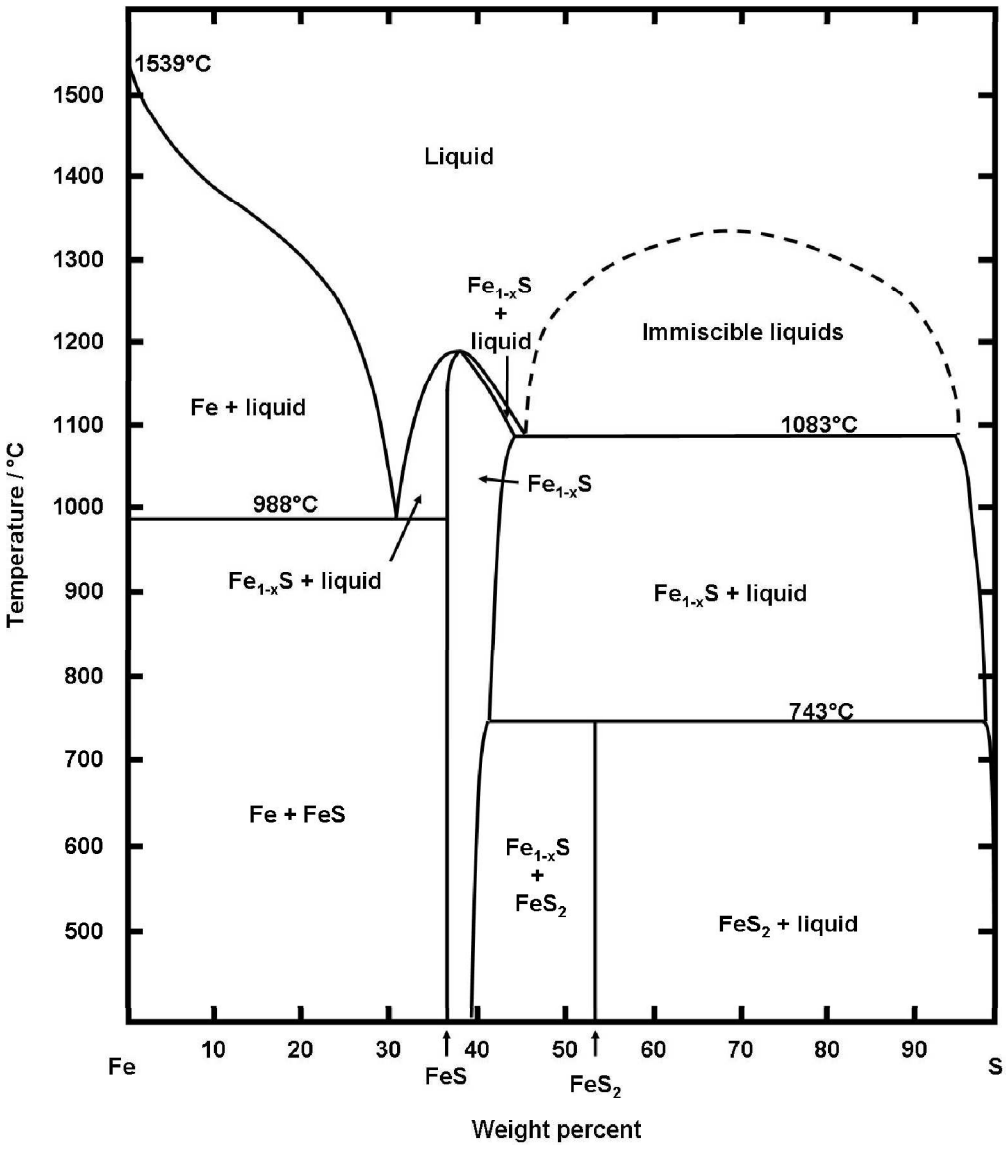

Figure 2.1: The system Fe-S (after Kullerud, 1967).

or with low-temperature pyrrhotite in a variety of geological environments (Kullerud, 1967). Little is known about the thermal stability of mackinawite, therefore it is not shown as stable phase in Figure 2.1.

Pyrrhotite, $Fe_{1-x}S$, varies in composition from 50 to 44 mole percent iron. It can crystallize in several structure types; hexagonal (Nakazawa & Morimoto, 1971; Morimoto et al., 1971), orthorhombic (Morimoto et al., 1971), monoclinic (Mukherjee, 1969) and triclinic (Clark, 1966) structures of pyrrhotite are known, with a variety of cell-parameters (summary found in Craig & Scott, 1974, Table CS-1). Pyrrhotite melts congruently and exists in an eutectic melting relationship with iron. A detailed description of the various pyrrhotite phases is given by Craig & Scott (1974).

Gamma iron sulfide, Fe_2S_3, has not been found in nature, but has been precipitated from an aqueous sulfide solution at 60°C (Yamaguchi & Wada, 1973). It has a spinel structure ($F\,d3m$, $a = 9.87$ Å) similar to greigite. Nothing is known about its thermal stability, wherefore it is not shown as stable phase in Figure 2.1.

Smythite, Fe_9S_{11}, has a pseudorhombohedral structure related to that of monoclinic pyrrhotite (Taylor & Williams, 1972). It occurs as exsolution lamella in monoclinic pyrrhotite (Bennett et al., 1972). Natural smythites contain 0.4 to 7.5 wg % Ni. Little is known about the stability of smythite, wherefore it is not shown as a stable phase in Figure 2.1.

Greigite, Fe_3S_4, is another poorly known phase of the Fe-S system that crystallizes in the spinel structure ($F\,d3m$, $a = 9.876$ Å; Uda, 1967). It is found in low temperature environments. Because of its unknown thermal stability, it is not shown as a stable phase in Figure 2.1.

The most common phase of the Fe-S system is pyrite. Pyrite, FeS_2, is stable up to 743°C, where it melts incongruently to form pyrrhotite and an almost pure sulfur liquid (Ehlers, 1972). Below 400°C the phase-relationships become more complex due to the polymorphism of pyrrhotite and the formation of additional compounds. The structure of pyrite is discussed in detail below.

Marcasite, FeS_2, is a polymorph of pyrite and crystallizes in the orthorhombic space group $P\,mmm$ with $a = 4.436$ Å, $b = 5.414$ Å and $c = 3.381$ Å (Buerger, 1937). The marcasite structure type is related to that of rutile and $CaCl_2$. Buerger (1934) proposed that pyrite and marcasite have slightly different compositions. Marcasite is slightly deficient in sulfur relative to pyrite which was nearly stoichiometric FeS_2. Kullerud (1967) found that marcasite could invert to pyrite as low as 150°C in the presence of excess sulfur, but not below 400°C in the absence of sulfur.

2.2 The crystallographic properties of pyrite

Pyrite, FeS_2, was one of the first crystal structures that was solved by X-ray diffraction (Bragg, 1913). It has cubic symmetry as shown in Fig. 2.2. Pyrite crystallizes with the space group $Pa\bar{3}$ (No. 205) including four formula units of FeS_2 per unit cell (a = 5.418 Å; Parker & Whitehouse, 1932). In the pyrite structure, sulfur ions occur as S_2 dumbbells. Further, the pyrite structure is related to the NaCl structure, where the iron atoms and centers of S_2 dumbbells resemble the sodium and chlorine atoms, respectively. Thus, the iron atoms are arranged in a face-centered-cubic (fcc) sublattice in which sulfur atoms are embedded, occupying positions along the $\langle 111 \rangle$ directions, thus the ions occupy the Wyckoff positions 4a and 8c, respectively. The 24 coordinates of the eight sulfur atoms in the unit cells are described in $Pa\bar{3}$ by a single parameter u. The coordinates of the iron and sulfur in the unit cell are:

$$\text{Fe} \qquad 0,0,0 \quad 0,1/2,1/2 \quad 1/2,1/2,0 \quad 1/2,0,1/2$$

and

$$\text{S} \quad \pm \quad (u,u,u \quad u+1/2,1/2\text{ -}u,u \quad \text{-}u,u+1/2,1/2\text{ -}u \quad 1/2\text{ -}u,\text{ -}u,u+1/2).$$

The fractional coordinate u has a value between 0.384 and 0.386 (Zwinscher, 1995). Pyrite possesses two different centers of inversion in its structure. One inversion center is located at the sites of the iron atoms, and the second is located at the center of S_2 units.

Pyrite consists of two different bonds; the Fe-S and S-S bonds. The bond lengths of Fe-S and S-S are approximately 2.262 Å and 2.177 Å, respectively. Each iron atom is coordinated by six sulfur atoms in a slightly distorted octahedron and each sulfur atom is coordinated by three iron atoms and one sulfur atom in a distorted tetrahedron. The FeS_6 octahedra are linked through corner sharing (Fig. 2.3; Ndlovu & Monhemius, 2005). The S-S bond is a unique characteristic of the pyrite structure type and the S_2 group can be considered as a distinct structural and chemical unit (Nesbitt et al., 1998).

Pyrite has been found in over 80 different crystal forms, but usually it is found in three main forms (Dana, 1903). The most common crystal forms including their symmetries, are pictured in Fig. 2.4, the hexahedron, octahedron and pentagondodecahedron which are terminated by the {100}, {111} and {210} faces, respectively (Murowchick & Barnes, 1987). Rarely, pyrite occurs in the form of a rhombic dodecahedron terminated by the {110} faces.

There has long been interest in deviations of pyrite stoichiometry from the ideal ratio and its impact on properties. Ideally pyrite has an atomic ratio S : Fe = 2 and

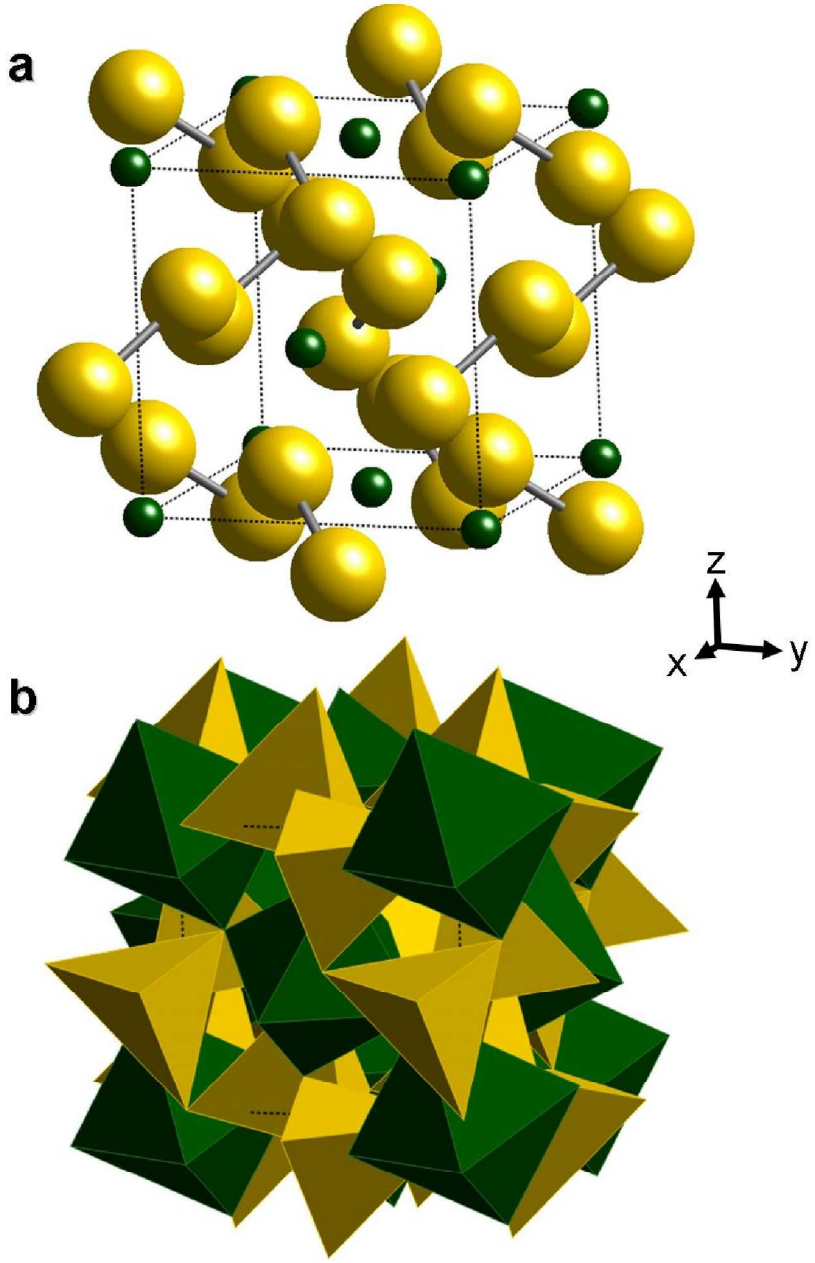

Figure 2.2: Ball & stick and polyhedral models of the structure of pyrite, $Pa\bar{3}$. a) The green and yellow spheres represent the iron and sulfur atoms, respectively. Fe and S_2 centers are arranged in a face-centered cubic lattice, similar to the NaCl structure (Fe and S_2 centers resemble the positions of sodium and chlorine, respectively). b) The green and yellow polyhedron represent the coordination polyhedra surrounding the iron and sulfur atoms, respectively. Fe atoms are six-fold coordinated by S atoms (octahedron), while the latter are four-fold coordinated by three Fe atoms and another S atom (tetrahedron). Graphics were drawn with the software *CrystalMaker* (Palmer, 2000).

a density of $\rho = 5.01\,\mathrm{g/cm^3}$. Buerger (1934) summarized the chemical analysis and density data obtained from natural samples. Smith (1942) concluded that natural crystals with S : Fe ratios less than 2 have iron atoms residing on sulfur positions because their densities were greater than the theoretical value of $5.01\,\mathrm{g/cm^3}$. On the other hand, the data of Juza et al. (1932) and Birkholz et al. (1991) suggest missing sulfur atoms in the lattice. Birkholz et al. (1991) concluded that sulfur deficiency is due to Schottky defects. Ellmer & Hopfner (1997) undertook a detailed analysis of earlier work to the extent of non-stoichiometry and, together with theoretical arguments concerning the energetics of vacancy formation, concluded that deviations from ideal stoichiometry do not exceed 1 at %. Considerable interest in the electrical properties of pyrite has arisen partly because of its possible use in photoelectrochemical and photovoltaic applications, particularly in solar cells. Excellent reviews on the subject are provided elsewhere, for example, by Ennaoui & Tributsch (1984).

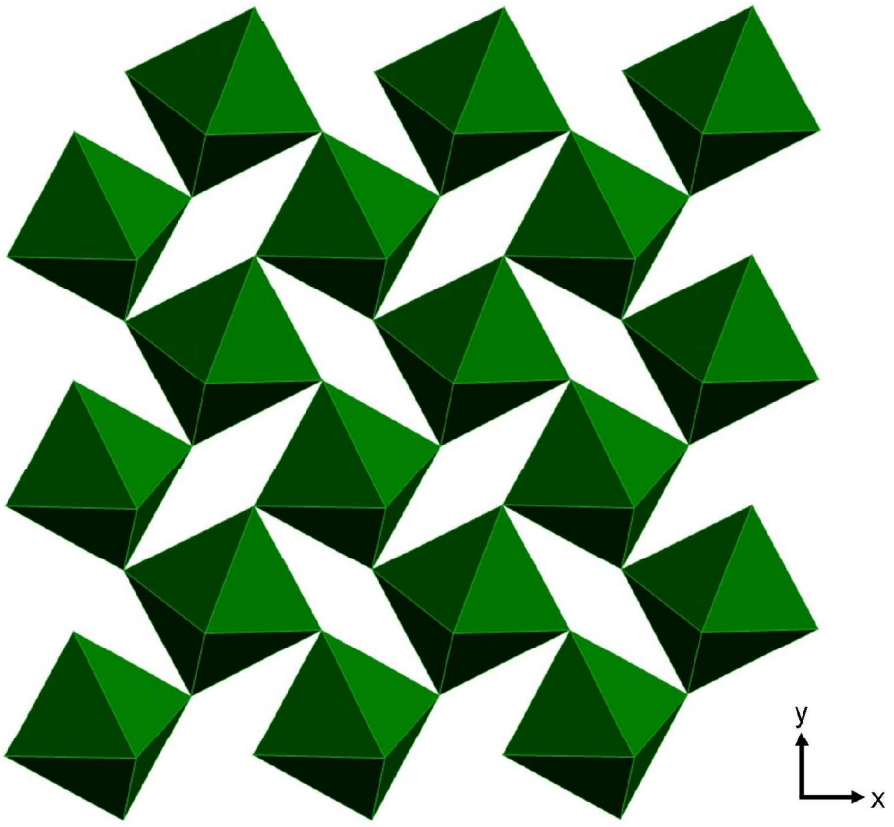

Figure 2.3: Projection on (001) of the pyrite structure, showing a polyhedral model for the Fe atoms, shown as FeS_6-octahedra, in the pyrite structure. The S atoms reside at the corners of the octahedra and are not shown.

Pyrite is diamagnetic and semiconducting properties are observed. Natural pyrite exhibits both n- and p-type semiconductor properties, sometimes within the same crystal (Pearce et al., 2006; Abraitis et al., 2004). It has been suggested that naturally grown pyrite formed at low temperature (up to 390°C; Willeke et al., 1992) tends to be p-type (iron-deficient), whereas high-temperature pyrite tends to be n-type (sulfur-deficient). The same was observed for synthetic crystals, however, usually they appear to be n-type (Willeke et al., 1992; Schieck et al., 1990). Pyrite is an interesting candidate for photovoltaic energy conversion and its non-toxicity and its composition from abundant elements were considered as particular advantages of pyrite, e.g. as cathodic material in thermal batteries, based on Li(alloy) / FeS_2 electrochemical system (Jaegermann & Tributsch, 1983; Ennaoui et al., 1985; Pemsler et al., 1990).

Pyrite has a poor to no cleavage, yielding rough fracture (Rosso & Vaughan, 2006) and vacancies are common on sulfide mineral surfaces. By forming vacancies, surfaces are stabilized during alteration processes and attain charge neutrality. Formation energies for neutral vacancies in sulfide minerals can be addressed by using molecular modeling approaches (Fiechter, 2004).

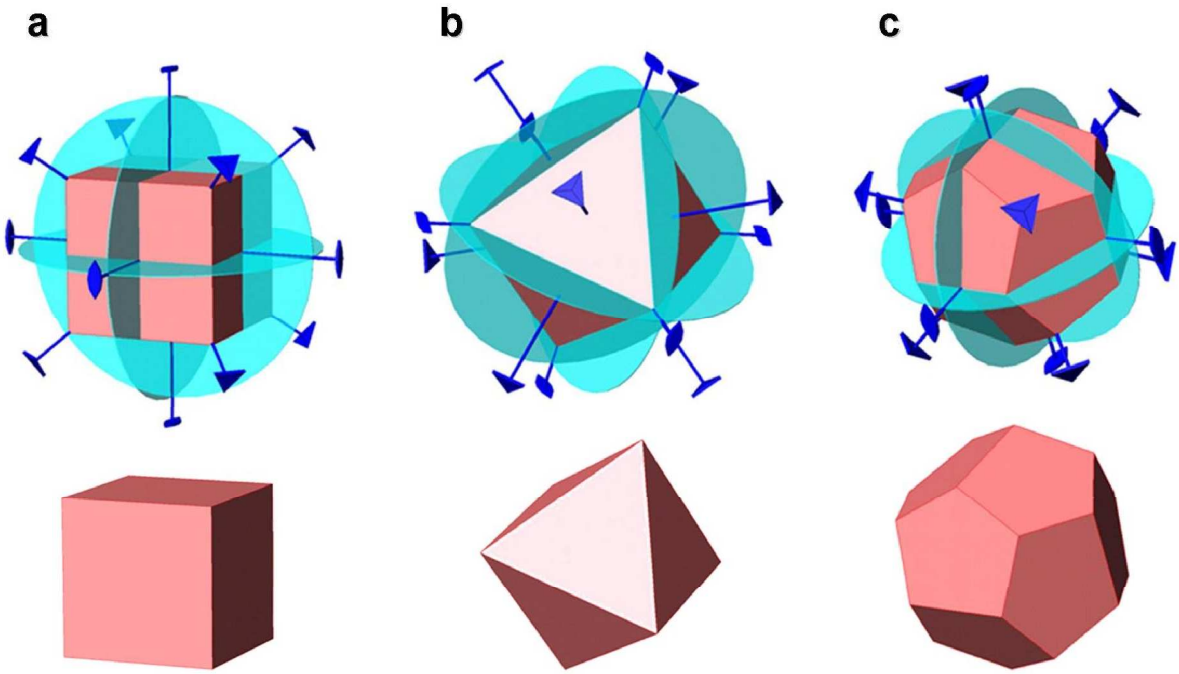

Figure 2.4: Common crystal forms of pyrite shown with symmetry elements, three mirror planes perpendicular to each axis, three two-fold axes of rotation parallel to each axis and four three-fold inversion axes of rotation ($\bar{3}$) parallel $\langle 111 \rangle$ directions. a) hexahedron, {100}, b) octahedron, {111}, and c) pentagondodecahedron, {210}.

However, natural pyrite can contain a host of minor and trace elements, occurring up to several percent, at the position of iron atoms: Ag, Au, Cd, Co, Cu, Hg, Mo, Ni, Pb, Ru, Sn, Tl, Zn and for sulfur: As, Bi, Sb, Se, Te (Abraitis et al., 2004).

2.2.1 Structural defects

Imperfections in crystal structures are classified according to their type such as point defects, line defects, or plane defects (Fig. 2.5). Point defects are Schottky, Frenkel and impurity defects. The absence of an ion in the crystal lattice is termed a Schottky defect (Fig. 2.5a). For electrical neutrality, the total charge on the cation vacancies must equal that of the anion vacancies. A Frenkel defect (Fig. 2.5b) represents the absence of an ion from its proper structural site and a dislocation of this same ion at an interstitial site. This is more common for cations than anions, because anions tend to be larger. Impurity defects will change the chemical composition of a 'perfect' crystal (Figs. 2.5c, d). The amounts of impurities are generally so small (ppm to ppb) that they cannot be detected analytically. However, some properties such as color may be strongly affected by trace impurities.

Line defects are commonly known as dislocations, because they create an offset in the crystal structure. There are two types: edge dislocations (Fig. 2.5e) and screw dislocations (Fig. 2.5f). The presence of line defects allows a crystal to deform under stress. Screw dislocations are structural defects arranged along a screw axis that normally is not present in the structure. Such spiral steps are of importance during crystal growth, because new ions or atoms, which are added to the outside surface of a growing crystal, are best housed along the edge. If screw dislocations arise from step defects, those defects do not end. Screw dislocations run through the entire crystal.

Planar defects represent two-dimensional zones with slightly misoriented blocks. In ideal crystals the structure is regarded as a rigorously continuous and symmetric repeat of unit cells. This implies short-range as well as long-range order. In real crystals areas may be slightly misoriented, as in a mosaic structure. Each part in the mosaic has short-range order but the whole crystal lacks long-range order. Another planar defect is a stacking fault (Fig. 2.5g) in which a regular sequence of atom-layers is interrupted by an improperly positioned layer, or when one of the ideally required layers is missing. Examples of this are sequences of ions (or atoms) in cubic closest packing interrupted by a layer from a hexagonal closest packing sequence.

As all these defects are expressed on the crystal surface, defects such as steps, kinks, and vacancies can have a significant effect on the reactivity of surfaces. The structural environments around atoms at defect sites are different than the environment of a atom on a 'perfect' surface. These structural differences can affect the local charge distribution and create dipole moments that change the local chemical behavior of the surface. Steps and kinks can also play an important role in crystal growth and have a strong influence on resulting crystal habits. Different experimental techniques (e.g. Scanning tunneling microscopy; Eggleston & Hochella, 1992) have shown that structural defects

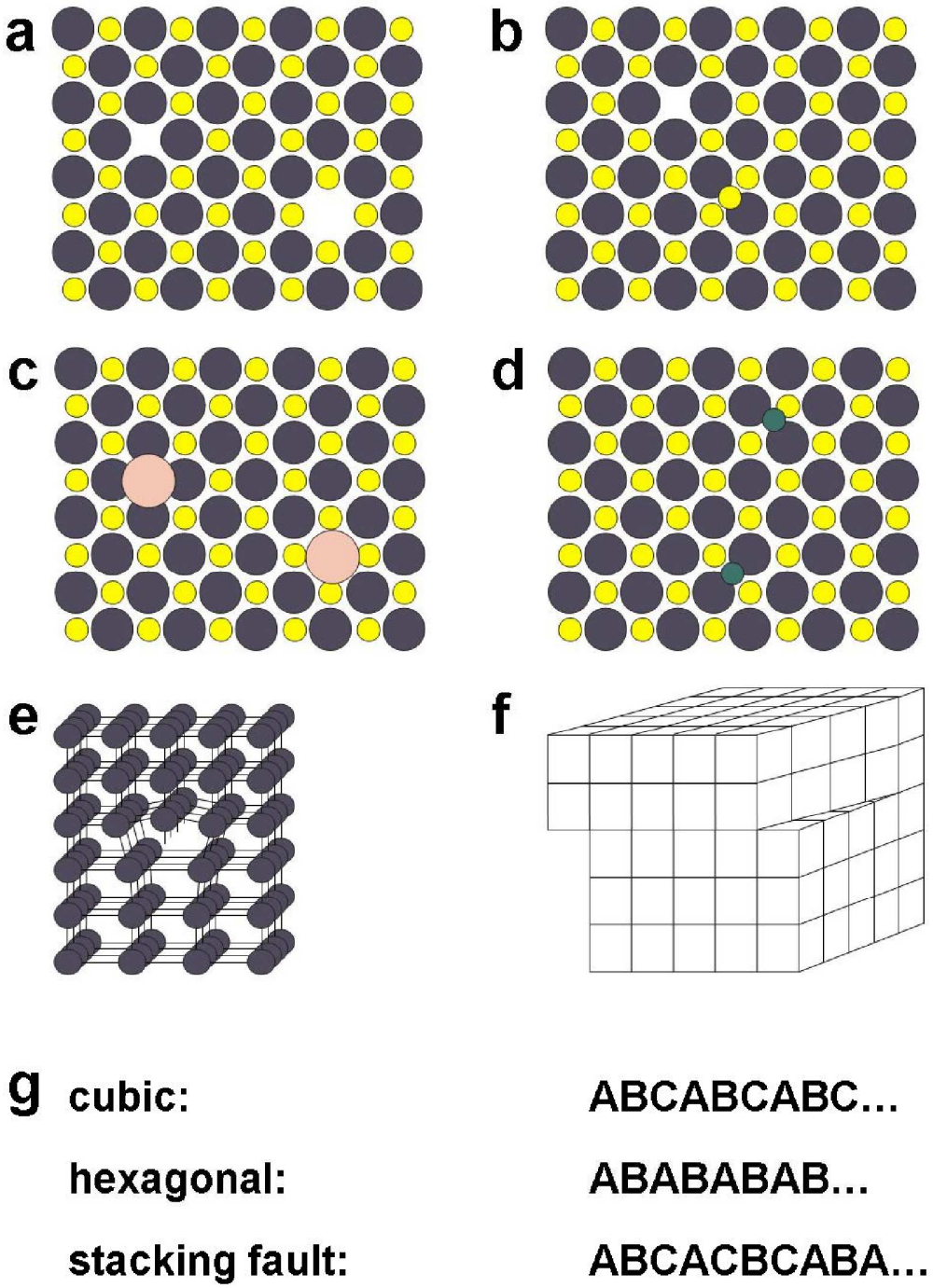

Figure 2.5: Structure defects of minerals. (a) Schottky defect consisting of a single cation and a single anion vacancy. (b) A Frenkel defect consists of a vacant cation site with cations occupying an interstitial position, that is not normally occupied in the ideal structure. (c) Impurity in the form of a Schottky defect. (d) Impurity in the form of a Frenkel defect. (e) Edge dislocation in a simple cubic lattice. (f) Screw dislocation. (g) Layer stacking sequence of cubic and hexagonal areas.

(or imperfections) on an atomic scale are common in crystals. Such imperfections affect basic properties of crystalline materials such as strength, conductivity, mechanical deformation, color and serve as areas where dissolution commences (e.g. Rosso et al., 2000).

2.2.2 Surfaces

The structure of a surface plays a key role in its reactivity. Different faces of a mineral not only expose different geometries but also different atomic arrangements. A classification of surfaces was developed by Tasker (1979). Tasker envisioned three surface types of an ionic crystal as based on the electrostatic stability of their cation and anion arrangements (Fig. 2.6). Type I surfaces consist of planes containing both cations and anions where each plane is charge neutral. Type II surfaces are composed of alternating planes of anions and cations that are arranged in such a way that no net surface dipole moment exists. Type III surfaces are also composed of alternating charged planes, but are arranged in such a way that there is a permanent dipole moment normal to the surface. Type III surfaces are termed polar surfaces and they have large surface energies and are unstable. The surface types I and II are non-polar and are stable with respect to reconstruction.

In the rock salt structure type, {100} and {210} surfaces are type I. Faces {211} and {221} are combinations of type I and II, whereas {111} surfaces are polar, type III surfaces. To explain the occurrence of these surfaces, Tasker (1979) concluded that {111} surfaces must be stabilized by a more complex defect structure, which is embodied in surface roughening. Because the pyrite structure is closely related to the rock salt structure their surface behavior should be similar. It is observed that pyrite {100} surfaces are the most common and the roughness of {111} faces is usually visible

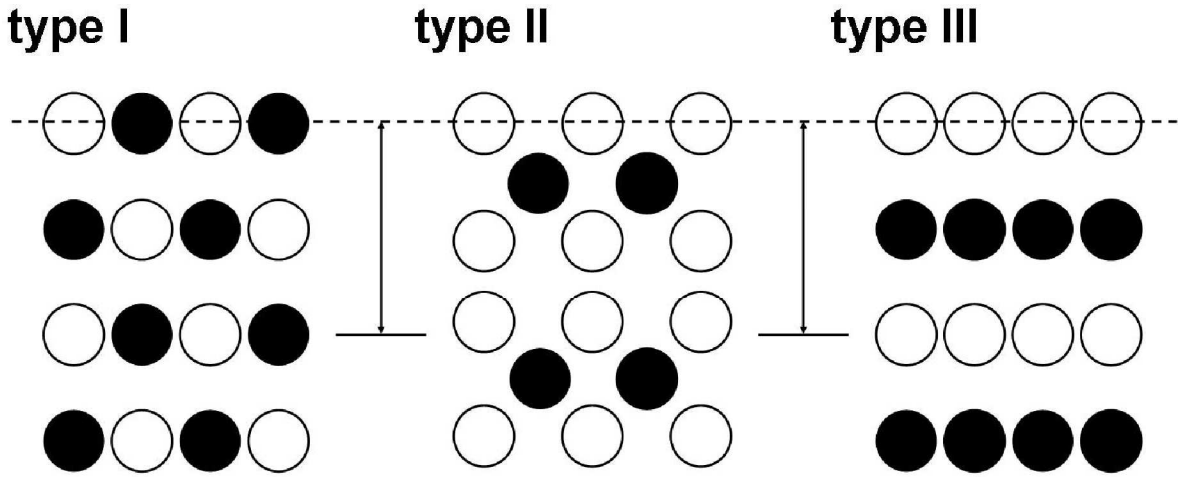

Figure 2.6: Surface classification, according to Tasker (1979), based on the structure of the repeat unit (indicated by arrows) perpendicular to the surface (dashed line). Type I and II surfaces are non-polar, charge neutral and stable, whereas a Type III surface is polar and unstable.

macroscopically.

According to the calculations of Hung et al. (2002b), the relative activity for pyrite faces follows the order: {210} > {111} > {100}. Thus, the {210} surface is one of the less stable for pyrite. However, stability calculations of pyrite {211} and {221} are not available.

Surface structure of pyrite {100}

The structure of the {100} surfaces of pyrite is drawn schematically in Fig. 2.7. The 2D unit cell of the surface describes a square, with the repeat vector length of the lattice parameter of the unit cell ($a = 5.418$ Å in the model). The unsaturated atoms at the surface layer are: iron atoms, five-fold coordinated by sulfur atoms and sulfur atoms that are three-fold coordinated by two iron atoms and one sulfur atom.

The surface energies of {100} were calculated by several investigators, e.g. Hung et al. (2002b). It was found that an expansion and contraction of atomic planes is concentrated at the upper few atomic planes and rapidly damped within a few atomic layers of the surface (Rosso & Vaughan, 2006). Owing to the reduced coordination at the surface, the uppermost sulfur layer expands outward, while the uppermost iron layer contracts. The uppermost Fe-S bond lying closest to the [001] direction shortens by approximately 0.1 Å. The uppermost S-S bond length remains unchanged (Andersson et al., 1994; Cai & Philpott, 2004; Hung et al., 2002a). Several studies (Eggleston & Hochella, 1992; Siebert & Stocker, 1992; Eggleston et al., 1996) have shown that the {100} surfaces of pyrite consist of regions having short range order characterized by imperfections such as steps.

Surface structure of pyrite {111}

Despite the fact that the {111} surfaces are stable, prominent growth faces of pyrite, they are not planes of weakness in the structure that can be cleaved. Such surfaces of pyrite have been shown by several investigations to be complex (Hochella et a., 1998). The {111} surface of pyrite can either be sulfur or iron terminated (Guevremont et al., 1998b). Several computational investigations of the structure of pyrite {111} are available (de Leeuw et al., 2000; Rosso, 2001; Hung et al., 2002b). The hexagonal 2D unit cell of the surface describes a diamond, with the repeat vector length of $a = 7.662$ Å. There are unsaturated iron atoms at the surface layer, three-fold coordinated by sulfur atoms.

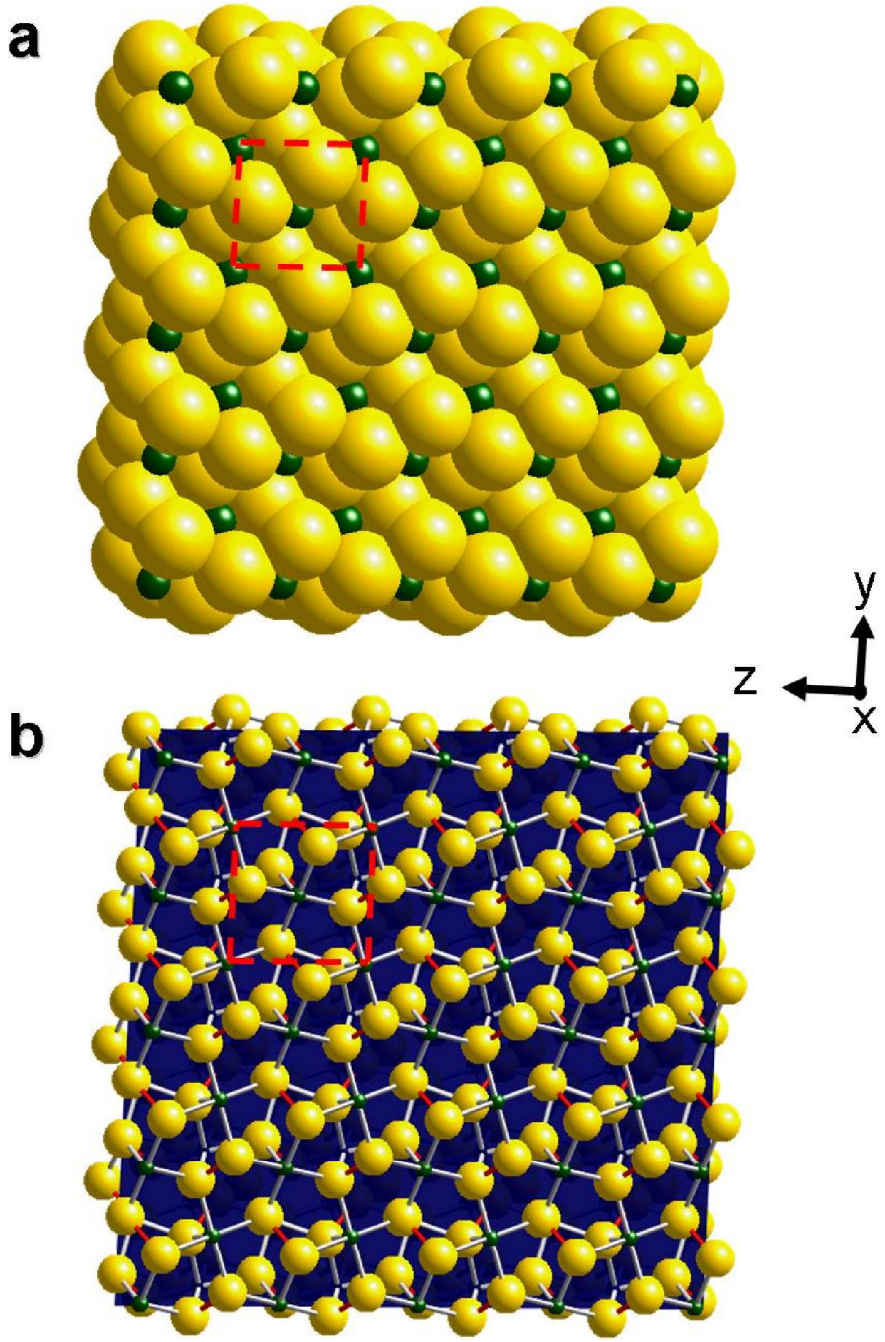

Figure 2.7: (100) surface structure of pyrite, showing the square 2D unit cell (red dashed square), with cell parameter $a = 5.418$ Å; yellow and green balls represent the S and Fe atoms, respectively; a) space filling model, b) ball & stick model including the bonds, red S-S, grey Fe-S. At the surface, unsaturated atoms are present, one type of iron atoms with five bonds to neighboring sulfur atoms and one type of sulfur atoms, with two bonds to iron atoms and one to another sulfur atom. Graphics were drawn with the software *CrystalMaker* (Palmer, 2000).

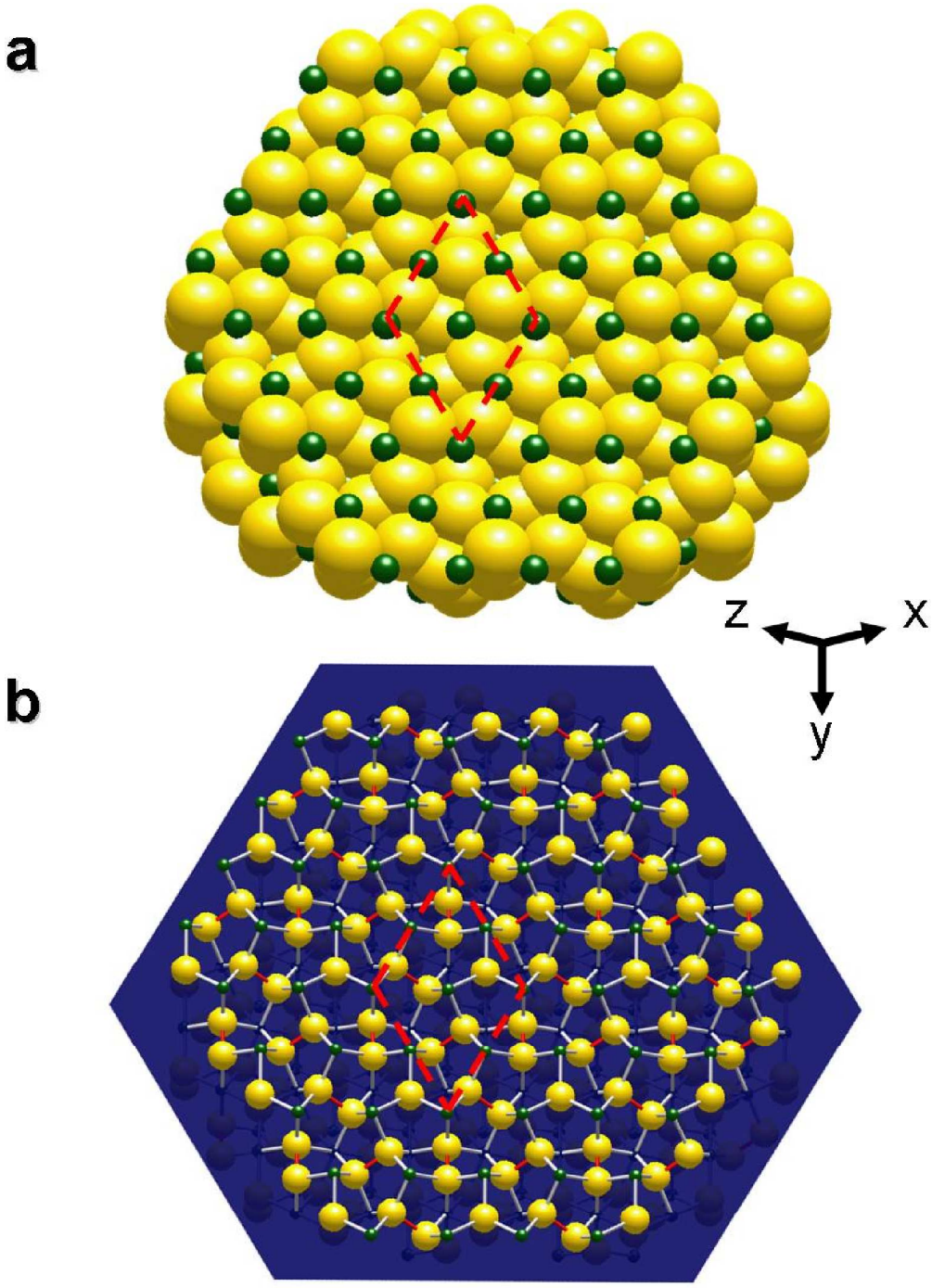

Figure 2.8: (111) surface structure of pyrite, showing the hexagonal 2D unit cell (red dashed square), with cell parameters $a = 7.662$ Å, $\gamma = 120°$; yellow and green balls represent the S and Fe atoms, respectively; a) space filling model, b) ball & stick model including the bonds, red S-S, grey Fe-S. At the surface unsaturated Fe atoms are present, with three bonds to neighboring sulfur atoms. Graphics were drawn with the software *CrystalMaker* (Palmer, 2000).

Surface structure of pyrite {210}

The structure of {210} surfaces is shown in Fig. 2.9. The 2D unit cell of the surface describes a rectangle with the repeat vector lengths of $a = 5.418$ Å and $b = 12.115$ Å. There are unsaturated atoms at the surface layer. The charge-neutral {210} surface is terminated by alternating rows of four- and five-fold coordinated iron atoms, as well as three-fold coordinated sulfur atoms (Fig. 2.9). The iron atoms are coordinated by sulfur atoms and the sulfur atoms are coordinated by two iron and one sulfur atom. Density-functional theory calculations of Hung et al. (2002a) have shown that both the four- and five-fold coordinated iron atoms contract the surface, decreasing the Fe-S distance underneath by approximately 0.1 Å.

Surface structure of pyrite {211}

Little is known about the {211} surfaces of pyrite. Because these surfaces are of interest for this study, Fig. 2.10 shows the structure of a (211) surface including the rectangular 2D unit cell with repeat vector lengths of $a = 7.662$ Å and $b = 9.384$ Å. The {211} surfaces are terminated by alternating rows of three- and five-fold coordinated iron atoms, as well as two- and three-fold coordinated sulfur atoms (Fig. 2.10). The iron atoms are coordinated by sulfur atoms. The two-fold coordinated sulfur atoms are coordinated by one iron and one sulfur atom, while the three-fold coordinated sulfur atoms are coordinated by one sulfur and two iron atoms.

Surface structure of pyrite {221}

In addition little is known about the {221} surfaces of pyrite, however, the surfaces are also of interest for this study, Fig. 2.11 shows the structure of a (221) surface including the 2D unit cells, with the repeat vector lengths of $a = 7.662$ Å, $b = 12.115$ Å and $\gamma = 71.565°$. The {221} surfaces are terminated by alternating rows of three- and four-fold coordinated iron atoms, as well as two- and three-fold coordinated sulfur atoms (Fig. 2.11). The iron atoms are coordinated by sulfur atoms. The two-fold coordinated sulfur atoms are coordinated by one iron and one sulfur atom, while the three-fold coordinated sulfur atoms are coordinated by one sulfur and two iron atoms.

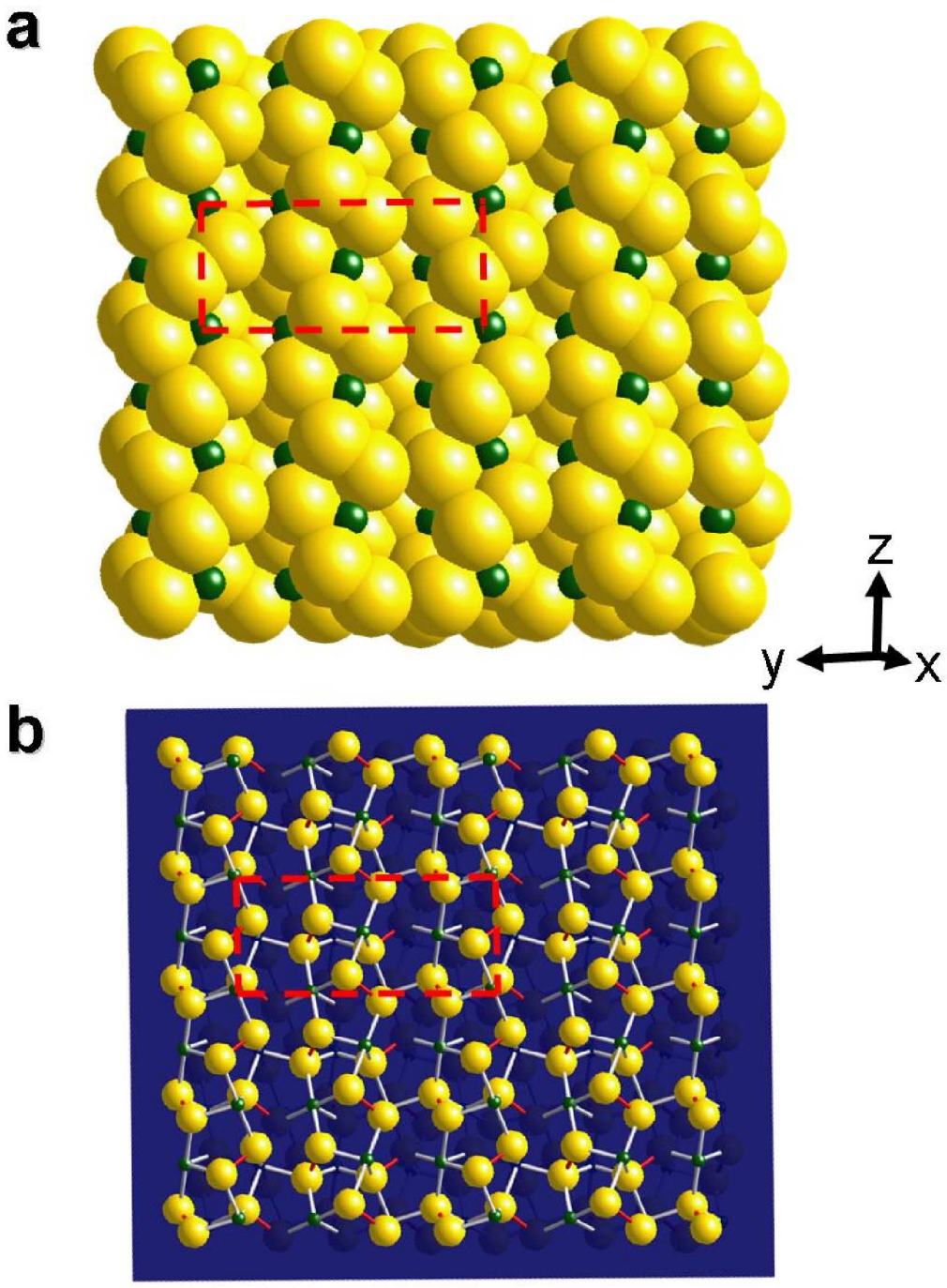

Figure 2.9: (210) surface structure of pyrite, showing the rectangular 2D unit cell (red dashed square) with cell parameters $a = 5.418\,\text{Å}$, $b = 12.115\,\text{Å}$; yellow and green balls represent the S and Fe atoms, respectively; a) space filling model, b) ball & stick model including the bonds, red S-S, grey Fe-S. At the surface unsaturated atoms are present, two types of iron atoms with the first having four and the second five bonds to neighboring sulfur atoms and one type of sulfur atoms, with two bonds to iron and one to another sulfur atom. Graphics were drawn with the software *CrystalMaker* (Palmer, 2000).

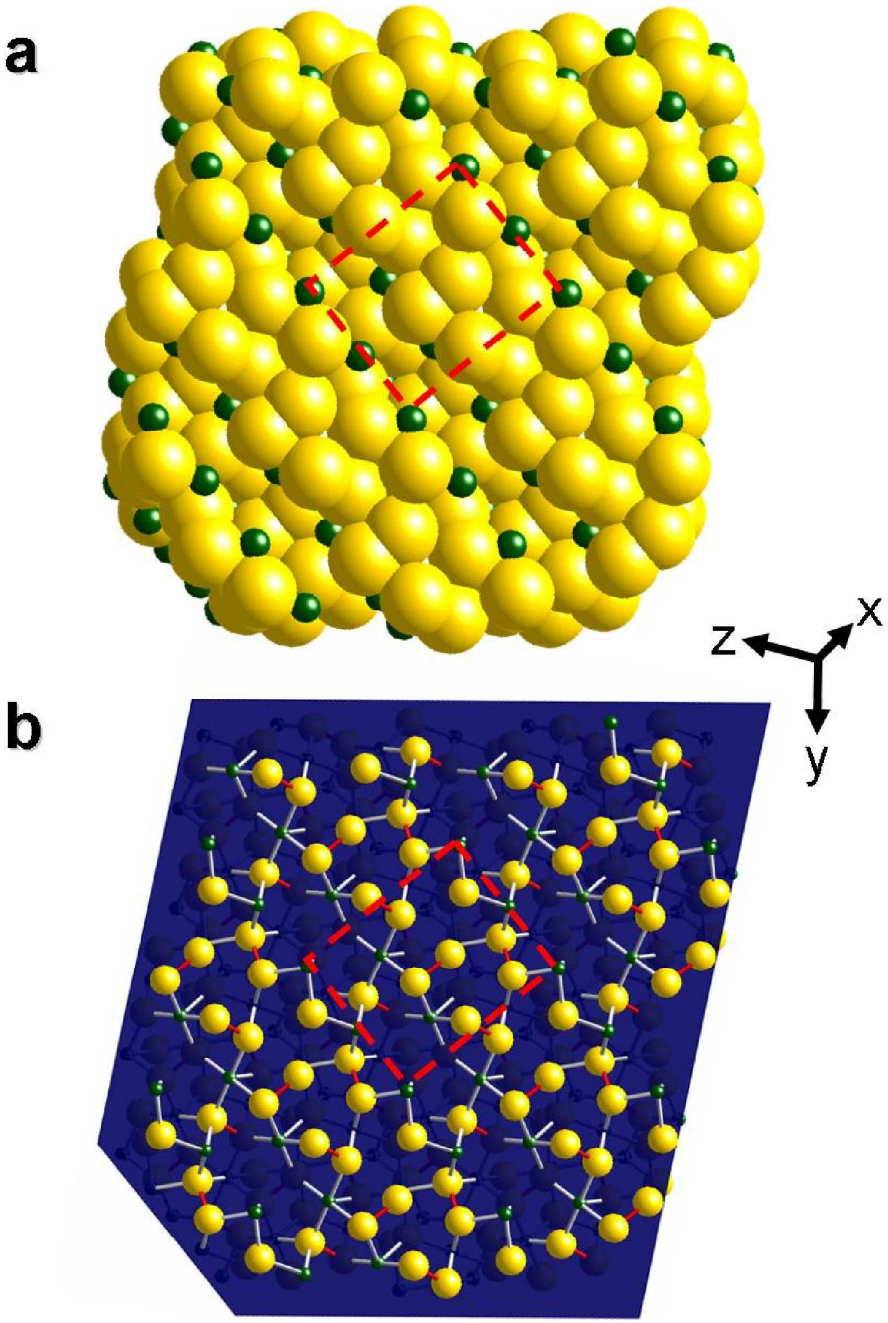

Figure 2.10: (211) surface structure of pyrite, showing the rectangular 2D unit cell (red dashed square), with cell parameters $a = 7.662\,\text{Å}$, $b = 9.384\,\text{Å}$; yellow and green balls represent the S and Fe atoms, respectively; a) space filling model, b) ball & stick model including the bonds, red S-S, grey Fe-S. At the surface unsaturated atoms are present, two types of iron atoms with the first having three and the second five bonds to neighboring sulfur atoms and two types of sulfur atoms, with the first having one bond to an iron and one to another sulfur atom and the second having two bonds to iron and one to another sulfur atom. Graphics were drawn with the software *CrystalMaker* (Palmer, 2000).

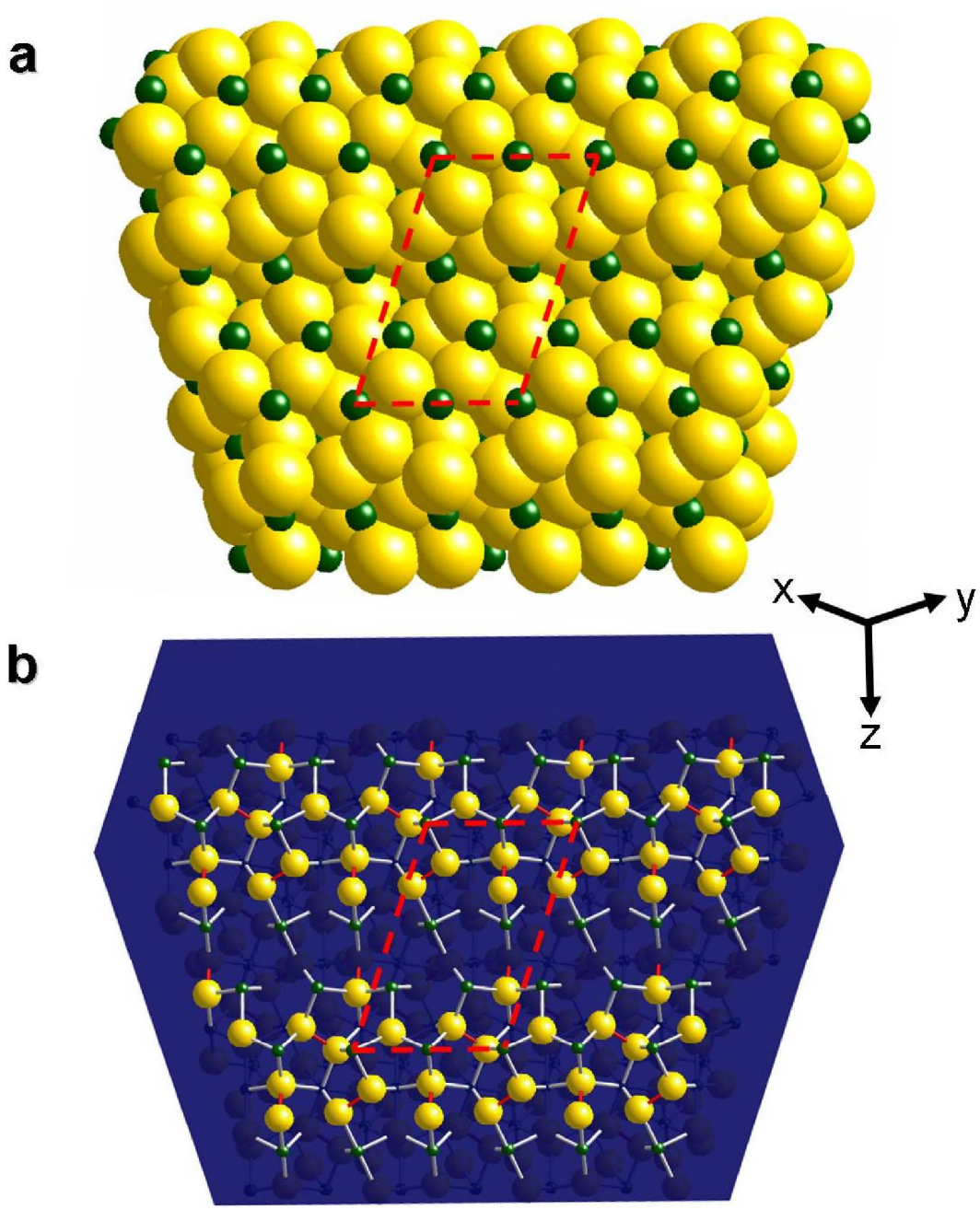

Figure 2.11: (221) surface structure of pyrite, showing the 2D unit cell (red dashed square), with cell parameters $a = 7.662\,\text{Å}$, $b = 12.115\,\text{Å}$ and $\gamma = 71.565°$; yellow and green balls represent the S and Fe atoms, respectively; a) space filling model, b) ball & stick model including the bonds, red S-S, grey Fe-S. At the surface unsaturated atoms are present, two types of iron atoms with the first having three and the second four bonds to neighboring sulfur atoms and two types of sulfur atoms, with the first having one bond to an iron and one to another sulfur atom and the second having two bonds to iron and one to another sulfur atom. Graphics were drawn with the software *CrystalMaker* (Palmer, 2000).

2.2.3 Lattice vibrations

It is possible to determine, from group theory considerations, the number of Raman- and Infrared-active modes of pyrite (Lutz & Willich, 1974). There are 3 acoustical and 33 optical modes in the pyrite structure. The decomposed irreducible representation follows:

$$\Gamma = \mathrm{A}_g + \mathrm{E}_g + 3\,\mathrm{T}_g + 2\,\mathrm{A}_u + 2\,\mathrm{E}_u + \mathrm{T}_u + 5\,\mathrm{T}_u.$$

The gerade vibrations ($\mathrm{A}_g + \mathrm{E}_g + 3\mathrm{T}_g$) are active in the first-order Raman spectrum; the ungerade modes $2\mathrm{A}_u$, $2\mathrm{E}_u$ and the lattice translations (T_u) are optically inactive, while $5\mathrm{T}_u$ modes are infrared active. The Raman active modes comprise one totally symmetric mode (A_g), one doubly degenerate mode (E_g), and three triply degenerate modes (T_g). For the A_g mode, the S_2 dumbbells show stretching vibrations which are in phase. For the E_g mode, the displacements of the sulfur atoms are perpendicular to the S-S bond axis and the T_g type modes can be described by various librational and stretching motions or their combinations (Sourisseau et al., 1991). According to the pyrite single-crystal Raman results reported by Vogt et al. (1983), all these modes can be assigned as 379 (A_g), 343 (E_g) and 350, 377, 435 cm^{-1} (T_g). Following the first IR measurements of Lutz & Willich (1974), Lutz et al. (1985) investigated the complete far-IR absorption and reflection spectra of pyrite. The five IR active modes comprise three vibrations in the crystal. For the IR-modes at 293 and $348\,\mathrm{cm}^{-1}$, the displacements of sulfur atoms are perpendicular to the S-S bond axis. The modes at 402 and $415\,\mathrm{cm}^{-1}$ can be described as displacements of sulfur atoms perpendicular to the S-S bond axis along $\langle 112 \rangle$ directions and the mode at $425\,\mathrm{cm}^{-1}$ involves stretching vibrations of the S_2 dumbbells (Lutz & Willich, 1985). The Raman- and IR-active modes involve only movements of the sulfur atoms, and, therefore, the phonon frequencies give information on the forces governing the stretching and librational motions of the S_2 units.

2.3 Crystal growth

Crystals can grow from solid states, solutions, melts and vapors. The atoms in solutions, melts and vapors have a random distribution, but with changing temperature, pressure, or concentration they may crystallize into an ordered arrangement of the crystalline state. The first stage in the growth of a crystal involves nucleation. This implies that growth can commence only after a nucleus has been formed. Many nuclei may not lead to further crystal growth, because in a saturated solution, melt or vapor, there is also a tendency for nuclei to redissolve (Wilke & Bohm, 1988), because they have a large surface area with respect to volume. A high surface area implies that there are many atoms with unsatisfied chemical bonds. Hence, such a crystal with a high surface area is more soluble than a crystal with a larger volume in which most of the atoms have completely satisfied chemical bonds. Thus, a nucleus needs to grow rapidly enough to reduce its surface energy and solubility in order to form a crystal.

The growth of a nucleus can act in different ways. Fig. 2.12 shows various possibilities of how connecting units (atoms, molecules) can interact with a nucleus surface. A connecting unit (orange cube) interacts in the case of a closed layer with one side (a), whereas at edges two sides (b) and at corners three sides (c) are involved. The ability of attachment is greatest at corners and least at closed layers. With respect to this adhesion mechanisms, the structure of each growing surface determine the growth velocity. Thus, different crystal surfaces do not grow with the same velocity. Surfaces with the slowest growth rate determine the crystal form, as shown schematically in Fig. 2.13. The dashed lines represent the growth velocity, thus, in this model the slowest

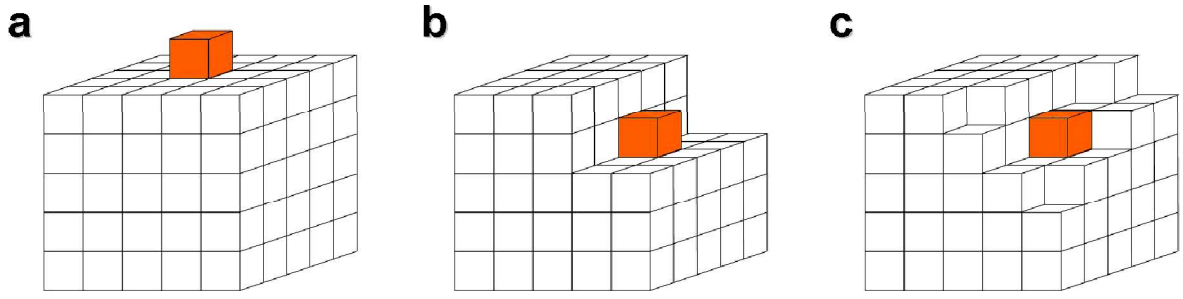

Figure 2.12: Various possibilities of crystal growth on surfaces; connecting unit is shown as block (orange) a) attachment to a closed layer of a crystal; b) attachment at a step structure of a crystal surface; c) attachment at a corner structure of a crystal surface. The attachment of units at surfaces is controlled by the number of unsatisfied chemical 'unit-sites' at the outer surfaces. The number of unsatisfied unit-sites are a) closed layer = 1, over b) step structure = 2 to c) corner structure = 3.

growing face ({111}) determines the crystal form.

Wöhler (1836) first described the synthesis of pyrite. For the growth of single crystals, melt techniques cannot be used because pyrite has no melting point, but exhibits a peritectic decomposition point at 743°C. There it decomposes to FeS and sulfur (Chapter 2.1). Single crystals were prepared by flux growth (Wilke et al., 1967) and chemical vapor transport (CVT) (Bouchard, 1968; Butler et al, 1971; Fiechter et al., 1986; Willeke et al., 1992). The most frequently used technique is the CVT with halogens as transporting agents (Fiechter et al., 1986; Blenk et al., 1993). However, many of the crystals grown by this method were reported to be sulfur deficient (Fiechter et al., 1992). This can be attributed to a low sulfur activity during growth that is difficult to control. However, the mechanism behind pyrite formation is not fully understood, mainly because of experimental difficulties (Schoonen & Barnes, 1991a,b,c).

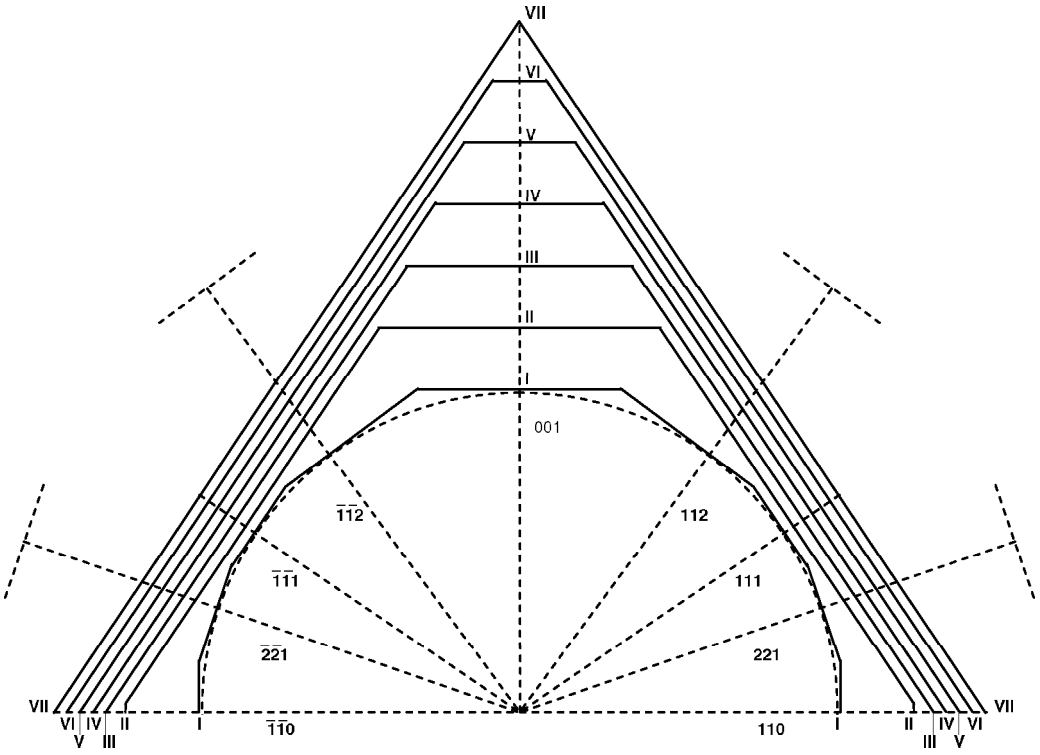

Figure 2.13: Kinematic evolution of a sphere during growth (after Spangenberg, 1935). Growth velocity pictured with length of the straight, dashed lines. The faster growing surfaces {100}, {211}, {221} and {110} disappear. Thus, the slow growing surfaces {111} determine the crystal shape (VII).

2.3.1 CVT - a single crystal growth method for pyrite

Chemical vapor transport (CVT) is a method that can be used to grow large crystals that cannot be grown from the melt because they have a peritectic decomposition and / or very high melting points. Pyrite decomposes at 743°C into $Fe_{1-x}S$, liquid sulfur and gaseous sulfur species (Chapter 2.1), therefore CVT lends itself as a possible method of crystal growth. Pyrite consists of two elements having significantly different vapor pressures, therefore a transporting agent (e.g. $AlBr_3$) has to be added to increase the iron activity in the vapor phase (Tomm et al., 1995).

CVT pyrite experiments are mostly carried out in closed silica-tubes (e.g. inner diameter 10-20 mm; length 10-20 cm; for general aspects see Schäfer, 1964). Prior to loading, the tubes are cleaned and dried. The starting material is introduced into the ampoule and the transporting agent is added. After the tube is evacuated, it is sealed off. The loaded tube is placed in a temperature gradient (two- or more-zone tube furnace). The reaction utilized in the CVT halogen (Hal) transport of pyrites is:

$$FeS_2(s) + Hal_2(g) \rightleftharpoons FeHal_2(g) + \tfrac{2}{x} S_x(g),$$

where the indices (s) and (g) denote solid and gaseous state, respectively. Several halogens such as iodine, chlorine, bromine can be used for the transport reaction. In the experiments performed for this work, mainly bromine in the form of $AlBr_3$ was used as a transporting agent, even though there is little known about the properties of complexes formed between transition metals and aluminum bromide. Kendall et al. (1923) measured the melting points of mixtures of $FeBr_2$ and $AlBr_3$. Gregory & Laughlin (1977) studied the nature of the molecules formed in the vapor phase of such mixtures. Hargittai et al. (1996) observed aluminum tribromide in the vapor phase to occur in monomeric and dimeric forms, with increasing amount of monomers as the temperature of the vapor increases. Aluminum tribromide forms a molecular crystal consisting of dimeric units, and these dimers persist when evaporated. Thus, the transport of iron from the hot to the cold side of the silica-tube is possible with the formation of iron-aluminum-bromide complexes. The principal vaporization reactions are:

$$2\,FeBr_2(s) + Al_2Br_6(g) + Br_2(g) \quad = \quad 2\,FeAlBr_6(g)$$

and

$$2\,FeAlBr_6(g) + Al_2Br_6(g) \quad = \quad 2\,FeAl_2Br_8(g) + Br_2.$$

At high temperature ($\geq$ 650°C), the decomposition of pyrite to FeS_{1+x}(s) and S(g) becomes important, whereby experiments indicate that this reaction is driven to the pyrite side with moderate sulfur pressure (Hulsmann et al., 1935; Voigt & Meisel, 1936; Rosenquist, 1954). To prevent an intergrowth of FeS_2 and FeS, the temperature and transporting agent concentration must be chosen such that FeS cannot be stable. According to Wolf et al. (1978), pyrite releases a significant amount of sulfur that causes a dramatically decrease of the transport rate, which becomes zero at 725°C. The best transport conditions have been found by Fiechter et al. (1986) for a temperature gradient 700 $\rightarrow$ 580°C.

As mentioned above, different transporting agents can be used for pyrite growth via CVT. Several authors used chlorine as a transporting agent to synthesize pyrite single crystals (e.g. Bouchard, 1968; Lutz et al., 1974; Yamada et al., 1979). The crystals, prepared by Yamada et al. within 10 days, feature for crystals larger than 500 µm {100}, {111} and {210} faces, while smaller ones show mainly {100}. Fiechter et al. (1986) synthesized pyrite via CVT using chlorine and bromine as transporting agents. Their crystals showed mainly {111} surfaces, but also {100}, {210} and {211} were observed. Blenk et al. (1993) and Schieck et al. (1990) synthesized pyrite crystals by CVT using bromine in the form of $AlBr_3$, $FeBr_2$ or $FeBr_3$ as transporting agents. Blenk et al. found crystals with mainly {100} surfaces and *p*-type conductivity. Unusual is the fact that Schieck et al. synthesized their crystals with the same method and the same transporting agents, but higher temperatures than Blenk et al. and they found *n*-type conductivity. Their crystals showed {100}, {111}, {210} and {221} faces.

Chapter 3

Microbiology

This chapter presents an overview over microbiology and focuses on the differences of the two main kingdoms Bacteria and Archaea and discusses the microbial strains used for the dissolution experiments.

3.1 Microorganisms

Microorganisms are the most abundant organisms on earth. They are ubiquitous in soil, water, and as symbionts of other organisms. Most are minute, usually 0.5 - 5.0 µm in size. However, the species *Thiomargarita* may reach 750 µm in diameter (Schulz et al., 1999). All organisms generally have cell walls, like plant and fungal cells, but with another compositions.

The first bacteria were observed by Leeuwenhoek in 1683 using a single-lens microscope of his own design. The name bacterium is derived from the Greek word *bakthrion* meaning *small stick* and was introduced by Ehrenberg in 1828. Pasteur (1822-1895) and Koch (1843-1910) described the role of bacteria as conveyors and causes of disease or pathogens. Not until 1956 were the microorganisms defined in the phylogenetic tree of life. Copeland (1956) defined for the first time the microorganisms in an own kingdom Mychota, later renamed Monera, Procaryota, or Bacteria. During the 1960s bacteria were recognized as one of two major divisions of the phylogenetic tree of life, the procaryotes (cells without a nucleus) and eucaryotes (cells with a nucleus). The advent of molecular systematics challenged this view. Woese (1977) divided the procaryotes into two groups based on 16S rRNA sequences and called the two kingdoms Eubacteria and Archaebacteria. He argued that Eubacteria, Archaebacteria and the Eucaryotes all evolved separately and, in 1990, emphasized this by promoting them to domains, which were renamed the Bacteria, Archaea and Eucarya. Fig. 3.1 shows the present phylogenetic tree of life with its three domains and highlights the positions of

the microorganisms used in this study.

Procaryotes reproduce asexually. They reproduce by binary fission or simple cell division. During this process, one cell divides into two daughter cells with the development of a transverse cell wall. However, genetic variations can occur within individual cells through recombination e.g. mutation (random genetic change within a cell's own genetic code). The long existence of microorganisms (approximately 3.8 billion years) has enabled them to evolve a great genetic diversity. They are far more diverse than

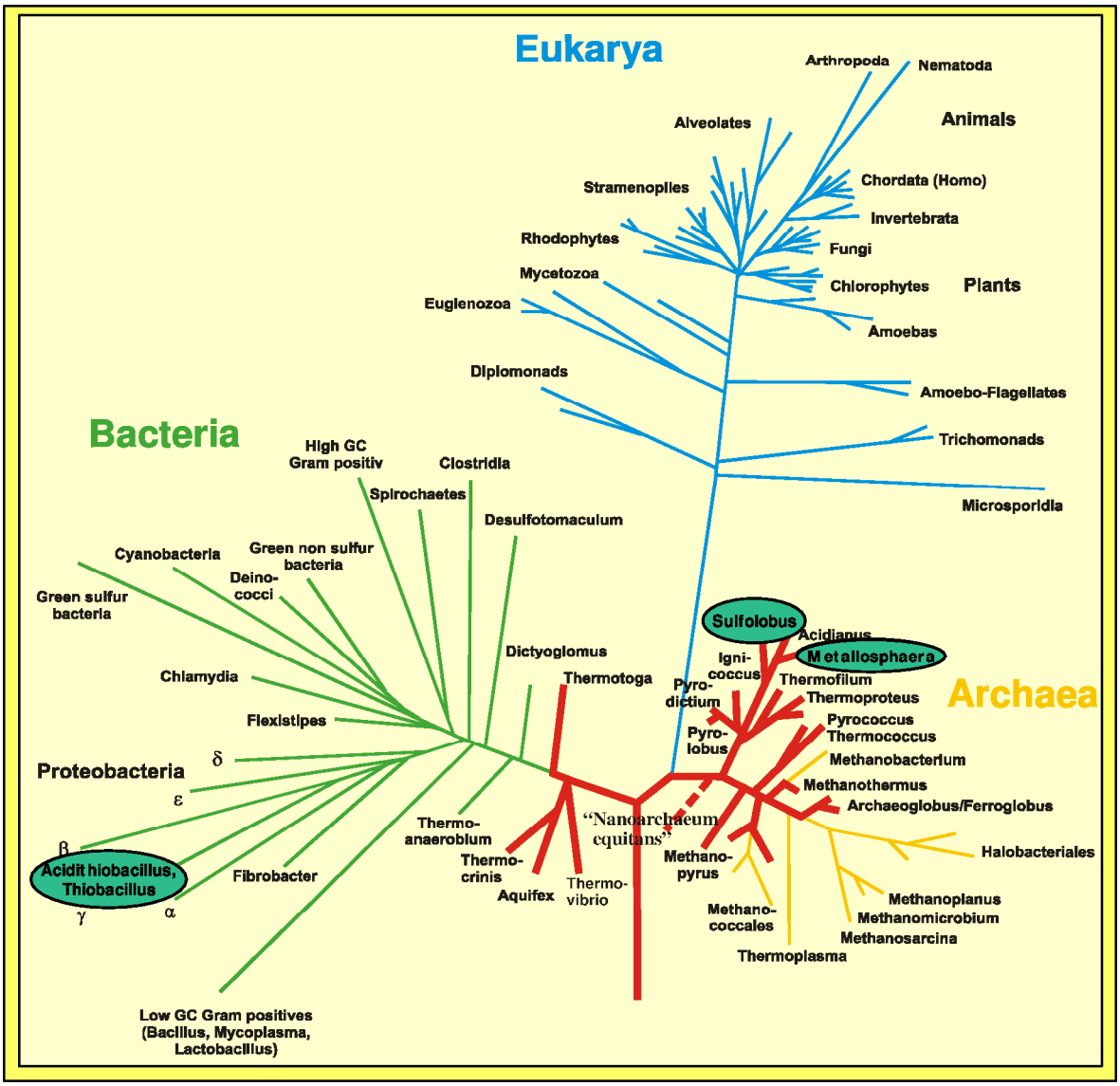

Figure 3.1: The present phylogenetic tree of life, including the three kingdoms, Eucarya, Bacteria and Archaea. The position of the microorganisms used for this study are highlighted.

e.g. mammals or insects. For instance, the genetic difference between *Escherichia coli* and *Thermus aquaticus* is larger than the difference between humans and oak trees (Alcamo, 1997). Procaryotes come in a variety of different shapes. Most are rod-, sphere-, or helix-shaped and they are referred to as bacilli, cocci, and spirillum, respectively. Shape is no longer considered a defining factor in the classification of microorganisms. However, many genera are named for their shape (e.g. *Bacillus, Streptococcus, Staphylococcus, Sulfolobus*) and this is still important for their identification.

At the Earth's surface and in the subsurface some microbial cells live planktonic, but most exist attached to surfaces (Hazen et al., 1991). Since microorganisms influence mineral surface chemistry at attachment sites (Silverman & Ehrlich, 1964). These sites can be important for mineral dissolution. The association of microorganisms with pyrite oxidation and the formation of acid-mine drainage has a long history. It began with the discovery that microbes can utilize inorganic compounds, as well as organic compounds, as a basis for their metabolism. Winogradsky (1887) recognized that some microbes could derive their metabolic energy from the oxidation of inorganic compounds such as iron and sulfur. This property generates one of the major divisions among microorganisms, namely the chemotrophs that gain energy from the oxidation of inorganic compounds, and the heterotrophs (like ourselves), who gain energy from the oxidation of organic compounds. Autotrophic organisms obtain their carbon for growth through CO_2 fixation. Organisms that uptake solar radiation as their source of energy and produce cellular carbon from CO_2 fixation are known as photoautotrophs (Sokolova & Karavaiko, 1968).

In industry, microorganisms are used to dissolve metals from minerals. This process is named biomining and significantly different from the traditional methods of extreme heat or toxic chemicals, which has a deleterious effect on the environment. Using microbes such as *Thiobacillus ferrooxidans* to dissolve copper from mine tailings has improved recovery rates and reduced operating costs. Moreover, the use of microbes permits the treatment of low grade ores (e.g. Rawlings, 2002). Further, biooxidation of metals from sulfide materials and the bioconcentration of metals from solutions is an important field of research. Another project is the use of biological methods for the reduction of sulfur in coal. The main biomining organisms have several common physiological features. They are all chemolithoautotrophic and they are able to oxidize ferrous iron or reduce inorganic sulfur (or both) as electron donors (Rawlings, 2002). This ability to solubilize metal-sulfides is successfully used in biomining operations (Tuovinen, 1990; Rawlings, 2002). The reactions involved in ferrous iron oxidation have been studied by Lundgren (1980), Ingledew (1982), Cox & Boxer (1986), Tuovinen (1990), Blake II. & Shute (1994), Rawlings (2002) and Rohwerder et al. (2003). The

by-product of sulfur oxidation is sulfuric acid and hence, these organisms are acidophilic and most of them live within the pH range 1.5 - 2.0. This extreme acidophility applies even to those biomining organisms that can only oxidize iron. Mineral decomposition can take place at temperatures up to 85°C (Rawlings, 2002). Recent reviews on the biodiversity of microorganisms from acid environments are given by Johnson & Roberto (1997), Norris (1997), Johnson (1998) and Hallberg & Johnson (2001).

3.2 Bacteria

For this work, four bacterial strains were used, *Thiobacillus sphaeroides* (strain SP 5/1), *Thiobacillus prosperus* (strain LM 3) and two strains of *Acidithiobacillus ferrooxidans* (strains HV 2/2 and VC 15/2). Fig. 3.2 shows the typical rod-shape of *Thiobacillus sphaeroides* (a) and *Acidithiobacillus ferrooxidans* (b), attached to pyrite. The cell shape of *Thiobacillus prosperus* is similar.

The members of the genus *Acidithiobacillus* (formerly *Thiobacillus*) are rod-shaped eubacteria. *Acidithiobacillus ferrooxidans* was the first bacterium isolated and described in detail that is connected to pyrite oxidation (Colmer & Hinkle, 1947). Later it was found to be widely distributed involving the treatment of pyritic material (Beck, 1967). It is found wherever sulfide minerals occur in an acidic environment (Berry & Murr, 1978). *Acidithiobacillus ferrooxidans* is a chemolithoautotrophic bacterium that obtains energy from the oxidation of ferrous iron, elemental sulfur or partially oxidized sulfur compounds (Vishniac, 1974; Brierley, 1978; Lundgren, 1980; Harrison, 1984; Tuovinen, 1990; Rawlings, 2002). It is able to grow on water-insoluble metal-sulfides like pyrite, chalcopyrite or sphalerite (Lundgren et al., 1986). It is characterized by its ability to oxidize ferrous iron to ferric iron (Colmer & Hinkle, 1947), enhancing the dissolution process due to the strong oxidizing capacity of ferric iron. According to Rawlings (2002), *Acidithiobacillus ferrooxidans* is a pyrite oxidizing organism living in the temperature range 20° - 35°C and pH 1.8 - 2.0. As may be expected from bacte-

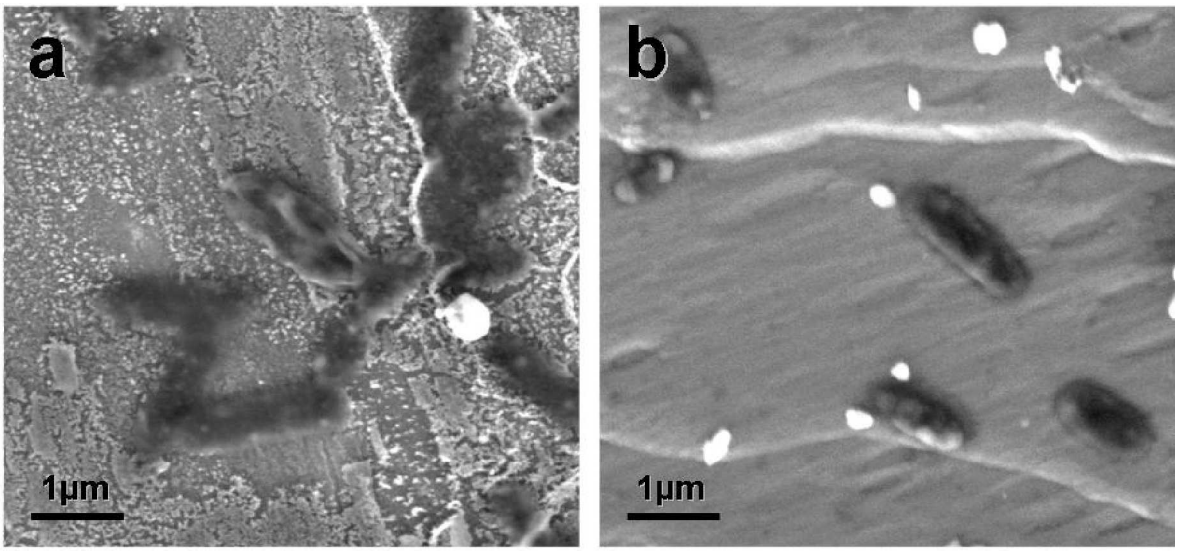

Figure 3.2: Cell shape of two bacterial strains attached at pyrite surfaces. a) *Thiobacillus sphaeroides*, b) *Acidithiobacillus ferrooxidans* (VC 15/2).

ria growing in a mineral-rich environment, these bacteria are remarkably tolerant to a wide range of soluble metal ions (Leduc & Ferroni, 1994). *Thiobacillus prosperus* is the first halotolerant metal-mobilizing bacterium isolated (Huber & Stetter, 1989) and similar to *Acidithiobacillus ferrooxidans*, it may extract metal ions from sulfidic ores. The strain *Thiobacillus sphaeroides* is not described in literature, however, it is known that this organism oxidizes pyrite similar to *Acidithiobacillus ferrooxidans*.

3.3 Archaea

Four strains of Archaea, *Sulfolobus metallicus* (strain Kra 23), *Metallosphaera sedula* (strain TH 2) and two strains of *Sulfolobus* sp. (strains HV 5 and VE 2) were used in this study. *Sulfolobus metallicus* and *Metallosphaera sedula* in their typical appearance are shown in Fig. 3.3 attached to pyrite. The cell shape of *Sulfolobus* sp. are similar to *Sulfolobus metallicus*.

Many archaea are extremophiles. They may live at high temperatures exceeding 100°C and can be found in geysers and black smokers. Therefore, they are called thermophiles. Others are found in cold habitats (psychrophiles) or in highly saline (halophiles), acidic (acidophiles), or alkaline water. However, other Archaea are mesophiles, and are found in marshland, sewage, and soil environments. Hot springs and hydrothermal systems occurring within volcanic areas are inhabited by hyperthermophilic microorganisms, some of them living at temperatures up to 110°C. Hyperthermophiles grow anaerobically or aerobically. In high temperature ecosystems primary production is independent of solar energy (Segerer et al., 1993).

Fuchs et al. (1996) concluded that the thermoacidophilic genera *Sulfolobus* (Brock et al, 1972) and *Metallosphaera* (Huber et al., 1989) belong to the order of the *Sulfolobales* (Stetter, 1989). *Sulfolobales* were isolated from hot, acidic muds, waters, and soils in continental solfataric fields (hot, liquid sulfur source) and from smoldering mining dumps. Their optimal growth temperatures are between 65° and 90°C at pH values

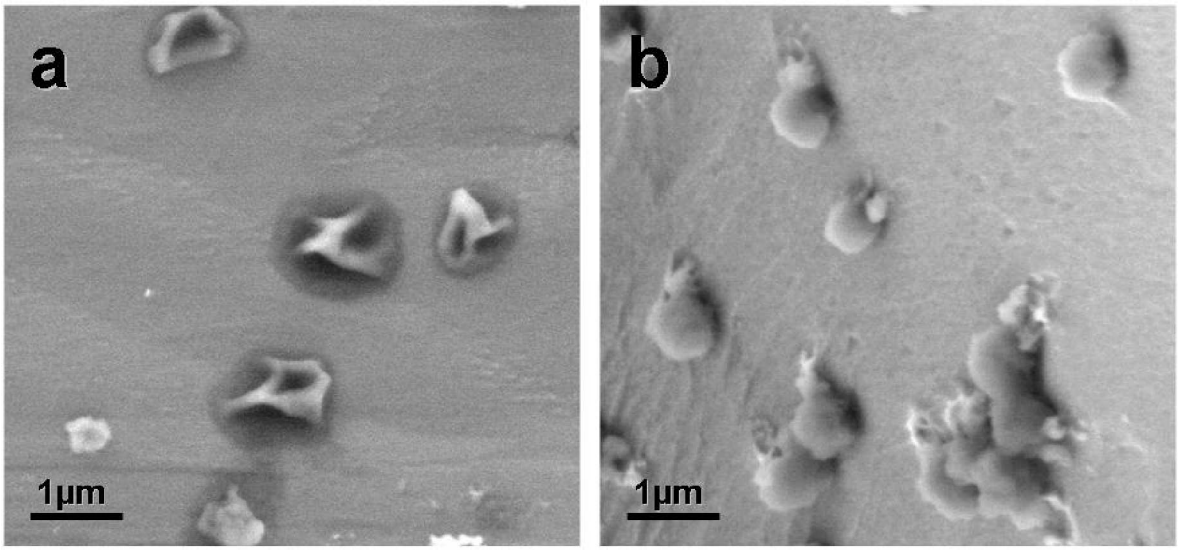

Figure 3.3: Cell shape of two archaeal strains attached at pyrite surfaces. a) *Sulfolobus metallicus*, b) *Metallosphaera sedula*.

around 2 (Brierly & Murr, 1973b). The dissolution of mineral concentrates by some strains of *Sulfolobus* at 70°C is about three-times faster than dissolution by mesophilic mineral oxidizing bacteria at 30°C (Marsh et al., 1983; Norris & Parrott, 1986; Norris & Barr, 1988b).

Many of the most important mineral biooxidation studies have been carried out in laboratories using a strain of *Sulfolobus metallicus* (Huber & Stetter, 1991). These autotrophic archaea grow by oxidizing ferrous iron, inorganic sulfur compounds, or sulfide ores. *Sulfolobus metallicus* is thermophilic and grows at an optimum temperature of 68°C and a pH range of about 1.3 - 1.7. *Sulfolobus metallicus* is capable of oxidizing minerals such as arsenopyrite and chalcopyrite (Norris, 1997).

Metallosphaera sedula are aerobic iron- and sulfur-oxidizing chemolithotrophic organisms that are also able to grow on complex organics such as yeast extract or casamino acid (Huber et al., 1989). *Metallosphaera sedula* has been reported to grow at pH 1.0 - 4.5 and is able to oxidize a variety of minerals at temperatures of 75 - 85°C. *Metallosphaera*-like organisms are reported to be potentially the most efficient organism for the high-temperature biooxidation of pyrite ores (Norris, 1997).

Chapter 4

Metal-sulfide oxidation

In the previous two chapters pyrite and various microbial strains have been described. In this chapter an introduction into pyrite oxidation will be given. In the first section, the abiotic oxidation of pyrite will be presented. The second section deals with the microbial influence on pyrite oxidation.

4.1 Pyrite oxidation

The importance of the oxidation of pyrite in aqueous solutions has prompted numerous studies, both experimental and theoretical (McKibben & Barnes, 1986; Moses et al., 1987; Eggleston et al., 1996; Abraitis et al., 2004). Pyrite oxidation in nature is neither a purely chemical, nor a purely microbial process. It is the result of a complex interplay of processes dependent on rock type, mineral structure, mineral chemistry, fluid abundance, fluid chemistry, microbial community and temperature. It is a process which includes several types of oxidation-reduction reactions, hydrolysis and complex ion formation, solubility controls and kinetic effects.

In 1967 Basolo & Pearson pointed out that the elementary steps of redox reactions almost always involve the transfer of only one electron at a time and thus the oxidation of pyrite (S^{1-}) to sulfate (S^{6+}) must require seven elementary steps. This process is further complicated by the fact that pyrite is a semiconductor and the reactions are electrochemical in nature. This means that electrons can move in the mineral so that the various reactions happen at different sites (Kelsall et al., 1999; Rimstidt & Vaughan, 2003). Because so many electrons must be removed from each sulfur atom to oxidize it to sulfate, this oxidation process is complex and difficult to understand in pyrite oxidation. Oxidative dissolution always produces a mineral with a decreased cation content (increased sulfur content). Substantial cation loss from minerals can occur when cations have high mobility, but iron diffusion rates are low in pyrite, so

this process is limited to the near surface region. It produces surface polysulfide groups as shown by X-ray photoelectron spectroscopy studies (Buckley & Riley, 1991). The key to understand pyrite oxidation is to follow the oxidation of the sulfur atom at the surface.

$$\begin{aligned} \textit{pyrite}\text{–S-S} &\rightarrow \textit{pyrite}\text{–S-S}^{+} + e^{-}, \\ \textit{pyrite}\text{–S-S}^{+} + \mathrm{H_2O} &\rightarrow \textit{pyrite}\text{–S-S-OH} + \mathrm{H}^{+}, \\ \textit{pyrite}\text{–S-S-OH} &\rightarrow \textit{pyrite}\text{–S-SO} + e^{-} + \mathrm{H}^{+}, \\ \textit{pyrite}\text{–S-SO} &\rightarrow \textit{pyrite}\text{–S-SO}_2 + 2e^{-} + 2\mathrm{H}^{+}, \end{aligned}$$

and

$$\textit{pyrite}\text{–S-SO}_2 \rightarrow \textit{pyrite}\text{–S-SO}_3 + 2e^{-} + 2\mathrm{H}^{+}.$$

There is a tendency for the -S-SO_3 species to break away from the surface as a thiosulfate complex. This can be described as

$$\textit{pyrite}\text{–S-SO}_3 \rightarrow \textit{pyrite} + \mathrm{MS_2O_3}.$$

This oxidation mechanism is named after this complex as the *thiosulfate pathway* (Schippers et al., 1996; Rohwerder et al., 2003). The final step in sulfur oxidation is pH dependent. At low pH, the majority of terminal S-SO_3 groups obtain a proton (S-SO_3H) which promotes the transfer of electrons to the S-S bond, leaving sulfur with a positive charge. This leads to further nucleophilic attack by a water molecule to produce SO_4^{2-}, which is released into the solution.

$$\textit{pyrite}\text{–S-S-O}_3 \rightarrow \textit{pyrite}\text{–S} + \mathrm{HSO_4^-} + \mathrm{e}^{-} + \mathrm{H}^{+}.$$

Borda et al. (2003) investigated the step-wise oxidation of the disulfide group during pyrite oxidation by ferric iron using *in situ* attenuated total reflectance Fourier transform infrared spectroscopy. They concluded that the spectra collected during pyrite oxidation are consistent with the existence of more than a single sulfur species at the pyrite surface. The presence of multiple sulfur species at the pyrite surface confirms the step-wise oxidation of the disulfide group.

The dissolution mechanism of pyrite by ferric iron in acidic solutions involves the removal of iron and oxidized sulfur. The surface sulfur groups are slightly negatively charged due to an unshared electron pair (Luther 1987, 1990). As a result, ferric iron bonds to sulfur through a vacant orbital, thus, forming a bond through which electron transfer can occur. Luther (1987) suggested an oxidation mechanism starting with the following steps:

$$Fe(H_2O)_6^{3+} \rightarrow Fe(H_2O)_5^{3+} + H_2O$$

and

$$pyrite\text{–S-S} + Fe(H_2O)_5^{3+} \rightarrow pyrite\text{–S-S}^{+} + Fe(H_2O)_5^{2+} \ .$$

Subsequently, following this path, the hydrated ferrous iron remains in solution and the surface group formed reacts with another $Fe(H_2O)_6^{3+}$, further oxidizing sulfur. This is accompanied through the attachment of one oxygen (from H_2O) to the pyrite surface and a release of two protons. This process continues until ferrous iron and thiosulfate ($S_2O_3^{2-}$) are formed. Hence, the overall oxidation reactions of pyrite by ferric iron are (Schippers & Sand, 1999):

$$FeS_2 + 6\,Fe^{3+} + 3\,H_2O \rightarrow S_2O_3^{2-} + 7\,Fe^{2+} + 6\,H^{+}$$

and

$$S_2O_3^{2-} + 8\,Fe^{3+} + 5\,H_2O \rightarrow 2\,SO_4^{2-} + 8\,Fe^{2+} + 10\,H^{+}.$$

At low pH the pyrite oxidation rate is controlled by ferric iron, which oxidizes pyrite 3 to 100 times faster than does oxygen (Singer & Stumm, 1970; Nordstrom, 1982; McKibben & Barnes, 1986; Moses et al., 1987; Luther, 1990; May et al., 1997; Edwards et al., 1999). According to the Arrhenius equation the rate of chemical oxidation of pyrite by ferric iron will increase with increasing temperature. Boogerd et al. (1991) and Bouffard et al. (2006) studied the stoichiometry and kinetics of the reaction between pyrite and ferric iron from 45 up to 75°C. They found that the pyrite oxidation rate was sensitive and rose with temperature.

Buckley & Woods (1987) and Nordstrom & Southam (1997) postulated that when pyrite is attacked by an acid solution, the iron is etched from the surface layer, leaving a sulfur-rich surface. Several studies, using X-ray photoelectron spectroscopy and Raman spectroscopy, confirmed that initial dissolution under acidic conditions first releases iron and forms a layer containing disulfide, monosulfide, and polysulfides (Sasaki, 1994; Nesbitt & Murr, 1994). Chander et al. (1993) showed that a sulfur-rich layer is formed, and covered with a layer of iron oxides, hydroxides, sulfate or oxy-sulfide ions. The formation of layers on the pyrite surface can influence the relative rates of pyrite oxidation (Hiskey et al., 1982). Additionally, the formation of elemental sulfur layers and the formation of jarosite ($AFe_3(SO_4)_2(OH)_6$, with A = Na, K, Rb, H_3O, NH_4, Ag, Tl) can have important consequences. Even thin precipitate layers have a significant effect on the actual surface structure (Keller & Murr, 1982).

Only a few investigations of pyrite oxidation were performed in dependence of face-symmetries. However, the efficiency of the oxidation processes and the mineral

solubility will depend on the physical and chemical properties of the surfaces. The surfaces limit the reactivity between the solid and liquid phases. Structural imperfections for a given face serve as highly reactive sites for the oxidation process (Schaufuss et al, 1998; Guevremont et al., 1998a). Guevremont et al. (1998b) demonstrated that the initial oxidation rate of a (111) surface of pyrite is more rapid than a (100) surface. More investigations addressing the differences of etching effects on different oriented pyrite surfaces are needed.

4.2 Microbial effects of pyrite oxidation

The parameters for microbial oxidation of pyrite are temperature, pH, ionic concentration and the microbial strain. Microbial etching is done through oxidation of insoluble metal-sulfides to sulfuric acid by specialized lithoautotrophic microorganisms that contain dissolved metal ions (Ehrlich, 1990; Tuovinen, 1990). Biological oxidation requires an acidic solution (Colmer et al., 1950), the presence of oxygen, carbon dioxide and humidity (Hallmann et al., 1993).

The oxidizing organisms can either attach to surfaces or stay planktonic in solution. However, for a given microbial strain, not all organisms have to attach completely to the mineral surface or stay completely planktonic in solution. Most organisms occur attached and planktonic in different amounts. Rodríguez et al. (2003) demonstrated for *Acidithiobacillus*, *Leptospirillum* sp. and *Sulfolobus* sp. that a relationship exists between attachment of cells at surfaces and mineral dissolution rates. They concluded that the biooxidation process can be divided into three stages. An initial stage, with extensive attachment to the pyritic phase, which is important in order to obtain high dissolution rates. In a second stage, the attachment diminishes due to the saturation of the surface by the attached cells. This limitation, together with the presence of ferrous iron in solution, produces an increase in the concentration of free cells, which use ferrous iron as an energy source via oxidation to ferric iron. Finally, in a third stage, a balance between free and attached cells is reached, giving rise to a *cooperative* mechanism. In this case, the attached cells attack the pyrite generating ferrous iron (*contact* mechanism), which is released into the solution. This ferrous iron is oxidized by the free cells in solution, regenerating the oxidizing agent, ferric iron. Thus, the microbial influence of the planktonic organisms during pyrite oxidation is a catalytic one, where ferrous iron is oxidized to ferric iron. The resulting ferric iron ions come into contact with a mineral surface, breaking chemical bonds, are reduced and reenter the cycle (Tributsch, 2001; Sand & Gehrke, 2006), in the same way as described above. This cyclic microbial oxidative action of ferric iron in solution is called *non-contact* mechanism (Fig. 4.1).

However, some organisms have evolved strategies which require a biofilm for surface contact. Organisms like e.g. *Acidithiobacillus ferrooxidans* produce layers of extracellular polymeric saccharide (EPS). These strains attach rapidly to minerals (Rodríguez et al., 2003; Acuna et al., 1986) and after the initial attachment of the cells a monolayered biofilm develops within a few days (Edwards et al., 1998), that covers the mineral surface with cells embedded in a continuous EPS layer (Rojas-Chapana et al., 1996; Schippers et al., 1999). Thus, the EPS layer attaches the bacteria to a mineral

surface and forms the matrix in which the cells divide and eventually form a biofilm. Iron species within the EPS layer have been estimated to have concentrations up to 53 g/L, which can be maintained only by the formation of complexes with glucuronic acid (Harneit et al., 2006). The iron impregnated EPS layer serves as reaction space in which the high concentration of ferric iron can mount a chemical attack on the mineral. In the process, the ferric iron is reduced to ferrous iron which is reoxidized to ferric iron by the iron-oxidizing microbes via the reaction

$$14\,Fe^{2+} + 3.5\,O_2 + 14\,H^+ \rightarrow 14\,Fe^{3+} + 7\,H_2O.$$

This microbially mediated reoxidation of ferrous iron can result in a localized increase in pH within the EPS near the surface of the mineral (Rawlings, 2002). However, the oxidation process via the EPS layer is not fully understood. There are two proposals on how the processes could function (Sand & Gehrke, 2006). The first considers an electron tunneling effect. It is known that electrons can bridge distances of up to 2 nm by tunneling from one electron hole to another (Medvedev & Stuchebrukhov, 2001). Consequently, the ferric iron ions have to be located less than this distance from the pyrite surface. The second proposal is that ferrous iron-glucuronic acid complexes in EPS layers are not stable (Harneit et al., 2006). Hence, the ferrous iron ions are allowed to migrate in the EPS space. There, they will be oxidized by the enzymatic system of the cells, serve as a substrate and can enter the cycle again. Sand & Gehrke (2006) found that cells with many iron ions (up to 50 g/l; Sand, personal discussion) and glucuronic acid in the EPS layer exhibit higher oxidation activity than those with low amounts of these constituents. Thus, the EPS layer enables ferric iron to cycle through to the mineral surface and oxidize pyrite. Corrosion pits and high resolution electron microscopy show that these mechanisms are localized and depend on the specific conditions which microbes create. For this mechanism, the term *contact* mechanism is proposed (Fig. 4.1).

However, in nature, multiple types of microbial oxidation coexist, including *non-contact*, *contact* and a recently discovered *cooperative* (symbiotic) mechanism (Tributsch, 2001). Tributsch has shown that during the oxidation of pyrite the EPS layer of *Aciditihiobaillus ferrooxidans* becomes loaded with mineral fragments and colloidal sulfur and that much of this is released into the environment. The particles released in this apparently wasteful process feed other bacteria in a *cooperative* oxidation interaction. All three oxidation mechanisms are shown in Fig. 4.1.

According to Berry & Murr (1977) and Bennett & Tributsch (1978), organisms are able to distinguish between favorable and less favorable sites for energy extraction, selecting the site of attack according to the availability of nutrients. Such selectivity

for microbial attack is additional evidence for the involvement of a chemical carrier in the oxidation mechanism. It is known that chemical etching proceeds faster in regions where the crystal periodicity is disturbed, because of the presence of additional free bonds for chemical interactions and because of the increased surface area (Chapter 2). Berry & Murr (1977) noted that in studies involving the acid-bacterial etching of pyrite it was observed that different etching or corrosion patterns occur. They seem to result

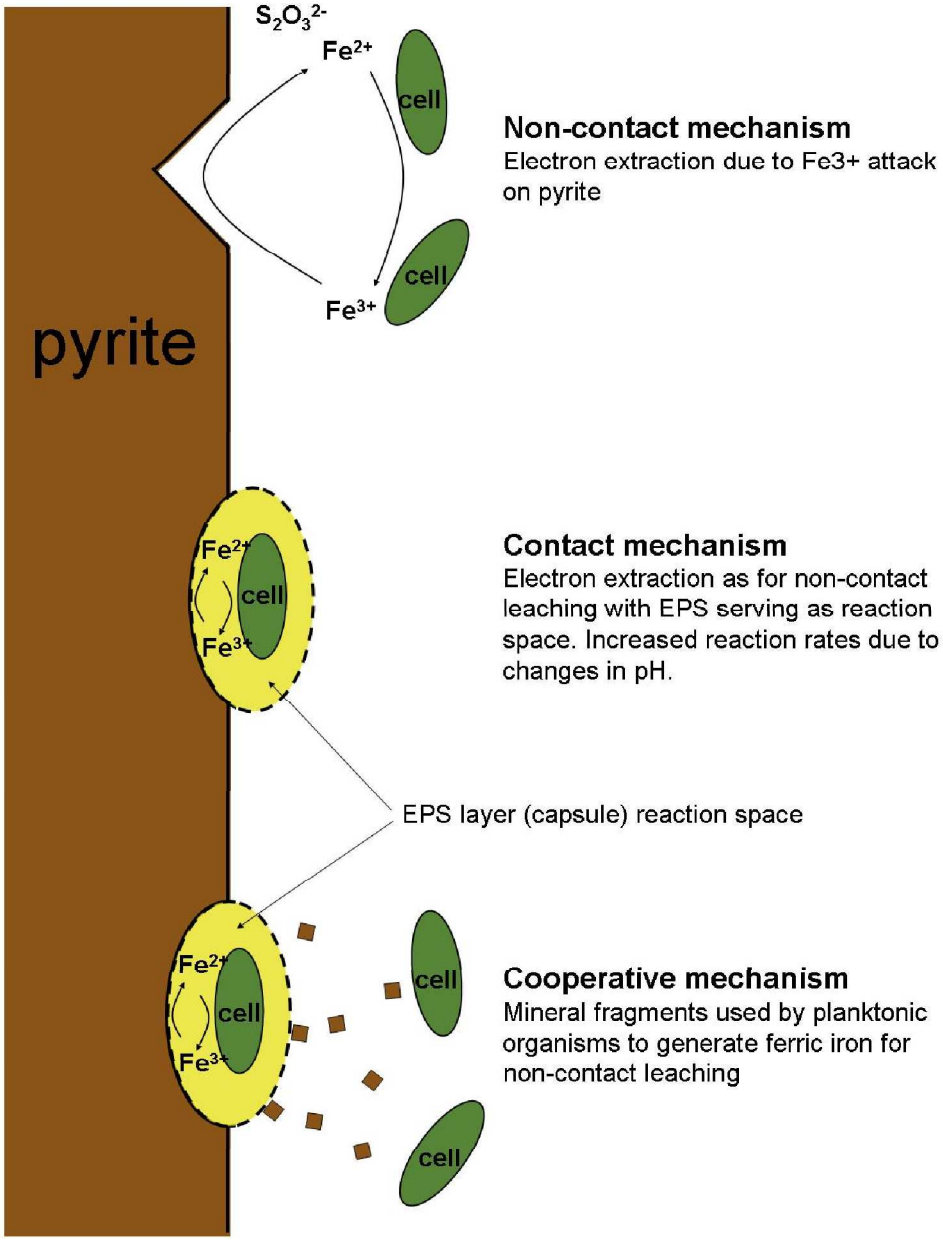

Figure 4.1: Schematic diagram illustrating the proposed mechanisms of pyrite biooxidation.

in large part from differences in the face-symmetry of the mineral surfaces exposed to microbe containing media. The observation that the features formed by microbial activity are sometimes inclined with respect to the surface on which they are found also indicates an influence of the substrate. This suggests that it is more favorable for the microbes to obtain their energy from solid surfaces that are characterized either by weak chemical bonding or by an increased surface area for chemical interaction along cracks of polycrystals. In this regard, Edwards & Rutenberg (2001) studied the role of microtopographical surface features of sulfide minerals in aligning bacterial adhesion. Their experimental data show a correlation between microbial cell alignment and crystallographic directions. Additionally, they found that the depth of a surface feature, such as a scratch, is less important than its cross-sectional shape. Furthermore, surface features that conform to the bacterial shape can strongly alter local bacterial adhesion energies, even with heights of only 10 nm. Hence, small local surface alterations due to bacterial metabolism could strongly affect local adhesion, and may account for the observed bacterial distributions on mineral surfaces. Thus, the effective distance of the interaction is much shorter than the scale of bacteria, i.e. much less than a micron.

Keller & Murr (1982), Aoki (1999) and Ndlovu & Monhemius (2005) investigated the influence of face-symmetry on the mechanism of pyrite biooxidation. They used {100}, {110}, {111} and {211} faces to compare the extent of dissolution of the pyrite surface in iron(III)sulfate solution and in *Acidithiobacillus ferrooxidans* containing media. They studied abiotic etching under different temperatures. Differences in the reaction rates of the pyrite faces in both abiotic and biological solutions have been observed. The etching features by ferric iron etching are characterized by etch pits having symmetries that can be correlated to the face-symmetries, while acid-bacterial etching produces more complex etching patterns with pits having, in some cases, forms that can not be correlated to face-symmetries. The results show that the surface properties of mineral sulfides control the evolution of corrosion patterns and the initial oxidation kinetics in acid bacterial etching.

Several publications describe the differences of the pure pyrite oxidation and those with microbial influence. Singer & Stumm (1970) and Brierley et al. (1973a) proposed that microbial processes are 10^3-10^6 times faster than chemical oxidation. Nordstrom (1982) determined the kinetic data on pyrite oxidation, compares available data on the inorganic versus microbial oxidative mechanisms and describes the occurrence of mineral products resulting from pyrite oxidation. Additionally, acid waters resulting from pyrite oxidation may precipitate a large suite of soluble and insoluble iron minerals depending on pH, degree of oxidation and solution composition. The investigations of Keller & Murr (1982), Norman & Snyman (1988) and Ndlovu & Monhemius (2005)

showed differences of abiotic and microbial oxidation on pyrite surfaces. The observation is that bacterial oxidation progressed from fine cracks to pits, to progressively wider and longer grooves until the mineral was destroyed, while chemical oxidation produced pits like inverted pyramids. Thus, the two types of etching are distinct in their morphological representation.

Chapter 5

Experimental methods and approach

This chapter focuses on the experimental methods used in this work. In section 5.1 the preparation of natural, cut and synthetic pyrite surfaces is presented. The chemicals used for the microorganisms and the growth control of those is described in section 5.2. Section 5.3 deals with the biological and abiotic etching experiments, while section 5.4 deals with the characterization of the samples before and after exposure to oxidation conditions.

5.1 Pyrite preparation

In this section the preparation of natural, cut and synthetic pyrite surfaces is discussed. In the first subsection, the treatment of the natural and cut surfaces is recorded, while in the second subsection, the growth of synthetic pyrite single crystals is addressed.

5.1.1 Natural and cut pyrite surfaces

Natural single crystals of pyrite from Spain (Navajun) and samples of unknown origin from the mineral collection of the Institute of Geosciences, University of Kiel, were cut into approximately 200 µm thick sections. The size of the crystals was about 2 to 3 cm edge length. The form was determined from the morphology. Hexahedral {100} faces were cut from the spanish pyrite crystals and octahedral {111} faces as well as pentagondodecahedral {210} faces were prepared from the samples of the institute collection. The crystals were cut using a Logitech Model 15 saw with a diamond blade. Individual platelets were mounted onto glass slides using UHU hard-glue. Pyrite sections with natural surfaces as well as internal sections were ground to below maximum thickness of approximately 200 µm. One side of the internal sections was polished to a

1 µm finish using Al_2O_3 powder. Upon grinding and polishing the pyrite sections were removed from the glass slides and cleaned with organic solvents (ethanol, petroleum ether) to remove all glue. The final face of the cut pyrite slices was checked by Laue X-ray backscattering. Crystal samples with deviations of more than 5° from the specified face were rejected.

5.1.2 Synthetic pyrite

Synthetic pyrite crystals were grown via chemical vapor transport - CVT (Wilke & Bohm, 1988; Chapter 2.3.1) in evacuated and sealed quartz ampoules (13 mm in diameter and 20 - 30 cm in length) under a temperature gradient from 743 to 623°C. The quartz ampoules contained starting materials of polycrystalline pyrite, additional sulfur and halogenide as transporting agent. The reaction of the components follows the overall equation:

$$FeS_2(s) + Hal_2(g) \leftrightarrow FeHal_2(g) + S_2(g), \qquad \text{with Hal} = I, Br, Cl.$$

The direction of this reaction is temperature dependent. At high temperatures (T = 743°C) the reaction runs from the left to the right side, whereupon at T = 623°C the reaction is reversed. Thus, with increasing temperature the vapor contains more sulfur and iron-halogenide-complexes. Ultimately, on the low temperature side the vapor phase is saturated, and solid FeS_2 begins to form nuclei and precipitates (Klein & Hurlbut, 1999; Chapter 2.3). The growth velocity of a stable nucleus of pyrite under the above described conditions is of the order of 50 Å/s (Tomm et al., 1995).

The furnace used was a horizontal, 4-zone oven (KriZu-4PU, Dr. Harm Elektronik). The four different zones were individually manageable and controllable via control software. This software allows up to 50 program steps for each zone. In addition, heating rate, duration and end temperature of each zone in each step can be programmed. The temperature over the oven length was measured with an external thermocouple and is shown in Fig. 5.1. The difference between the desired and the observed temperatures are negligible (less than +/- 1 %). The placement of a silica-tube, the temperature gradient applied and the growth zone of the crystals are shown in Fig. 5.1. Heating rates and durations of the experiments are given in Tabs. 5.1, 5.2.

For the synthesis experiments polycrystalline pyrite was produced. It was synthesized from iron (MERCK, 1.03819.0500, pro analysi, 10 µm) and sulfur (ALDRICH, 231-722-6, Sulfur powder, -100 mesh, sublimed), in evacuated and sealed silica-tubes at temperatures of around 700°C, in the above described 4-zone oven. The conditions used for the synthesis are listed in Tab. 5.1. The products were characterized by X-ray powder diffraction. Polycrystalline pyrite was used as basic material to synthesize pyrite

Table 5.1: Heating rates and durations of experiments to synthesize polycrystalline pyrite.

Ramp cycle	zone 1 (°C)	zone 2 (°C)	zone 3 (°C)	zone 4 (°C)	time (h)	heating rate (°C/h)
1	300	300	300	300	4	100
2	500	500	500	500	3	100
3	650	663	676	700	50	100
4	25	25	25	25	2	-500

single crystals. Thus, the starting material consisted of about 1.5 g polycrystalline pyrite, approximately 30 mg sulfur and 0.04 mMol/cm^3 halogen. Additional sulfur was added, in order to increase the vapor pressure of sulfur and to avoid sulfur deficiency of the pyrite crystals, as suggested by Birkholz et al. (1991). A variety of transporting agents was used including iodine in the form of I_2 (MERCK, 4760, Iodine, resublimed),

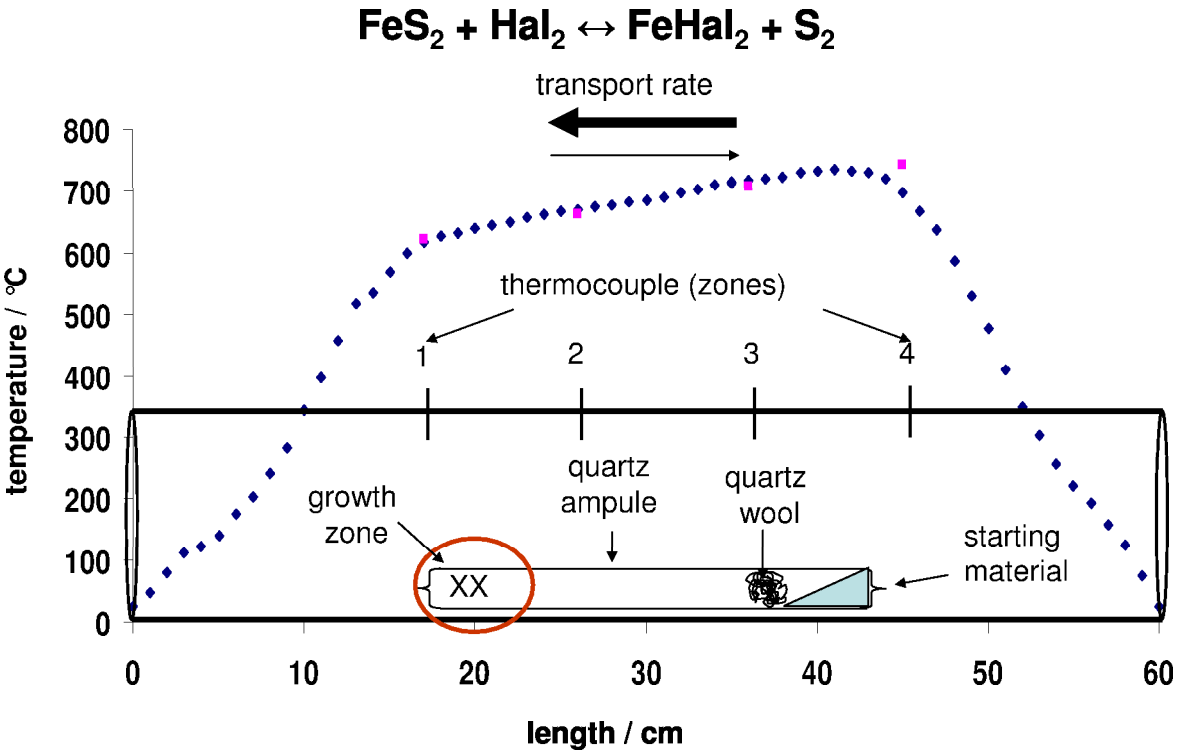

Figure 5.1: Schematic representation of CVT pyrite growth. The blue diamonds represent the temperature profile over the oven length in cm. The temperatures are presented by the red squares with: zone 1 = 623°C, 2 = 663°C, 3 = 707°C, 4 = 743°C.

Table 5.2: Heating rates and durations of experiments to synthesize pyrite single crystals from polycrystalline pyrite powder. Ramp cycle 5 is to deposit excessively sulfur on the side of the starting material.

Ramp cycle	zone 1 (°C)	zone 2 (°C)	zone 3 (°C)	zone 4 (°C)	time (h)	heating rate (°C/h)
1	300	300	300	300	4	100
2	500	500	500	500	3	100
3	743	707	663	623	30	100
4	623	663	707	743	240	100
5	450	400	300	200	10	-500
6	25	25	25	25	2	-500

bromine as $AlBr_3$ (Strem Chemicals, LOT#B 0308043, Aluminumbromide, 99 %) and chlorine as K_2PtCl_6 (Alfa Aesar, 012169, Potassiumhexachloroplatinate(IV)). After placing the starting materials into the silica-tubes, they were evacuated and welded shut. The duration and temperature values of the experiments are listed in Tab. 5.2. The growth experiments of the pyrite crystals were finished after approximately 12 days.

5.2 Microbial cultures

Microbial strains used in this study include strains of the mesophilic Bacteria *Thiobacillus sphaeroides* (strain SP 5/1), *Acidithiobacillus ferrooxidans* (strains HV 2/2 and VC 15/2), *Thiobacillus prosperus* (strain LM 3) and the thermophilic Archaea *Sulfolobus metallicus* (strain Kra 23), *Metallosphaera sedula* (strain TH 2), and the *Sulfolobus* strains HV 5 and VE 2.

The optimal growth conditions of the various strains are listed in Tab. 5.3, while the composition of the media are listed in the text below. The medium M1 (Huber et al., 1986) was used for all mesophilic cultures and contains 0.33 g KCl, 2.75 g $MgCl_2 \cdot 6\,H_2O$, 0.4 g $MgSO_4 \cdot 7\,H_2O$, 1.25 g NH_4Cl, 0.14 g $CaCl_2$, 0.14 g K_2HPO_4, 0.14 g KH_2PO_4, 0.5 g NaCl and 10 ml trace mineral solution (Balch et al, 1976) in 1000 ml distilled H_2O. The pH was adjusted using 0.1 N H_2SO_4.

For the cultivation of the archaeal organisms, the medium of Allen (1959), modified by Brock et al. (1972), was used. This medium contains 1.3 g $(NH_4)_2SO_4$, 0.28 g KH_2PO_4, 0.25 g $MgSO_4 \cdot 7\,H_2O$, 0.07 g $CaCl_2 \cdot 2\,H_2O$, 0.02 g $FeCl_3 \cdot 6\,H_2O$, 1.8 mg $MnCl_2 \cdot 4\,H_2O$, 4.5 mg $Na_2B_4O_7 \cdot 10\,H_2O$, 0.22 mg $ZnSO_4 \cdot 7\,H_2O$, 0.05 mg $CuCl_2 \cdot 2\,H_2O$, 0.03 mg $NaMoO_4 \cdot 2\,H_2O$, 0.03 mg $VOSO_4 \cdot 2\,H_2O$, 0.01 mg $CoSO_4$ and 1 l distilled or deionized water. The pH was adjusted with 10 N H_2SO_4.

Table 5.3: Optimal growth conditions of the various strains used in the etching experiments.

Organism	Strain	T / °C	pH	
Acidithiobacillus ferrooxidans	HV 2/2	37	2.5	Colmer & Hinkel (1947)
	VC 15/2	37	2.5	Colmer & Hinkel (1947)
Thiobacillus prosperus	LM 3	37	2.5	Huber & Stetter (1989)
Thiobacillus sphaeroides	SP 5/1	30	2.5	Huber & Rachel (unpublished)
Metallosphaera sedula	TH 2	75	2.5	Huber et al. (1989)
Sulfolobus metallicus	Kra 23	65	2.5	Huber & Stetter (1991)
Sulfolobus sp.	HV 5	85	2.5	Huber et al. (1986)
	VE 2	85	2.5	Huber et al. (1986)

5.2.1 Epifluorescence microscopy

To determine the number of cells on pyrite surfaces and the ratio of attached to unattached cells, pyrite sections were periodically observed using epifluorescence microscopy. To do this, a component in the specimen is marked with a fluorescent molecule called a fluorophore. In this study, the cells were marked by a modified 4'-6-Diamidino-2-phenylindole (DAPI) staining procedure according to Huber et al. (1985). DAPI forms fluorescent complexes with natural double-stranded DNA (excitation wavelength 365 nm). These complexes were visualized using an Olympus BX 60 phase contrast microscope with an oil immersion objective UPlanFl 100/1.3 of the University of Regensburg. The cells are illuminated with light of a specific wavelength, which is absorbed by the fluorophores causing them to emit longer wavelengths of light. The principle of the technique is shown in Fig. 5.2. Typical components of an epifluorescence microscope are the light source, the excitation filter, the dichroic beam splitter, the objective and the barrier filter. The filters and the dichroic beam splitter are chosen to match the spectral excitation and emission characteristics of the fluorophore used to mark the cells. The excitatory light is passed through the objective and then onto the cells. The fluorescence in the cells gives rise to emitted light which is focused to the detector by the same objective that is used for the excitation. A barrier filter between the objective and the detector filters out the excitation light from fluorescent light. Since most of the excitatory light is transmitted through the cells, only reflected excitatory light reaches the objective together with the emitted light and this method, therefore, gives an improved signal to noise ratio. With this technique it is possible to estimate the number of cells at surfaces as well as planktonic cells and, thus, to determine the ratios of attached to unattached cells.

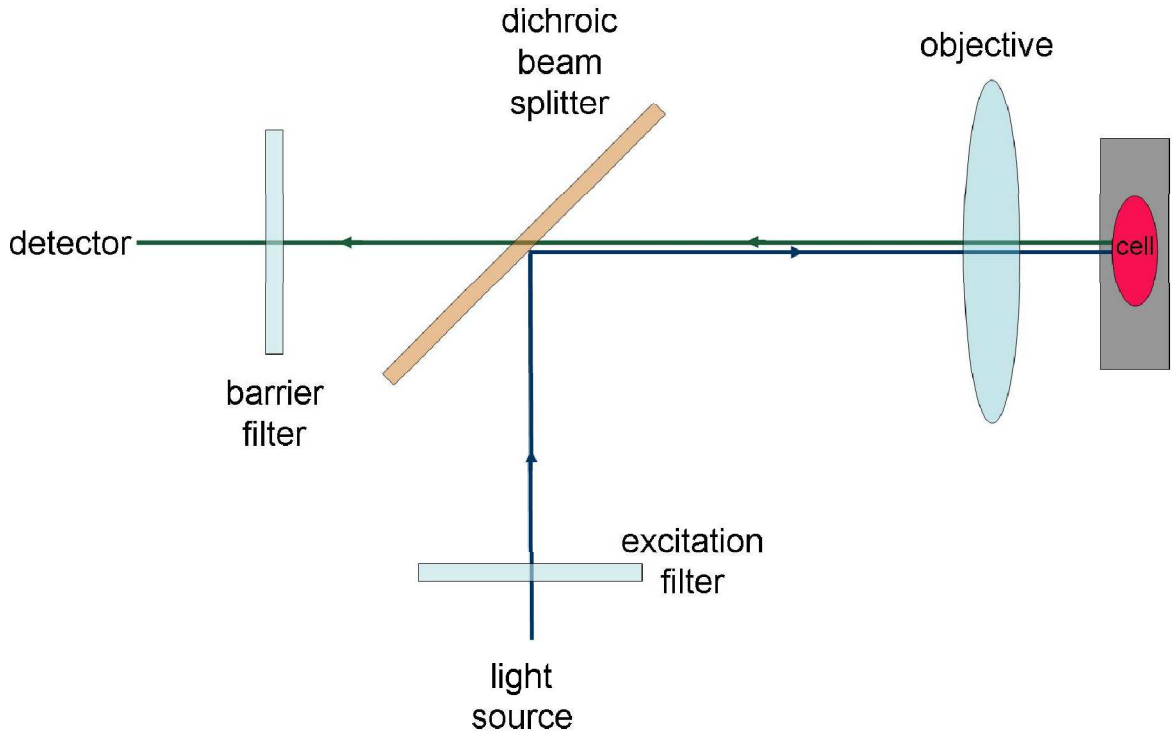

Figure 5.2: Principle of epifluorescence microscopy. Light passes through the excitation filter, through the dichroic beam splitter, the objective and onto the cell. Fluorophore molecules in the cell fluoresce. This backscattering light passes through the objective, the beam splitter and the barrier filter into the detector.

5.3 Etching experiments

This part focuses on the etching experiments. Several different experiments were performed, a summary of the experiments can be found in Tabs. 5.4, 5.5 and in the following subsections. They are divided into biological and abiotic experiments. The biological experiment will be discussed first. The second part addresses the abiotic experiments.

5.3.1 Biological experiments

Up to eight different microbial strains were used for the biological experiments (Chapter 5.2). In addition, different faces natural and cut pyrite surfaces were used (Chapter 5.1.1), as were synthetic pyrite crystals (Chapter 5.1.2). The identification code for the natural and cut pyrite surfaces consists of a two character code, where the first character describes the surface studied, the second describes the type of treatment. The identification codes are:

hexahedral face	{100}	=	C·
octahedral face	{111}	=	O·
pentagondodecahedral face	{210}	=	P·
natural surfaces		=	·N
cut surfaces		=	·P

Thus, six different surfaces of the natural and cut pyrites are possible: CN, CP, ON, OP, PN, PP. Synthetic pyrite single crystals are labeled with S. Tab. 5.4 contains all biological etching experiments.

The washed pyrite sections and synthetic crystals were put into 200 ml Erlenmeyer flasks containing 30 ml of the corresponding medium (Section 5.2). Afterwards, the medium was inoculated with 0.2 ml of the pre-cultures and the Erlenmeyer flasks were shaken at 30, 37°C (mesophilic Bacteria) and at 65, 75, 85°C (thermophilic Archaea) with 120 rpm. Each pyrite type was exposed to the strains in separated flasks. Experiments without incubation were performed as control experiments.

Table 5.4: List of biological experiments performed.

Incubation period	*Acidithiobacillus ferrooxidans*		*Thiobacillus prosperus*	*Thiobacillus sphaeroides*	*Metallosphaera sedula*	*Sulfolobus metallicus*	*Sulfolobus* sp.		Control inoculated
	HV 2/2	VC 15/2	LM 3	SP 5/1	TH 2	Kra 23	HV 5	VE 2	
1 day					CN,CP	CN,CP			
3 days					CN,CP	CN,CP			
5 days					CN,CP	CN,CP			
1 week	CN,CP		CN,CP		CN,CP	CN,CP			
					S	S			
2 weeks	CN,CP		CN,CP		CN,CP	CN,CP			
					S	S			
3 weeks	CN,CP		CN,CP		CN,CP	CN,CP			
4 weeks	CN,CP		CN,CP		CN,CP	CN,CP			
					S	S			
5 weeks	CN,CP		CN,CP		CN,CP	CN,CP			
6 weeks	CN,CP, ON,OP, PN,PP	CN,CP, ON,OP, PN,PP	CN,CP, ON,OP, PN,PP	CN,CP, ON,OP, PN,PP	CN,CP, ON,OP, PN,PP	CN,CP, ON,OP, PN,PP	CN,CP, ON,OP, PN,PP	CN,CP, ON,OP, PN,PP	CN,CP, ON,OP, PN,PP

C· = hexahedral face, {100},
O· = octahedral face, {111},
P· = pentagondodecahedral face, {210}
·N = natural surface,
·P = cut surface,
S = synthetic pyrite crystal

5.3.2 Abiotic experiments

The abiotic etching experiments were performed similarly to the biological experiments. Two oxidants were used, iron(III)sulfate ($Fe_2(SO_4)_3$) and sulfuric acid (H_2SO_4). The etching experiments with iron(III)sulfate were performed with a concentration of 5 g / l at two temperatures, 30 and 70°C. Those with sulfuric acid were performed with three concentrations, 0.1 N, 1 N and 10 N at 37°C. The pyrite samples were placed in 200 ml of the corresponding oxidant. Both were filled into Erlenmeyer flasks, stirred and heated when necessary.

The identification codes of the surfaces follow those described previously (page 54). Tab. 5.5 gives an overview for all abiotic etching experiments.

Table 5.5: List of abiotic experiments performed.

Incubation period	0.1 N	1 N	10 N	iron(III)sulfate 30°C	iron(III)sulfate 70°C
	sulfuric acid				
1 day	CN,CP	CN,CP	CN,CP	CN,CP,S	CN,CP,S
3 days				CN,CP,S	CN,CP,S
8 days	CN,CP	CN,CP	CN,CP	CN,CP,S	CN,CP,S
14 days				CN,CP,S	CN,CP,S
23 days				CN,CP,S	CN,CP,S
28 days	CN,CP	CN,CP	CN,CP	CN,CP,S	CN,CP,S
35 days				CN,CP,S	CN,CP,S

C· = hexahedral face, {100},
O· = octahedral face, {111},
P· = pentagondodecahedral face, {210},
·N = natural surface,
·P = cut surface,
S = synthetic pyrite crystal

5.4 Sample characterization

X-ray diffraction (XRD) and microprobe

X-ray powder diffraction, using a Siemens D5000 X-ray diffractometer with CuK_α (λ = 1.5418 Å) radiation over the range of 25 to 90° 2θ at a scan rate of 0.03° / min, was used to analyze the crystallinity and composition of pyrite. The patterns were analyzed using the DIFFRACplus Evaluation software package. Further, the crystals were analyzed with a Jeol JXA 8900R Microprobe at the University of Kiel with an accelerating voltage of 15 kV and a beam current of 30 mA using fayalite (fay85276) as standard for iron, pyrite (pyritMAC) as standard for sulfur and anorthite (an137041) as standard for aluminum. The diameter of the electron beam was approximately 1 µm. Each spot was measured for 15 s and the background for 7 s.

To obtain information on the quality of single crystal surfaces within the penetration depth of the X-rays, these were analyzed using a Bruker AXS D8-Discover X-ray microdiffractometer in horizontal geometry, via rocking-curves. This system uses a point focus X-ray source with Cu radiation, Ni filter and V-Groove channel-cut Ge-220-Monochromator. The sample is mounted on a 1/4 circle Euler cradle with xyz-table and as detector a scintillation counter with either an automatic slit or triple bouncing analyzer crystal was used.

Scanning Electron Microscopy (SEM - EDX)

All surfaces were characterized using scanning electron microscopy (SEM) prior to exposure, to allow assessment of etching effects. Three different instruments were used: a Jeol JSM-6500F of the Geophysical Laboratory, Carnegie Institution of Washington DC, a Philips XL30 SEM with a LaB_6 cathode of the Faculty of Technology of the University of Kiel, and a FEI Quanta 400 field emission SEM of the University of Regensburg. All three systems were equipped with an energy-dispersive X-ray spectrometer (EDX; EDAX Genesis). Pyrite samples were mounted onto standard SEM Al-stubs with Leit-C Plast and studied without additional sputter coating. The characterization of the samples prior to exposure was documented in detail so that it was possible to characterize the same region of the sample after the etching experiments. The sections were removed from the Al-stubs using ethanol, petroleum ether and hexane. After rinsing with distilled water, the samples were exposed to dissolution conditions. Upon removal from dissolution conditions, the pyrite samples were thoroughly rinsed with doubly-distilled water to prevent surface precipitation. The samples were air dried and kept in a desiccator before SEM investigations.

Optical two-circle reflection-goniometer

Synthetic single crystals were indexed by comparing measured angles of their faces and calculated angles. The angles were measured using a two circle reflection-goniometer after Federov & Goldschmidt (1892; Fig. 5.3). The optical two-circle goniometer of STOE (Model F) consists of two independently turntables, a horizontal (H) and a vertical (V) system with measurable angles ξ and η, respectively. The values ξ and η of the circle rotation needs to be established for each face in reflection, describing a vector with its origin in the center of the instrument and hence, in the center of the crystal (S). With this measured vectors, the angles of the plane normals between the different planes can be calculated. The measured angles between face normals enables one to make conclusions on the face index through comparison with calculated angles.

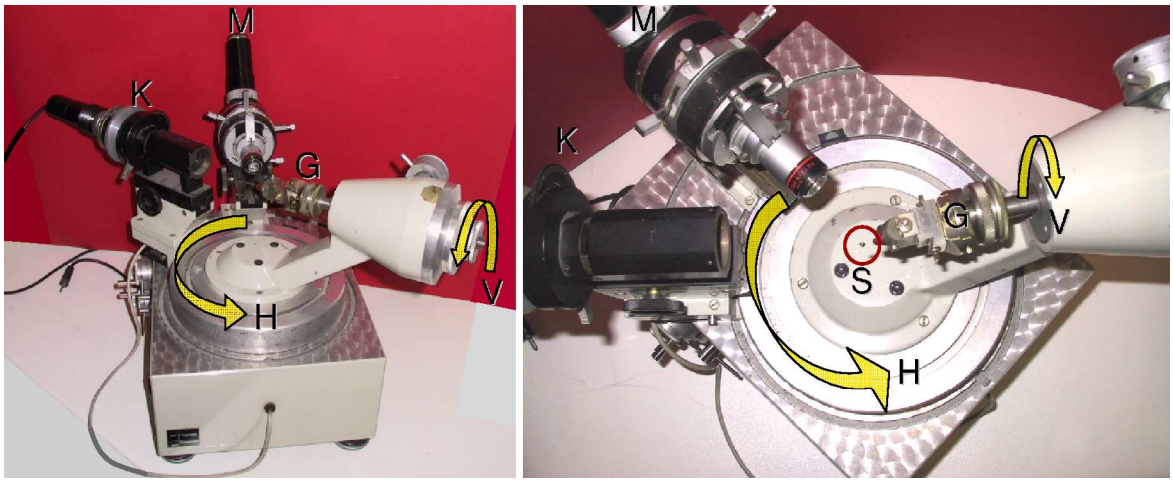

Figure 5.3: Optical 2-circle-goniometer (STOE) with the two turntables ξ (H - horizontal) and η (V - vertical). The collimator (K - light source) is connected to the horizontal circle, whereas the goniometer head (G) with the sample (S) is attached to the vertical circle (V). The microscope (M) is fixed.

Confocal white light microscopy (μ-Surf)

The topography of the surfaces was characterized using confocal white light microscopy. The instrument, a NanoFocus μ-Surf at the Faculty of Technology of the University of Kiel, performs non contact 3D-measurement of complex surfaces. The setup is drawn schematically in Fig. 5.4. In the confocal mode, white light passes through the aperture I and the dichroic mirror and is focused by the microscope objective on the sample. The light, reflected by the sample, is reflected by the mirror to the detector. Only light from the areas in focus are able to pass through the aperture II and are, thus, detectable. Emissions from regions below and above the focal plane (not shown) are severely attenuated by the aperture and do not contribute to the final confocal image. Thus, the topography of a surface can be mapped by this method. The used NanoFocus μ-Surf provides high vertical and lateral resolution (vertical +/- 2 nm).

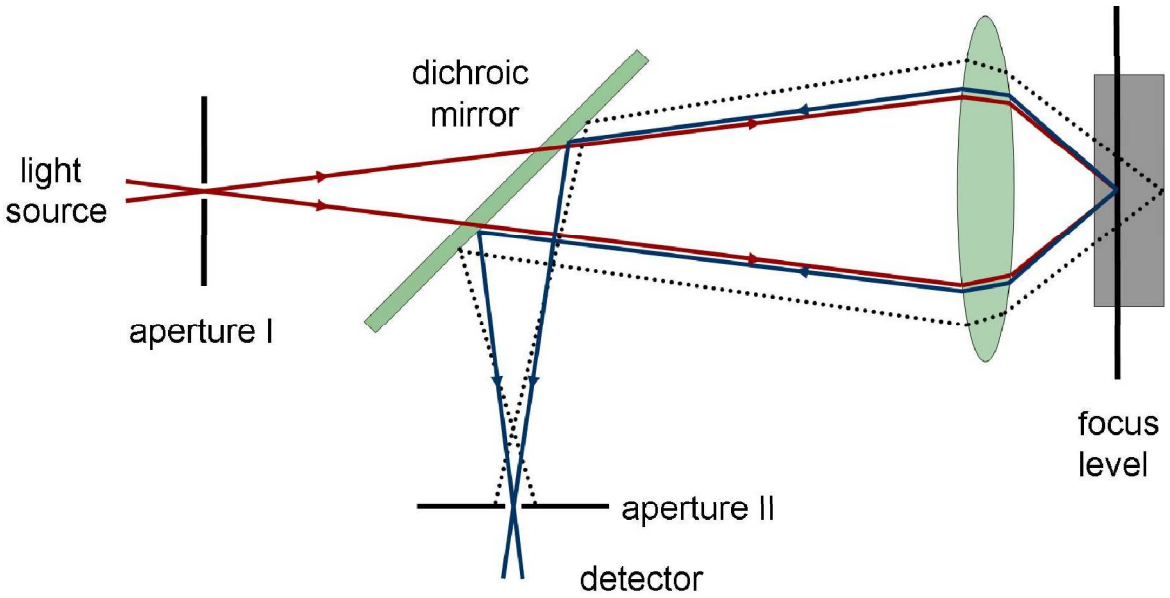

Figure 5.4: The principle of confocal microscopy. Light passes through aperture I and the dichroic mirror and is focused by the microscope objective on the sample. The backscattering light is reflected by the mirror to the detector. Only those emissions from the in focus areas are able to pass through the aperture II and are detectable.

Infrared Spectroscopy

The lattice vibrations of pyrite were studied via infrared spectroscopy (IR). Measurements in the far IR (40 - 400 cm^{-1}) and middle IR (400 - 4000 cm^{-1}) were performed at room temperature under vacuum using a Bruker Infrared Microscope (Model FS 66/V) at the University of Kiel. Two types of pellets for measurement were prepared under vacuum. The first type consisted of polyethylene, weighing 50 mg each and contained 1 wt % of the sample to be studied, was used for the spectral region 80 - 500 cm^{-1}. Whereas pellets of KBr, weighing 200 mg each and also containing 1 wt % of the sample to be studied, were used for the region 400 - 2000 cm^{-1}. Additionally, sample-free pellets of both types were prepared as standards. To remove absorbed water from the KBr pellets, they were kept in an oven for 24 h at 120°C before collecting the spectra. The spectra were generated by Fourier transformation of 512 interferometer scans and were recorded as absorbance.

Raman spectroscopy

The Raman-active lattice vibrations were studied with Raman spectroscopy. Here, monochromatic light is directed through the sample. Measurements were performed at room temperature under ambient conditions using a confocal Raman microscope alpha 300 R from WITec GmbH.

Chapter 6

Results

In this chapter the results of the various experiments are presented. In section 6.1 biological and abiotic etching experiments on natural and cut pyrite surfaces are described. In systematic studies, the effect of time, surface type and face-symmetry ({100}, {111}, {210}) are addressed. The biological experiments were performed using the eight strains of mesophilic Bacteria and thermophilic Archaea described in Chapters 3 and 5.2. The abiotic experiments were performed using sulfuric acid in different concentrations and iron(III)sulfate at two temperatures. The surfaces were analyzed with scanning electron microscopy and confocal white light microscopy before and after etching.

In section 6.2 the results of the synthesis and characterization of high quality pyrite single crystals, with up to five forms, are given. The crystals were synthesized by the chemical vapor transport technique (CVT) and the faces were indexed by two-circle reflection-goniometry. The composition and stoichiometry of the pyrite crystals were determined by electron microprobe analysis and structural properties were characterized with powder X-ray diffraction measurements. Spectral properties of the crystals were studied by powder IR spectroscopy and single-crystal Raman spectroscopy. The topography of crystal surfaces were studied by scanning electron microscopy and confocal white light microscopy. The structural quality of the crystal faces were analyzed by high-resolution X-ray diffraction, via rocking-curves.

In section 6.3 biological and abiotic etching experiments on synthetic pyrite surfaces are presented. In systematic studies the effect of face-symmetry ({100}, {111}, {210}, {211}, {221}), temperature and time are addressed. The biological experiments were performed using two strains of thermophilic Archaea (*Metallosphaera sedula, Sulfolobus metallicus*). The abiotic experiments were performed using iron(III)sulfate at 30 and 70°C. The surfaces were analyzed with scanning electron microscopy and confocal white light microscopy before and after etching.

6.1 Dissolution of natural and cut pyrite surfaces

To study the effects of a variety of microbial strains, surface type (natural, cut) and face-symmetry ({100}, {111}, {210}), three successive studies were made. The first study was a longtime study of six weeks incubation. In the second study, incubation times of one, three and five days were investigated and the third study addressed durations of one, two, three, four and five weeks. In addition, abiotic experiments using sulfuric acid of different concentrations (0.1 N, 1 N, 10 N) and iron(III)sulfate at 30°C and 70°C were performed. After exposure to sulfuric acid and iron(III)sulfate the surfaces were characterized after one day, one week, four weeks and one, two, four weeks, respectively.

6.1.1 Biological dissolution

The effects of microbial metabolic activity on natural and cut {100} pyrite surfaces are shown in Figs. 6.1 and 6.2. In both figures panels a - d show a compilation of low magnification electron micrographs of bacterially oxidized surfaces, while surfaces in panels e - h were etched by archaeal strains. The surfaces of all incubated samples were more strongly altered by archaeal than bacterial strains. Microbiological monitoring of the cultures during incubation showed that each culture containing pyrite showed metabolic activity. Cell densities were in the order of 10^8 cells per ml, with different ratios of planktonic to attached cells. The ratio of coexistence between planktonic and attached cells is 80 : 20 for *Thiobacillus sphaeroides*, 5 : 95 for *Acidithiobacillus ferrooxidans*, 40 : 60 for *Metallosphaera sedula* and 50 : 50 for *Sulfolobus metallicus* (Huber, Rachel, Klingl, personal communication).

In order to study the effect of growth media on pyrite etching, pyrite samples were exposed to the same growth media conditions (composition, pH, temperature, shaking) as the microbial etching experiment, yet were not inoculated with microorganisms. These samples did not show any surface oxidation effects after six weeks of incubation, but granular precipitations were observed, as can be seen exemplarily for the archaeal medium in Fig. 6.3 (the same areas before and after exposure are marked with ellipses). Consequently, the dissolution features observed after biological oxidation are attributed to the active microbial metabolism.

The different types of etching effects observed on the surfaces are shown in Fig. 6.4. There are large-scale features such as channel-like structures etched through the whole sample, shown in Fig. 6.4a, several hundreds of microns in length and tens of microns wide, etched by *Metallosphaera sedula* after two weeks of incubation, as well as on a smaller scale with individual etching features in the order of a few µm (e.g. Fig. 6.4b),

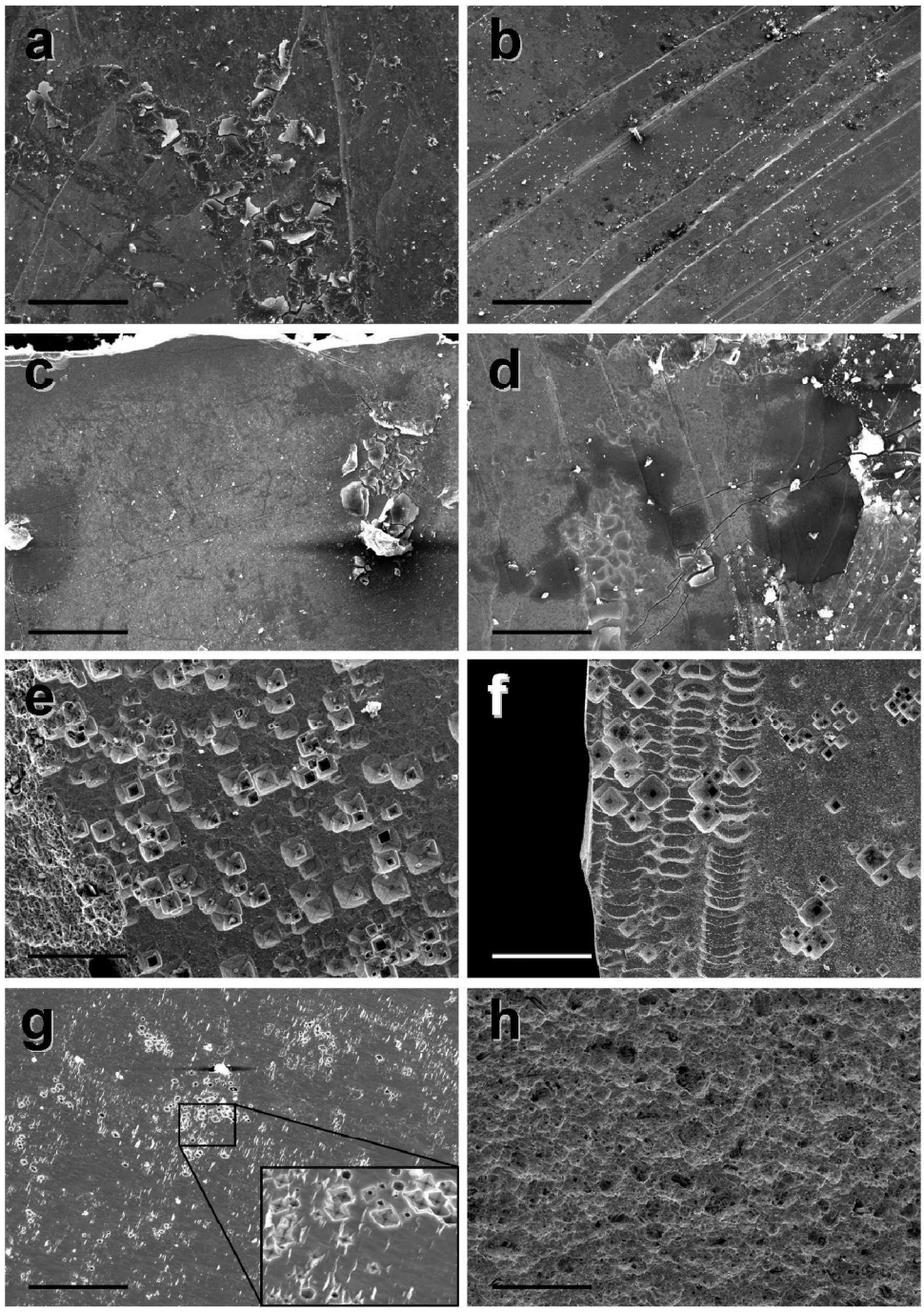

Figure 6.1: Electron micrographs showing microbially mediated pyrite surface etching of natural {100} surfaces after six weeks incubation. Bacterial strains used are a) *Acidithiobacillus ferrooxidans* (strain HV 2/2), b) *Acidithiobacillus ferrooxidans* (strain VC 15/2), c) *Thiobacillus prosperus*, d) *Thiobacillus sphaeroides*, and the archaeal strains e) *Metallosphaera sedula*, f) *Sulfolobus metallicus*, g) *Sulfolobus* sp. (strain HV 5), and h) *Sulfolobus* sp. (strain VE 2). The scale bar represents 200 µm.

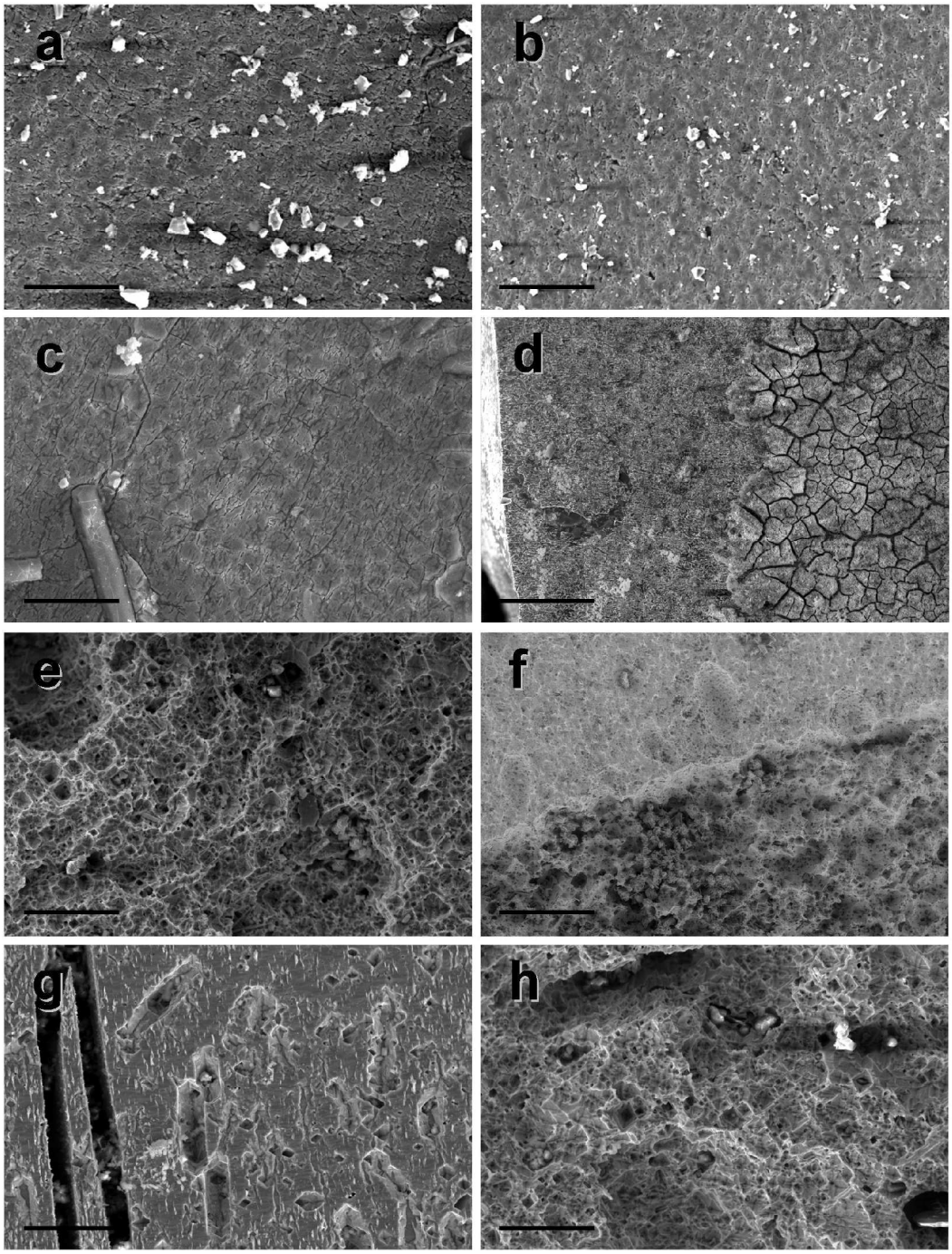

Figure 6.2: Electron micrographs showing microbially mediated pyrite surface etching of cut {100} surfaces after six weeks incubation. Bacterial strains used are a) *Acidithiobacillus ferrooxidans* (strain HV 2/2), b) *Acidithiobacillus ferrooxidans* (strain VC 15/2), c) *Thiobacillus prosperus*, d) *Thiobacillus sphaeroides*, and the archaeal strains are e) *Metallosphaera sedula*, f) *Sulfolobus metallicus*, g) *Sulfolobus* sp. (strain HV 5), and h) *Sulfolobus* sp. (strain VE 2). The scale bar represents 50 µm.

produced by *Thiobacillus sphaeroides* within six weeks. The dark elongated spots are remains of *Thiobacillus sphaeroides* cells (arrow). Characteristic and frequently observed features on {100} faces are inverted pyramidal structures (euhedral dissolution pits) as exemplified in Figs. 6.4c and d, both produced by *Sulfolobus metallicus*. Further observed surface dissolution results were 'sausage-shaped' features as shown in Fig. 6.4d. These structures appear to be multiple pyramids etched superimposing (inset). In this example the tips of inverted pyramids are truncated at a certain depth, in contrast to the individual pyramidal etching features (Fig. 6.7).

Irregular linear features produced by *Thiobacillus prosperus* after six weeks incubation were found (Fig. 6.4e); fine, curved long grooves with a length of several µm and

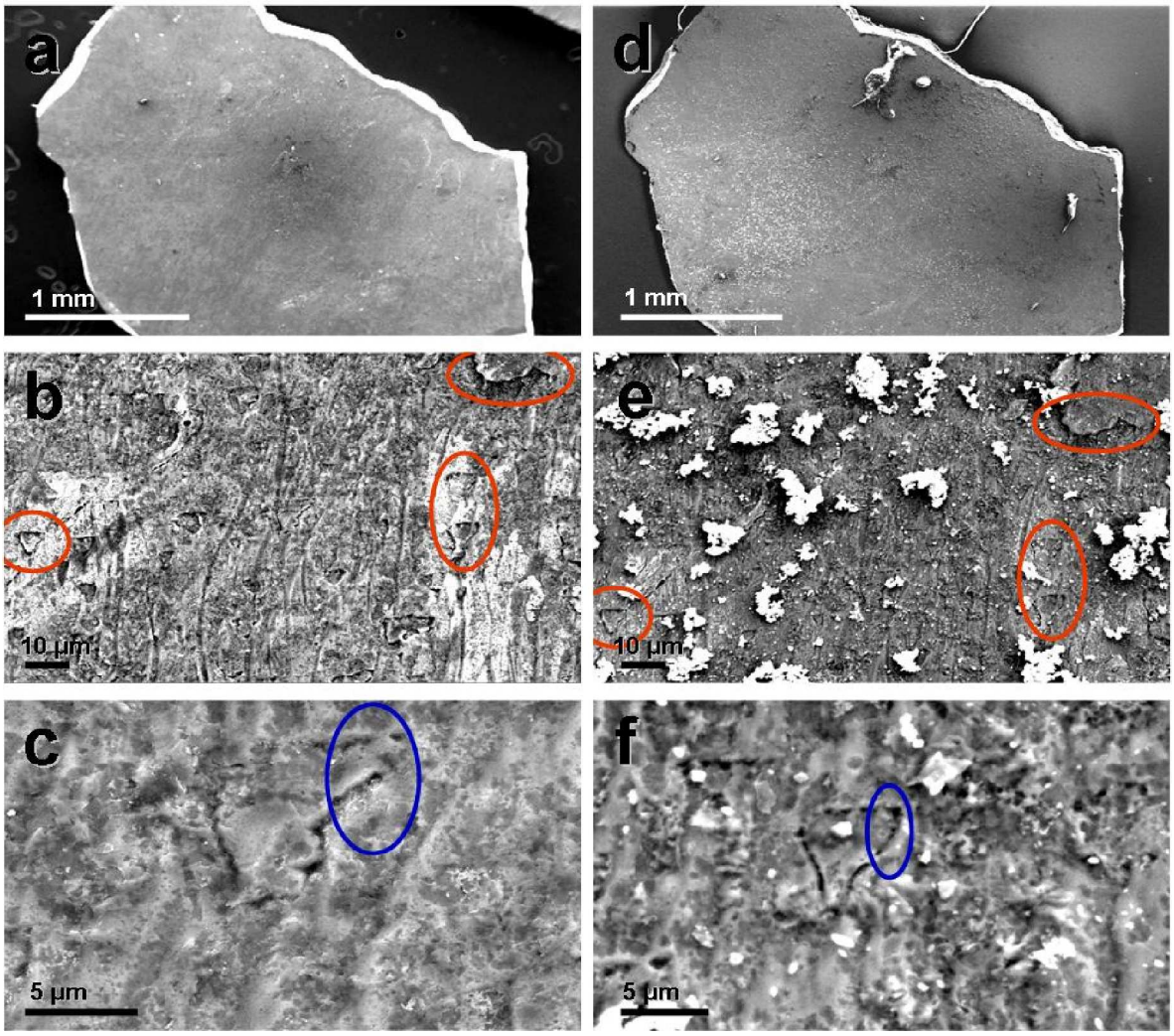

Figure 6.3: SEM images of a (100) pyrite surface before (a, b, c) and after (d, e, f) six weeks of exposure to the archaeal medium without microbes. The same areas before and after exposure are marked with ellipses.

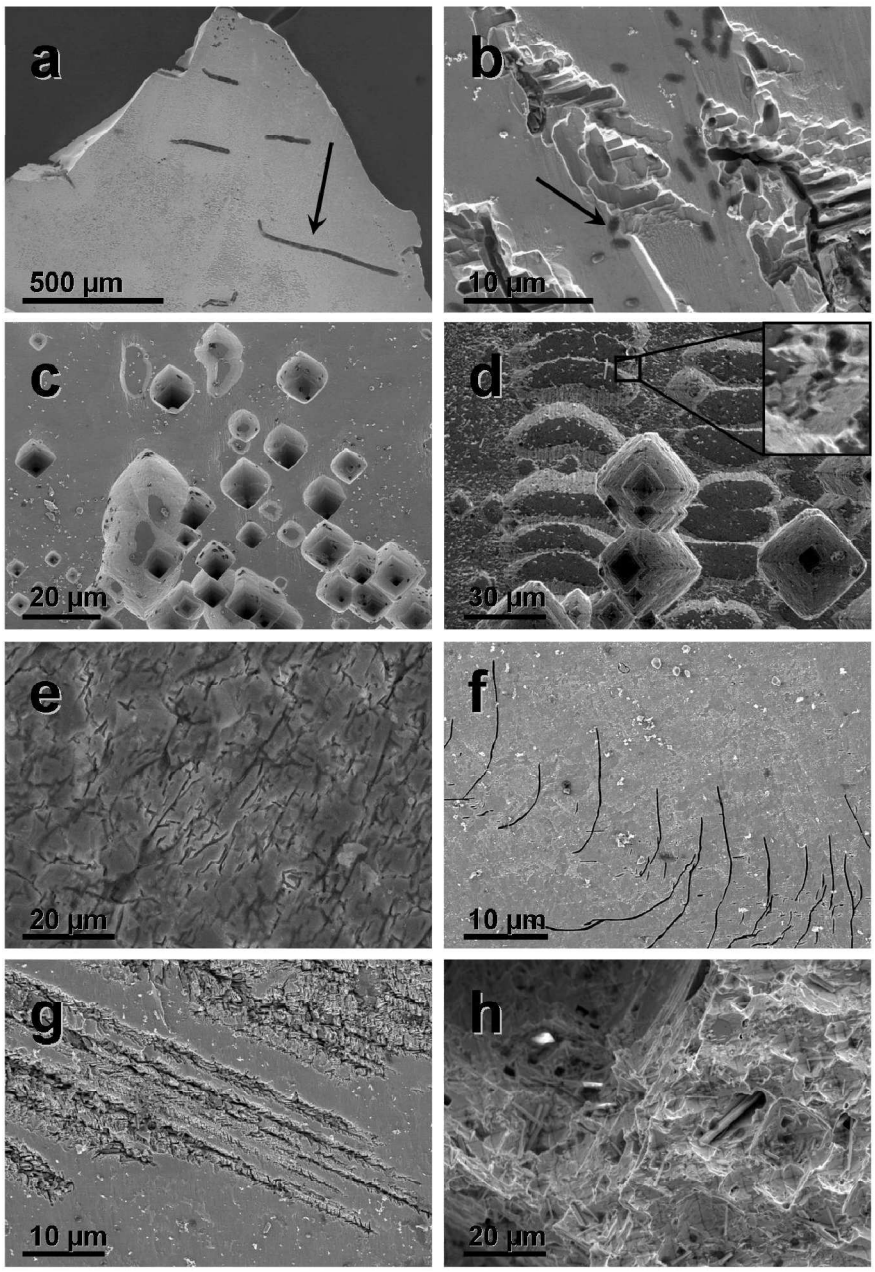

Figure 6.4: Selection of electron micrographs showing characteristic dissolution features on natural and cut {100} pyrite surfaces. a) channel-like structures (e.g. arrow), *Metallosphaera sedula* (two weeks); b) small-scale etching features in quasi-parallel and perpendicular arrangement, *Thiobacillus sphaeroides* (six weeks); c) inverted etching pyramids, *Sulfolobus metallicus* (two weeks); d) 'sausage-shape' etching features, *Sulfolobus metallicus* (six weeks); e) irregular patterns on cut surface, *Thiobacillus prosperus* (six weeks); f) curved elongated grooves, *Metallosphaera sedula* (five days); g) linear etching features, *Acidithiobacillus ferrooxidans* (HV 2/2, six weeks); h) multiple overlaying inverted etching pyramids, *Sulfolobus* sp. (HV 5, six weeks).

a diameter in the sub-µm-range (around 200 nm; Fig. 6.4f), etched by *Metallosphaera sedula* in five days. This structure appears to have been there before etching (compare Fig. 6.11). Other structures were straight linear etching features as shown in Fig. 6.4g. Figure 6.4h shows a heavily altered pyrite surface after six weeks incubation with *Sulfolobus* sp. (strain HV 5). The spongy surface texture results from numerous multiply overlaying etch pyramids of various sizes (sub-µm to tens of µm; Fig. 6.4h). All examples presented in Fig. 6.4 are observed on natural and cut {100} pyrite faces. The observations made on {100} faces are portable to dissolution effects observed on {111} and {210} faces, as shown for natural surfaces after six weeks of incubation in Figs. 6.5 and 6.6. Again, the surface features etched by bacterial strains (panels a - d) are less pronounced than produced by archaea (panels e - h) and archaeal etching produced mainly euhedral pits.

Fig. 6.7 shows a quasi-three-dimensional view of the 'sausage-shape' etching features of *Sulfolobus metallicus* on a (100) surface. The profiles run along the red and green arrows. It is obvious that the multiple pyramidal structures end at a certain depth, while the various depths are not necessarily the same for each structure (both profiles). The red-lined profile runs across a single pyramidal structure, which is significantly deeper etched into the surface (-3.5 µm), than the surrounding multiple pyramidal structures. Thus, for this sample, it appears that dissolution of the pyrite surfaces happens layer-wise.

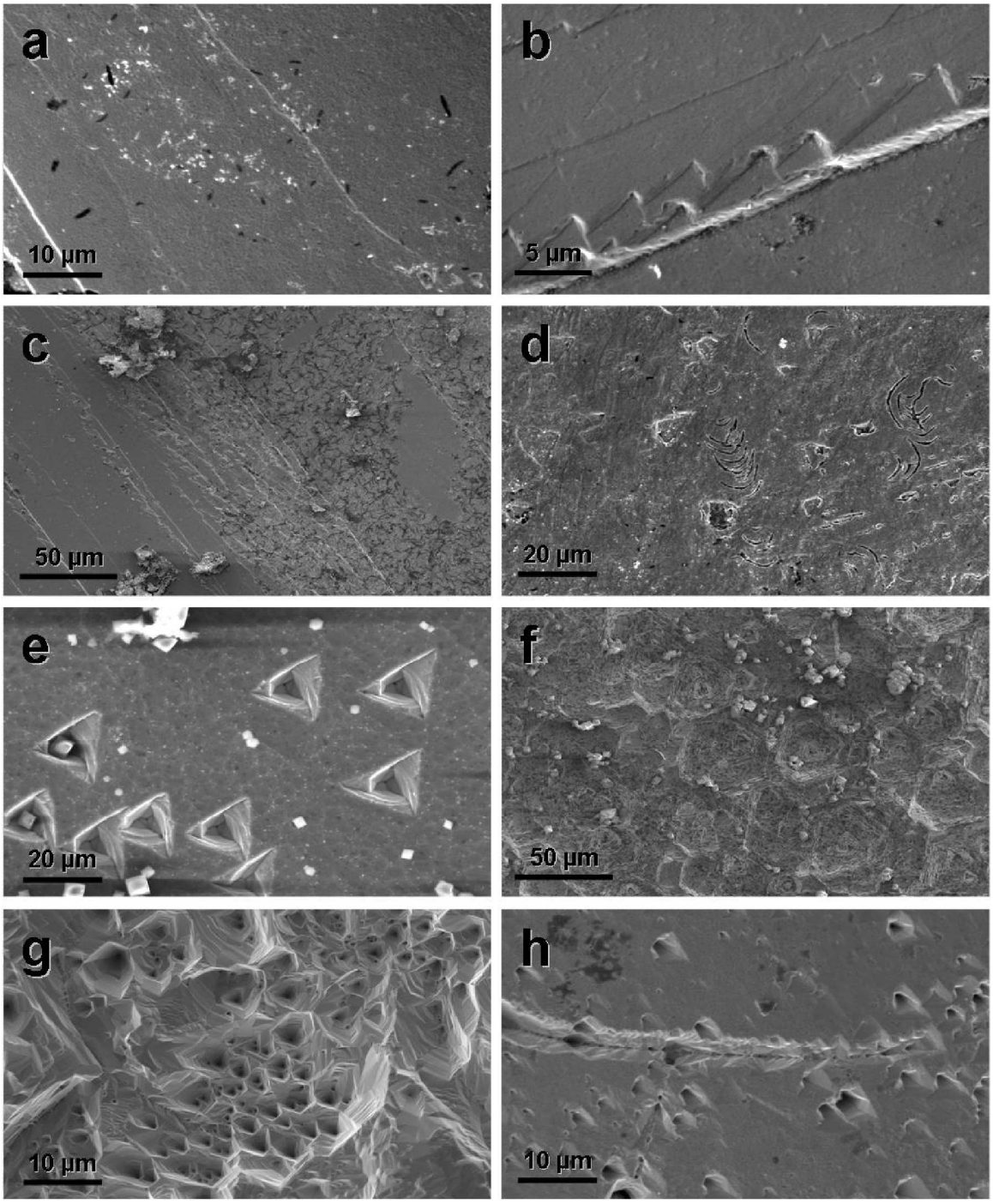

Figure 6.5: Electron micrographs showing microbially mediated pyrite surface etching of natural {111} surfaces after six weeks incubation; bacterial strains used are a) *Acidithiobacillus ferrooxidans* (strain HV 2/2), b) *Acidithiobacillus ferrooxidans* (strain VC 15/2), c) *Thiobacillus prosperus*, d) *Thiobacillus sphaeroides*, and the archaeal strains e) *Metallosphaera sedula*, f) *Sulfolobus metallicus*, g) *Sulfolobus* sp. (strain HV 5), and h) *Sulfolobus* sp. (strain VE 2). The scale bar represents 200 µm.

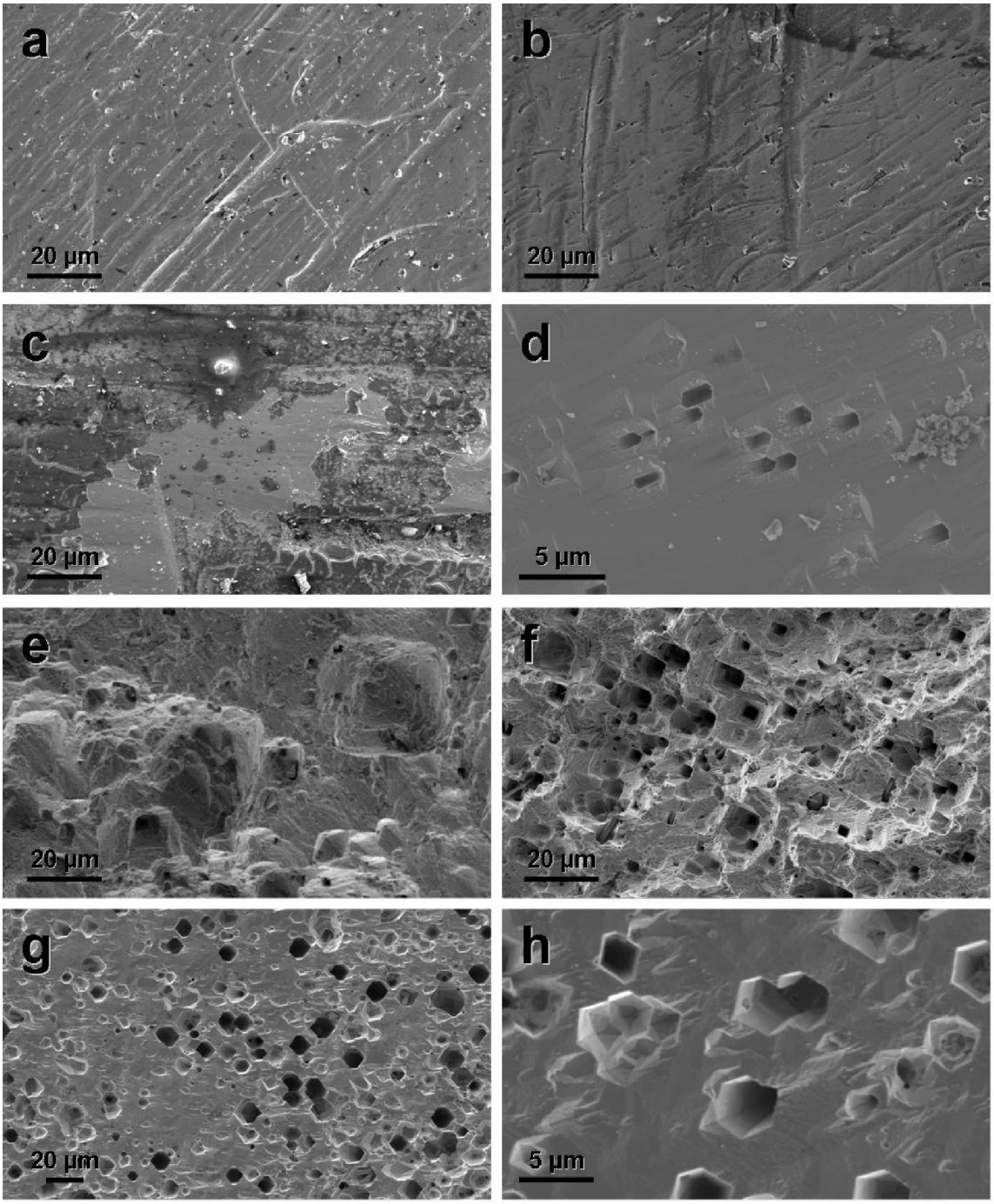

Figure 6.6: Electron micrographs showing microbially mediated pyrite surface etching of natural {210} surfaces after six weeks incubation; bacterial strains used are a) *Acidithiobacillus ferrooxidans* (strain HV 2/2), b) *Acidithiobacillus ferrooxidans* (strain VC 15/2), c) *Thiobacillus prosperus*, d) *Thiobacillus sphaeroides*, and the archaeal strains e) *Metallosphaera sedula*, f) *Sulfolobus metallicus*, g) *Sulfolobus* sp. (strain HV 5), and h) *Sulfolobus* sp. (strain VE 2). The scale bar represents 200 µm.

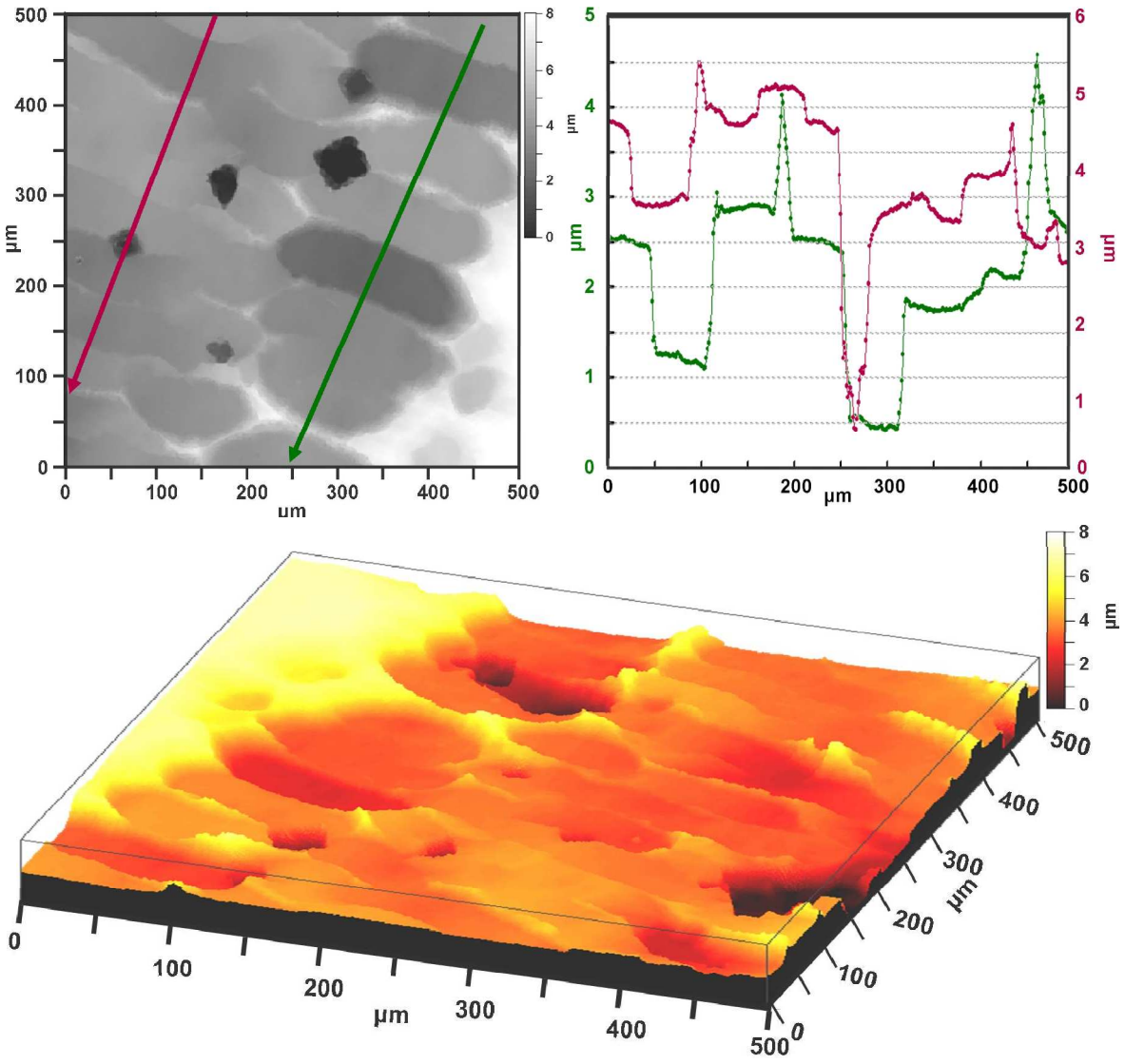

Figure 6.7: µ-Surf image and profiles of the sausage-shaped structures on pyrite (100) after six weeks of incubation with *Sulfolobus metallicus*. A quasi-three-dimensional view of the surface, including the directions, where the profiles are measured. The profile along the red arrow, includs a single pyramidal structure (deep hole), while the profile along the green arrow, shows the different structure depths.

6.1.2 Effects of discontinuities and impurity minerals

As described above, two types of pyrite surfaces were investigated, namely natural and cut. Although the pyrites were single crystals, SEM investigations of the cut surfaces revealed that the crystals contained several different impurity mineral phases (Fig. 6.8). Figure 6.8a shows EDX maps of a surface (secondary electron image top left) with three mineral inclusions containing silicon, aluminum and oxygen, whereas the pyrite matrix shows only iron and sulfur. Confocal Raman analysis showed that these minerals are unspecified hydrated aluminosilicates that also contain small rutile crystals (Furic et al., 2005) and quartz (Schmidt & Ziemann, 2000) inclusions (Fig. 6.8b).

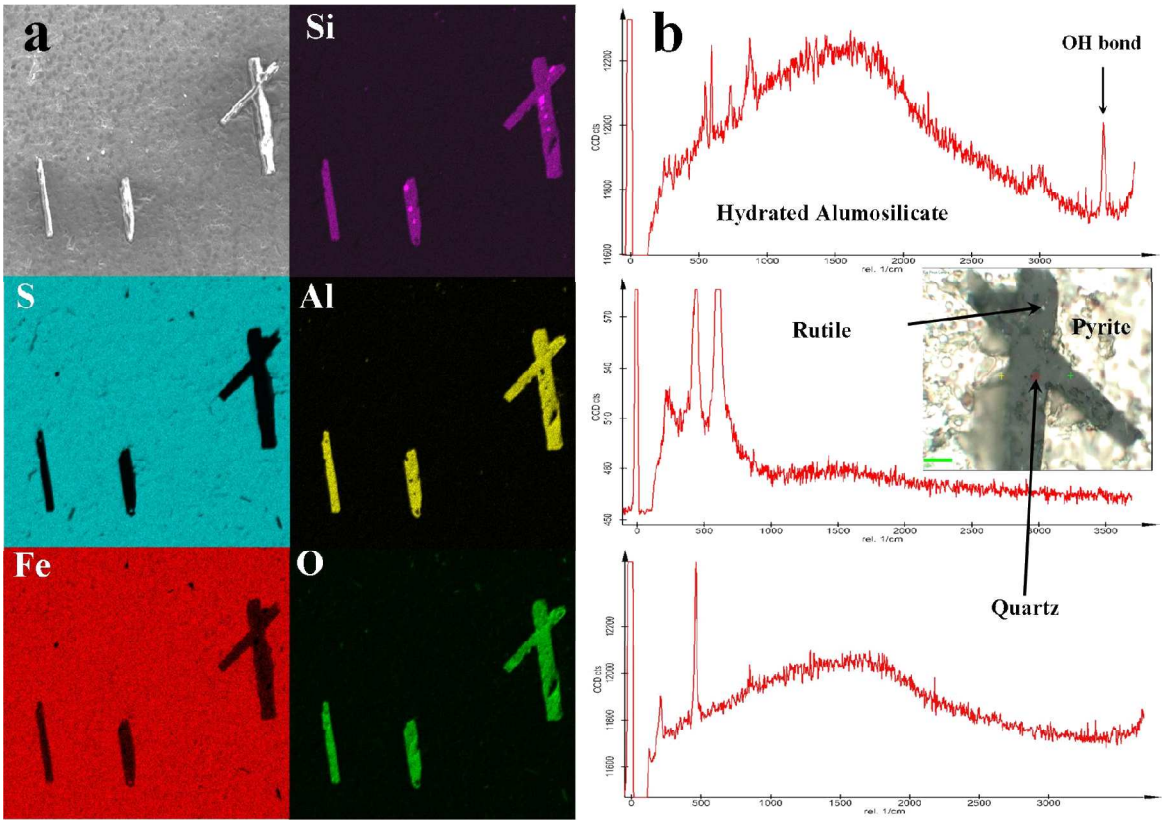

Figure 6.8: a) Secondary electron image (top left) showing area of analysis for EDX maps of S, Fe (pyrite matrix) and Si, Al and O for included crystals. b) shows confocal Raman spectra of an unspecified hydrated aluminosilicate (top), rutile (center) and quartz (bottom). The inset shows an optical image of the same crystal as analyzed in a) flipped at 180°. The quartz inclusion in b) corresponds with elevated Si concentration observed in the Si map in a).

These mineral inclusions create weaknesses on the cut surfaces and serve as regions at which pronounced etching occurs (Fig. 6.9, 6.10). Deep channels are observed around the large ($\sim 100\,\mu m$) mineral inclusions, whereas the pyrite surfaces otherwise appear to be heavily pitted with multiple inverted pyramidal structures overlaying and intersecting. This is shown in Fig. 6.2h. The development of this 'chaotic' appearance may further be mediated by effects as shown in Fig. 6.9a, showing the presence of numerous small ($\sim 1\,\mu m$ diameter, $\sim 5\,\mu m$ length) needle-shaped minerals released from the pyrite matrix by the etching process. Figure 6.9b shows impurity minerals associated with numerous cells of *Sulfolobus metallicus* (red arrows). Note that individual cells appear in etched grooves in the pyrite.

The effects of microbial etching on {100} surfaces are observable in Figs. 6.10 and 6.11. Both Figs. show the same pyrite surface before (Figs. 6.10a, b and 6.11a) and after incubation (6.10c, d and 6.11b). While Fig. 6.10 shows cut {100} pyrite surfaces, etched by *Sulfolobus metallicus* for six weeks, the structures in Fig. 6.11 were produced on a natural (100) pyrite surface by *Metallosphaera sedula* within five days. Discontinuities on the untreated pyrite surface (Fig. 6.10a, b and 6.11a) were observed at the same location after initial sample characterization, and it appears, that the discontinuities served as regions of preferred etching. The figures demonstrate directly the effect of impurity minerals, and unspecified surface discontinuities on the development of channel-like etching structures. In Fig. 6.10d features are hundreds

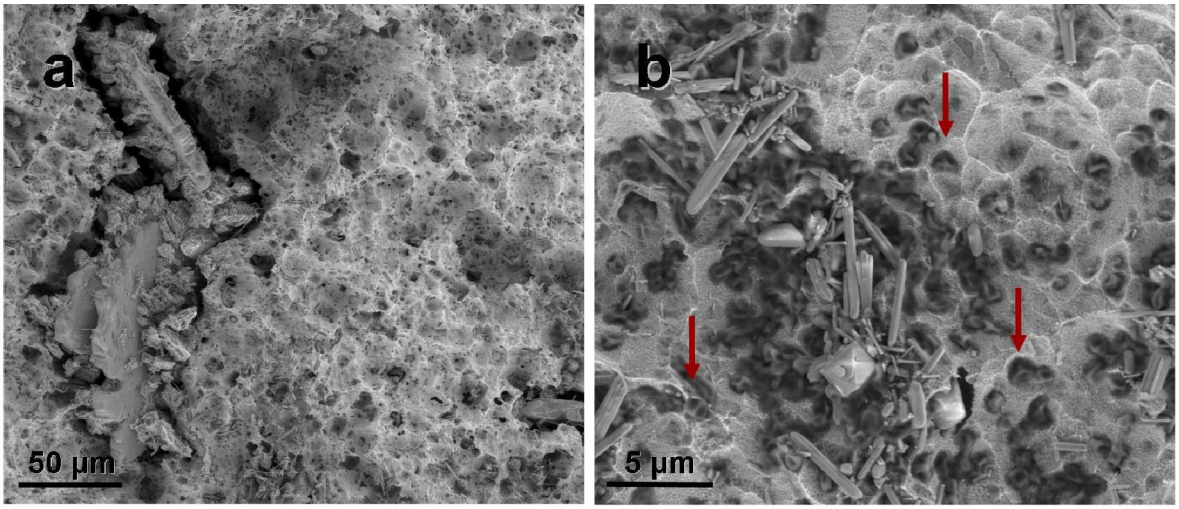

Figure 6.9: {100} cut pyrite surfaces after six weeks incubation with *Sulfolobus metallicus*. a) secondary minerals with pronounced etching at the border to the pyrite matrix; b) released secondary minerals and cells of *Sulfolobus metallicus* (red arrows).

of microns long and tens of microns wide, while in Fig. 6.11 the features are tens of microns long and hundreds nm wide. The different sizes on the different surfaces reflect the effect of time.

Different regions within some pyrite surfaces were observed, as can be seen in Figs. 6.10d, 6.12). The SEM image of Fig. 6.12 shows different areas at the pyrite surface; the etching features of the left part shows a few euhedral etching pits, whereas the etch pattern of the right area is sponge-like. This could be a result of structural or chemical differences between the two areas. The EDX maps of Fig. 6.12 show that there are indeed differences in composition. The matrix on both sides contain iron and sulfur from pyrite. The pictures on the right show titanium and oxygen coming from impurity rutile TiO_2 (compare Fig. 6.8). Thus, indicating a significant difference in composition of both areas.

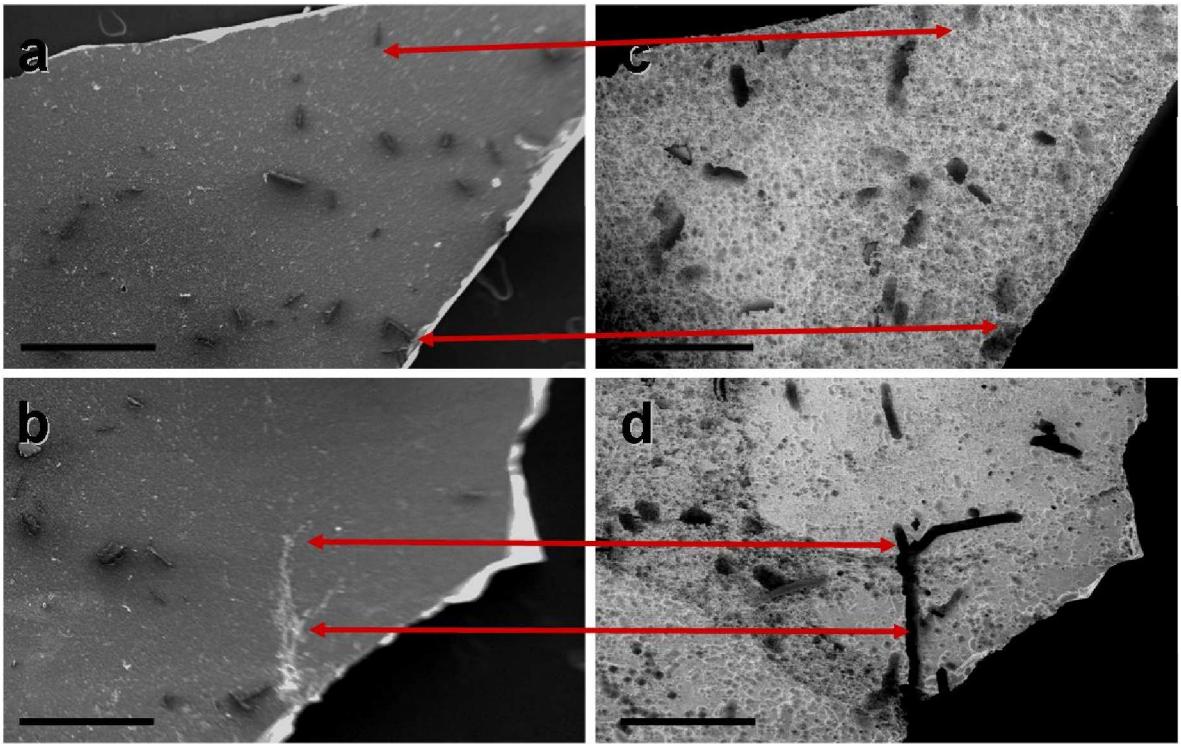

Figure 6.10: {100} cut pyrite surfaces before (a, b) and after six weeks incubation with *Sulfolobus metallicus* (c, d). a) secondary minerals are visible at the surface and result in pronounced etch pits (arrows, c); b) unspecified surface discontinuities are visible at the surface and result in pronounced channel etching structures (arrows, d). The scale bar represents 500 µm.

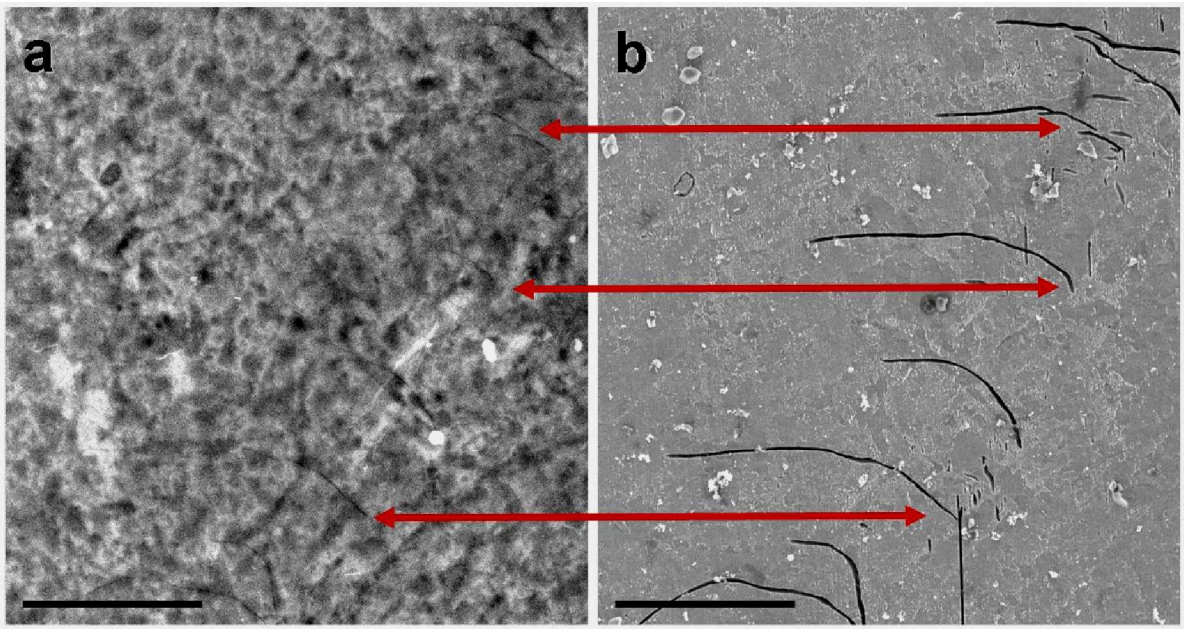

Figure 6.11: Natural (100) pyrite surface before (a) and after five days incubation with *Metallosphaera sedula* (b). Surface discontinuities served as areas of pronounced etching. The scale bar represents 10 µm.

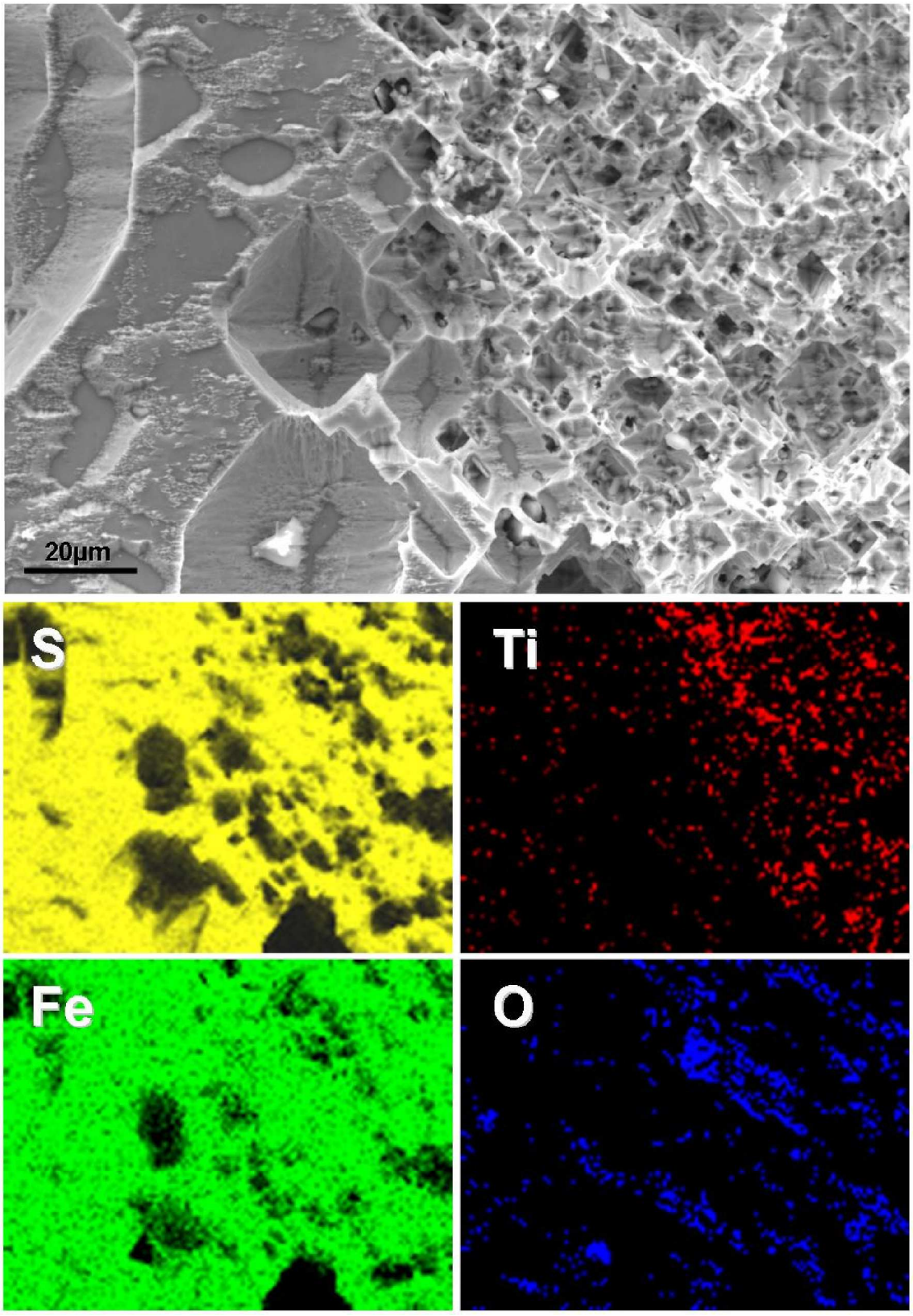

Figure 6.12: SEM image (top) showing area of EDX analysis of (100) pyrite. Measured were S and Fe (pyrite matrix) and Ti and O for embedded crystals.

Fig. 6.13 shows a rocking-curve map over the surface of the same sample used for Fig. 6.12. The area of less titanium and oxygen content is marked (top left, blue frame). The mapping in Fig. 6.13 shows the measured 200 peak of the (100) surface. The mapping direction is indicated by the black arrow. As shown in Fig. 6.13 exemplarily for scan no. 25, the shape of a single rocking-curve is the average intensity of the irradiated area (grey ellipse reflects the beam size) and the maximum intensity of the peak in scan no. 47 is lowered, which reflects the hole in the pyrite sample at this point. The peak maxima position of scans 13 to 25 is 16.54° θ. The kink of the peak maxima position between scan areas 13 - 25 and 25 - 58 indicates an inhomogeneity of the surface structure of this sample. It appears that the upper part reflects one grain (blue ellipse, euhedral etch pits, Fig. 6.12; from scan 13 to 25 ≡ 1 mm), while the lower part is another slightly tilted grain (sponge structures, Fig. 6.12; from scan 25 to 58). Thus, the differences in composition (Fig. 6.12) and grain orientation (Fig. 6.13) result in differences of etch patterns.

Examples of cell attachment at pyrite surfaces are shown in Fig. 6.14. The density of cells on the surfaces, however, varies between microbial strains (as described

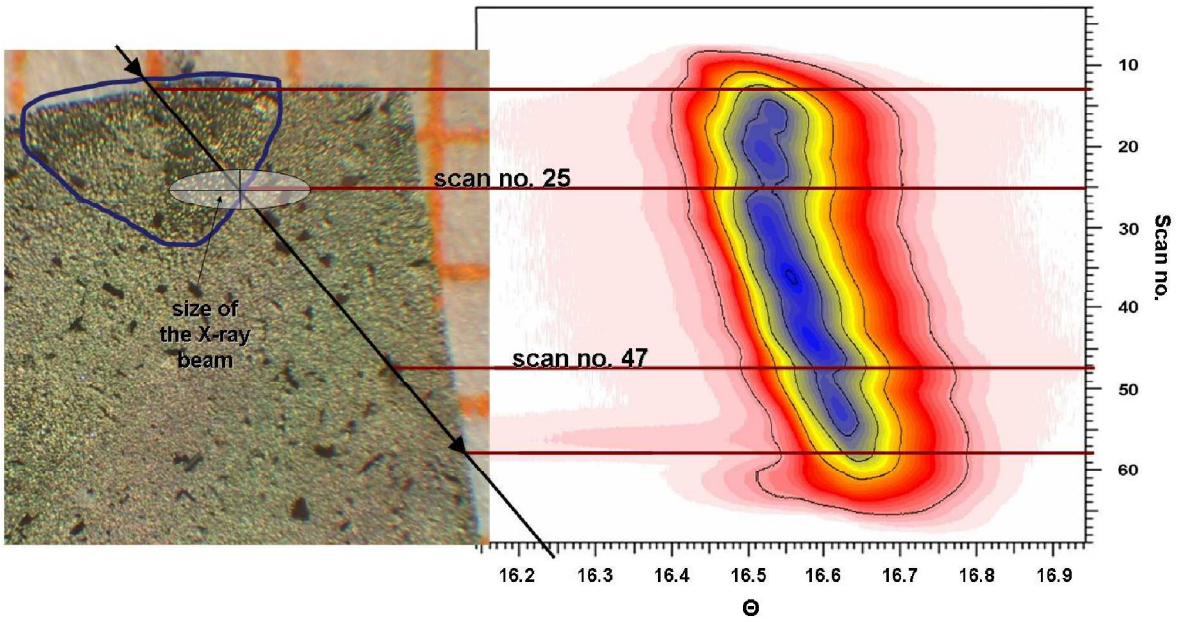

Figure 6.13: Light microscope image and map of rocking-curves of the 200 peak over pyrite surface, following the black arrow. The grey ellipse reflects the X-ray beam size and therefore the average area of the integrated intensity per scan. The full width at half maximum were between 100 and 150 arcsec. The blue frame indicates the area with less titanium and oxygen content (Fig. 6.12).

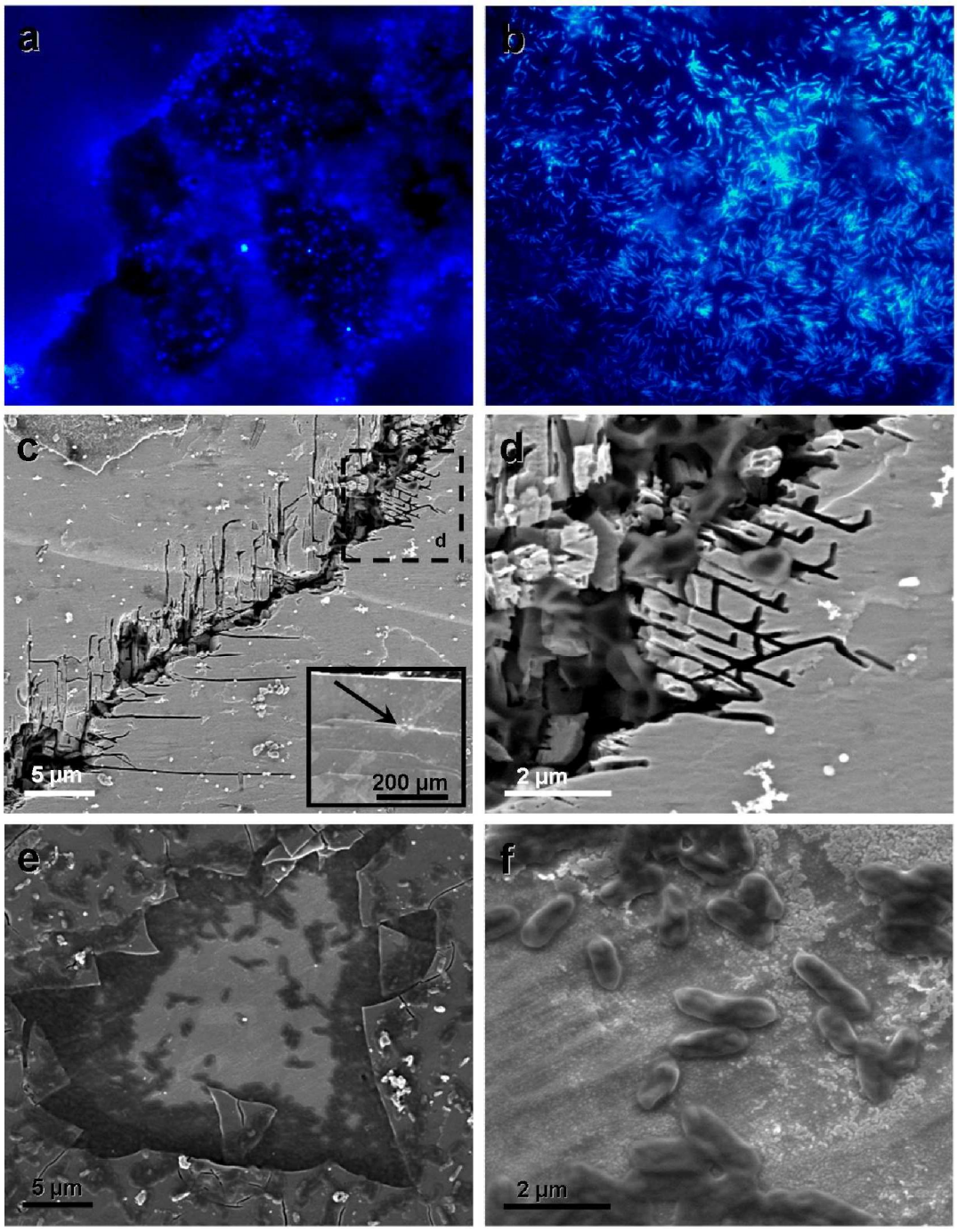

Figure 6.14: Examples of cell attachment to pyrite surfaces observed with epifluorescence microscopy (a, b); example in a) shows *Sulfolobus metallicus* after 42 days of incubation, and b) shows *Thiobacillus prosperus*, after 7 days of incubation. c) and d) show *Sulfolobus metallicus* on a natural (100) pyrite surface after five days of incubation (square indicates zoom area of image d); e) and f) show SEM images of attached *Thiobacillus sphaeroides* cells after six weeks incubation.

above). Epifluorescence microscopy revealed coccoid (although truly lobed) cells of *Sulfolobus metallicus* (Fig. 6.14a) and rod-shaped cells of *Thiobacillus prosperus* colonizing the pyrite surface (Fig. 6.14b) with a random distribution. This contradicts previous reports, where attachment occurs preferred along crystallographic directions (Edwards et al., 1999). The SEM images in Figs. 6.14c and d show cell attachment of *Sulfolobus metallicus* on a natural (100) pyrite surface after five days of incubation. In Fig. 6.14d cells of *Sulfolobus metallicus* can be seen inside the central etched channel, which was not present prior to incubation. However, a discontinuity on the untreated pyrite surface (inset Fig. 6.14c) was observed in the same location after initial sample characterization. Again, this discontinuity served as region of preferred cell attachment and subsequent etching resulting in nanometer-sized elongated dissolution features radiating away from the cells and the discontinuity. This suggests that microbial activity influences locally the solution with producing sulfuric acid and ferric iron. The SEM images in Figs. 6.14e (arrow) and f show cells of *Thiobacillus sphaeroides* on a natural {100} pyrite surfaces after six weeks of incubation.

6.1.3 Time resolved studies

Figure 6.15 shows representative results of the time-resolved studies. The bacterial strains *Acidithiobacillus ferrooxidans* (panels a) and *Thiobacillus prosperus* (panels b), and the archaeal strains *Metallosphaera sedula* (panels c) and *Sulfolobus metallicus* (panels d) were used. Natural {100} faces were incubated with these cultures and then recovered and analyzed after one (Figs. 6.15-1), three (Figs. 6.15-3) and six weeks (Figs. 6.15-6). After one week of incubation with bacterial strains, the surfaces appeared largely unaltered with no clear etching features being present (Figs. 6.15a1, b1). After three weeks of incubation with bacterial strains, distinct etching features appeared, with large parts of the mineral surface remaining unaltered (Figs. 6.15a3, b3). Multiple small-scale etching features are present after six weeks of incubation with bacterial strains (as in Fig. 6.15a6, b6) that are dispersed across the sample surface and are associated with remains of cells of *Thiobacillus prosperus* (Fig. 6.15b6, rod-shaped shadows). In contrast, surfaces incubated with the archaeal strains *Metallosphaera sedula* and *Sulfolobus metallicus* already showed significant oxidation effects after one week of incubation (Figs. 6.15c1, d1). These effects become more pronounced with time as exemplified by the increasing number and size of inverted etching pyramids. After three weeks of incubation with archaeal strains, the complete surface is altered (Figs. 6.15c3, d3). The diameter of the pyramids after three weeks is in the range of 10 to 30 µm and exceeds 100 µm after six weeks (Figs. 6.15c, d show cutouts of the surfaces, to compare the size of the dissolution features directly with those etched by the Bacteria). On the natural {100} surfaces etched by Archaea, remains of archaeal cells were found (exemplary in Fig. 6.15d3; arrow). The cells preferably attach inside the etch structures. Similar to Fig. 6.1, the effects of surface alteration by the bacterial strains is less pronounced than those etched by archaea strains.

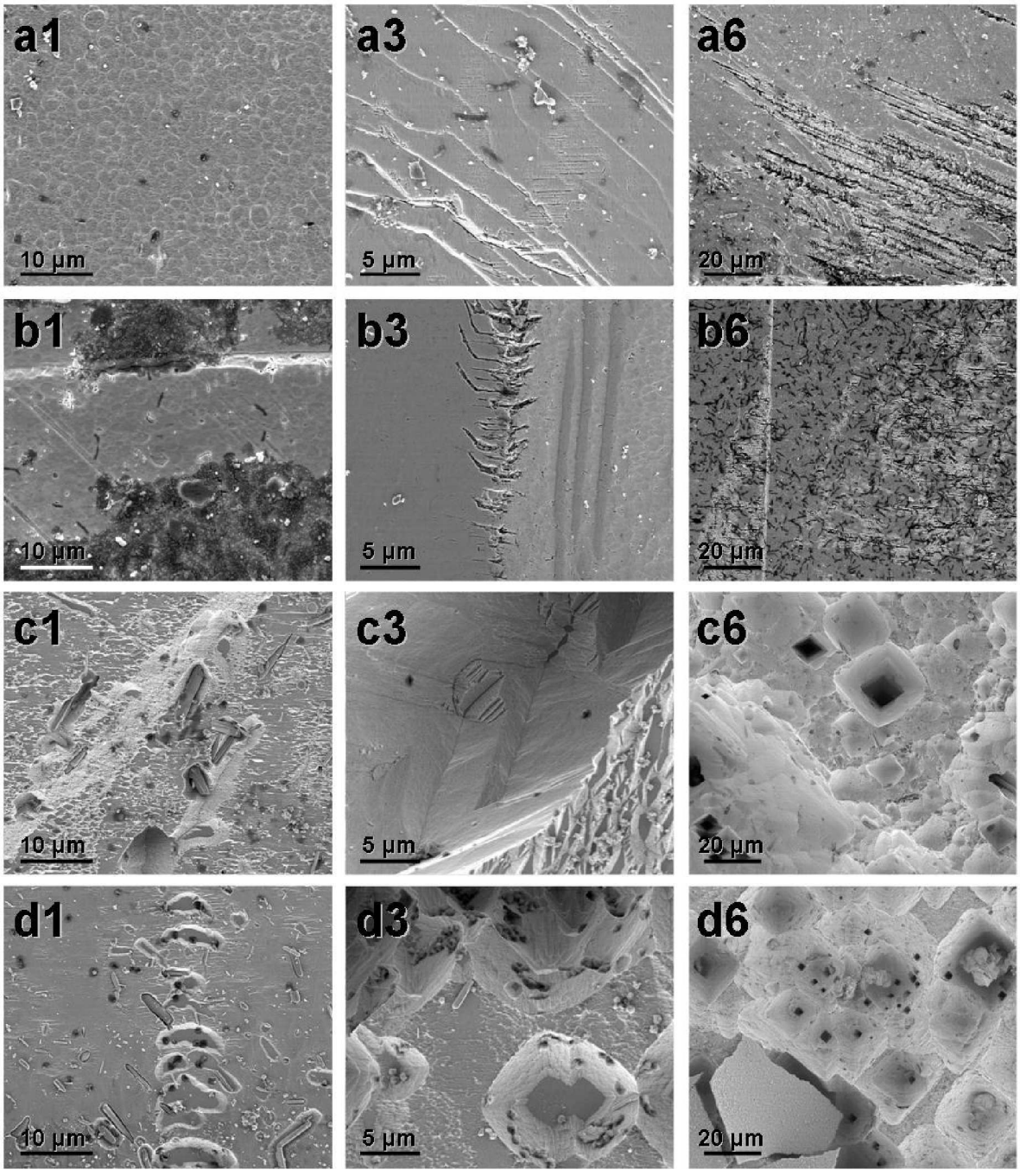

Figure 6.15: SEM images of representative examples for time-resolved microbially mediated etching experiments. Images show pyrite surfaces etched by *Acidithiobacillus ferrooxidans* (a), *Thiobacillus prosperus* (b), *Metallosphaera sedula* (c) and *Sulfolobus metallicus* (d). The numbers of the images 1, 3 and 6 specify the time of incubation, one week, three weeks and six weeks, respectively.

6.1.4 Etch pit shape as a function of face-symmetry

Fig. 6.16 shows etch features after six weeks of incubation with the culture *Sulfolobus* sp. (strain HV 5). The natural (100) pyrite surface shows inverted pyramids (Fig. 6.16a). Examples of etching pyramids produced by *Sulfolobus metallicus* on (100) faces are shown in the inset. The symmetries of the face patterns on the (100) surface corresponds to $2mm$. Inverted etching pyramids present on natural {111} faces, as shown in Fig. 6.16b, have a three-fold (3) symmetry. Figure 6.16c shows etching structures on a (210) surface. Here features appear as irregular hexagons on the mineral surface following the symmetry of m. Occasionally irregular pentagons appear (inset).

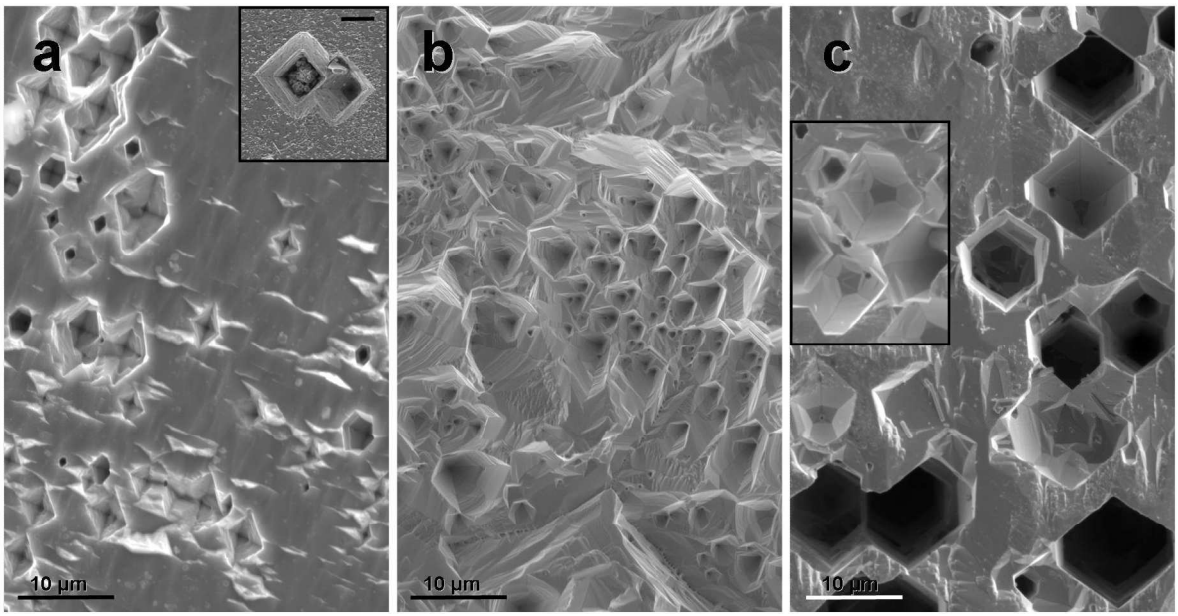

Figure 6.16: SEM images of dissolution features generated after six weeks of incubation with *Sulfolobus* sp. (strain HV 5). a) shows inverted pyramidal structures on a natural (100) face (inset scale bar 10 µm); b) shows triangular features on a natural (111) face; c) shows irregular inverted hexagons on a natural (210) face. The inset in c) shows irregular pentagons in the bottom end on an etching feature that appears as an irregular hexagon at the mineral surface. All etching features represent the corresponding symmetries on the surfaces: {100} - $2mm$, {111} - 3 and {210} - m.

6.1.5 Abiotic dissolution

Abiotic control experiments were performed with natural and cut {100} faces exposed to 0.1 N, 1 N and 10 N sulfuric acid and iron(III)sulfate solution at 30 and 70°C. Experimental times were one day, one week and four weeks.

The crystal faces appeared largely unaltered after exposure to sulfuric acid for one day, independent of concentration. Characteristic surface features (Fig. 6.17) were present on all faces after one week. Figure 6.17a shows that etching features after one week in 0.1 N sulfuric acid with increasing abundance after four weeks (Fig. 6.17b). Dissolution features in the 100 nm range after four weeks of exposure (inset Fig. 6.17b) may indicate commencement of dissolution. Micrometer sized irregular etching features developed in 1 N sulfuric acid after one week (Fig. 6.17c) with increasing abundance after four weeks in 1 N sulfuric acid (Fig. 6.17d). Linear etching features were produced after one week in 10 N sulfuric acid (Fig. 6.17e). Inverted pyramids few hundred nm in diameter developed in low abundance on the same pyrite face (inset Fig. 6.17e) and with increasing abundance after four weeks (Fig. 6.17f). These results show that there is no noticeable difference in type and abundance of surface features on natural {100} pyrite faces as a function of sulfuric acid concentration. For cut {100} faces, structures identical to those described in Fig. 6.4e were observed after four weeks in 1 N and 10 N sulfuric acid (Fig. 6.17g, h).

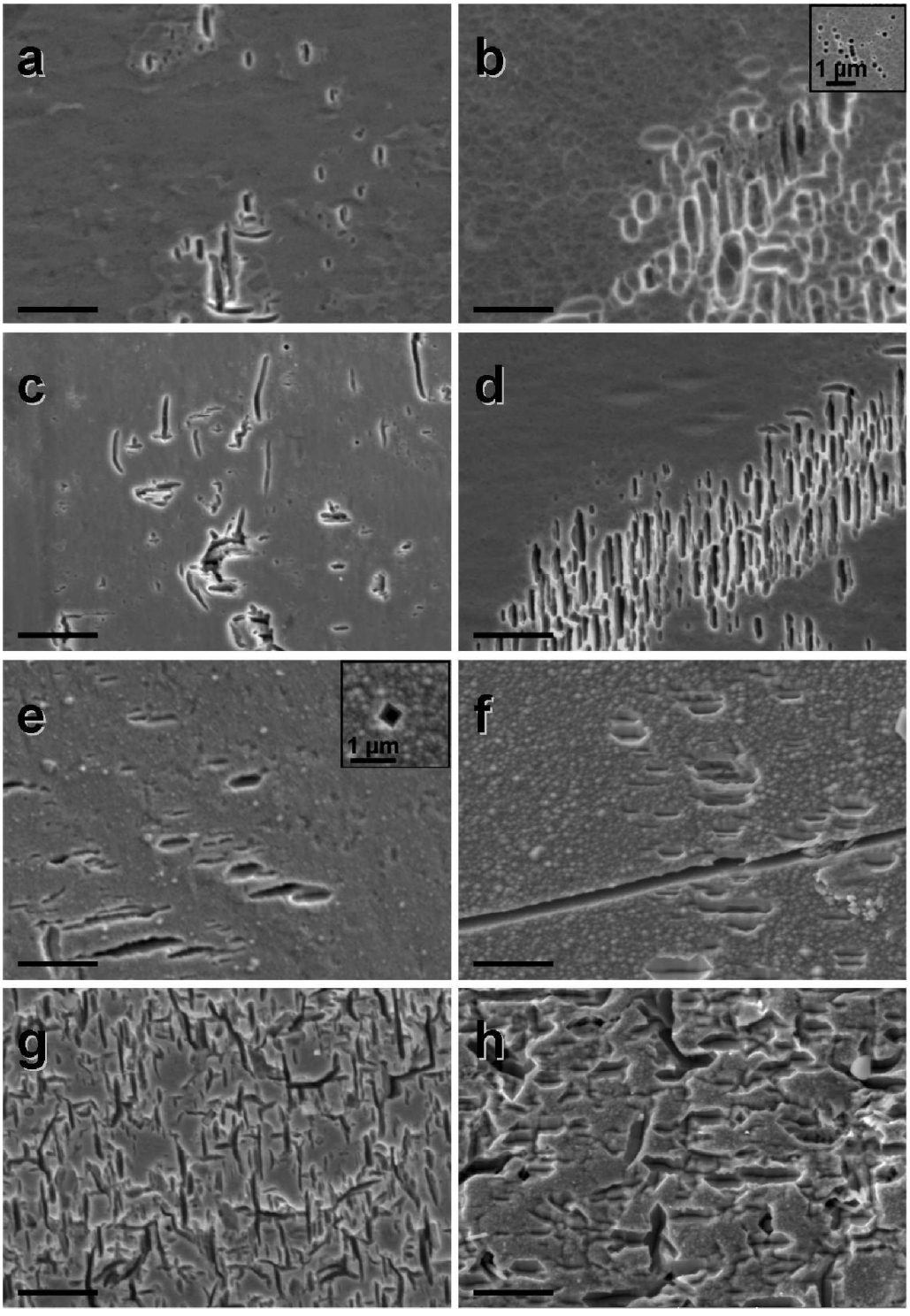

Figure 6.17: SEM images of {100} pyrite faces after sulfuric acid etching. a) natural surface, 0.1 N sulfuric acid (one week); b) after four weeks in 0.1 N sulfuric acid; c) natural {100} surface, 1 N sulfuric acid (one week); d) after four weeks in 1 N sulfuric acid; e) natural surface after one week in 10 N sulfuric acid; f) after four weeks in 10 N sulfuric acid; g) cut surface, 1 N sulfuric acid (four weeks); h) cut surface, 10 N sulfuric acid (four weeks). The scale bar represents 50 µm.

The effect of abiotic iron(III)sulfate etching was investigated, as well as the effect of temperature and time. During the experiments, the pH and temperature trend were monitored (Tab. 6.1). The effects of iron(III)sulfate etching on natural and cut {100} pyrite surfaces are shown in Fig. 6.18 and 6.19, respectively. Panels a and b show the experiments at 30°C and 70°C, respectively, recovered and analyzed after one (6.18-1, 6.19-1), eight (6.18-8, 6.19-8) and thirty (6.18-30, 6.19-30) days. After one day exposure, features of a few microns appeared on all surfaces for both temperatures (Figs. 6.18a1, b1 and Figs. 6.19a1, b1). Dissolution took place at edges (Fig. 6.19b1), rifts (Fig. 6.18a1) and defect structures (Fig. 6.18b1). The size of the features increased after one week of exposure. Dissolution effects were more pronounced at 70°C. Upon four weeks of exposure at 70°C, the surface of the samples were completely altered (Figs. 6.18a30 and b30). The dissolution of cut surfaces displayed no difference in dissolution patterns of the natural surfaces. For all etched pyrite surfaces it became apparent that surface dissolution was more pronounced at 70°C and in contrast to microbial produced features mostly euhedral structures were observed.

Table 6.1: pH and temperature trend during iron(III)sulfate etching of pyrite. Experiment durations up to 34 days and two temperatures were applied (30°C - RT; 70°C - HT).

Time / days	pH_{RT}	T_{RT} / °C	pH_{HT}	T_{HT} / °C
3	1.76	29.0	1.72	68.0
6	1.75	30.6	1.65	68.0
7	1.75	30.6	1.67	65.0
8	1.76	30.0	1.72	69.5
9	1.75	29.5	1.70	66.0
10	1.77	29.0	1.69	69.0
13	1.76	30.2	1.66	71.5
15	1.75	29.5	1.67	73.5
17	1.77	29.5	1.67	72.2
20	1.76	29.2	1.67	70.0
22	1.77	29.6	1.65	72.0
24	1.75	29.5	1.65	75.3
29	1.76	29.9	1.65	71.0
31	1.77	29.1	1.63	71.3
34	1.75	30.1	1.66	71.0

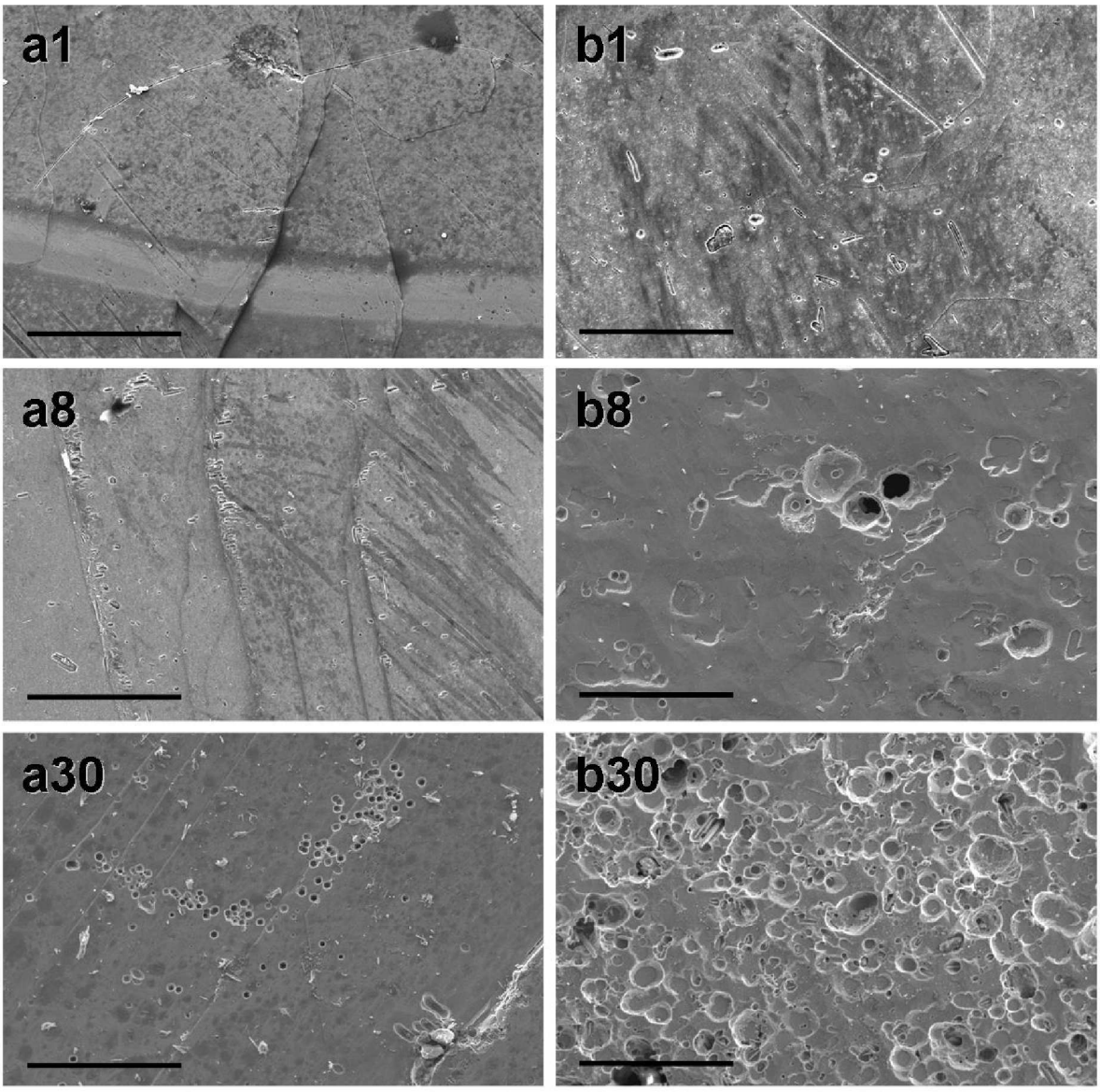

Figure 6.18: SEM images of natural {100} pyrite faces etched with iron(III)sulfate, after one day (1), one week (8) and four weeks (30). a) etched at 30°C; b) etched at 70°C. The scale bar represents 50 µm.

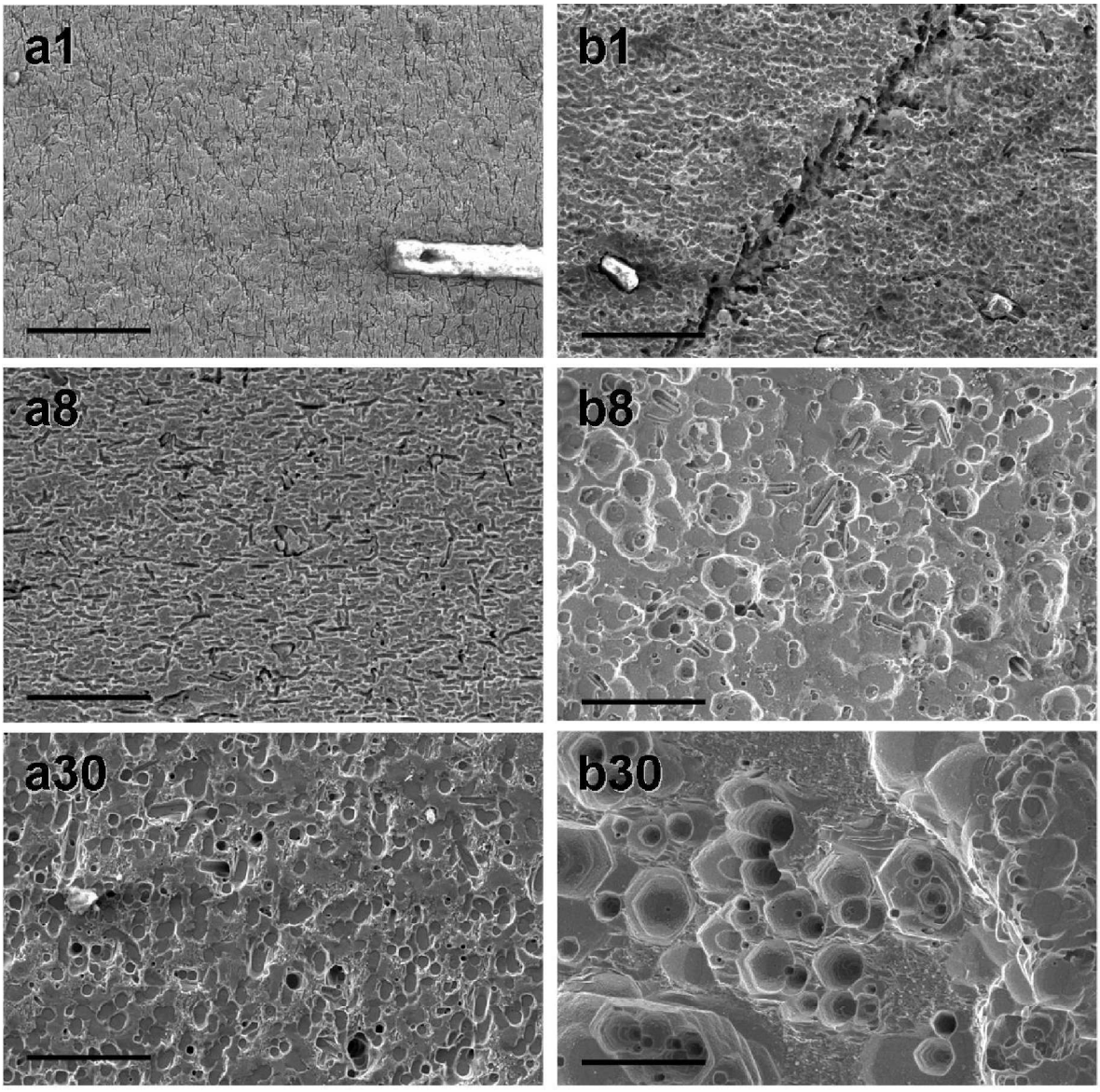

Figure 6.19: SEM images of cut {100} pyrite faces etched with iron(III)sulfate, after one day (1), one week (8) and four weeks (30). a) etched at 30 °C; b) etched at 70°C. The scale bar represents describes 20 µm

6.2 Synthesis and characterization of pyrite crystals

Understanding the crystal morphology of any material is important. The morphology of a crystal is the result of the relative growth rates of its different faces. A general rule is that slowest growing faces are expressed in the crystal habit. The growth rates for the various crystal faces are determined by a number of parameters such as solvent, degree of supersaturation, duration, temperature and impurity materials. Variations in any of these may lead to dramatic modifications in crystal morphology.

The crystals obtained in the experiments were subjected to a systematic morphological analysis. Sizes of up to 8.5 mm in diameter and up to five forms were found. The pyrite single crystals having smooth surfaces were grown after 12 days in a gradient of 743°C - 623°C via CVT (Chapter 2.3.1). Crystal growth occurs at the cooler end of the silica-tube. The average rate of iron and sulfur transport is up to 3 mg/h. The average transport rate was calculated by dividing the weight of the growing crystals by the growth time. Crystal faces were indexed with an optical two-circle reflection-goniometer (Chapter 5.4). It was observed that the crystals exhibit up to five crystal forms, {100}, {111}, {210}, {211} and {221} habits. The numbers of divers forms of some crystals are listed in Tab. 6.2. Here it is to note that not all surfaces for each crystal were indexed, however, the surface frequencies in Tab. 6.2 are representative for whole crystals. It became apparent that the synthesized crystals show different habits (Fig. 6.20), even though they were synthesized under the same conditions. Crystals with edge lengths less than 2 mm exhibit preferably five forms, while those with edge lengths of over 2 mm exhibit four forms (without {211}). Further, there are crystals which show mainly {100} and {111} habits (H81, S1MH4).

Examples of the synthetic crystals are shown in Fig. 6.20. Again, all crystals were synthesized under the same conditions via CVT (743 → 623 °C; $AlBr_3$; 12 days). The crystal in Fig. 6.20a (label: 2a-XX-I) shows {100}, {111}, {210} and {221} faces, the size is $5.2 \times 5.8 \times 6\,mm^3$; crystal b (not listed in Tab. 6.2) exhibits mainly {100} faces with a size of approximately $2 \times 2 \times 0.2\,mm^3$; crystal c (name: H81) shows {100}, {111} and {210} faces, with dimensions of $1 \times 1.5 \times 1\,mm^3$; crystal d (name: S-II-Ms) exhibits all five forms with extension of $1.5 \times 1.5 \times 1.5\,mm^3$. The largest crystal shows edge lengths of $8.5 \times 7 \times 4\,mm^3$ (example not shown). In all cases the relative sizes of the {211} and {221} faces are smaller than other accumulated faces of a sample.

Table 6.2: Observed frequencies of forms and sizes of selected synthetic crystals. It was not possible to index all surfaces, however, the shown surface frequencies resemble the whole crystal.

Crystal name	No. of measurable faces	Number of {100}	{111}	{210}	{211}	{221}	Size / mm^3
1a-XX-I	31	4	5	8	6	8	$1.2 \cdot 1.2 \cdot 1.2$
1a-XX-II	27	4	3	7	9	4	$1.7 \cdot 1.4 \cdot 1.5$
2a-XX-I	22	5	4	5	·	7	$5.2 \cdot 5.8 \cdot 6.0$
2a-XX-II	30	4	5	8	·	13	$4.5 \cdot 3.8 \cdot 4.4$
H3	15	1	3	2	8	1	$0.7 \cdot 0.8 \cdot 0.8$
H81	7	1	4	2	·	·	$1.0 \cdot 1.5 \cdot 1.0$
H142	9	1	2	2	1	3	$1.2 \cdot 0.8 \cdot 1.0$
H23	11	1	2	3	·	5	$0.6 \cdot 1.5 \cdot 1.2$
H304	11	2	2	2	·	5	$1.0 \cdot 0.8 \cdot 1.0$
Z3	9	2	3	2	2	·	$1.0 \cdot 0.8 \cdot 0.8$
Z81	15	1	2	3	5	4	$1.1 \cdot 0.8 \cdot 1.0$
Z141	8	1	1	1	5	·	$1.1 \cdot 1.2 \cdot 1.1$
Z23	10	·	4	2	2	2	$1.2 \cdot 1.2 \cdot 1.2$
Z304	8	2	1	1	4	·	$0.9 \cdot 0.6 \cdot 0.7$
S1MH1	8	·	3	4	·	1	$1.7 \cdot 1.3 \cdot 1.4$
S1MH2	10	2	4	1	·	3	$1.6 \cdot 1.4 \cdot 1.5$
S1MH4	9	2	2	·	·	5	$1.7 \cdot 1.1 \cdot 1.0$
S1MG1	11	2	4	3	·	2	$2.5 \cdot 1.8 \cdot 2.1$
S1MG2	9	1	3	·	1	4	$1.5 \cdot 1.4 \cdot 1.4$
S1MG4	15	1	1	5	1	7	$1.8 \cdot 1.5 \cdot 1{,}6$
S1SH1	23	1	3	2	6	11	$1.8 \cdot 1.2 \cdot 1.5$
S1SH2	8	·	2	3	2	1	$1.2 \cdot 1.4 \cdot 1.3$
S1SH4	16	2	·	6	4	4	$2.4 \cdot 2.2 \cdot 2.3$
S1SG1	7	2	2	3	·	·	$1.5 \cdot 1.3 \cdot 1.3$
S1SG2	7	3	3	·	·	1	$1.8 \cdot 1.6 \cdot 1.6$
S1SG4	16	2	3	3	4	4	$1.5 \cdot 1.9 \cdot 1.4$
S-II-Ms	11	1	2	3	4	1	$1.5 \cdot 1.5 \cdot 1.5$

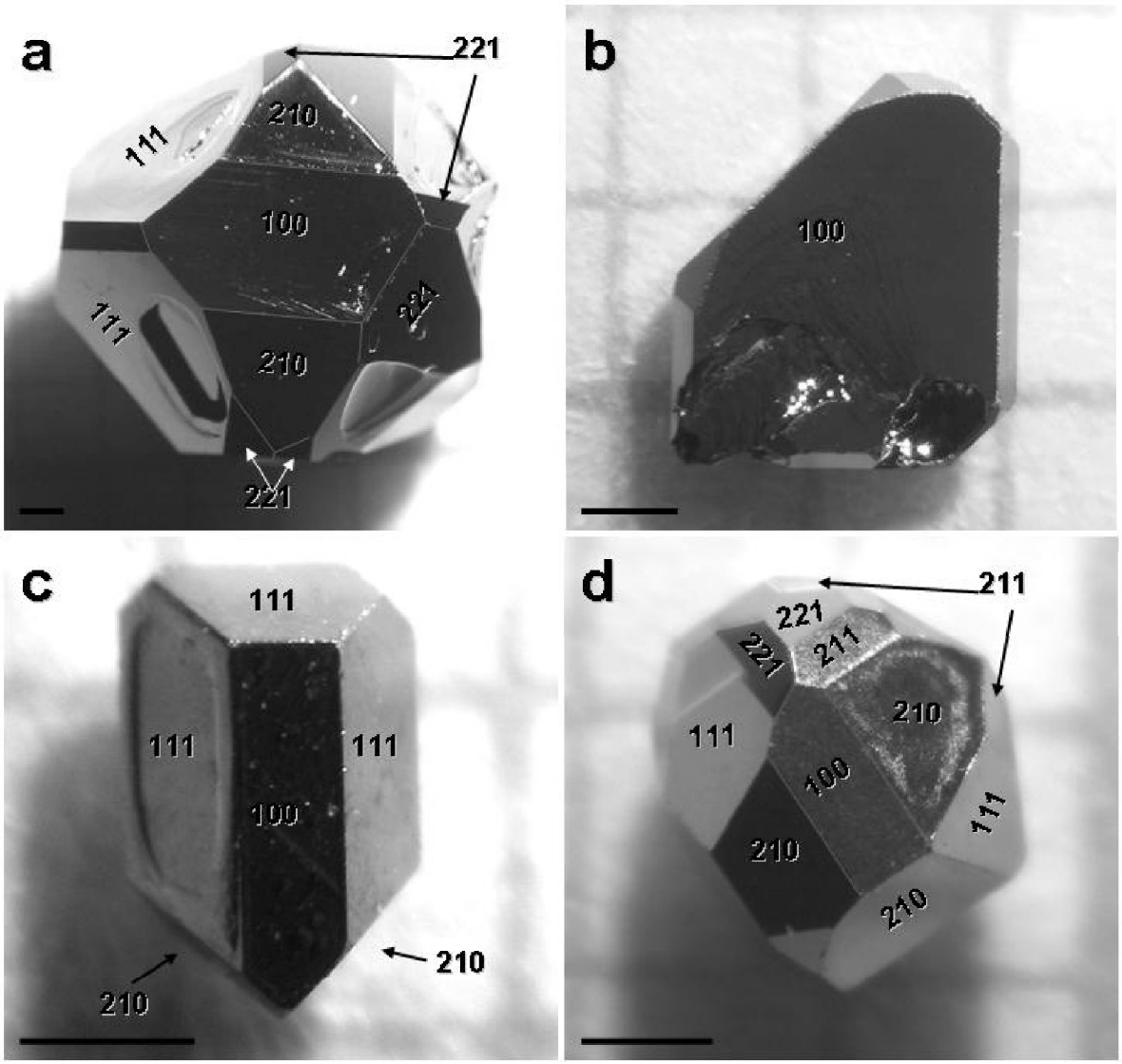

Figure 6.20: Different habits of synthetic pyrite single crystals synthesized by CVT with $AlBr_3$ as transporting agent in the temperature range 743 - 623°C for 12 days. Crystal a (2a-XX-I) shows four forms ({100}, {111}, {210}, {221}), the size of this crystal is $5.2 \times 5.8 \times 6\,mm^3$; the size of crystal b is $2 \times 2 \times 0.2\,mm^3$ and the shape is dominated by {100}; crystal c (H81) shows mainly {100}, {111} and {210} faces and is $1 \times 1.5 \times 1\,mm^3$ in size; crystal d (S-II-Ms) exhibits five forms ({100}, {111}, {210}, {211}, {221}), the size of this crystal is $1.5 \times 1.5 \times 1.5\,mm^3$. The scale bars corresponds to 500 µm.

The surfaces were analyzed using SEM, μ-Surf and XRD techniques. Traces of spiral growth were not found on any face, but occasionally steps of growth layers were observed on {100} faces. Fig. 6.21 shows a SEM image of steps on a (100) surface. It shows that the steps follow one crystallographic axis ([010]). Fig. 6.22 shows a quasi-three-dimensional μ-Surf image of steps on a (100) surface, including two profiles. The green profile shows step heights of 100 and 300 nm. The red profile is parallel to the step and shows within the error of +/- 2 nm a planar surface over 50 μm (the gradient of 8 nm results from the preparation prior to the measurement with the μ-Surf and is no growth structure). The observed steps are edges between {100} and {210} faces (Paulitsch, 1951) and resemble the typical pyrite striation. These straight steps appear only on {100}, but not on other faces.

X-ray powder diffraction patterns of the synthetic crystals show the single phase pyrite. Fig. 6.23 shows a typical diffraction pattern. The calculated curve (black line) describes all observed peaks (red circles). The difference curve is shown in the diagram (blue line). The calculated lattice parameter $a = 5.417(1)$ Å is in good agreement with literature values ($a = 5.418$ Å, Brostigen & Kjekshus, 1969; Fiechter et al., 1992).

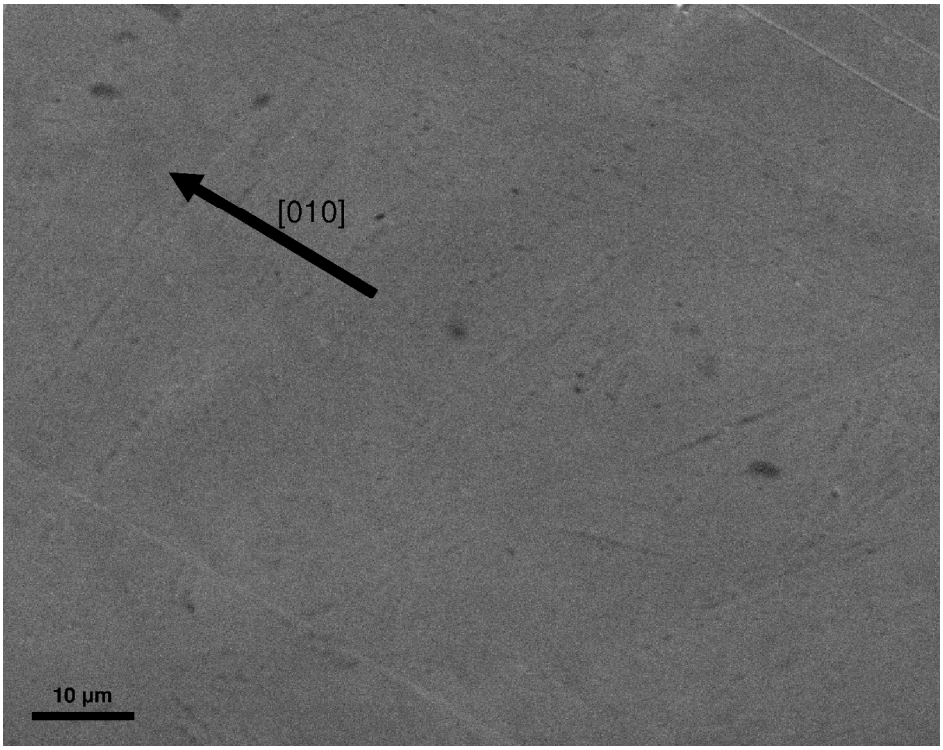

Figure 6.21: SEM image of a synthetic (100) surface of pyrite. The visible edges (left corner) follow the [100] direction and represent typical pyrite striation (growth boundaries between {100} and {210} faces; Paulitsch, 1951).

Electron microprobe measurements to detect possible sulfur deficiency showed no significant deviation. Given the accuracy of the electron microprobe, there is no evidence of non-stoichiometry of the pyrite and S / Fe ratio was observed to be 1.98(8).

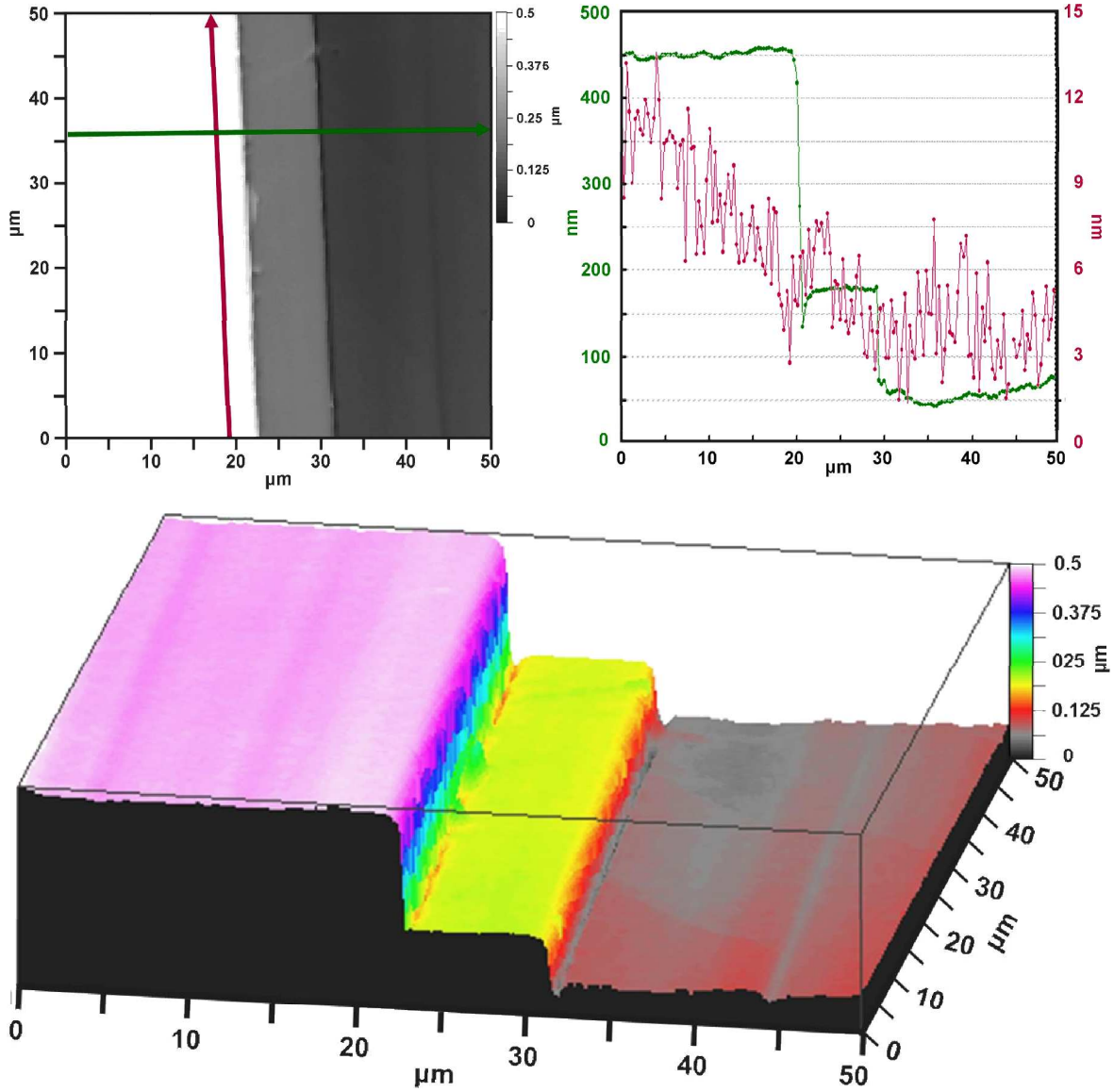

Figure 6.22: µ-Surf image and profiles of steps on a $50 \times 50\,\mu m^2$ area of a synthetic pyrite (100) face. Including a quasi-three-dimensional view of the surface and two profiles. The profiles were measured along the arrows. The green profile was measured perpendicular to the steps and shows step heights of 100 and 300 nm. The red profile runs parallel the steps, shows the planar (100) surface (the gradient of 8 nm is a result of the sample preparation prior to the measurement and no surface structure).

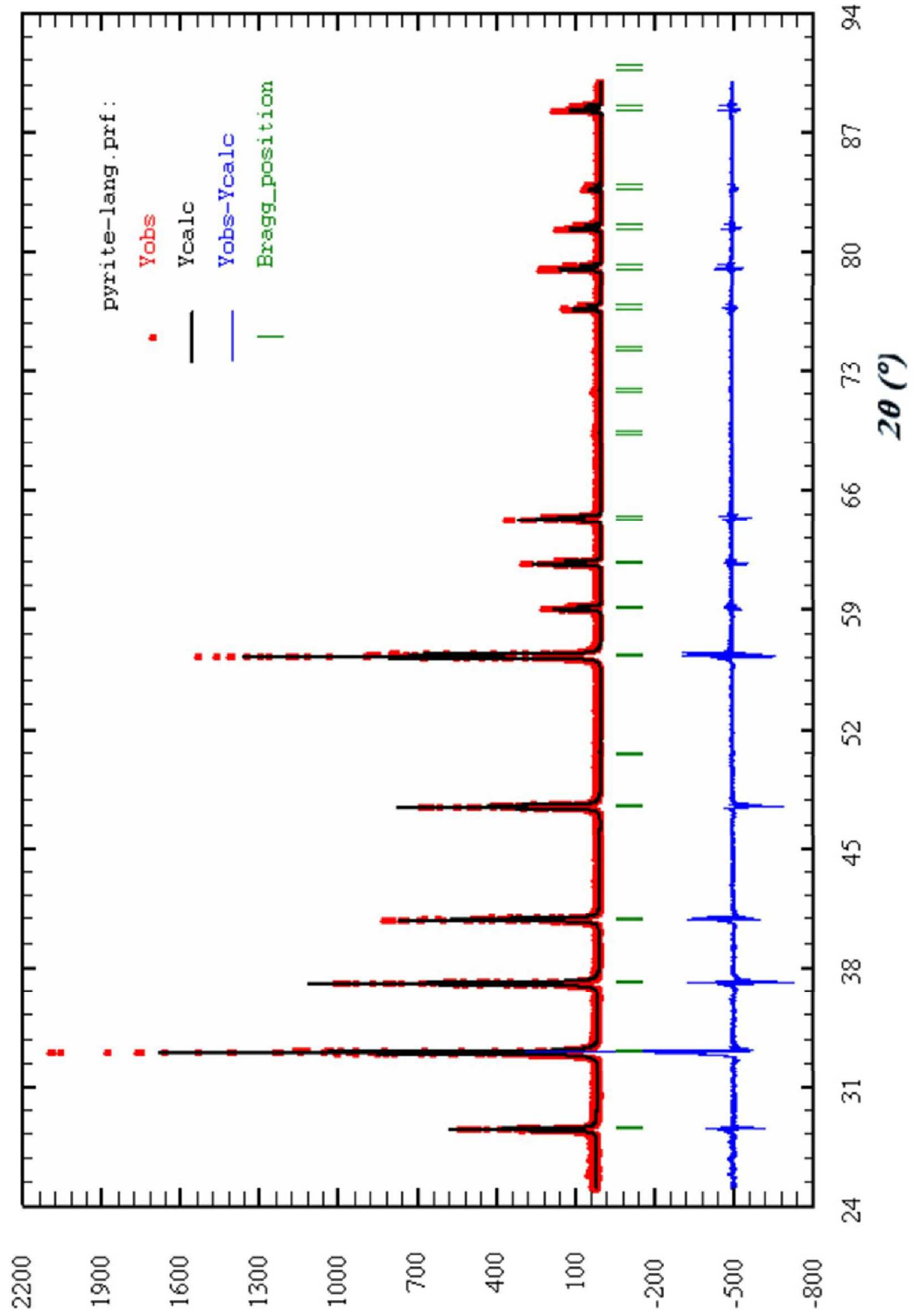

Figure 6.23: Powder X-ray diffractogram of synthetic pyrite. All peaks could be indexed and assigned to pyrite.

The results of IR measurements are shown in Fig. 6.24. The spectrum shows five IR modes at 293, 348, 402, 415 and 425 cm^{-1}. The observed modes are in agreement with those of Verble & Wallis (1969) and Lutz et al. (1985). There are five infrared-active modes in the pyrite structure (Chapter 2.2.3). All five modes were observed by Lutz & Willich (1985) and four (without the very weak mode at 425 cm^{-1}) by Verble & Wallis (1969).

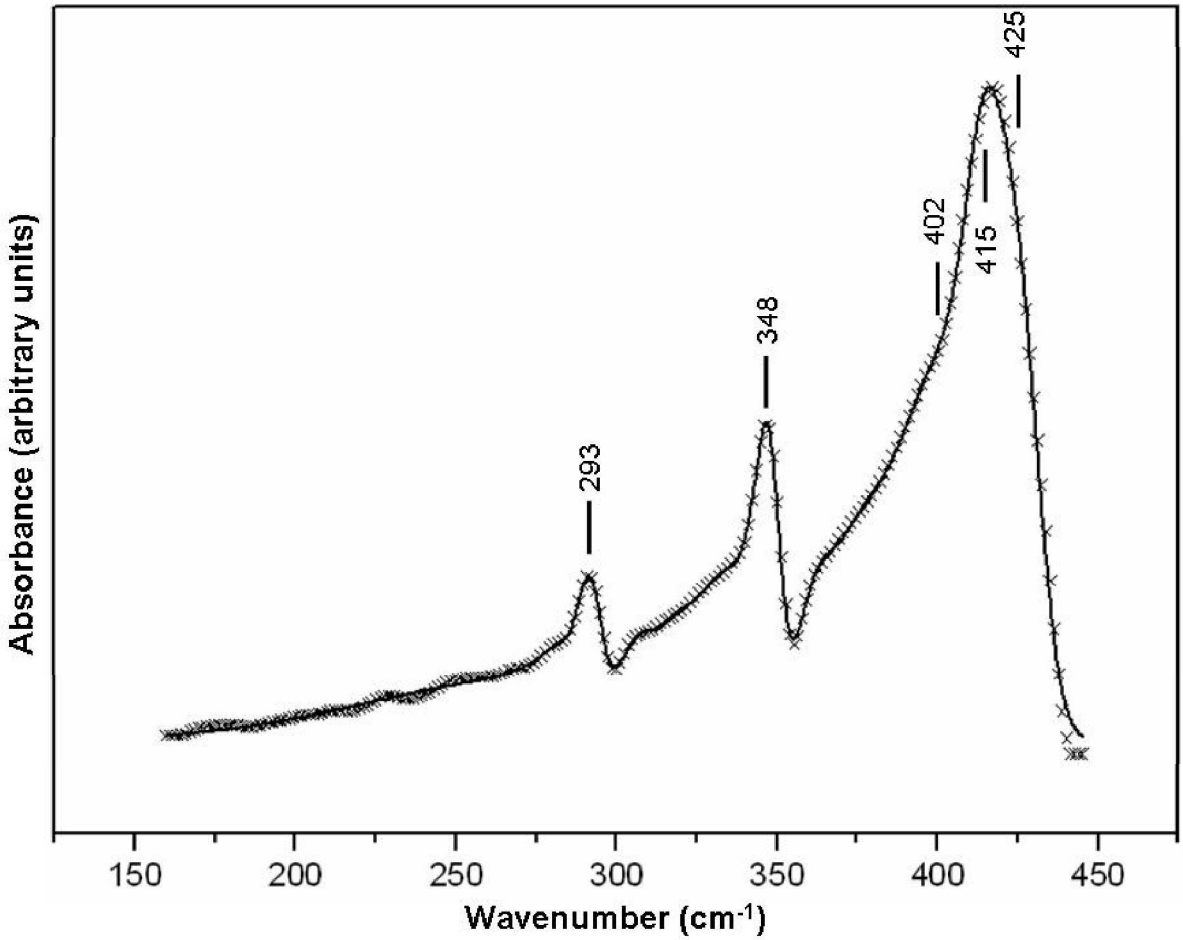

Figure 6.24: IR spectrum of pyrite. The crosses are experimental values, and the line is the best fit.

Fig. 6.25 shows a Raman spectrum of synthetic pyrite. The spectrum agrees well with published data of Mernagh & Trudu (1993) and Ushioda (1972). Three bands were observed at 354, 387 and 446 cm $^{-1}$ (Fig. 6.25). The spectrum shows one peak at 387 cm^{-1} agreeing with the reported frequency of the A_g mode. The $T_g(2)$ mode (theoretically: 377 cm^{-1}; Vogt et al., 1983) does not influence the fitted A_g peak position because its intensity is weak compared to the intensity of the A_g mode that dominates the spectrum. The peak at 354 cm^{-1} agrees with the reported frequency of the E_g mode. The $T_g(1)$ mode (theoretically: 350 cm^{-1}; Vogt et al., 1983) is weak compared to the intensity of the E_g mode and does not influence the fitted E_g peak position. The third observed peak is located at 446 cm^{-1} and agrees with the former reported frequency of the $T_g(3)$ mode. Thus, the A_g and $T_g(2)$ and the E_g and $T_g(1)$ modes are nearly coincident with each other (Vogt et al., 1983) and cannot be resolved in the present Raman spectra.

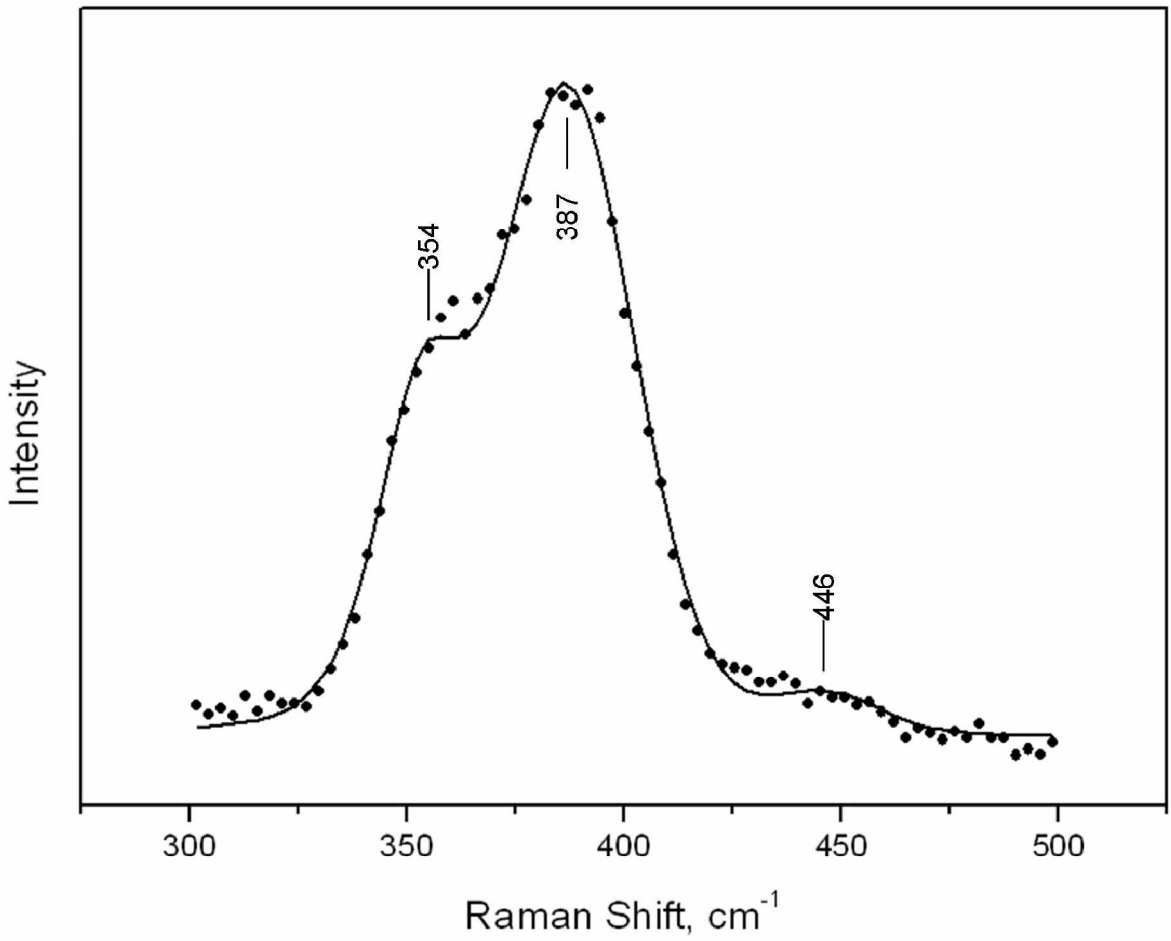

Figure 6.25: Raman spectrum of pyrite. Data are unsmoothed and no background was subtracted. The points are experimental values and the line is the best fit.

The structural quality of the crystal faces were checked by high resolution XRD. Rocking-curve maps were measured and a typical map for a synthetic (100) surface is shown in Fig. 6.26. The left part shows a SEM image of the crystal. The black arrow represents the direction of the mapping and the grey ellipse represents the size of the used X-ray beam. Thus, the map is an average of the area which is hit by the X-ray beam. However, the map was recorded using a (100) diffracting plane and a (200) reflex of a pyrite single crystal. The full width at half maximum (FWHM) were between 40 and 80 arcsec for the measured crystals indicating a high crystalline quality. The peak maxima position does not change over the mapping, indicating homogeneity over the whole surface.

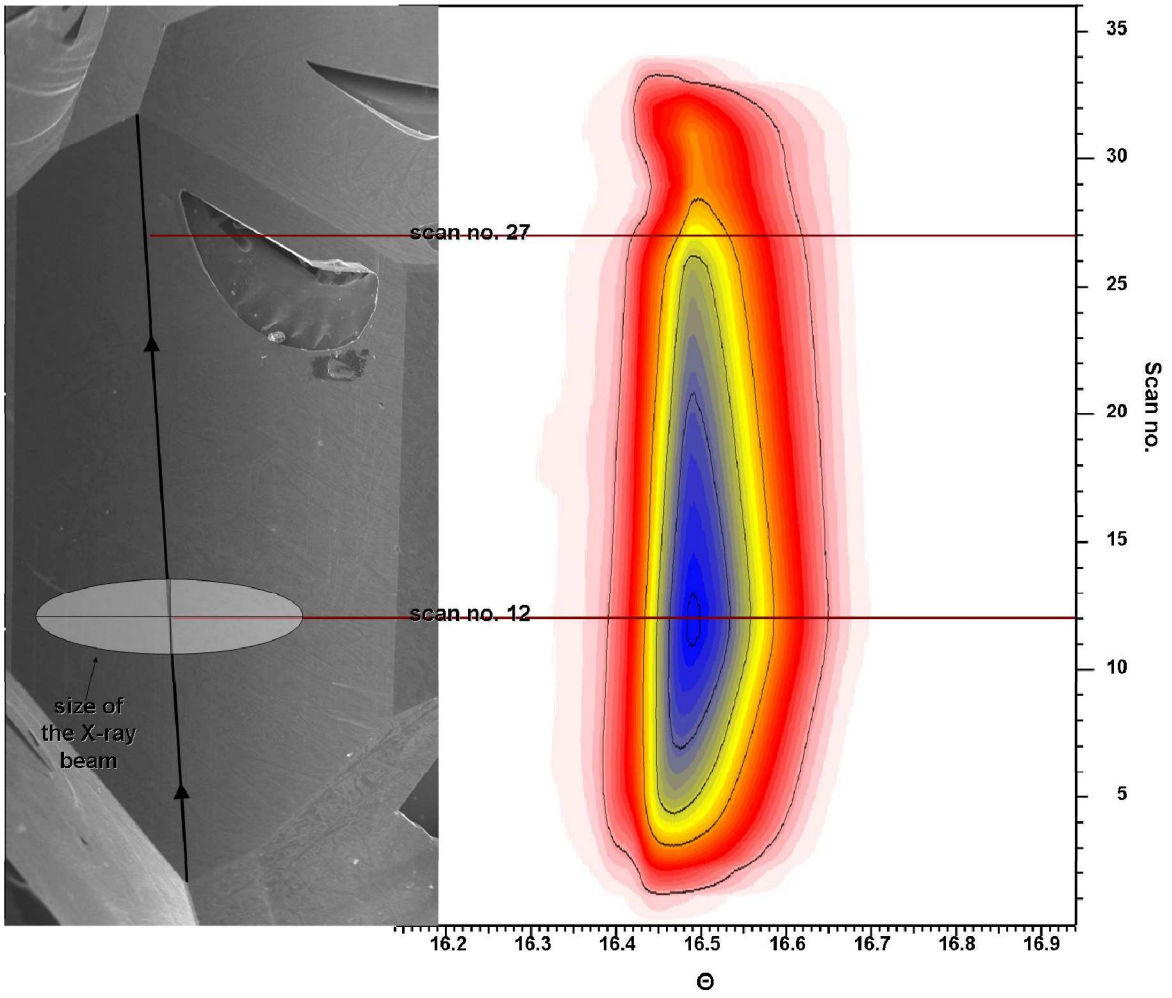

Figure 6.26: SEM image and map of rocking-curves of the 200 peak of a synthetic (100) pyrite surface measured along the black arrow. The ellipse reflects the X-ray beam size and therefore the average area of the integrated intensity per scan. The full width at half maximum were between 40 and 80 arcsec.

6.3 Dissolution of synthetic pyrite crystals

In this section the results of biological and abiotic oxidation of synthetic pyrite surfaces are presented. Biological oxidants were two archaeal strains, namely *Metallosphaera sedula* and *Sulfolobus metallicus*. As abiotic oxidant iron(III)sulfate at 30 and 70°C was used. During all biological experiments metabolic activity and layered or granular precipitations were observed, as in previous experiments (Chapter 6.1). Cell densities of 1-2·10^8 and 5-8·10^7 cells per ml were measured for *Metallosphaera sedula* and *Sulfolobus metallicus*, respectively. Epifluorescence microscopically investigations show, that *Metallosphaera sedula* cells attached with approximately 60 % probability on pyrite surfaces, while the rest remained planktonic in solution. For *Sulfolobus metallicus*, the corresponding ratio was about 50 : 50. Examples of attached cells of *Metallosphaera sedula* (a) and *Sulfolobus metallicus* (b) on {111} pyrite surfaces are shown in Fig. 6.27. The cells were fixed in glutaraldehyde, but some appear deflated and collapsed. This may be a result of a dehydration process and low pressure in the vacuum chamber of the SEM. The cell attachment in our experiments does not exhibit any preferred direction, at contradiction with previous reports where cells were aligned along crystallographic directions (Edwards et al., 1999).

SEM investigations of biological and abiotic etched pyrite surfaces were performed

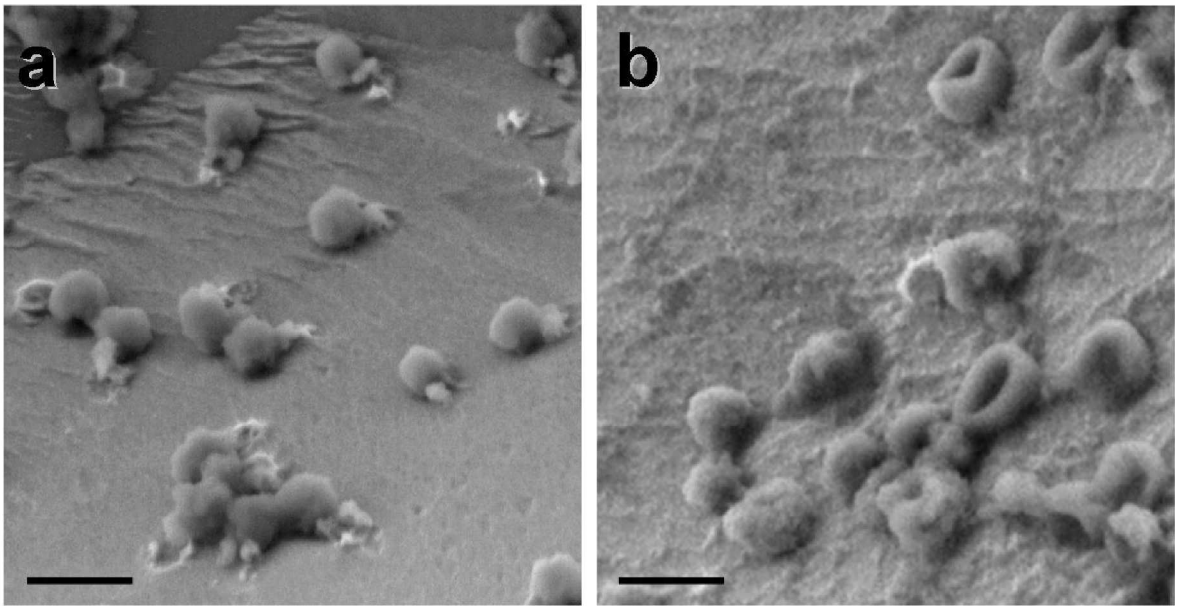

Figure 6.27: Microorganisms attached on {111} pyrite surfaces; a) cells of *Metallosphaera sedula*; b) cells of *Sulfolobus metallicus*. The scale bars represent 1 µm.

after one, two and four weeks of incubation. For biological experiments with *Metallosphaera sedula* the single crystals that were used are S1MG1 / S1MH1, S1MG2 / S1MH2 and S1MG4 / S1MH4. The crystals used for incubation with *Sulfolobus metallicus* are S1SG1 / S1SH1, S1SG2 / S1SH2 and S1SG4 / S1SH4. In the abiotic etching experiments, pyrite single crystals Z81, Z142 and Z304 were used for exposure at 30°C. Crystals H81, H142 and H304 were used for abiotic etching at 70°C. The last characters of the sample labels indicate the incubation time for one (1), two (2) and four (4) weeks of incubation. All samples are listed in Tab. 6.2 with face multiplicities and dimensions.

In the following sections, the dissolution features at the surfaces are discussed, separated to faces. Control experiments without any oxidant did not show any surface dissolution after the same time of incubation (data not shown). Consequently, the dissolution features observed are attributed to microbial and iron(III)sulfate (Fe^{3+}) activities.

6.3.1 Etch features on {100} pyrite surfaces

Figs. 6.28 and 6.29 show the typical appearance of {100} pyrite faces after biological and abiotic etching, respectively. Figs. 6.28a, c, e and 6.28b, d, f show pyrite faces etched by *Metallosphaera sedula* and *Sulfolobus metallicus*, respectively. Figs. 6.29a, c, e and 6.29b, f show pyrite faces etched by iron(III)sulfate at 30°C and 70°C, respectively. Incubation times for both experiments are one (a, b), two (c, d) and four (e, f) weeks. The arrows on the SEM images indicate the [010] and [001] directions of the surfaces. Layered precipitations become visible in Fig. 6.29a after iron(III)sulfate etching. No sample with {100} faces after two weeks of exposure to iron(III)sulfate at 70°C was present.

The symmetries of the euhedral etching features in Figs. 6.28 and 6.29 depend on the face-symmetry of the pyrite face. The face-symmetry of {100} faces is $mm2$. Thus, the symmetry elements consist of two mirror planes and one twofold axis. All symmetries are visible in each etch pit. The edges of the structures follow the ⟨010⟩ and ⟨011⟩ directions. Here it appears that smaller etch pits (inset in Fig. 6.28b) show mainly ⟨011⟩ edges, while larger pits also show edges in the ⟨010⟩ directions. The indices of the etched faces inside the etch pits has not been determined, but µ-Surf investigations showed that the bottom face inside the structures are parallel the etched (100) face (Fig. 6.30), indicating the bottom face as (100). Therefore, etch pits on a (100) face, produced after one week of incubation by *Metallosphaera sedula*, was analyzed using the µ-Surf technique. Fig. 6.30 shows a quasi-three-dimensional µ-Surf image of an etch pit on a (100) surface ($50 \times 50\,\mu m^2$), including two profiles. The

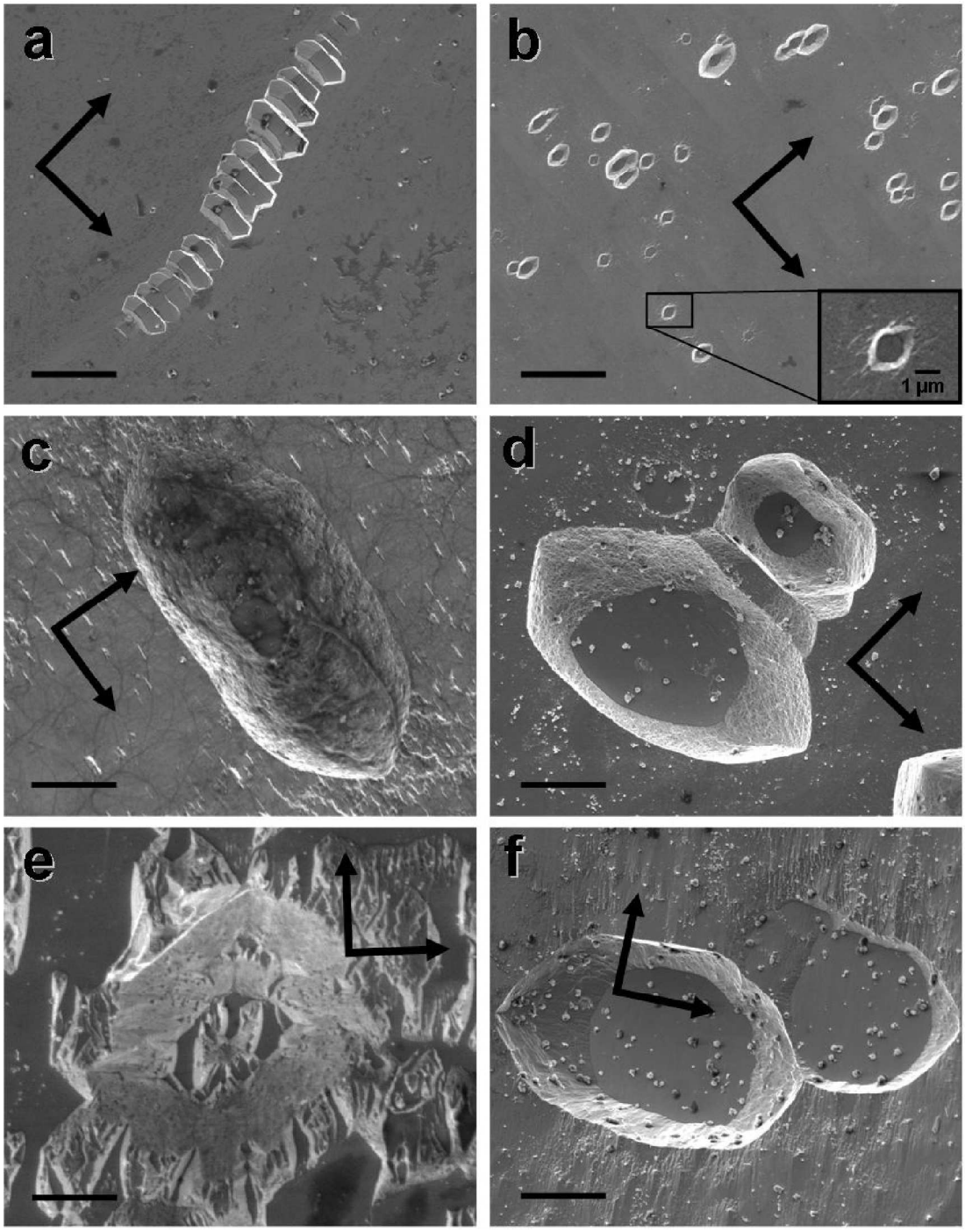

Figure 6.28: SEM images of pyrite {100} faces etched by the archaeal strains *Metallosphaera sedula* (a, c, e) and *Sulfolobus metallicus* (b, d, f), for three time intervals, one week (a, b), two weeks (c, d) and four weeks (e, f). Arrows indicate the [010] and [001] directions on surfaces. The round structures in a), d) and f) are cells; the scale bars represent 10 µm.

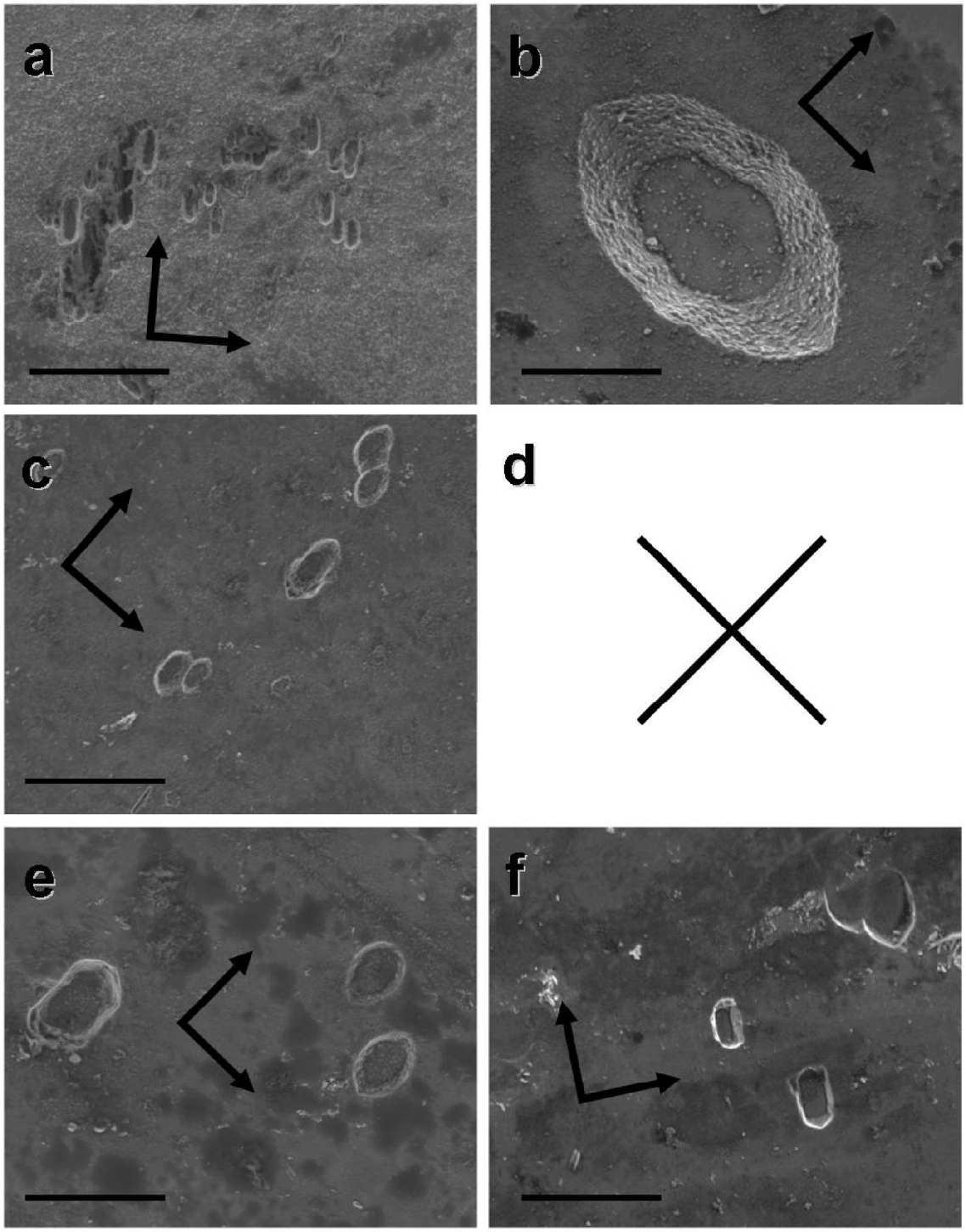

Figure 6.29: SEM images of pyrite {100} faces etched by iron(III)sulfate at 30°C (a, c, e) and 70°C (b, f), for three time intervals, one week (a, b), two weeks (c, d) and four weeks (e, f). Arrows indicate the directions [010] and [001] on surfaces. The scale bars represent 10 µm.

profiles follow the [010] and [001] directions and show a feature depth of approximately 800 nm. Because the edges of the pits follow the ⟨011⟩ and ⟨010⟩ directions, the etch pit faces at the side are {hkk} and {h0l} faces.

However, by comparing the dissolution effects of abiotic and biological oxidation, no significant differences were observed between the shape of the structures, but instead in the feature sizes. The size of the observed features, produced by iron(III)sulfate at 70°C after one week of exposure (Fig. 6.29b), are significantly larger (approximately

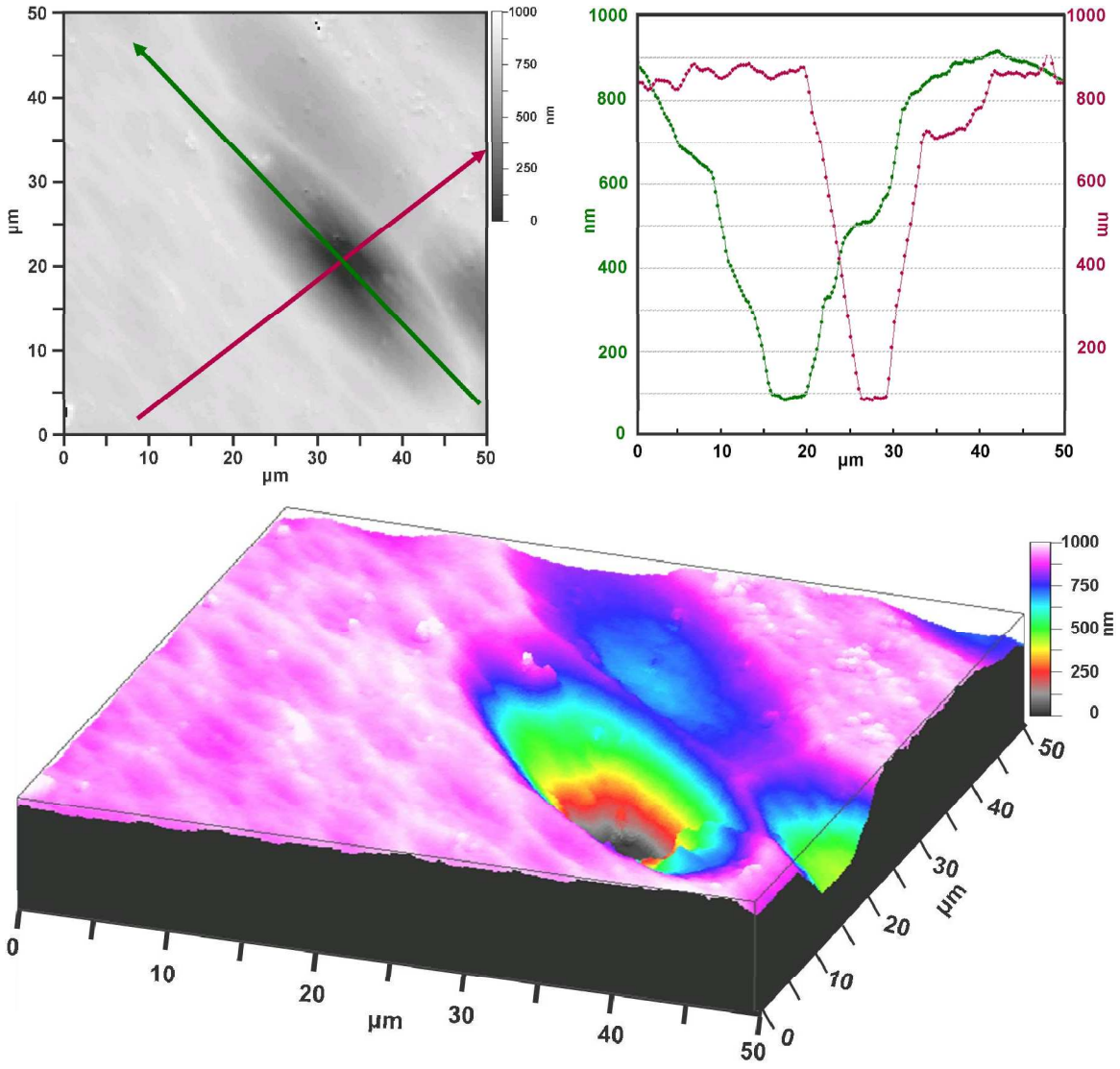

Figure 6.30: µ-Surf image and profiles of characteristic etch structures on a (100) face, here induced by *Metallosphaera sedula* after one week of incubation. The investigated area is $50 \times 50\,\mu m^2$. Including a quasi-three-dimensional view of the surface. The profiles were measured along the arrows, both parallel ⟨010⟩ directions.

$15 \times 25\ \mu m^2$) than all other observed features after the same time period. The size of these features are in the range of the observed features after two weeks of exposure to microbes. After iron(III)sulfate etching at 30°C, such sizes of etch pits were never observed, and feature sizes produced after four weeks of incubation with iron(III)sulfate at 70°C (Fig. 6.29f; approximately $5 \times 3\ \mu m^2$) are, surprisingly, also smaller.

For the biological and iron(III)sulfate at 30°C experiments, an increase in size of the etch pits as a function of incubation times is visible. Thus, except for the experiments with iron(III)sulfate at 70°C, larger etch pits for longer incubations are observed. In addition, the etching features produced by *Metallosphaera sedula* are more pronounced than those produced by *Sulfolobus metallicus*.

6.3.2 Etch features on {111} pyrite surfaces

Figs. 6.31 and 6.32 show the appearance of {111} pyrite faces after biological and abiotic etching, respectively. Figs. 6.31a, c, e and 6.31b, d, f show pyrite faces etched by *Metallosphaera sedula* and *Sulfolobus metallicus*, respectively. Figs. 6.32a, c, e and 6.32b, d, f show pyrite faces etched by iron(III)sulfate at 30°C and 70°C, respectively. Incubation times for both experiments are one (a, b), two (c, d) and four (e, f) weeks. The arrows on the SEM images indicate the [110] direction on the surfaces. Granular precipitations become visible in Fig. 6.31d after exposure to *Sulfolobus metallicus*.

The symmetries of the euhedral etching features present in Figs. 6.31 and 6.32 depend on the face-symmetry of the pyrite surface. The face-symmetry of {111} surfaces is a three-fold axis (3) perpendicular to the surface. These three-fold axes are visible in the centers of each etch pit. The indices of the etched faces inside the etch pits has not been determined, but the edges of all pits follow ⟨110⟩ directions. Thus, the etch pit faces need to have an index of {hhl}, therefore they should be {211} or {221} faces. Both faces feature characteristic angles with {111} faces (theoretically 19.47 and 15.79°, respectively). Fig. 6.33 shows a quasi-three-dimensional μ-Surf image of an etch pit on a (111) face ($50 \times 50\,\mu m^2$) with two profiles. The profiles follow directions perpendicular to ⟨110⟩ and show a feature depth of approximately 1.5 μm. The measured angles between the basis face and the etched faces are approximately 18(2)°C. Thus, with the resolution of the instrument, it is not clear which indices could be given to the etched faces.

As for the {100} faces, no significant differences between the shape of the dissolution structures produced by biological and abiotic etching were observed for {111} surfaces. But again, the sizes of the observed features, produced by iron(III)sulfate at 70°C after one week of exposure (Fig. 6.32b) are significantly larger (approximately $15 \times 15\,\mu m^2$) than all other observed features after the same time period, and moreover the sizes are in the range of the observed features after two weeks of exposure to microbes. Again, after iron(III)sulfate etching at 30°C and, surprisingly, also after two and four weeks of incubation with iron(III)sulfate at 70°C (Fig. 6.32f; approximately $8 \times 8\,\mu m^2$) such sizes of etch pits were never observed. Further, after four weeks of incubation by microbes no single etch pits appeared, but intertwining features, as were observed for microbial etching of natural pyrite surfaces (Chapter 6.1; Fig. 6.5).

For both microbial and iron(III)sulfate experiments, an increase in the amount of etch pits after increase of the incubation times is visible. Etching features produced by *Metallosphaera sedula* and iron(III)sulfate at 70°C are more pronounced than those produced by *Sulfolobus metallicus* and iron(III)sulfate at 30°C.

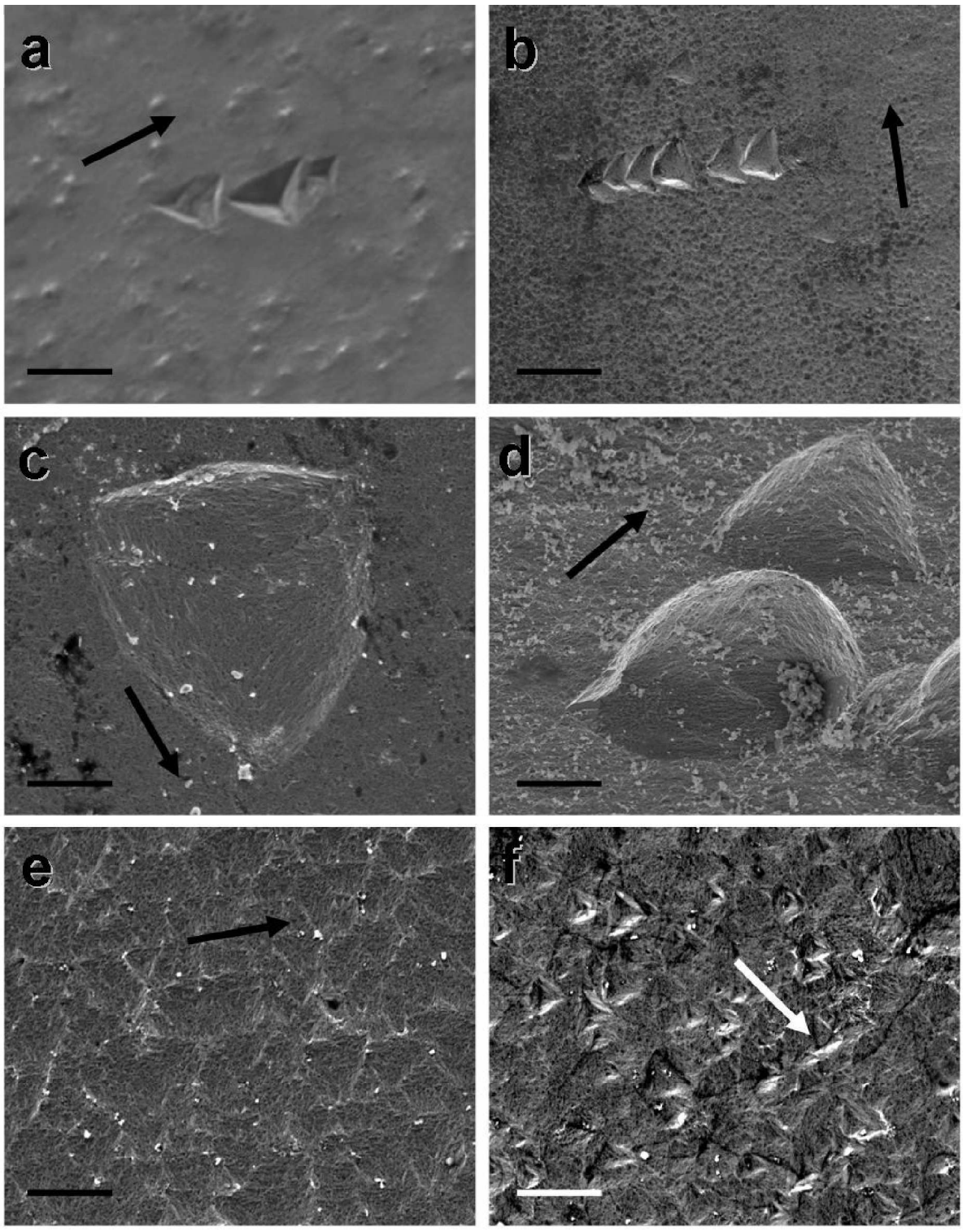

Figure 6.31: SEM images of pyrite {111} faces etched by the archaeal strains *Metallosphaera sedula* (a, c, e) and *Sulfolobus metallicus* (b, d, f), for three time intervals, one week (a, b), two weeks (c, d) and four weeks (e, f). Arrows indicate the direction [110] on surfaces. The scale bars represent 5 µm.

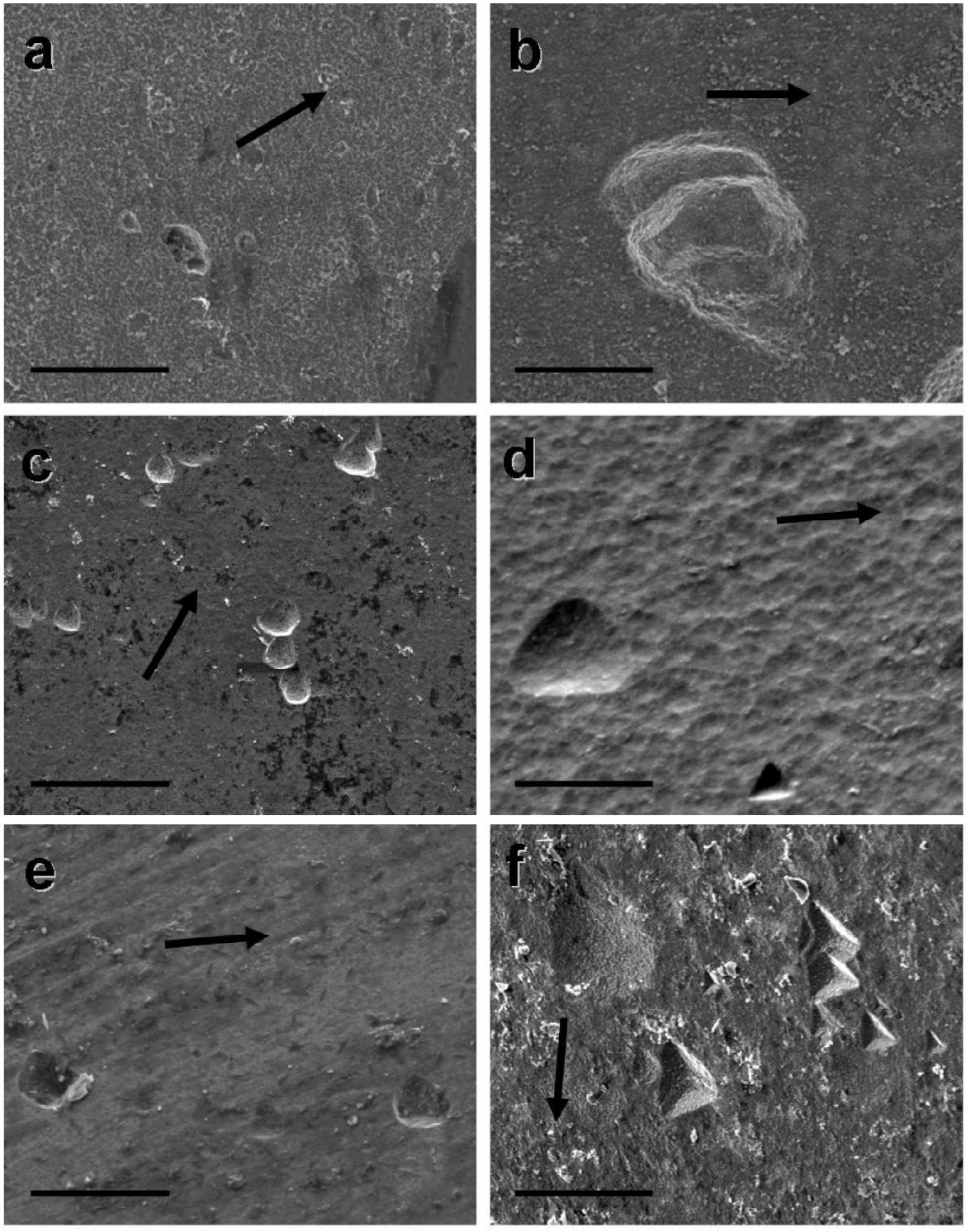

Figure 6.32: SEM images of pyrite {111} faces etched by iron(III)sulfate at 30°C (a, c, e) and 70°C (b, f), for three time intervals, one week (a, b), two weeks (c) and four weeks (e, f). Arrows indicate the direction [110] on surfaces. The scale bars represent 10 µm.

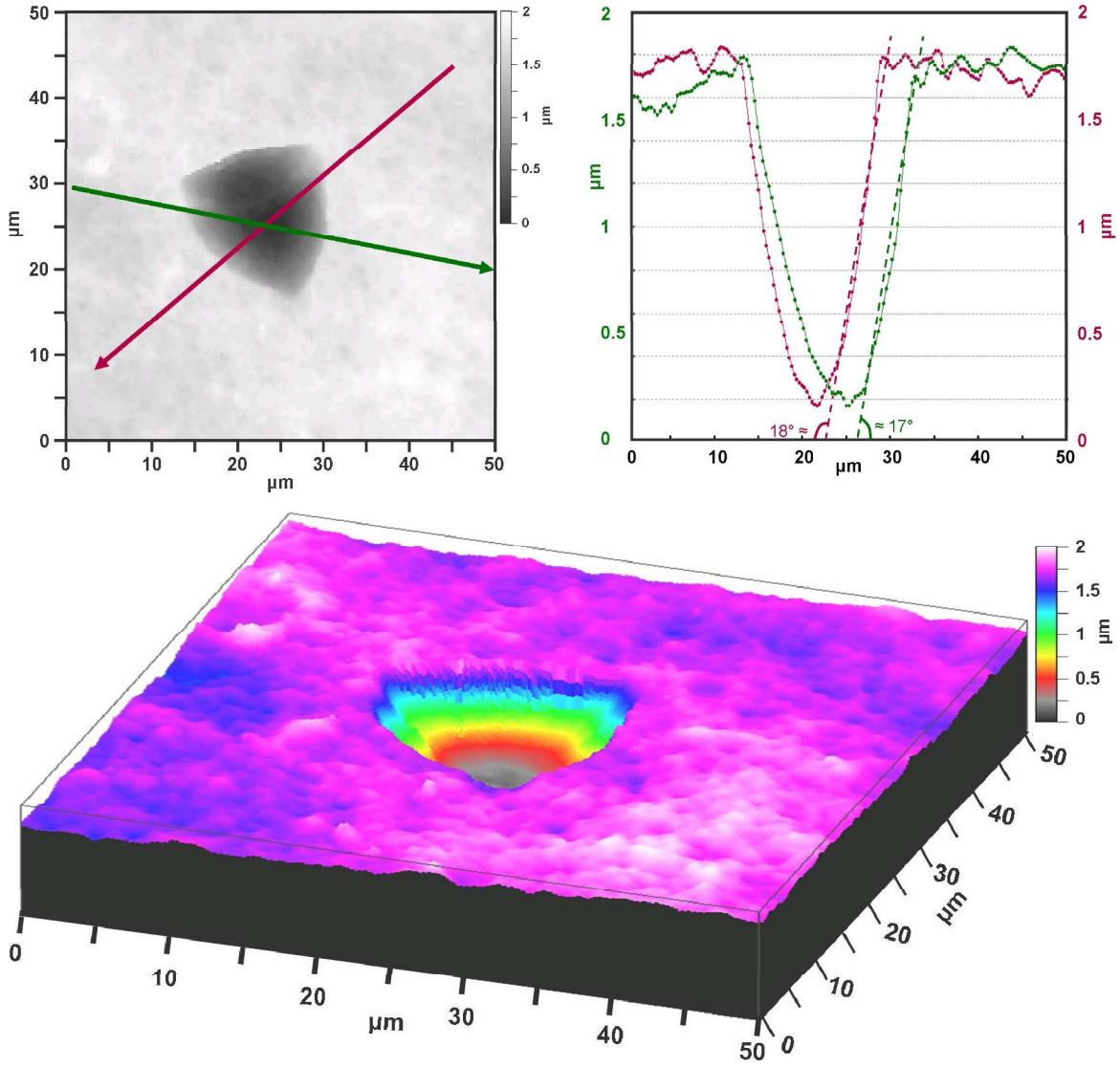

Figure 6.33: µ-Surf image and profiles of a characteristic etch structure on a (111) face, here induced by *Metallosphaera sedula* after two weeks of incubation. The investigated area is $50 \times 50\,\mu m^2$. Including a quasi-three-dimensional view of the surface. The profiles were measured along the arrows. Both profiles were measured perpendicular $\langle 110 \rangle$ directions.

6.3.3 Etch features on {210} pyrite surfaces

Figs. 6.34 and 6.35 show the appearance of {210} pyrite faces after biological and abiotic etching, respectively. Figs. 6.34a, c, e and 6.34b, d, f show pyrite faces etched by *Metallosphaera sedula* and *Sulfolobus metallicus*, respectively. Figs. 6.35a, c, e and 6.35d, f show pyrite faces etched by iron(III)sulfate at 30°C and 70°C, respectively. Incubation times for both experiments are one (a, b), two (c, d) and four (e, f) weeks. The arrows on the SEM images indicate the $[\bar{1}20]$ (black) and $[\bar{1}21]$ (red) directions on the surfaces. No sample with {210} faces was present after one week of exposure to iron(III)sulfate at 70°C.

The symmetry of {210} faces is a mirror plane m. The position of the mirror plane, m, follows the black arrows shown on the SEM images of Figs. 6.34 and 6.35, thus, follows the $[\bar{1}20]$ direction. The shape of the etch pits in Figs. 6.34 and 6.35 show this mirror plane, m. The indices of the faces inside the etch pits were not determined. However, the edges of the structures follow [001] and $\langle\bar{1}21\rangle$ directions. The [001] direction is perpendicular to the $[\bar{1}20]$ direction and {hk0} and {210} faces show the [001] direction as cutting edge. Thus, etched faces optionally are {110} faces. Fig. 6.36 shows a quasi-three-dimensional µ-Surf image of an etch pit on a (210) surface ($50\,\mathrm{x}\,50\,\mu m^2$) with a profile. The profile follows the direction $[\bar{1}20]$ and shows a feature depth of approximately 3 µm and an angle of approximately 18° between the basis face (210) and the etched face. The theoretical angle between (210) and (110) faces is 18.4°, thus indicating an index (110) of the etched face.

The second direction of etch pit edges follows direction $\langle\bar{1}21\rangle$ (red arrow). Therefore, the two faces of the etch pits are $\{h\frac{h+1}{2}\bar{1}\}$ faces. This includes $\{11\bar{1}\}$ and $\{32\bar{1}\}$ faces. The angles for those faces with a (210) face are theoretically 14.9 and 17.2°, respectively. Again, with the resolution of the instrument (µ-Surf), it is not clear which form is correct.

As for the two previous described forms, no significant differences between the shape of the etch structures produced by microorganisms and iron(III)sulfate were observed. For all experiments an increase in size of the etch pits as a function of incubation time is observed. Again, the etching features produced by *Metallosphaera sedula* and iron(III)sulfate at 70°C are more pronounced than those produced by *Sulfolobus metallicus* and iron(III)sulfate at 30°C.

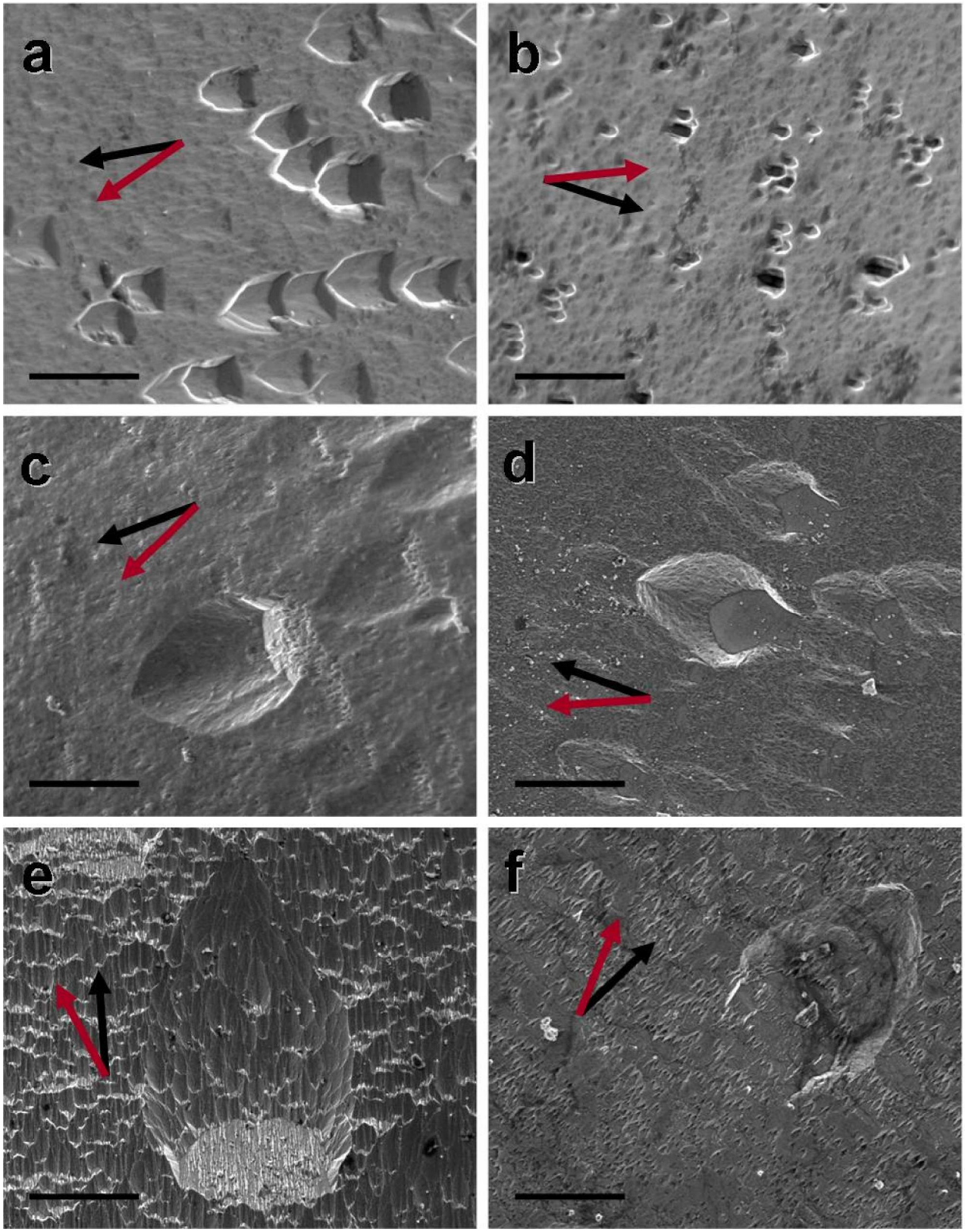

Figure 6.34: SEM images of pyrite {210} faces etched by the archaeal strains *Metallosphaera sedula* (a, c, e) and *Sulfolobus metallicus* (b, d, f), for three time intervals, one week (a, b), two weeks (c, d) and four weeks (e, f). Arrows indicate the direction $[\bar{1}20]$ (black) and $[\bar{1}21]$ (red) on surfaces. The scale bars represent 10 µm.

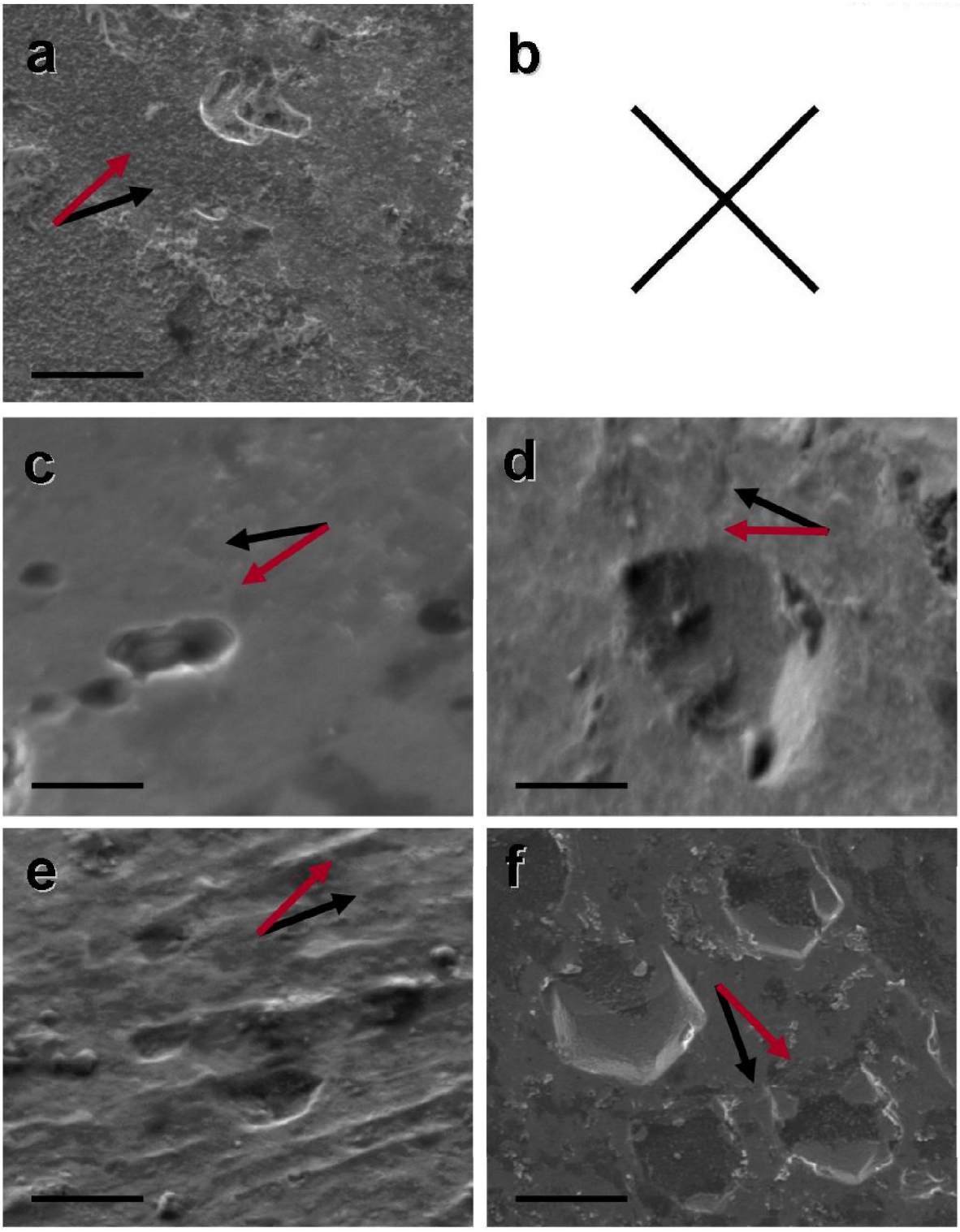

Figure 6.35: SEM images of pyrite {210} faces etched by iron(III)sulfate at 30°C (a, c, e) and 70°C (d, f), for three time intervals, one week (a), two weeks (c, d) and four weeks (e, f). Arrows indicate the directions [$\bar{1}$20] (black) and [$\bar{1}$21] (red) on surfaces. The scale bars represent 5 µm.

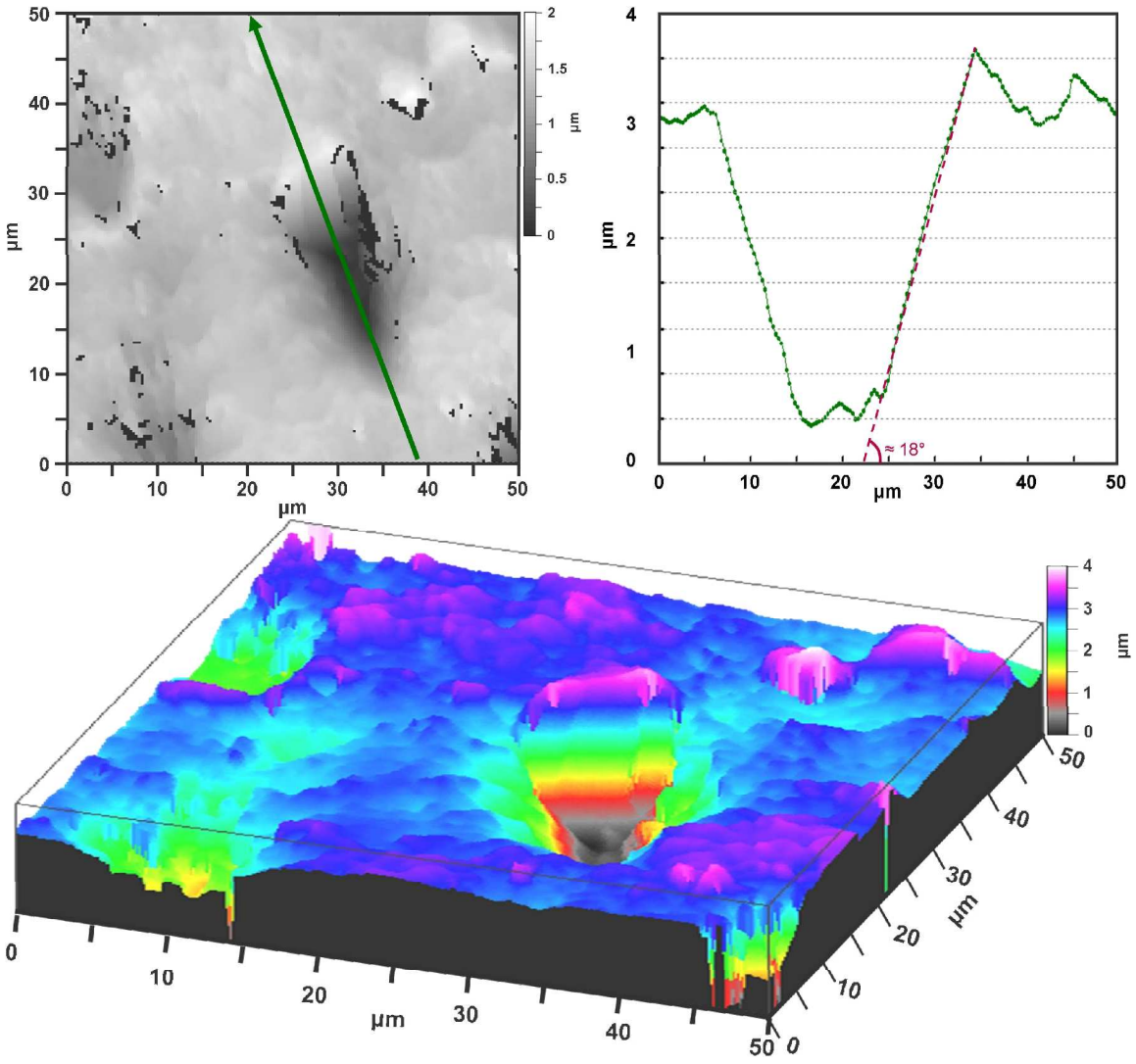

Figure 6.36: µ-Surf image and a profiles of a characteristic etch structure on a (210) face, here induced by *Metallosphaera sedula* after four weeks of incubation. The investigated area is 50 x 50 µm^2. Including a quasi-three-dimensional view of the surface. The profile was measured along the arrow, parallel [$\bar{1}$20] direction. The red lines indicate the measured angle between the basis face (210) and the etched face, approximately 18°.

6.3.4 Etch features on {211} pyrite surfaces

Figs. 6.37 and 6.38 show the exposed {211} pyrite faces after biological and abiotic etching, respectively. Figs. 6.37c and 6.37b, d, f show pyrite faces etched by *Metallosphaera sedula* and *Sulfolobus metallicus*, respectively. Figs. 6.38a, e and 6.38d show {211} pyrite faces etched by iron(III)sulfate at 30°C and 70°C, respectively. Incubation times for both experiments are one (a, b), two (c, d) and four (e, f) weeks. The arrows on the SEM images indicate the $[0\bar{1}1]$ direction on the surfaces. Because the {211} face is the rarest for synthetic pyrite (Chapter 6.2; Tab. 6.2), no sample with {211} faces was observed after one and four weeks of exposure to *Metallosphaera sedula* and iron(III)sulfate at 70°C, and after two weeks of exposure to iron(III)sulfate at 30°C. Therefore, except for *Sulfolobus metallicus* no conclusion for the evolution of the etch pits as a function of time is possible. However, for *Sulfolobus metallicus* an increase in size of the etch pits as a function of incubation time is observed. Moreover, the face-symmetry of (211) is the identity 1, and thus no characteristic etch pit or edges directions were observed.

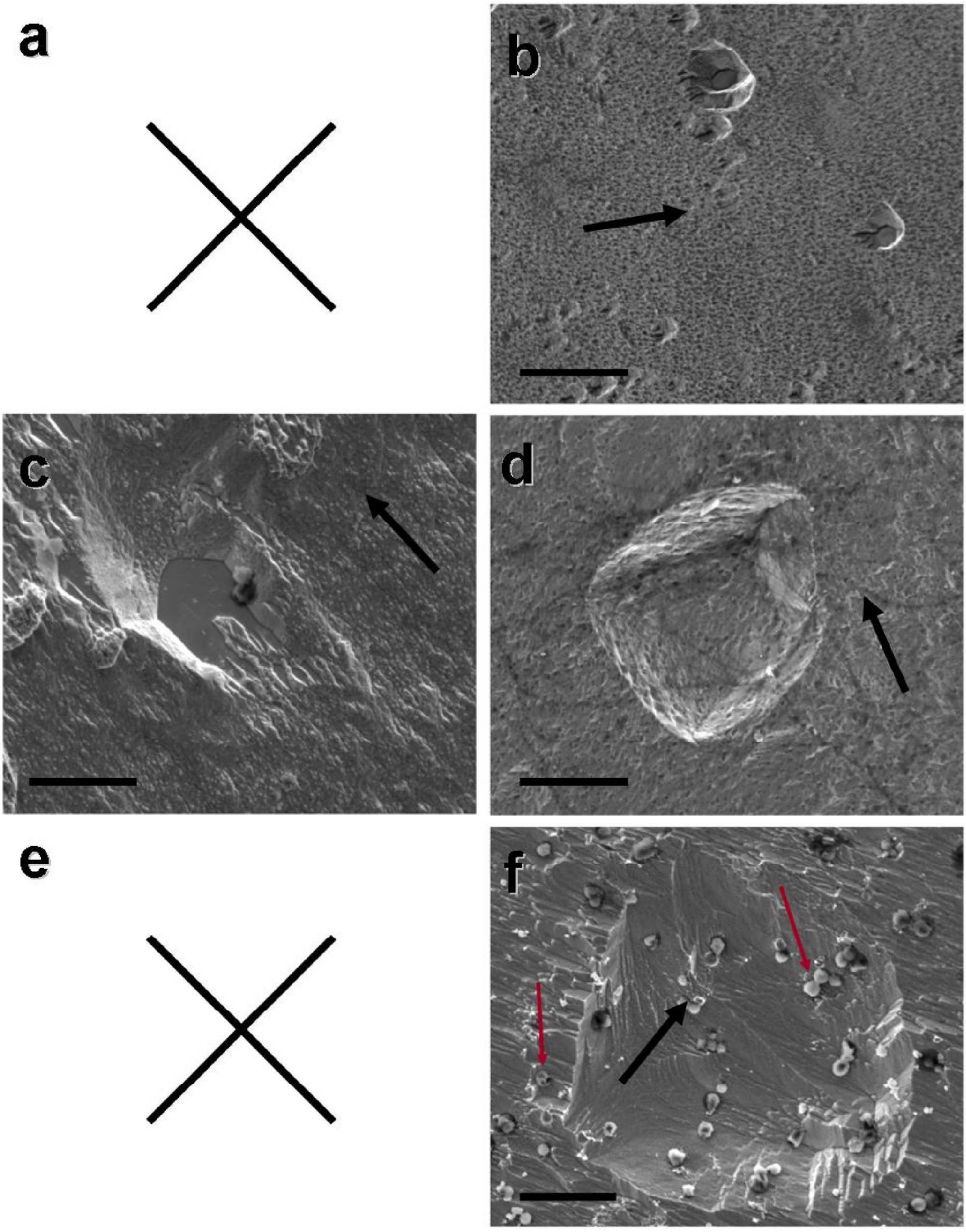

Figure 6.37: SEM images of pyrite {211} faces etched by the archaeal strains *Metallosphaera sedula* (c) and *Sulfolobus metallicus* (b, d, f), for three time intervals, one week (b), two weeks (c, d) and four weeks (f). Arrows indicate the direction $[0\bar{1}1]$ on surfaces. The round structures in c) and f) are cells (red arrows). The scale bars represent 5 µm.

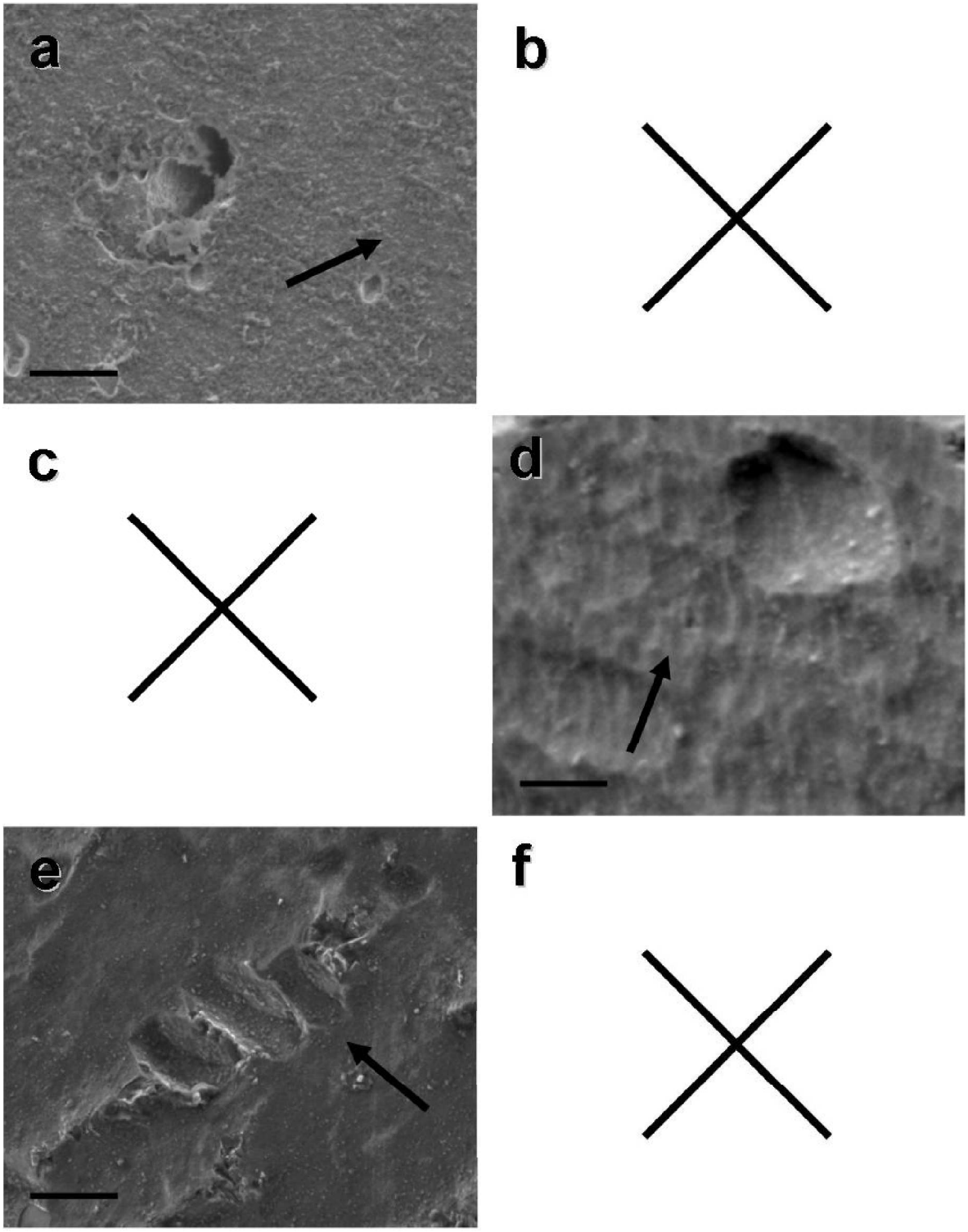

Figure 6.38: SEM images of pyrite {211} faces etched by iron(III)sulfate at 30°C (a, e) and 70°C (d), for three time intervals, one week (a), two weeks (d) and four weeks (f). Arrows indicate the direction $[0\bar{1}1]$ on surfaces. The scale bars represent 5 µm.

6.3.5 Etch features on {221} pyrite surfaces

Figs. 6.39 and 6.40 show {221} pyrite faces after biological and abiotic etching, respectively. Figs. 6.37a, c, e and 6.37b, d, f show pyrite faces etched by *Metallosphaera sedula* and *Sulfolobus metallicus*, respectively. Figs. 6.40a, c, e and 6.40d, f show {221} pyrite faces etched by iron(III)sulfate at 30°C and 70°C, respectively. Incubation times for both experiments are one (a, b), two (c, d) and four (e, f) weeks. The arrows on SEM images indicate the $[0\bar{1}1]$ directions on the surfaces. No sample with {221} faces was observed after one week of exposure by iron(III)sulfate at 70°C.

The symmetry of the {221} faces is the identity, 1. Again, no characterictic etch pits or edge directions were observed. And as for previous described forms {100}, {111} and {210}, no significant differences between the shape of the etch structures produced by microorganisms and iron(III)sulfate were observed. For all experiments an increase in size of the etch pits as a function of incubation time is observed. Moreover, the etching features produced by *Metallosphaera sedula* and iron(III)sulfate at 70°C are more pronounced than those produced by *Sulfolobus metallicus* and iron(III)sulfate at 30°C.

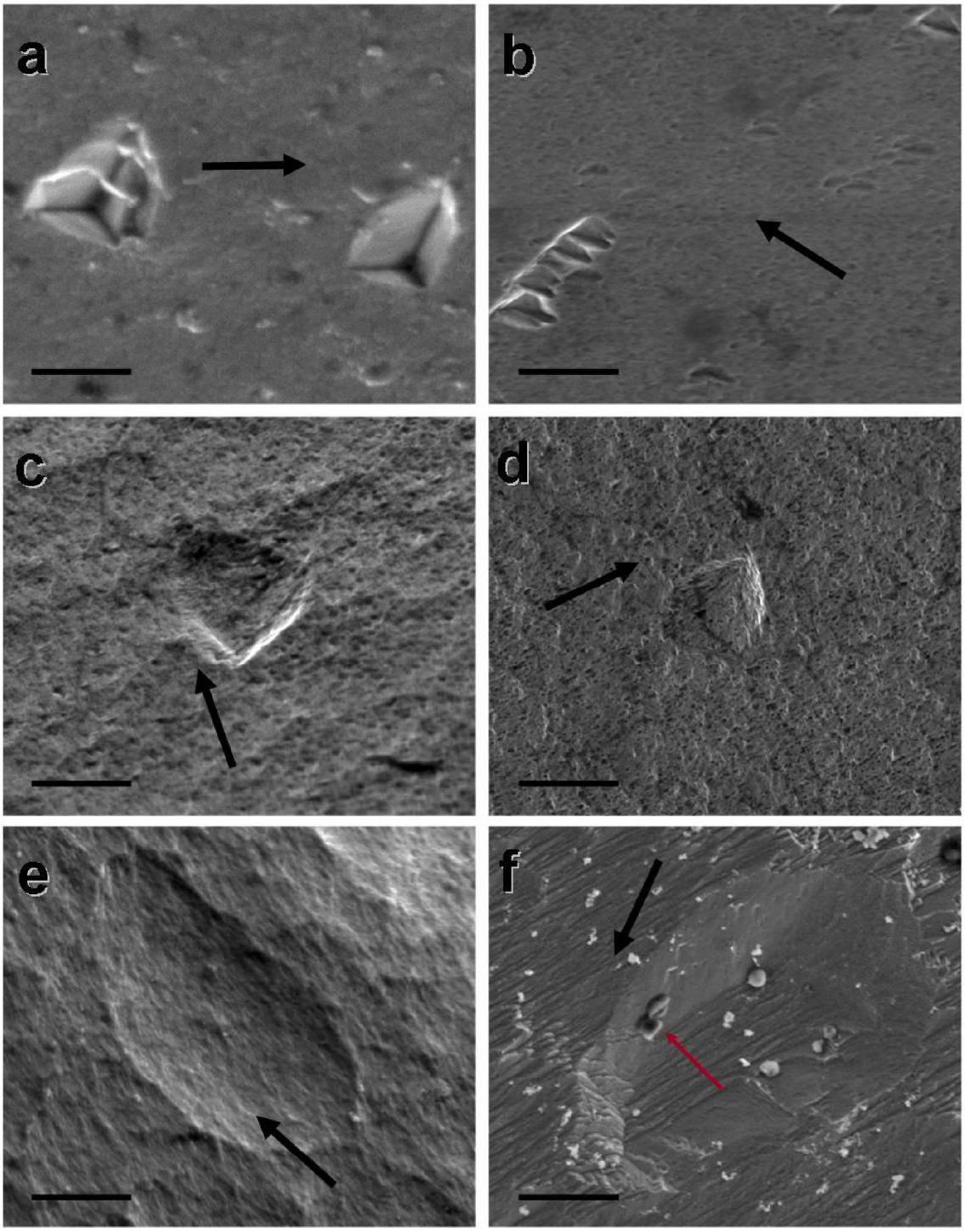

Figure 6.39: SEM images of pyrite {221} faces etched by the archaeal strains *Metallosphaera sedula* (a, c, e) and *Sulfolobus metallicus* (b, d, f), for three time intervals, one week (a, b), two weeks (c, d) and four weeks (e, f). Arrows indicate the direction $[0\bar{1}1]$ on surfaces. The round structures in f) are cells (red arrow). The scale bars represent 5 µm.

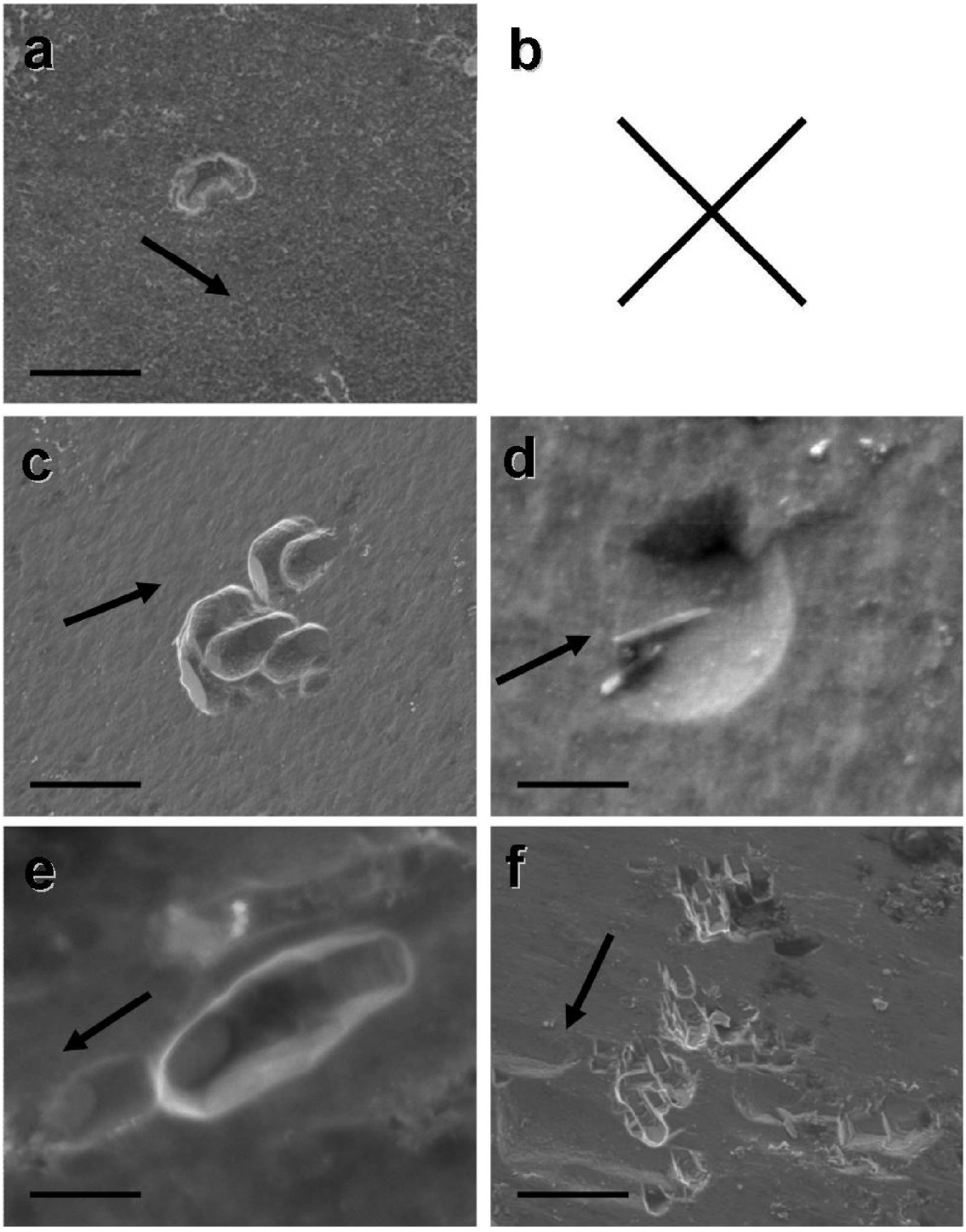

Figure 6.40: SEM images of pyrite {221} faces etched by iron(III)sulfate at 30°C (a, c, e) and 70°C (d, f), for three time intervals, one week (a), two weeks (c, d) and four weeks (e, f). Arrows indicate the directions $[0\bar{1}1]$ on surfaces. The scale bars represent 5 µm.

Chapter 7

Discussion

In this chapter a summary of this work is given. In section 7.1 the experiments of biological and abiotic oxidation of natural and cut surfaces are discussed. Section 7.2 gives a discussion of the synthesis and characterization of synthetic pyrite crystals and section 7.3 focuses on the results of biological and abiotic dissolution of synthetic pyrite.

7.1 Dissolution of natural and cut pyrite surfaces

In a series of systematic experiments, the effect of time (between one day and six weeks) and face-symmetry on biological and abiotic dissolution of natural and cut pyrite surfaces ({100}, {111}, {210}), were studied. Eight strains of mesophilic Bacteria and thermophilic Archaea (Chapters 3 and 5.2) were used for the biological experiments. Sulfuric acid and iron(III)sulfate were used as abiotic oxidants. Cell densities were measured using epifluorescence microscopy, showing that some microbial strains attach within a few days mostly to the mineral surface, whereas others predominantly remain planktonic in the liquid-growth medium. μ-Surf and SEM measurements show that etching effects appear after a few days of incubation.

Prior to oxidation experiments the orientation of the prepared surfaces were investigated using the Laue X-ray backscattering technique. Thus, spot measurements on the surfaces are given, which are not representative for the whole surface. Therefore, rocking-curve maps were taken (Fig. 6.13, 7.3). They showed intergrown crystal grains and the boundaries between two grains represent surface discontinuities. Microbially catalyzed surface dissolution starts at surface discontinuities and produces features including irregular channels, inverse pyramids, rectangular or round pits up to several 100 μm in size. Particularly in the case of cut surfaces, etch features are affected by the presence of inclusions (Figs. 6.8, 6.9, 6.10, 6.12). The interfaces between inclusions and the pyrite matrix serve as 'weak points', and here dissolution commences at

these boundaries and progress away from the mineral inclusion, ultimately releasing impurities from the pyrite crystal (Fig. 6.9b) and producing cavities (Fig. 6.2 h) or channel-like features in the surface (Fig. 6.10d). The spongy appearance after dissolution is the result of multiple superimposing and intersecting euhedral dissolution pits (Fig. 6.9). This shows that multiple surface sites are available for the dissolution process. On natural surfaces, defects such as steps, kinks, dislocations and vacancies are present and can act as 'weak points' and here dissolution commences. The dissolution features and their distribution on natural pyrite faces are fewer and more stand-alone located compared to those on cut surfaces (Figs. 6.11 and 6.14c). Because chemical reactivity is influenced by surface defects (Rosso et al., 1999, 2000; Higgins & Hamers, 1995, 1996) and polishing artificially adds (mechanical) defects to the surfaces, this results in multiple and randomly distributed dissolution pits.

Discontinuities on natural and cut surfaces serve as areas of preferred cell attachment (Figs. 6.14c and d), because fewer cells were observed in the surrounding surface areas. Here, microbial activity produces channel-like features (Fig. 6.11 and 6.14c, d) and in the case of Fig. 6.14c, d nanometer-sized elongated dissolution features radiating away from the discontinuity were produced. This suggests that microbial activity influences locally the solution. Sulfuric acid and ferric iron are produced as metabolic by-products, resulting in *non-contact* etching (e.g. Ingledew, 1982; Harrison, 1984). The ratio of planktonic versus attached cells for *Thiobacillus sphaeroides*, *Metallosphaera sedula* and *Sulfolobus metallicus* were found to be 80 : 20, 40 : 60 and 50 : 50, respectively. Thus, these organisms use both, the *contact* and the *non-contact* mechanisms. In contrast the planktonic versus attached ratio of *Acidithiobacillus ferrooxidans* was observed to be 5 : 95 indicating that this organism uses mainly the *contact* mechanism. This observation agrees with previous results of Mikkelsen et al. (2007) and Sand et al. (2006). After Bennett & Tributsch (1978) and Konishi et al. (1990) dissolution in the presence of attaching microbes results in local, crystallographically controlled etching that does not occur in the presence of planktonic microbes (Edwards et al., 1998). Here, it appears that surface properties and structures are the governing factors in the generation of dissolution features.

Time resolved studies shown in Fig. 6.15 confirm that the degree of surface dissolution increases with incubation time. The dissolution effects observed for the archaeal strains *Metallosphaera sedula* and *Sulfolobus metallicus*, (Figs. 6.15c and d, respectively) were more pronounced than for the bacterial strains *Acidithiobacillus ferrooxidans* and *Thiobacillus prosperus* (Figs. 6.15a and b, respectively), although optical density measurements indicated cultures of similar densities. The reasons for the differences between Archaea and Bacteria in pyrite surface dissolution are not known,

whether thermophilic cultures are metabolically more active than others, or not. Following the observations of the temperature dependent iron(III)sulfate etching (Fig. 6.18 and 6.19), the abiotic oxidation of pyrite occurs faster at higher than at lower temperatures. Because archaeal etching occurs at 65 - 85°C and bacterial etching at 30 - 37°C, the ferric iron activity as a function of temperature is important. However, Archaea produce significantly different structures than the bacterial strains (Figs. 6.1, 6.2, 6.4 and 6.15). Archaea produce mostly euhedral etch pits, while after incubation with bacterial strains non-euhedral etch pits occur. At the same time, dissolution features on pyrite surfaces, after incubation by archaeal strains, are more pronounced than those produced by Bacteria (Figs. 6.4e, g and 6.15a6, b3). This was observed by Karavaiko et al. (1994), who found differences between the etching of the bacterial strain *Thiobacillus ferrooxidans* and the archaeal strain *Sulfobacillus thermosulfidooxidans*.

The euhedral etching features are different for the faces {100}, {111} and {210}. The shape of the euhedral features follow face-symmetries, namely $2mm$, 3 and m respectively (Fig. 6.16). Most non-euhedral etching features also appear to follow crystallographic directions (e.g. Figs. 6.4e and g, 6.14c and d, 6.15a and b), with an exception shown in Fig. 6.11. The surface or crystal properties governing the formation of these features are unclear, but they may be related to impurities or crystallographic directions, as proposed by Eggleston et al. (1996). They observed during {100} pyrite oxidation studies with scanning tunneling microscopy that pyrite surfaces showed both oxidized and unoxidized areas. The borders between oxidized and unoxidized areas do not follow crystallographic directions over long distances, but they often occur to follow in short segments ⟨110⟩ and ⟨100⟩ directions.

Samples treated with bacterial strains show granular and layered mineral precipitates on their surfaces (Figs. 6.1a - d, and 6.2a - d). EDX measurements (Fig. 7.1) indicate that the granular precipitates are a phosphate, while the layered precipitates are jarosite ($AFe_3(SO_4)_2(OH)_6$, with A = Na, K, Rb, H_3O, NH_4, Ag, Tl) or a biofilm like EPS. No layered precipitates were observed on samples treated with archaeal strains nor for control samples (Fig. 6.3). Because the samples had identical preparations, it seems unlikely that the layered precipitates are conditional upon preparation. However, the media contain chemicals (Chapter 5.2) that could potentially react and build phosphates and sulfates, as observed after control experiments (Fig. 6.3). However, the experiments do not explain the exact cause for these observations. Konhauser et al. (1994) and Elsetinow et al. (2001) investigated the effect of phosphate on the oxidation of pyrite and found that it has no discernible effect on pyrite oxidation at pH < 3. For oxidation with bacterial strains that produce biofilms like EPS (e.g. *Acidithiobacillus ferrooxidans*; Chapter 4.2), nucleation reactions involving this EPS were proposed as

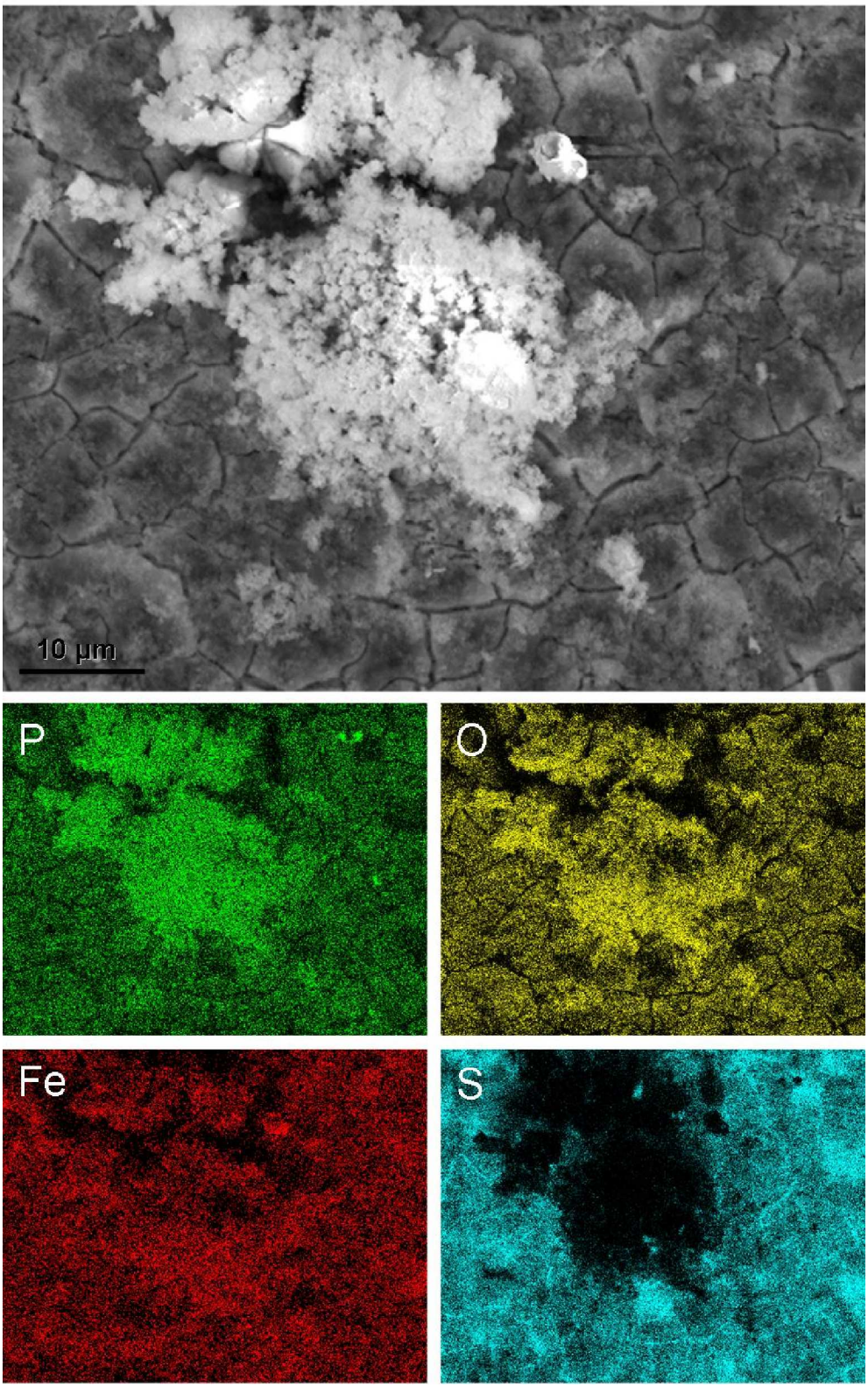

Figure 7.1: EDX maps of the bacterial precipitations.

factors for iron phosphate precipitation (Ueshima et al., 2004). However, it is not possible to determine if there is oxidation under this layer or if the layer acts as a barrier.

The abiotic experiments with sulfuric acid and iron(III)sulfate as oxidants show that resulting features resemble the results obtained after microbially mediated etching. The absence of euhedral etching features after sulfuric acid etching (Fig. 6.17), on a scale comparable to the microbially influenced samples, results from the non-solubility of pyrite in acid (Sand et al., 2001). Only small euhedral etching features were observed (insets in Figs. 6.17b and e), with several hundred nm in size. These structures are significantly smaller and fewer in number than those observed after exposure to archaeal strains or iron(III)sulfate etching (Figs. 6.18 and 6.19). The oxidation with iron(III)sulfate produced euhedral etch pits that are similar to those produced by Archaea. For all iron(III)sulfate etched pyrite samples, surface dissolution was more pronounced at 70 than at 30°C. This correlates with a higher ferric iron activity at higher temperatures (Keller & Murr, 1982; Boogerd et al., 1991; Bouffard et al., 2006). Similar observations were made by Keller & Murr (1982) and Blight et al. (2000), who altered pyrite surfaces in sulfuric acid, iron(III)sulfate and microbially active media. Their iron(III)sulfate oxidation is characterized by etch pits having symmetries related to the face-symmetry, while sulfuric acid and microbial oxidation produce more complex etching patterns with pits having, in some cases, forms that can not be correlated with face-symmetries.

7.2 Synthesis and characterization of pyrite crystals

The goal of crystal synthesis and characterization was to obtain high quality pyrite single crystals. These were used for further investigation of effects on abiotic and biological dissolution experiments as a function of face-symmetry. Therefore, it is important to synthesize crystals with diverse faces, well-defined surface structures and well-defined composition. The crystals were synthesized by the chemical vapor transport technique (CVT), and it was possible to obtain euhedral crystals up to 8.5 mm in diameter (Fig. 6.20; Tab. 6.2). The crystal faces were indexed by two-circle reflection-goniometry and showed that the habits have the forms {100}, {111}, {210}, {211} and {221} (Fig. 6.20; Tab. 6.2). The composition and stoichiometry of the crystals were determined by electron microprobe analysis; the ratio of S / Fe was found to be 1.98(8). Structural properties were characterized with X-ray powder diffraction, spectral properties of the crystals were studied by powder IR spectroscopy and single-crystal Raman spectroscopy, all attesting the high quality of the synthetic crystals. Transmission electron microscopic examination showed that the crystals did not contain significant numbers of structural defects. The properties of crystal surfaces were studied by scanning electron microscopy and confocal white light microscopy. The structural quality of the crystal faces was analyzed by high-resolution X-ray diffraction, via rocking-curves.

As noted earlier, synthetic crystals show sizes up to 8.5 mm in diameter and diverse forms. In order to check whether the crystal size rises with synthesis time, experimental durations up to six weeks were used, but the crystal size remained the same. The explanation is that crystals reach an equilibrium state with the vapor. Experiments with different temperatures and different transporting agents ($AlBr_3$, I_2, and K_2PtCl_6) were also carried out. The best results were obtained using $AlBr_3$ as transporting agent, a temperature range of 743 - 623°C and with growth periods of 12 days. The rate of iron and sulfur transport was up to 3 mg/h. This transport rate is in agreement with the rates observed by Yamada et al. (1979), but not with those of Fiechter et al. (1986) who observed transport rates up to 6 mg/h. The synthetic crystals showed excellent quality and microprobe analysis showed no aluminum or bromine impurities. Nevertheless, the growth velocity for a stable nucleus of pyrite under the experimental conditions is on the order of 50 Å/s (Tomm et al., 1995). This high growth rate could be responsible for formation of point defects which, however, were not detected. Several investigations to verify structure defects were performed. For example, transmission electron microscopy studies revealed that the crystals did not contain significant numbers of defects.

Even though the crystals were grown under the same conditions, different habits

were found. The habits of the synthetic crystals consist of a maximum of five forms (Fig. 6.20). A schematic diagram of a crystal with these five forms is shown in Fig. 7.2, including the symmetry operations of $m\bar{3}$, the crystal class of pyrite. Thus, the symmetries of the faces are, $mm2$ for {100}, 3 for {111}, m for {210} and 1 for {211} and {221}. The sizes of {211} and {221} faces were the smallest, while {211} is the rarest form. This results from faster growth of {211} and {221} faces. Thus, during longer growth experiments {211} and {221} faces should disappear. Therefore, synthesis experiments with durations up to six weeks were performed. However, no dependence of obtained faces as a function of synthesis time was observed. Crystals grown over longer periods showed the same habits as those grown in shorter times.

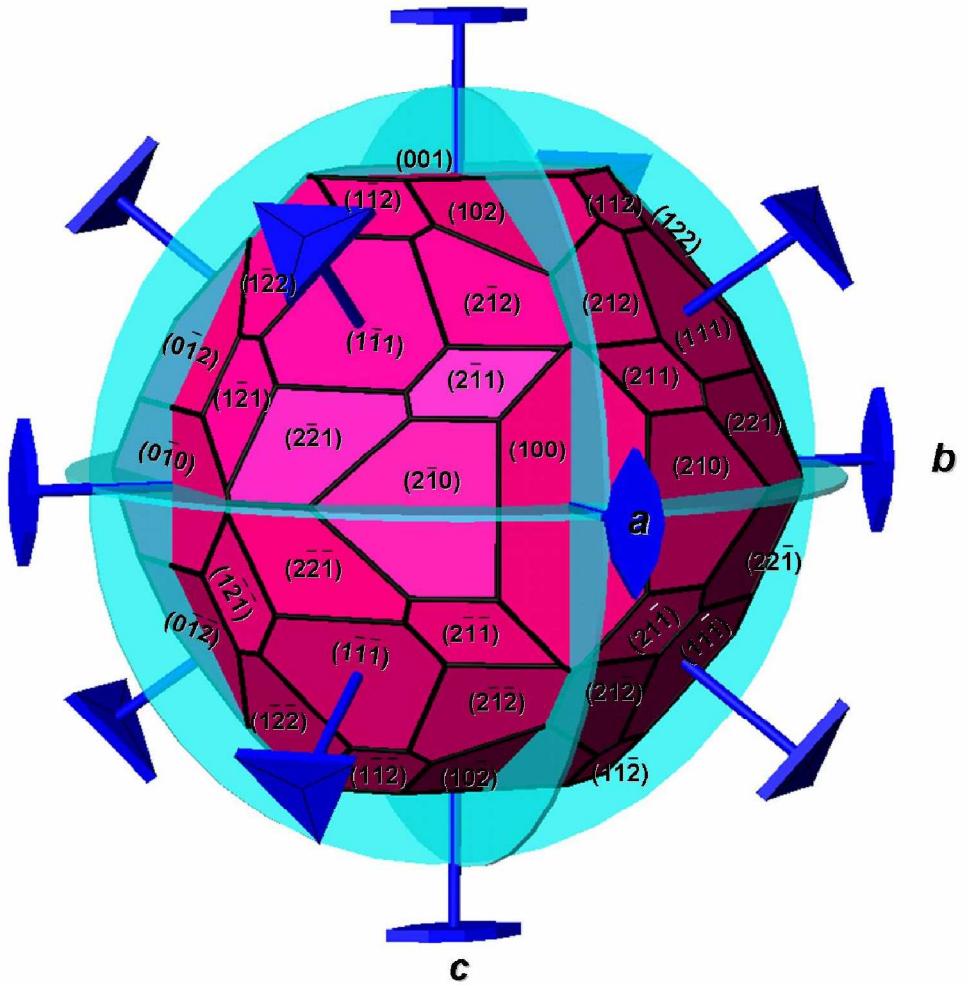

Figure 7.2: Schematic illustration of a pyrite single crystal with five different forms {100}, {111}, {210}, {211}, {221} and symmetry elements. Faces {100} have $mm2$ symmetry; {111} show 3-fold axis; {210} exhibit m symmetry; faces {211} and {221} offer a symmetry of 1.

The quality of the surfaces was studied using the μ-Surf technique and high-resolution XRD. The topographic analysis showed a few steps on {100} faces that were otherwise flat, untextured faces. High-resolution XRD analysis indicated the high crystalline quality of the synthetic crystals (Fig. 6.26). For comparison, a rocking-curve map was measured for a natural (100) pyrite. This map is shown in Fig. 7.3, where the left part of the figure shows a SEM image of the surface. The black arrow represents the direction of the mapping and the grey ellipse the size of the X-ray beam. The full width at half maximum of the rocking-curves of the natural pyrite surfaces were between 100 and 150 arcsec, while those of synthetic surfaces were between 40 and 80 arcsec. Thus, the mosaicity of the natural pyrite surfaces is greater. Further, the rocking-curve map of the natural sample shows that the peak maxima position of scans 12 to 26 is 16.54° θ. The kink of the peak maxima between scan areas 12 - 26 and 26 - 64 indicates an inhomogeneity of the surface structure. Both areas reflect a crystal grain. On synthetic surfaces such kinks or intergrown crystal grains were not observed. This attests again the high quality of the synthetic crystals.

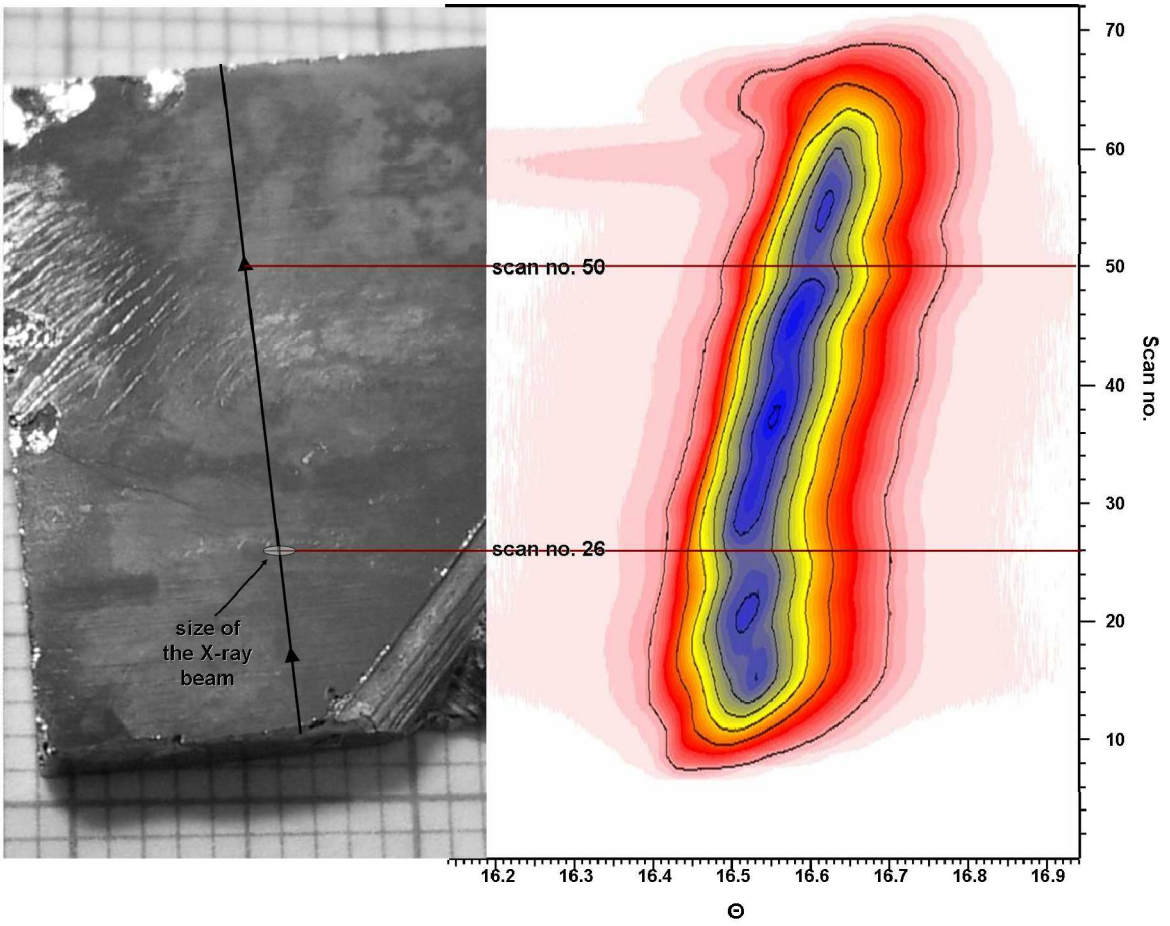

Figure 7.3: Light microscope image and map of rocking-curves of the 200 peak along the black arrow of a natural (100) pyrite surface. The ellipse reflects the X-ray beam size and therefore the average area of the integrated intensity per scan. The full width at half maximum were between 100 and 150 arcsec.

7.3 Dissolution of synthetic pyrite crystals

Here, the results of biological and abiotic etching experiments on synthetic pyrite surfaces ({100}, {111}, {210}, {211}, {221}) are discussed. In systematic studies, the effects of time (one, two and four weeks of incubation) and face-symmetry were studied. The biological experiments were performed using two strains of thermophilic Archaea (*Metallosphaera sedula, Sulfolobus metallicus*). Abiotic experiments were performed with iron(III)sulfate. Epifluorescence microscopy showed that the strains attach partly to the mineral surface, whereas the rest remain planktonic. SEM and µ-Surf studies showed cell attachment and etching effects over the whole time period. Etch features, dependent on face-symmetry, up to several 10 µm in size were produced. The same was observed after abiotic experiments with iron(III)sulfate. However, after abiotic oxidation layered and granular precipitations were observed, while during biological oxidation only granular precipitations were found. The precipitations were not determined, but these occurrence has been observed by several authors and addressed as jarosite or other iron-rich minerals (e.g. Keller & Murr, 1982; Mikkelsen et al., 2007).

Differences in biological and abiotic oxidation are noticeable for etch pit size, while the etch pit shapes are similar for the same faces. This indicates similar etching processes for archaeal and iron(III)sulfate oxidation. For biological oxidation of pyrite, two main processes were proposed by Rohwerder et al. (2003), namely *contact* and *non-contact* mechanisms (Chapter 4.2). Therefore, ratios of planktonic versus attached cells for both strains were investigated. *Metallosphaera sedula* showed a ratio of 60 : 40, *Sulfolobus metallicus* of 50 : 50, indicating that both organisms use both biooxidation mechanisms, which is in agreement with earlier investigations (e.g. Mikkelsen et al., 2007). It became apparent that surface dissolution for all etched pyrite samples was more pronounced for *Metallosphaera sedula* than for *Sulfolobus metallicus* or iron(III)sulfate. Similar results were found by Mikkelsen et al. (2007).

For all abiotic etched pyrite samples, surface dissolution was more pronounced at 70°C than at 30°C. This correlates with a higher ferric iron activity at higher temperatures (Keller & Murr, 1982; Boogerd et al., 1991; Bouffard et al., 2006). Because the experiments with *Metallosphaera sedula* were performed at 75°C and those with *Sulfolobus metallicus* at 65°C, the activity of ferric iron (*non-contact* mechanism) is significantly higher for *Metallosphaera sedula* than for *Sulfolobus metallicus*. Thus, the larger features after incubation by *Metallosphaera sedula* are a result of higher metabolic (higher cell densities) and ferric iron activity compared to *Sulfolobus metallicus*. However, there is still no explanation for oxidation rates or cell attachment as a function of face-symmetry, because during all experiments, oxidation effects and cell

attachment on the various faces of the same crystal were observed to be of the same quantity and size.

As in previous experiments, the shape of the euhedral etch pits varies with faces and reflects the face-symmetry. Observed etch features and the structure of the faces are shown schematically in Fig. 7.4, where Fig. 7.4a shows the sturcture of a (100) surface including the 2D unit cell (red dashed line) and the directions of the etch pit edges (blue dashed line). The image shows that the edges follow the ⟨001⟩ and ⟨011⟩ directions and either are iron or sulfur terminated. This is in accordance with studies of Eggleston et al. (1996), who observed during {100} pyrite oxidation borders (edges) between oxidized and unoxidized areas, following ⟨110⟩ and ⟨100⟩ directions. The same was observed for {111} and {210} faces (Fig. 7.4b and c, respectively). For {211} and {221} faces no characteristic etch pits were observed. Therefore, these faces are not shown in Fig. 7.4. The results indicate that the face-symmetries plays a key role in the etching process of pyrite crystals.

Experiments with natural and cut surfaces (Chapters 6.1.2, 7.1) showed the effect of defect sites and inclusions for the oxidation processes. It is obvious that etch pits on synthetic surfaces are more stand-alone, because the mosaicity and thus defects are more pronounced for natural and cut than for synthetic surfaces. Figs. 6.18, 6.19 and 6.29 show natural, cut and synthetic {100} surfaces, after exposure to iron(III)sulfate solution. The figures show many intersecting etch pits on the natural and cut surfaces, while on synthetic surfaces stand-alone features occur. This occurred for both temperatures and also for biological dissolution. Thus, etch pits on synthetic faces are measurable and etched faces could be indexed. Measurements of etch pits using μ-Surf technique (Fig. 6.30, 6.33, 6.36) showed that produced faces inside etch pits on {111} and {210} faces could be indexed as {211} or {221} and {110} faces, respectively. However, more detailed characterizations of these structures are needed, to index all produced faces.

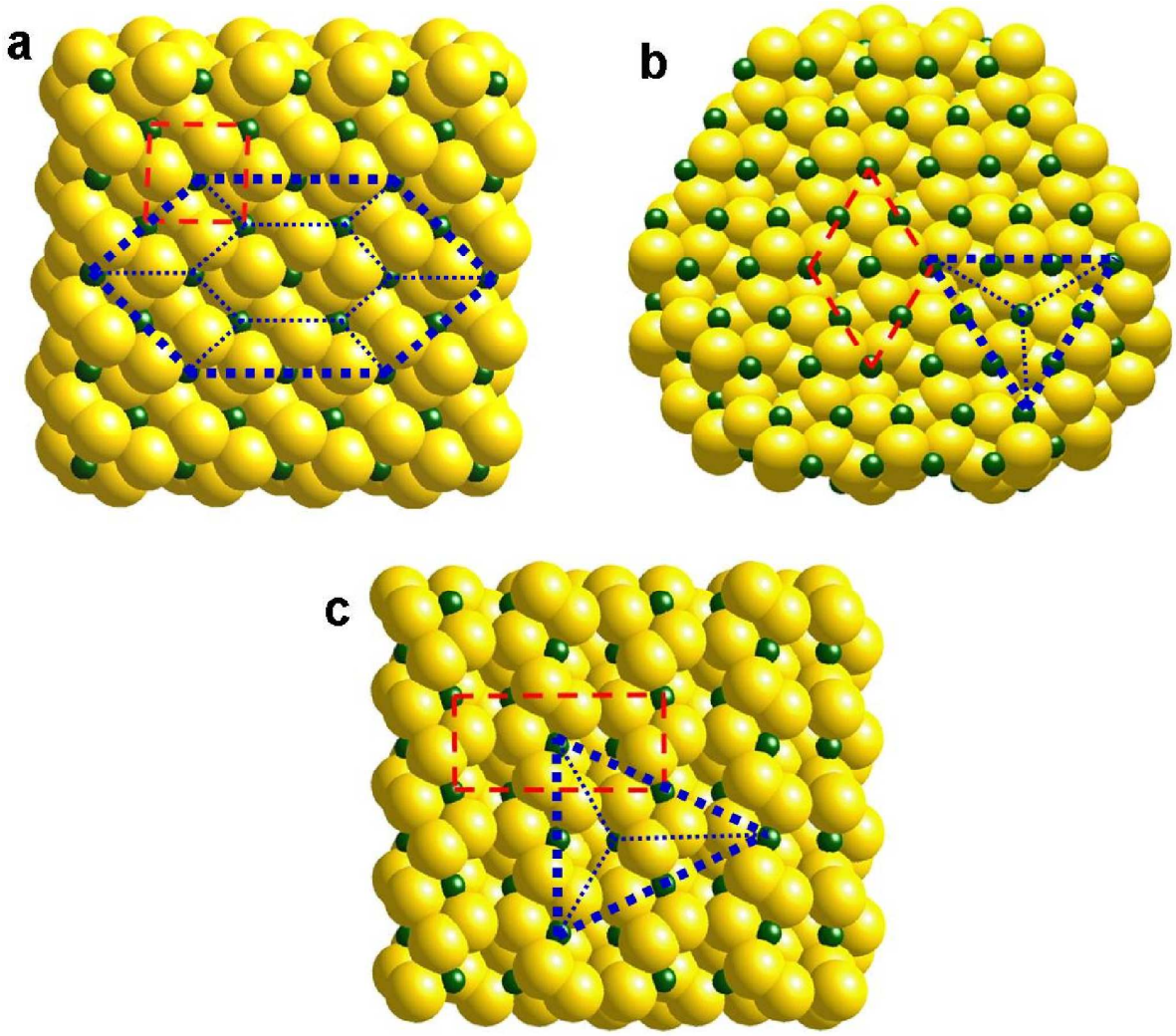

Figure 7.4: Surface structure of pyrite (100) (a), (111) (b) and (210) (c) faces, including the rectangular 2D unit cells (red dashed square), and the shapes of the euhedral etch pits (blue dashed bodies). Graphics were drawn with the software *CrystalMaker* (Palmer, 2000).

7.4 Conclusion

The experiments elucidate the relationship between the surface types (natural, cut, synthetic), face-symmetries ({100}, {111}, {210}, {211}, {221}), incubated oxidants (Bacteria, Archaea, sulfuric acid, iron(III) sulfate), incubation time (one day to six weeks) and temperature (30 - 85°C) on dissolution features on pyrite surfaces. There are differences in the numbers of dissolution features between natural, cut and synthetic surfaces, because surface imperfections serve as preferred dissolution sites and microbial surface attachment. Thus, the highest number of dissolution features was found on cut surfaces followed by natural surfaces and fewest numbers were found on synthetic surfaces. This results in more stand-alone and well measurable etch pits on synthetic surfaces. Significant differences in surface dissolution effects between bacterial and archaeal strains were observed, with Archaea producing more pronounced and euhedral etch pits as a function of face-symmetry. However, attached cells influence the circumfluent solution, producing pyrite dissolution in close association with the organisms. Time resolved studies confirm that the degree of surface dissolution increases with incubation time and experiments addressing the effect of temperature showed more pronounced etching effects at higher temperatures. Similarities of dissolution effects were observed on synthetic surfaces in abiotic and biological experiments. Euhedral etch pits were produced with slight differences in sizes. Further, dissolution patterns produced by iron(III)sulfate etching resemble those observed after archaeal etching. Both produced euhedral etch pits. During all experiments, the archaeal strain *Metallosphaera sedula* produced more pronounced dissolution effects than all other oxidants. This can be explained by the higher metabolic activity of the archaeal strain *Metallosphaera sedula* and the higher activity of ferric iron at higher temperatures. Both lead to higher oxidation rates, higher dissolution rates, and consequently to more pronounced surface dissolution. This observation agrees with those of Norris (1997), who proposed, that *Metallosphaera sedula* is the mose efficient organism of biooxidation. However, microbial effects are more pronounced than abiotic effects suggesting that microbial activity has a distinct influence on surface oxidation.

Chapter 8

Summary and outlook

The study of dissolution mechanisms of differently treated pyrite surfaces by various biological and abiotic oxidants was presented in this work. Differences of cell attachment and dissolution of the various microbial strains on {100} pyrite surfaces, as well as differences in dissolution of a microbial strain on various pyrite faces was studied. Ratios of planktonic versus attached cells showed that the strains used in different percentages *contact* and *non-contact* dissolution mechanisms. Dissolution features on natural and cut {100} pyrite surfaces, after exposure to bacterial and archaeal strains, showed distinct differences. Archaeal etching is characterized by euhedral etch pits having symmetries of the surfaces, while bacterial etching produced precipitations, as well as more complex etching patterns with etch pits having, in some cases, forms that can not be correlated to face-symmetries. Hence, for bacterial strains no analysis of dissolution features as a function of face-symmetry is possible. The shapes of the euhedral etch pits produced by Archaea are dependent on face-symmetry. However, the experiments with natural and cut pyrite surfaces showed impurities and defects in natural crystals. Thus, pyrite crystals were synthesized with well-defined surface structures and composition. The synthetic crystals showed up to five different forms. With these crystals it was possible to perform dissolution experiments whereby the various faces were exposed to exactly the same conditions. Thus, cell attachment and dissolution features as a function of face-symmetry were studied. Here only archaeal dissolution was investigated, because experiments with bacterial strains showed no etch effects or cell attachment on synthetic pyrite. However, no preference of cell attachment as a function of face-symmetry was found. Both archaeal strains produced similar etch pits as on natural and cut surfaces, though being less superimposed and more stand-alone. The etch pits reflected the symmetry of the faces. Etch pits are not mainly induced by microbial contact as proposed in literature, because attached cells inside the etch pits as well as on the surface around were found. For all experiments it appears that pyrite

dissolution by *Metallosphaera sedula* is more pronounced than by the other oxidants. This may be a result of both, higher metabolic activity as well as higher ferric iron activity at higher temperatures.

Abiotic dissolution experiments were performed using sulfuric acid and iron(III) sulfate. Dissolution induced by iron(III)sulfate is more pronounced than by sulfuric acid for all abiotic oxidation experiments. The oxidation caused by sulfuric acid revealed dissolution features that are independent of concentration, whereas the dissolution features after exposure to iron(III)sulfate were similar in size and shape to those observed after archaeal etching. The effect of temperature with iron(III)sulfate dissolution was studied and found to be more pronounced at higher temperatures. This indicates a higher activity of ferric iron at higher temperatures. Through a comparison of the abiotic and biological dissolution features, it is apparent that bacterial influenced dissolution is less pronounced than dissolution by sulfuric acid, while dissolution by iron(III)sulfate is less pronounced than by Archaea. All experiments were also performed to address the effect of time, hardly surprisingly, that the degree of surface dissolution increased with incubation time and it was shown that within a few days cell attachment and dissolution commences.

With this study, the effects of various parameters during abiotic and biological dissolution were investigated. However, for a better understanding more study is needed. For example, it is important to know what kind of precipitations are present to eliminate the precipitations after bacterial etching. It is also important to know if there is oxidation under these precipitations or if these precipitations act as a barrier. For future investigations these precipitations need to be removed and characterized. Further, to validate the importance of dissolution rates as a function of face-symmetry, synthetic crystals with one form are required. Investigations are also needed to determine which faces appear inside the etch pits. All these aspects show that more work is required to understand the interaction between microbes and pyrite surfaces.

Bibliography

Abraitis, P., Pattrick, R. and Vaughan, D. (2004). Variations in the compositional, textural and electrical properties of natural pyrite: A review. *International Journal of Mineral Processing* **74** 41–59

Acuna, J., Peirano, I. and Jerez, C. (1986). *in vivo* and *vitro* methylation of proteins from chemolithotrophic microorganisms: A possible role in chemotaxis. *Biothechnology and Applied Biochemistriy* **8** 309–317

Alcamo, I. (1997). *Fundamentals of Microbiology*. Menlo Par, California: Benjamin Cumming

Allen, M. (1959). Studies with *Cyanidium caldarium*, an anomalously pigmented chlorophyte. *Archives of Microbiology* **32** 270–277

Andersson, C., Brattsand, R., Hallber, A., Engman, L., Persson, J., Moldeus, P. and Cotgreave, I. (1994). Diaryl tellurides as inhibitors of lipid peroxidation in biological and chemical systems. *Free Radical Research* **20** 401–410

Aoki, A. (1999). Acid-bacterial leaching of pyrite single crystal. *International Biohydrometallurgy Symposium* **A** 119–125

Balch, W. and Wolfe, R. (1976). New approach to the cultivation of methanogenic bacteria: 2-mercaptoethanesulfonic acid (HS-CoM)-dependent growth of *Methanobacterium ruminantium* in a pressureized atmosphere. *Applied and Environmental Microbiology* **32** 781–791

Basolo, F. and Pearson, R. (1967). *Mechanisms of Inorganic Reactions: A Study of Metal Complexes in Solution*. Wiley, New York

Beck, J. (1967). The role of Bacteria in copper mining operations. *Biotechnology and Bioengineering* **9** 487–497

Bennett, C., Graham, J. and Thornber, M. (1972). New observations on natural pyrrhotites. Part I - Mineragraphic techniques. *American Mineralogist* **57** 445–462

Bennett, J. and Tributsch, H. (1978). Bacterial leaching patterns on pyrite crystal surfaces. *Journal of Bacteriology* **134** 310–317

Berry, V. and Murr, L. (1977). An SEM study of bacterial catalysis and its effect on surface reactions at sulfide phases in the leaching of low-grade copper ore. *Scanning Electron Microscopy* **1** 137–146

Berry, V. and Murr, L. (1978). *Metallurgical applications of bacterial leaching and related microbiological phenomena*, Direct observations of Bacteria and quantitative studies of their catalytic role in the leaching of low-grade, copper-bearing waste, 103–136. Murr, L., Terma, A. and Bruiley, J. (eds.), Academic Press, New York

Biltz, W., Voigt, A. and Meisel, K. (1936). Beiträge zur systematischen Verwandtschaftslehre. 69. I) Über das System Nickelmonosulfid / Nickeldisulfid / Schwefel. *Zeitschrift für Anorganische und Allgemeine Chemie* **228** 278

Birkholz, M., Fiechter, S., Hartmann, A. and Tributsch, H. (1991). Sulfur deficiency in iron pyrite (FeS_{2-x}) and its consequences for band-structure models. *Physical Review B* **43** 11926–11936

Blake II, R. and Shute, E. (1994). Respiratory enzymes of *Thiobacillus ferrooxidans*: Kinetic properties of an acid-stable iron : rusticyanin oxidoreductase. *Biochemistry* **33** 9220–9228

Blenk, O., Bucher, E. and Willeke, G. (1993). p-type connduction in pyrite single crystals prepared by chemical vapor transport. *Applied Physics Letters* **62** 2093–2095

Blight, K., Ralph, D. and Thurgate, S. (2000). Pyrite surfaces after bio-leaching: A mechanism for bio-oxidation. *Hydrometallurgy* **58** 227–237

Boogerd, F., vanden Beemd, C., Stoelwinder, T., Bos, P. and Kuenen, J. (1991). Relative contributions of biological and chemical reactions to the overall rate of pyrite oxidation at temperatures between 30°C and 70°C. *Biotechnology and Bioengineering* **38** 109–115

Borda, M., Strongin, D. and Schoonen, M. (2003). A vibrational spectroscopic study of the oxidation of pyrite by ferric iron. *American Mineralogist* **88** 1318–1323

Bouchard, R. (1968). The preparation of single crystals of FeS_2, CoS_2, and NiS_2 pyrites by chlorine transport. *Journal of Crystal Growth* **2** 40–44

Bouffard, S., Rivera-Vasquez, B. and Dixon, D. (2006). Leaching kinetics and stoichiometry of pyrite oxidation from a pyrite-marcasite concentrate in acid ferric sulfate media. *Hydrometallurgy* **84** 225–238

Bragg, W. (1913). The analysis of crystals by the X-ray spectrometer. *Proceedings of the Royal Society of London* **A 89** 468–489

Brierley, C. (1978). Bacterial leaching. *Critical Reviews in Microbiology* **6** 207–262

Brierley, C., Brierley, J. and Murr, L. (1973a). Using the SEM in minig research. *Journal of Research and Development* **24** 24–28

Brierley, C. and Murr, L. (1973b). Leaching: Use of a thermophilic and chemoautrophic microbe. *Science* **179** 488–491

Brock, T., Brock, K., Belly, R. and Weiss, R. (1972). *Sulfolobus*: A new genus of sulfur-oxidizing bacteria living at low pH and high temperature. *Archives of Microbiology* **84** 54–68

Brostigen, G. and Kjekshus, A. (1969). Redetermined crystal structure of FeS_2 (pyrite). *Acta Chemica Scandinavica* **23** 2186–2188

Bryner, L. and Anderson, R. (1957). Microorganisms in leaching sulfide minerals. *Industrial and Engineering Chemistry* **49** 1721

Bryner, L., Beck, J., Davis, D. and Wilson, D. (1954). Microorganisms in leaching sulfide minerals. *Industrial and Engineering Chemistry Research* **46** 2587–2592

Buckley, A. and Riley, K. (1991). Self-induced floatability of sulphide minerals: Examination of recent evidence for elemental sulphur as the hydrophobic entity. *Surface and Interface Analysis* **17** 655–659

Buckley, A. and Woods, R. (1987). The surface oxidation of pyrite. *Applied Surface Science* **27** 437–452

Buerger, M. (1934). The pyrite-marcasite relation. *American Mineralogist* **19** 37–61

Buerger, M. (1937). Interatomic distances in marcasite and notes on the bonding in crystals of löllingite, arsenopyrite and marcasite types. *Zeitschrift für Kristallographie* **97** 504–510

Burt, D., Wohletz, K. and Knauth, L. (2006). Mars and mine dumps. *EOS, Transactions, American Geophysical Union* **87** 549–552

Butler, S. and Bouchard, R. (1971). Single crystal growth of pyrite solid solutions. *Journal of Crystal Growth* **10** 163–169

Cai, J. and Philpott, M. (2004). Electronic structure of bulk and (001) surface layers of pyrite FeS_2. *Computational Materials Science* **30** 358–363

Carpenter, L. and Herndon, L. (1933). *Acid Mine Drainage from Bituminous Coal Mines*. West Virginia University, Morgantown, WV

Chander, S., Briceno, A. and Pang, J. (1993). Mechanism of sulfur oxidation in pyrite. *Minerals and Metallurgical Processing* 113–118

Clark, A. (1966). Stability field of monoclinic pyrrhotite. *Transactions of the Institution of Mining and Metallurgy (London)* **B 75** 232–235

Colmer, A. and Hinkle, M. (1947). The role of microorganisms in acid mine drainage: A preliminary report. *Science* **106** 253–256

Colmer, A., Temple, K. and Hinkle, M. (1950). An iron-oxidizing bacterium from the acid drainage of some bituminous coal mines. *Journal of Bacteriology* **59** 317–328

Cox, J. and Boxer, D. (1986). The role of rusticyanin, a blue copper protein, in the electron transport chain of *Thiobacillus ferrooxidans* grown on iron or thiosulfate. *Biotechnology and Applied Biochemistry* **8** 269–275

Craig, J. and Scott, S. (1974). Sulfide phase equilibria. *Reviews of Mineralogy and Geochemistry* **1** CS 1–110

Dana, E. (1903). *The system of mineralogy of James Dwight Dand*. Wiley, New York

Edwards, K., Goebel, B., Rodgers, T., Schrenk, M., Gihring, T., Cardona, M., Hu, B., McGuire, M., Hamers, R., Pace, N. and Banfield, J. (1999). Geomicrobiology of pyrite (FeS_2) dissolution: Case study at Iron Mountain, California. *Geomicrobiology Journal* **16** 155–179

Edwards, K. and Rutenberg, A. (2001). Microbial response to surface microtopography: The role of metabolism in localized mineral dissolution. *Chemical Geology* **180** 19–32

Edwards, K., Schrenk, M., Hamers, R. and Banfield, J. (1998). Microbial oxidation of pyrite: Experiments using microorganisms from an extreme acidic environment. *American Mineralogist* **83** 1444–1453

Eggleston, C., Ehrhardt, J.-J. and Stumm, W. (1996). Surface structural controls on pyrite oxidation kinetics: An XPS-UPS, STM, and modeling study. *American Mineralogist* **81** 1036–1056

Eggleston, C. and Hochella, M. (1992). Scanning tunneling microscopy of pyrite {100}: Surface structure and step reconstruction. *American Mineralogist* **77** 221–224

Ehlers, E. (1972). *The interpretation of geological phase diagrams*. W.H. Freeman and Company, San Francisco

Ehrlich, H. (1990). *Goemicrobiology*. Dekker, M. (ed.), Inc. New York

Ellmer, K. and Hopfner, C. (1997). On the stoichiometry of the semiconductor pyrite FeS_2. *Philosophical Magazine* **75** 1129–1151

Elsetinow, A., Schoonen, M. and Strongin, D. (2001). Aqueous geochemical and surface science investigation of the effect of phosphate on pyrite oxidation. *Environmental Science and Technology* **35** 2252–2257

Ennaoui, A., Fiechter, S., Goslowsky, H. and Tributsch, H. (1985). Photoactive synthetic polycrystalline pyrite (FeS_2). *Journal of the Electrochemical Society* **132** 1579–1582

Ennaoui, A. and Tributsch, H. (1984). Iron sulphide solar cells. *Solar Cells* **13** 197–200

Evans Jr., H., Milton, C., Chao, E., Adler, I., Mead, C., Ingram, B. and Berner, R. (1964). Valeriite and the new iron sulfide, mackinawite. *U.S. Geological Survey Professional Paper* **D 475** 64–69

Fiechter, S. (2004). Defect formation energies and homogeneity ranges of rock salt-, pyrite-, chalcopyrite- and molybdenite-type compound semiconductors. *Solar Energy Materials and Solar Cells* **83** 459–477

Fiechter, S., Brikholz, M., Hartmann, A., Dulski, P., Giersig, M. and Tributsch, H. (1992). The microstructure and stoichiometry of pyrite FeS_{2-x}. *Journal of Materials Research* **7** 1829–1838

Fiechter, S., Mai, J., Ennaoui, A. and Szacki, W. (1986). Chemical vapour transport of pyrite (FeS_2) with halogen (Cl, Br, I). *Journal of Crystal Growth* **78** 438–444

Fuchs, T., Huber, H., Burggraf, S. and Stetter, K. (1996). 16S rDNA-based phylogeny of the archaeal order *Sulfolobales* and reclassification of *Desulfurolobus ambivalens* as *Acidianus ambivalens* comb. nov. *Systematic and Applied Microbiology* **19** 56–60

Furic, K., Stoch, L. and Dutkiewicz, J. (2005). Raman study of TiO_2 role in $SiO_2-Al_2O_3-MgO-TiO_2-ZnO$ glass crystallization. *Spectrochimica Acta Part A: Molecular and Biomolecular Spectroscopy* **61** 1653–1659

Gregory, N. and Laughlin, W. (1977). Molecular complexes formed by interaction of iron(II)bromide, aluminum(III)bromide, and bromine. *Journal of Physical Chemistry* **81** 2228–2232

Gronvold, F. and Haraldsen, H. (1952). On the phase relations of synthetic and natural pyrrhotites. *Acta Chemica Skandinavica* **6** 1452–1469

Guevremont, J., Bebie, J., Elsetinow, A., Strongin, D. and Schoonen, M. (1998a). Reactivity of the (100) plane of pyrite in oxidizing gaseous and aqueous environments: Effects of surface imperfections. *Environmental Science and Technology* **32** 3743–3748

Guevremont, J., Elsetinow, A., Strongin, D., Bebie, J. and Schoonen, M. (1998b). Structure sensitivity of pyrite oxidation: Comparison of the (100) and (111) planes. *American Mineralogist Letters* **83** 1353–1356

Hallberg, K. and Johnson, D. (2001). Biodiversity of acidophilic prokaryotes. *Advanced and Applied Microbiology* **49** 37–84

Hallmann, R., Friedrich, A., Koops, H., Pommerening-Roeser, A., Rohde, K., Zenneck, C. and Sand, W. (1993). Physiological characteristics of *Thiobacillus ferrooxidans* and *Leptospirillum ferrooxidans* and physiochemical factors influence microbial metal leaching. *Geomicrobiology Journal* **10** 193–206

Hargittai, M., Kolonits, M. and Gödörhazy, L. (1996). Molecular geometry of monomeric and dimeric aluminum tribromide from gas phase electron diffraction. *Chemical Physics Letters* **257** 321–326

Harneit, K., Göksel, A., Kock, D., Klock, J.-H., Gehrke, T. and Sand, W. (2006). Adhesion to metal sulfide surfaces by cells of *Acidithiobacillus ferrooxidans*, *Acidithiobacillus thiooxidans* and *Leptospirillum ferrooxidans*. *Hydrometallurgy* **83** 245–254

Harrison Jr., A. (1984). The acidophilic thiobacilli and others acidophilic Bacteria that share their habitat. *Annual Review of Microbiology* **38** 265–292

Hazen, T., Jimenez, L. and de Vectoria, G. (1991). Comparison of Bacteria from the deep subsurface sediment and adjacent groundwater. *Microbial Ecology* **22** 293–304

Higgins, S. and Hamers, R. (1955). Spatially-resolved electrochemistry of the lead sulfide (galena) surface by electrochemical scanning tunneling microscopy. *Surface Science* **324** 263–281

Higgins, S. and Hamers, R. (1996). Chemical dissolution of galena (001) surface observed using scanning tunneling microscop. *Geochimica et Cosmochimica Acta* **60** 3067–3073

Hiskey, J. and Schlitt, W. (1982). *Interfacing Technologies in Solution Mining - Proceedings of the 2nd SME SPE International Solution Mining Symposium*, Aqueous Oxidation of Pyrite, 55–74. Schlitt, W. and Hiskey, J. (eds.), AIME, New York

Hochella, M., Rakovan, J., Rosso, K., Bickmore, B. and Rufe, E. (1998). *Mineral-Water Interfacial Reactions: Kinetics and Mechanisms*, New directions in mineral surface geochemical research using scanning probe microscopes, 1–22. Sparks, D. and Grundl, T. (eds.), American Chemical Society

Huber, G., Huber, H. and Stetter, K. (1986). Isolation and characterization of new metal-mobilizing bacteria. *Biotechnology and Bioengineering* **16** 239–251

Huber, G., Spinnler, C., Gambacorta, A. and Stetter, K. (1989). *Metallosphaera sedula* gen. and sp. nov. represents a new genus of aerobic, metal-mobilizing, thermoacidophilic Archaebacteria. *Systematic and Applied Microbiology* **12** 38–47

Huber, G. and Stetter, K. (1991). *Sulfolobus metallicus*, sp. nov., a novel strictly chemolithoautotrophic thermophilic archaeal species of metal-mobilizers. *Systematic and Applied Microbiology* **14** 372–378

Huber, H., Huber, G. and Stetter, K. (1985). A modified DAPI fluorescence staining procedure suitable for the visualization of lithotrophic bacteria. *Systematic and Applies Microbiology* **6** 105–106

Huber, H. and Stetter, K. (1989). *Thiobacillus prosperus* sp. nov., represents a new group of halotolerant metal-mobilizing Bacteria isolated from a marine geothermal field. *Archives of Microbiology* **151** 479–485

Hulsmann, O., Biltz, W. and Meisel, K. (1935). Beiträge zur systematischen Verwandtschaftslehre. 65. Tensionsanalyse des Systems CoS / CoS_2. *Zeitschrift für Anorganische und Allgemeine Chemie* **224** 73

Hung, A., Muscat, J., Yarovsky, I. and Russo, S. (2002a). Density-functional theory studies of pyrite FeS_2 (100) and (110) surfaces. *Surface Science* **513** 511–524

Hung, A., Muscat, J., Yarovsky, I. and Russo, S. (2002b). Density-functional theory studies of pyrite FeS_2 (111) and (210) surfaces. *Surface Science* **520** 111–119

Ingledew, W. (1982). *Thiobacillus ferrooxidans.* The bioenergetics of an acidophilic chemolitotroph. *Biochimica et Biophysica Acta* **683** 89–117

Jaegermann, W. and Tributsch, H. (1983). Photoelectrochemical reactions of FeS_2 (pyrite) with H_2O and reducing agents. *Journal of Applied Electrochemistry* **13** 743

Johnson, D. (1998). Biodiversity and ecology of acidophilic microorganisms. *FEMS Microbiol. Ecol.* **27** 307–317

Johnson, D. and Roberto, F. (1997). *Biomining: Theory, Microbes and Industrial Processes*, Heterotrophic acidophiles and their roles in the bioleaching of sulfide minerals, 259–279. Rawlings, D. (ed.); Berlin: Springer-Verlag

Juza, R., Biltz, W. and Meisel, K. (1932). Beiträge zur systematischen Verwandtschaftslehre. 57. Das Zustandsdiagramm Pyrit, Magnetkies, Troilit und Schwefeldampf, beurteilt nach Schwefeldampfdrücken, Röntgenbildern, Dichten und magnetischen Messungen. *Zeitschrift für Anorganische und Allgemeine Chemie* **205** 273

Karavaiko, G., Smolskajy, L., Golyshina, O., Jagovkina, M. and Egorova, E. (1994). Bacterial pyrite oxidation: Influence of morphological physical and chemical properties. *FUEL Processing Technology* **40** 151–165

Keller, L. and Murr, L. (1982). Acid-bacterial and ferric sulfate leaching of pyrite single crystals. *Biotechnology and Bioengineering* **24** 83–96

Kelsall, G., Yin, Q., Vaughan, D., England, K. and Brandon, N. (1999). Electrochemical oxidation of pyrite (FeS_2) in aqueous electrolytes. *Journal of Electroanalytical Chemistry* **471** 116–125

Kendall, J., Crittenden, E. and Miller, H. (1923). A study of the factors influencing compound formation and solubility in fused salt mixtures. *Journal of the American Chemical Society* **45** 963

Klein, C. and Hurlbut Jr., C. (1999). *Manual of Mineraolgy.* Mills, C. and Herbert, D. (eds.), John Wiley & Sons, INC.

Konhauser, K., Fyfe, W., Schultze-Lam, S., Ferris, F. and Beveridge, T. (1994). Iron phosphate precipitation by epilithic microbial biofilms in Arctic Canada. *Canadian Journal of Earth Sciences* **31** 1320–1324

Konishi, Y., Asai, S. and Katoh, H. (1990). Bacterial dissolution of pyrite by *Thiobacillus ferrooxidans. Bioprocess Engineering* **5** 231–237

Kullerud, G. (1967). *Researches in Geochemistry*, Sulfide Studies, 286–231. Abelson, P. (ed.), John Wiley and Sons, New York

Leathen, W., Braley Sr., S. and McIntyre, L. (1953). The role of Bacteria in the formation of acid from certain sulfuritic constituents associated with bituminous coal. I. *Thiobacillus Thiooxidans. Applied Microbiology* **1** 61–64

Leduc, L. and Ferroni, G. (1994). The chemolithotrophic bacterium *Thiobacillus ferrooxidans. FEMS Microbiological Reviews* **14** 103–120

de Leeuw, N., Parker, S., Sithole, H. and Ngoepe, P. (2000). Modeling the surface structure and reactivity of pyrite: Introducing a potential model for FeS_2. *Journal of Physical Chemistry* **B 104** 7969–7976

Lundgren, D. (1980). Ore leaching by Bacteria. *Annual Review of Microbiology* **34** 263–283

Lundgren, D., Valkova-Valachanova, M. and Read, R. (1986). Chemical reactions important in bioleaching and bioaccumulation. *Biotechnology and Bioengineering Symposium* **16** 7–22

Luther III, G. (1987). Pyrite oxidation and reduction: Molecular orbital theory consideration. *Geochimica et Cosmochimica Acta* **51** 3193–3215

Luther III, G. (1990). *Aquatic Chemical Kinetics: Reaction Rates of Processes in Natural Waters*, The frontier-molecular-orbital theory approach in geotechnical processes, 173–198. Stumm, W. (ed.), John Wiley & Sons, New York

Lutz, H., Bertram, K., Wrobel, G. and Ridder, M. (1974). Aluminiumchlorid als Transportmittel zum chemischen Transport von Übergangsmetallchalkogeniden. *Monatshefte für Chemie* **105** 849–952

Lutz, H., Schneider, G. and Kliche, G. (1985). Far-Infrared reflection spectra, TO- and LO-phonon frequencies, coupled and decoupled plasmon-phonon modes, dielectric constants, and effective dynamical charges of manganese, iron, and platinum group pyrite type compounds. *Journal of Physics and Chemistry of Solids* **46** 437–443

Lutz, H. and Willich, P. (1974). Pyritstruktur. FIR-Spektren und Normalkoordinatenanalyse von MnS_2, FeS_2 und NiS_2. *Zeitschrift für anorganische und allgemeine Chemie* **405** 176–182

Lyalikova, N. (1960). Participation of *Thiobacillus ferrooxidans* in the oxidation of sulfide ores in pyrite beds of the Middle Ural. *Mikrobiologiya* **29** 382–387

Malouf, E. and Prater, J. (1961). Role of Bacteria in the alteration of sulfide minerals. *Journal of Metals* **13** 353–356

Marsh, R., Norris, P. and Le Roux, N. (1983). *Recent Progress in Biohydrometallurgy*. Rossi, G. and Torma, A. (eds.), Associayone Mineraria Sarda, Iglesias, Italy

May, N., Ralph, D. and Hansford, G. (1997). Dynamic redox potential measurement for determining the ferric leach kinetics of pyrite. *Minerals Engineering* **10** 1279

McKibben, M. and Barnes, H. (1986). Oxidation of pyrite in low temperature acidic solutions: Rate laws and surface textures. *Geochimica et Cosmochimica Acta* **50** 1509–1520

Medvedev, D. and Stuchebrukhov, A. (2001). DNA repair mechanism by photolyase: Electron transfer path from the photolyase catalytic cofactor $FADH^-$ to DNA thymine dimer. *Journal of Theoretical Biology* **210** 237–248

Mernagh, T. and Trudu, A. (1993). A laser raman microprobe study of some geologically important sulphide minerals. *Chemical Geology* **103** 113–127

Mikkelsen, D., Kappler, U., Webb, R., Rasch, R., McEwan, A. and Sly, L. (2007). Visualisation of pyrite leaching by selected thermophilic Archaea: Nature of microorganism-ore interactions during bioleaching. *Hydrometallurgay* **88** 143–153

Morimoto, N., Nakazawa, H., Tokinami, M. and Nishiguchi, K. (1971). Pyrrhotites: Structure type and composition. In *Proceedings IMA-IAGOD Meeting 1970*, Vol. 2, 15–21. Society of Mineralogy and Geology of Japan

Moses, C., Nordstrom, D., Herman, J. and Mills, A. (1987). Aqueous pyrite oxidation by dissolved oxygen and by ferric iron. *Geochimica et Cosmochimica Acta* **51** 1561–1571

Mukherjee, B. (1969). Crystallography of pyrrhotite. *Acta Crystallographica* **B 25** 673–676

Murowchick, J. and Barnes, H. (1987). Effects of temperature and degree of supersaturation on pyrite morphology. *American Mineralogist* **72** 11–12

Nakazawa, H. and Morimoto, N. (1971). Phase relations and superstructures of pyrrhotite, $Fe_{1-x}S$. *Material Research Bulletin* **6** 345–358

Nathanson, A. (1902). Über eine neue Gruppe von Schwefelbakterien und ihren Stoffwechsel. *Mitteilungen aus dem Zoologischen Staatsinstitut Neapel* **15** 655–680

Ndlovu, S. and Monhemius, A. (2005). The influence of crystal orientation on the bacterial dissolution of pyrite. *Hydrometallurgy* **78** 187–197

Nesbitt, H., Bancroft, G., Pratt, A. and Scaini, M. (1998). Sulfur and iron surface states on fractured pyrite surfaces. *American Mineralogist* **83** 1067–1076

Nesbitt, H. and Muir, I. (1994). X-ray photoelectron spectroscopic study of a pristine pyrite surface reacted with water vapor and air. *Geochimica et Cosmochimica Acta* **58** 4667–4679

Nordstrom, D. (1982). *Acid Sulfate Weathering*. Soil Science Society of America

Nordstrom, D. and Southam, G. (1997). Geomicrobiology of sulfide mineral oxidation. *Reviews in Mineralogy and Geomicrobiology* **35** 361–390

Norman, P. and Snyman, C. (1988). The biological and chemical leaching of an auriferous pyrite/arsenopyrite flotation concentrate: A microscopic examination. *Geomicrobiology Journal* **6** 1–10

Norris, P. (1997). *Biomining: Theory, Microbes and Industrial Processes*, Thermophiles and bioleaching, 247–258. Rawlings, D. (ed.); Berlin: Springer-Verlag

Norris, P. and Barr, D. (1988). *Biohydrometallurgy: Proceedings of the International Symposium on Biohydrometallurgy*, Bacterial oxidation of pyrite in high temperature reactors, 532–536. Norris, P. and Kelly, D. (eds.), Science and Technology Letters, Kew Surrey, England

Norris, P. and Parrott, L. (1986). *Fundamental and Applied Biohydrometallurgy: Proceedings*, High temperature, mineral concentrate dissolution with *Sulfolobus*, 355–365. Lawrence, R. and Branton, R. (eds.), Elsevier, Amsterdam

Palmer, D. (2000). *CrystalMaker Software*. Bicester, Oxfordshire, England

Parker, H. and Whitehouse, W. (1932). Crystal structure of pyrite, FeS_2. *Philosophical Magazine* **14** 939–961

Paulitsch, P. (1951). Zur Häufigkeit der Pyritformen. *Mineralogy and Petrology* **2** 388–392

Pearce, C., Pattrick, R. and Vaughan, D. (2006). Electrical and magnetic properties of sulfides. *Reviews in Mineralogy and Geochemistry* **61** 127–180

Pemsler, J., Lam, R. and Litchfield, J. (1990). Discharge behavior and thermal stability of synthetic FeS_2 cathode material. *Journal of the Electrochemical Society* **137** 1–7

Powell, A. and Parr, S. (1919). A study of the forms in which sulfur occurs in coal. *West Virginia University Bulletin* **111** 1–62

Rawlings, D. (2002). Heavy metal mining using microbes. *Annual Review of Microbiology* **56** 65–91

Razzell, W. and Trussell, P. (1963). Isolation and properties of an iron-oxidiyzing *Thiobacillus*. *Journal of Bacteriology* **85** 595–603

Rickard, D. and Luther, G. (1995). *Geochemical Transformation of Sedimentary Sulfur*, Chemistry of iron sulfides in sedimentary environments, 168–193. Vairavamurthy, M. and Schoonen, M. (eds.), American Chemical Society Symposium Series 612, Washington, D.C.

Rimstidt, J. and Vaughan, D. (2003). Pyrite oxidation: A state-of-the-art assessment of the reaction mechanism. *Geochimica et Cosmochimica Acta* **67** 873–880

Rodríguez, Y., Ballester, A., Blazquez, M., González, F. and Munoz, J. (2003). Study of bacterial attachment during the bioleaching of pyrite, chalcopyrite, and sphalerite. *Geomicrobiology Journal* **20** 131–141

Rodríguez-Leiva, M. and Tributsch, H. (1988). Morphology of bacterial leaching patterns by *Thiobacillus ferrooxidans* on synthetic pyrite. *Archives of Microbiology* **149** 401–405

Rohwerder, T., Gehrke, T., Kinzler, K. and Sand, W. (2003). Bioleaching review part A: Progress in bioleaching: Fundamentals and mechanisms of bacterial metal sulfide oxidation. *Applied Microbial Biotechnology* **63** 239–248

Rojas-Chapana, J., Giersig, M. and Tributsch, H. (1996). The path of sulfur during the bio-oxidation of pyrite by *Thiobacillus ferrooxidans*. *FUEL* **75** 923–930

Rosenquist, T. (1954). A thermodynamic study of the iron, cobalt and nickel sulphides. *Journal of Iron and Steel Instruments* **176** 37–57

Rosso, K. (2001). Structure and reactivity of semiconducting mineral surfaces: Convergence of molecular modeling and experiment. *Reviews in Mineralogy and Geochemistry* **42** 199–271

Rosso, K., Becker, U. and Hochella jr., M. (1999). The interaction of pyrite {100} surfaces with O_2 and H_2O: Fundamental oxidation mechanisms. *American Mineralogist* **84** 1549–1561

Rosso, K., Becker, U. and Hochella jr., M. (2000). Surface defects and self-diffusion on pyrite {100}: An ultra-high vacuum scanning tunneling microscopy and theoretical modeling study. *American Mineralogist* **85** 1428–1436

Rosso, K. and Vaughan, D. (2006). Sulfide mineral surfaces. *Reviews in Mineralogy and Geochemistry* **61** 505–556

Rudolfs, W. (1922). Oxidation of iron pyrites by sulfur-oxidizing organisms and their use for making mineral phosphates available. *Soil Science* **14** 135–147

Sand, W. and Gehrke, T. (2006). Extracellular polymeric substances mediate bioleaching/biocorrosion via interfacial processes involving iron(III) ions and acidophilic bacteria. *Research in Microbiology* **157** 49–56

Sand, W., Gehrke, T., Jozsa, P.-G. and Schippers, A. (2001). (Bio)chemistry of bacterial leaching - direct vs. indirect bioleaching. *Hydrometallurgy* **59** 159–175

Sanhueza, A., Ferrer, I., Vargas, T., Amils, R. and Sanchez, C. (1999). Attachment of *Thiobacillus ferrooxidans* on synthetic pyrite of varying structural and electronic properties. *Hydrometallurgy* **51** 115–129

Sasaki, K. (1994). Effect of grinding on the rate of oxidation by oxygen in acid solution. *Geochimica et Cosmochimica Acta* **58** 4649–4655

Schaufuß, A., Nesbitt, H., Kario, I., Laajalehto, K., Bancroft, G. and Szargan, R. (1998). Reactivity of surface chemical states on fractured pyrite. *Surface Science* **411** 321–328

Schäfer, H. (1964). *Chemical Transport Reactions*. Academic Press: New York

Schieck, R., Hartmann, A., Fiechter, S., Könenkamp, R. and Wetzel, H. (1990). Electrical properties of natural and synthetic pyrite (FeS_2) crystals. *Journal of Materials Research* **5** 1567–1572

Schippers, A., Jozsa, P. and Sand, W. (1996). Sulfur chemistry in bacterial leaching of pyrite. *Applied and Environmental Microbiology* **62** 3424–3431

Schippers, A. and Sand, W. (1999). Bacterial leaching of metal sulfides proceeds by two indirect mechanisms via thiosulfate or via polysulfides and sulfur. *Applied and Environmental Microbiology* **65** 319–321

Schmidt, C. and Ziemann, A. (2000). In-situ raman spectroscopy of quartz: A pressure sensor for hydrothermal diamond-anvil cell experiments at elevated temperatures. *American Mineralogist* **85** 1725–1734

Schoonen, M. and Barnes, H. (1991a). Reactions forming pyrite and marcasite from solution: I. Nucleation of FeS_2 below 100°C. *Geochimica et Cosmochimica Acta* **55** 11495–1504

Schoonen, M. and Barnes, H. (1991b). Reactions forming pyrite and marcasite from solution: II. Via FeS precursors below 100°C. *Geochimica et Cosmochimica Acta* **55** 1505–1514

Schoonen, M. and Barnes, H. (1991c). Mechanisms of pyrite and marcasite formation from solution: III. Hydrothermal processes. *Geochimica et Cosmochimica Acta* **55** 3491–3504

Schulz, H., Brinkhoff, T., Ferdelman, T., Hernandez-Marine, M., Teske, A. and Jörgensen, B. (1999). Dense populations of a giant sulfur bacterium in namibian shelf sediments. *Science* **284** 493–495

Segerer, A., Burggraf, S., Fiala, G., Huber, G., Huber, R., Pley, U. and Stetter, K. (1993). Life in hot springs and hydrothermal vents. *Origins of Life and Evolution of the Biosphere* **23** 77–90

Siebert, D. and Stocker, W. (1992). Investigation of a (100) surface of pyrite by STM. *Physica status solidi* **A 134** K17–20

Silverman, M. and Ehrlich, H. (1964). Microbial formation and degradation of minerals. *Advanced and Applied Microbiology* **6** 153–206

Silverman, M., Rogoff, M. and Wender, I. (1961). Bacterial oxidation of pyritic materials in coal. *Applied Microbiology* **9** 491–496

Singer, P. and Stumm, W. (1970). Acidic mine drainage: the rate-determining step. *Science* **167** 1121–1123

Smith, F. (1942). Variation in the properties of pyrite. *American Mineralogist* **27** 1–19

Sokolova, G. and Karavaiko, G. (1968). *Physiology and Geochemical Activity of Thiobacilli*. Rabinovitz, E. (ed.), US Dept Commerce, Springfield, Virginia

Sourisseau, C., Cavagnat, R. and Fouassier, M. (1991). The vibrational properties and valence force fields of FeS_2, RuS_2 pyrites and FeS_2 marcasite. *Journal of Physics and Chemistry of Solids* **52** 537–544

Spangenberg, K. (1935). *Handwörterbuch der Naturwissenschaften, Bd. 10*, Wachstum und Auflösung der Kristalle, 362–401. Gustav Fischer Verlag, Jena

Stetter, K. (1989). *Bergey's Manual of Systematic Bacteriology*, Vol. 9, Order III. *Sulfolobales* ord. nov, 2250–2253. Staley, J., Bryant, M., Pfennig, N. and Holt, J. (eds.), Baltimore - Hong Kong - London - Sydney, Williams & Willkins

Tasker, P. (1979). The stability of ionic crystal surfaces. *Journal of Physics* **C 12** 4977–4984

Taylor, J. and Whelan, P. (1943). The leaching of cuprous pyrite and the precipitation of copper at Rio Tinto, Spain. *Transactions of the Institution of Mining and Metallurgy* **52** 35–71

Taylor, L. and Williams, K. (1972). Smythite, $(Fe,Ni)_9S_{11}$ - a redefinition. *American Mineralogist* **57** 1571–1577

Temple, K. and Colmer, A. (1951). The autotrophic oxidation of iron by a new bacterium - *Thiobacillus ferrooxidans*. *Journal of Bacteriology* **62** 605–611

Temple, K. and Delchamps, E. (1953). Autotrophic bacteria and the formation of acid in bituminous coal mines. *Applied Microbiology* **1** 255–258

Tomm, Y., Schiek, R., Ellmer, K. and Fiechter, S. (1995). Growth mechanism and electronic properties of doped pyrite (FeS_2) crystals. *Journal of Crystal Growth* **146** 271–276

Tributsch, H. (1976). The oxidative disintegration of sulfide crystals by *Thiobacillus ferrooxidans*. *Naturwissenschaften* **63** 88

Tributsch, H. (2001). Direct versus indirect bioleaching. *Hydrometallurgy* **59** 177–185

Trudinger, P., Lambert, I. and Skyring, G. (1972). Biogenic sulfide ores: A feasibility study. *Economic Geology* **67** 1114–1127

Tuovinen (1990). *Microbial mineral recovery*, Biological fundamentals of mineral leaching processes, 55–77. Ehrlich, H. and Brierley, C. (eds.), McGraw, New York

Uda, M. (1967). The structure of synthetic Fe_3S_4 and the nature of transition to FeS. *Zeitschrift für Anorganische und Allgemeine Chemie* **350** 105–109

Ueshima, M., Fortin, D. and Kalin, M. (2004). Development of iron-phosphate biofilms on pyritic mine waste rock surfaces previously treated with natural phosphate rocks. *Geomicrobiology Journal* **21** 313–323

Ushioda, S. (1972). Raman scattering from phonons in iron pyrite (FeS_2). *Solid State Communications* **10** 307–310

Verble, J. and Wallis, R. (1969). Infrared studies of lattice vibrations in iron pyrite. *Physical Review* **182** 783–789

Vishniac, W. (1974). *Bergey's manual of determinative bacteriology*, The genus *Thiobacillus*, 456–461. Buchanan, R. and Gibbons, N. (eds.), Williams and Wilkins, Baltimore

Vogt, H., Chattopadhyay, T. and Stolz, H. (1983). Complete first-order Raman spectra of the pyrite structure compounds FeS_2, MnS_2 and SiP_2. *Journal of Physics and Chemistry of Solids* **44** 869–873

Waksman, S. and Jåffe, J. (1921). Acid production by a new sulfur-oxidizing bacterium. *Science* **53** 216

Waksman, S. and Jåffe, J. (1922). Microorganisms concerned in the oxidation of sulphur in the soil II. *Thiobacillus thiooxidans*, a new suphur-oxidizing organism isolated from the soil. *Journal of Bacteriology* **7** 239–256

Wöhler, W. (1836). Künstliche Bildung von krystallisiertem Schwefelkies. *Liebigs Annalen* **17** 260

Wilke, K.-T. and Bohm, J. (1988). *Kristallzüchtung*. VEB Deutscher Verlag der Wissenschaften

Wilke, K.-T., Schultze, D. and Töpfer, K. (1967). Kristallisation von Disulfiden aus Schmelzlösungen. *Journal of Crystal Growth* **1** 41–44

Willeke, G., Blenk, O., Kloc, C. and Bucher, E. (1992a). Preparation and electrical transport properties of pyrite (FeS_2) single crystals. *Journal of Alloys and Compounds* **178** 181–191

Willeke, G., Dasbach, R., Sailer, B. and Bucher, E. (1992b). Thin pyrite (FeS_2) films prepared by magnetron sputtering. *Thin Solid films* **213** 271–276

Winogradsky, S. (1887). Über Schwefelbakterien. *Botanische Zeitung* **45** 489–507

Woese, C. (1977). Endosymbionts and mitochondiral origins. *Journal of Molecular Evolution* **10** 93–96

Wolf, E., Oppermann, H., Krabbes, G. and Reichelt, W. (1978). *Current Topics in Materials Science*, 697. Kaldis, E. (ed.), North-Holland, Amsterdam

Yamada, S., Nanjo, J., Nomura, S. and Hara, S. (1979). Morphology of iron pyrite crystals. *Journal of Crystal Growth* **46** 10–14

Yamaguchi, S. and Wada, H. (1973). Fe_2S_3 of the spinel type structure with lattice defect. *Kristall und Technik* **8** 1017–1019

Yund, R. and Hall, H. (1968). The miscibility gap between FeS and $Fe_{1-x}S$. *Materials Research Bulletin* **3** 779–784

Zwinscher, J. and Lutz, H. (1995). Lattice dynamics of spinel-type chlorides, oxides, sulphides and selenides. *Journal of Alloys and Compounds* **219** 103–106